CONTENTS

NUMERICAL ANALYSIS OF THERMAL COMFORT PARAMETERS IN LIVING QUARTERS

Aneta BOHOJŁO*

*phD student, Faculty of Mechanical Engineering, Bialystok University of Technology, ul. Wiejska 45 C, 15-351 Białystok

aneta.bohojlo@gmail.com

Summary: This paper includes an evaluation of ventilation conditions in a given living quarters – a room in a single-family house, based on local parameters of thermal comfort determined by numerical calculations. Global parameters (Predicted Mean Vote and Predicted Percentage of Dissatisfied) and local parameters (including: Resultant Temperature, Relative Humidity) were determined from numerical solution of transient case of living quarters ventilation in ANSYS-CFX software.

1. INTRODUCTION

Numerical modelling of ventilation in living quarters, office space and utility rooms has been a subject of many scientific papers over the past few years (Abanto et al., 2004; Evola and Popov, 2006; Lin et al., 2007; Stamou and Katsiris, 2006). Doing this kind of calculations allows an in-depth analysis of the ventilation issues already on the project stage, which significantly lowers the cost of the investment.

The goal of this paper is to determine the influence of a chosen ventilation type on the thermal comfort in living quarters by analysing the thermal comfort parameters which are the results of numerical calculations done in ANSYS-CFX software.

Defining the notion of thermal comfort in rooms is difficult, because it is highly individual and subjective. In order to define thermal comfort of large groups of people, special parameters of thermal comfort have been established. These factors were divided by the PN-EN ISO 7730:2006(U) norm into: global, comprehensively determining personal sensations, and local, describing the effect the particular elements of a micro-climate have on the satisfaction or dissatisfaction with the conditions in a given room and describing the negative effects they have on particular body parts.

2. THERMAL COMFORT FACTORS

Thermal comfort and discomfort factors were described in PN-EN ISO 7730: 2006(U) norm. The most important parameters of global comfort were considered to be the PMV – Predicted Mean Vote – expressed in a scale from -3 to +3 and PPD – Predicted Percentage of Dissatisfied. Local comfort and discomfort factors include: Draught Rating, Local Thermal Discomfort Caused by Warm or Cold Floor and Vertical Air Temperature Difference Between Head and Ankles.

PMV is calculated from the formula: (Fanger**,** 1974):

$$PMV = \left(0{,}352e^{-0{,}042(Q_M/A_{Du})} + 0{,}032\right)\{\frac{Q_M}{A_{Du}}(1-\eta) - 0{,}35\left[43 - 0{,}061\frac{Q_M}{A_{Du}}(1-\eta) - p_w\right] - 0{,}42\left[\frac{Q_M}{A_{Du}}(1-\eta) - 50\right] - 0{,}0023\frac{Q_M}{A_{Du}}(44-p_w) - 0{,}0014\frac{Q_M}{A_{Du}}(34-t_w) - 3{,}4\cdot 10^{-8}f_{cl}\left[(t_{cl}+273)^4 - (T_{mrt}+273)^4\right] - f_{cl}\alpha_k(t_{cl}-t_w)\} \quad (1)$$

where: A_{Du} is the DuBois area (surface area of a human body) $[m^2]$, Q_M is the metabolic heat $[W]$, η is the physical fitness p_w– partial pressure of water vapour in the surrounding air [mmHg], t_w is the air temperature [℃], f_{cl} is the ratio of the surface area of clothed body to the surface area of exposed body, t_{cl} – mean temperature of the clothed surface of human body [℃], T_{mrt} – mean radiant temperature [℃], α_k is the heat transfer through convection $[W/(m^2K)]$. The temperature t_{cl} is calculated from the formula:

$$t_{cl} = 35{,}7 - 0{,}032\frac{Q_M}{A_{Du}}(1-\eta) - 0{,}18\Lambda_{cl} \quad (2)$$
$$\{3{,}4\cdot 10^{-8}f_{cl}\left[(t_{cl}+273)^4 - (T_{mrt}+273)^4\right] + f_{cl}\alpha_k(t_{cl}-t_w)\}$$

where: Λ_{cl} is the thermal resistance coefficient of clothing [clo].

The Predicted Percentage of Dissatisfied expresses the heat sensations of a group of people dissatisfied with the thermal conditions in a given room. It is calculated from the formula (Fanger**,** 1974):

$$PPD = 100 - 95e^{(0{,}03353PMV^4 + 0{,}2179PMV^2)} \quad (3)$$

Draught Rating (DR) is calculated as follows (PN-EN ISO 7730:2006):

$$DR = (34-t)(\mathrm{v}-0{,}05)^{0{,}62}(0{,}37\mathrm{v}T_u + 3{,}14) \quad (4)$$

where: t and v is, respectively, temperature [℃] and mean air velocity $[m/s]$, T_u is the turbulence intensity; formula (4) is applicable within these parameters: $t = 20℃ \div 26℃$, $v < 0{,}5\ [m/s]$ i $T_u = 10\% \div 6\%$; for $v < 0{,}05\ [m/s]$ it is presumed that $v = 0{,}05\ [m/s]$, and in case of $DR >$

100%, the value of $DR = 100\%$ is accepted;

An important local indicator of thermal comfort is also the relative humidity *RH* calculated from the formula:

$$RH = \frac{\rho}{\rho_m} 100\% \; ; \tag{5}$$

ρ – water vapour density, ρ_m – density of saturated water vapour.

The felt air temperature is described numerically by determining the *DRT* – Dry Resultant Temperature, calculated from the formula (Awbi, 2003):

$$DRT = \frac{t_{mrt}+3{,}17\sqrt{v}}{1+3{,}17\sqrt{v}} [°C]; \tag{6}$$

where: t_{mrt} mean radiant temperature [°C], calculated from Stefan – Boltzman law, t – temperature [°C] I v – air velocity $[m/s]$; for $v < 0{,}1\ [m/s]$ it is presumed that $DRT = (tmrt+t)/2$.

PDV – percentage of dissatisfied from vertical air temperature difference between head and feet – is calculated from the following ratio (PN-EN ISO 7730):

$$PDV = \frac{100}{1+e^{(5{,}76-0{,}856\Delta t_v)}}, \tag{7}$$

where $\Delta t_v < 8$°C is the difference in temperatures between head and feet measured vertically [°C];

PDF – percentage of dissatisfied caused by warm or cold floor – is calculated from the formula (PN-EN ISO 7730):

$$PDF = 100 - 94e^{(-1{,}387+0{,}118t_f-0{,}0025t_f^2)}, \tag{8}$$

where t_f – floor temperature [°C].

After performing a numerical simulation of the ventilation in ANSYS-CFX, an evaluation of thermal comfort has been conducted. In order to do so, the global, *PMV* (1) and *PPD* (3), and local, *DR* (4), *RH* (5), *DRT* (6), *PDV* (7), *PDF* (8) parameters were applied.

3. DESCRIPTION OF LIVING QUARTERS

The calculations were done for an actual living quarter located in a single-family house from the 1970's. The geometry of the room with most important features is presented in Fig. 1. It represents the flow domain filled with work fluid. Because of the need to reduce the number of nodes in computational grid, shapes of most of the elements have been simplified. Such simplifications are commonly used in numerical calculations regarding the ventilation problems (Evola and Popov, 2006; Lin et al., 2007; Stamou and Katsiris, 2006), rarely are there publications where the geometry of the elements is more complex (Abanto et al, 2004; Sorensen and Voigt, 2003).

Room dimensions: 4m x 4m x 2,8m. The calculations include the following heat sources: human, radiator, computer and chandelier. Heat penetration through external walls and window was also taken into consideration. Heat gain from sunshine was neglected.

The room is ventilated using a trickle vent, and the air-exhaust is done through a vent connected to ventilation chimney. Air flow (inflow and outflow) is also possible through a crack under the door leading to the rest of the house.

Crack dimensions: 0,8m x 0,02m.

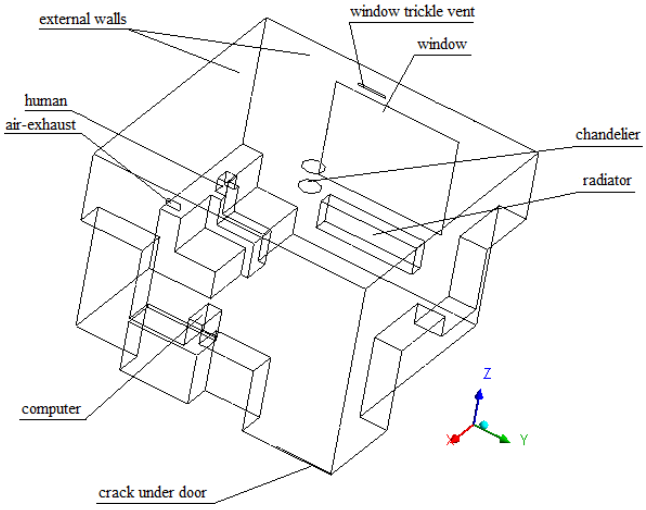

Fig. 1. Geometry of the subject room

4. MATHEMATICAL MODEL

The flow of air (working fluid) in a given room is governed by the basic laws of mechanics: conservation of mass, conservation of momentum and conservation of energy. These are their differential forms:

– continuity equation:

$$\frac{\partial \rho}{\partial t} + \nabla \cdot \left(\rho \vec{V}\right) = 0; \tag{9}$$

where ρ – density of the working fluid, $\vec{V}$ – is the velocity vector;

– Navier-Stokes equation:

$$\frac{\partial (\rho \vec{V})}{\partial t} + \nabla \cdot \left(\rho \vec{V} \otimes \vec{V}\right) = -\nabla p + \nabla \cdot \tau + \vec{f}; \tag{10}$$

where p is the pressure and

$$\tau = \mu(\nabla \vec{V} + \nabla \vec{V})^T - \frac{2}{3}\delta \nabla \cdot \vec{V}); \tag{11}$$

is the stress tensor, $\vec{f}$ – body forces

– energy equation:

$$\frac{\partial (\rho h_c)}{\partial t} - \frac{\partial p}{\partial t} + \nabla \cdot \left(\rho \vec{V} h_c\right) = \nabla \cdot (\lambda \nabla T) + \nabla\left(\vec{V} \cdot \tau\right) + \vec{V} \cdot \vec{f} + S_E \tag{12}$$

where $h_c = e + \frac{p}{\rho} + \frac{1}{2}V^2$ – total enthalpy, e – internal energy, λ – thermal conductivity, S_E – heat source.

The equations presented above need to be supplemented with proper initial and boundary conditions.

In case of turbulent flow, solving the Navier-Stokes equations is ineffective, because of the limited capabilities of modern computers, which does not allow for the proper density of computational grid. Because of this, the equations are substituted with Reynolds equations. In order to close the set of equations, additional equations are needed – the 'turbulence model'. In this paper, the $k - \varepsilon$ turbulence model was utilized in an RNG modified form, widely used in this type of calculations (Abanto J et al 2004).

The ANSYS-CFX software solves the fluid flow and heat transfer problems described by RANS equations using the control volume method, utilizing the shape function for estimating the variables within the control volume (ANSYS-CFX, 2006).

5. NUMERICAL MODELLING

Numerical modelling utilizing the ANSYS-CFX requires creating a geometrical model, computational grid, choosing the work fluid, determining the model of heat transfer and the type of flow (the turbulence model), defining the initial and boundary conditions, selecting the solution parameters and conducting the calculations.

In this case, the working fluid is a humid air, consisting of dry air (ideal gas parameters) and water vapour. Water vapour parameters were taken from the IAPWS IF97 library implemented in the ANSYS-CFX software. Additionally, a distinction was made between "fresh" air, flowing from outside, and "old" air, present in the room. As a result, the working fluid was a mixture (ideal) of "old" air, water vapour, and "fresh" air. The distinction of different kinds of air in the mixture allowed an easy analysis of air flowing from outside. Because of the importance of natural convection in the analysed case, the physical flow model included the gravity. Defining the thermal comfort parameters required determining the mean radiant temperature; in the physical model of the process the Discrete Transfer radiation model, recommended for this type of calculations by the ANSYS-CFX documentation, was applied.

The simulation was divided into two stages. The first stage was a transient simulation of natural convection caused by an abrupt "switching on" the internal heat sources: radiator (350W), chandelier (50W) and computer (95W). In still air, which was initially thermally homogeneous (20°C) with relative humidity of 40%, the human influence was also included. A person resting in seated position generates a heat flux (20W) and mass flow rate of water vapour (41 g/h) (Fanger**,** 1974). The calculations included the heat losses through non-transparent boundaries (external walls) with heat transfer coefficient of building build between 1976-1983, equalling 1,163 W/(m^{2}K) established according to PN-74/B03404 norm; and heat transfer coefficient of windows equalling 1,1 W/(m^{2}K). Reference pressure was 0.1MPa. For the purpose of these calculations, the outside temperature was assumed to be -5°C. The door to the room was closed, but the air flow was possible through the crack under the door (Fig. 1) with pressure difference equalling 0Pa. The air flowing out from the room had a temperature of 20°C and relative humidity of 40%.

In the second stage, 10 seconds after "switching on" the heat sources, the window vent was opened, which allowed the inflow of outside air of temperature -5°C and relative humidity 100%, as well as the air exhaust (outflow with 0.5Pa pressure difference) connected to ventilation chimney. The inflow of the outside air had a constant velocity of 0.5m/s, normal to the inflow surface. The calculations were continued until t=55s.

The calculations used RNG k-ε turbulence model with scaled wall function; the intensity of turbulence was set to 5%.

6. RESULTS. DISCUSSION

The calculations used a grid with 169338 nodes. The simulation was conducted until t=55s. The results presented in this paper reflect the thermal comfort for that moment.

In the first stage of simulation, that is during the natural convection over internal heat sources: human, radiator, computer and chandelier, a convective current moving up towards ceiling could be observed. The most intensive ascending stream was located over the radiator, parallel to the surface of window.

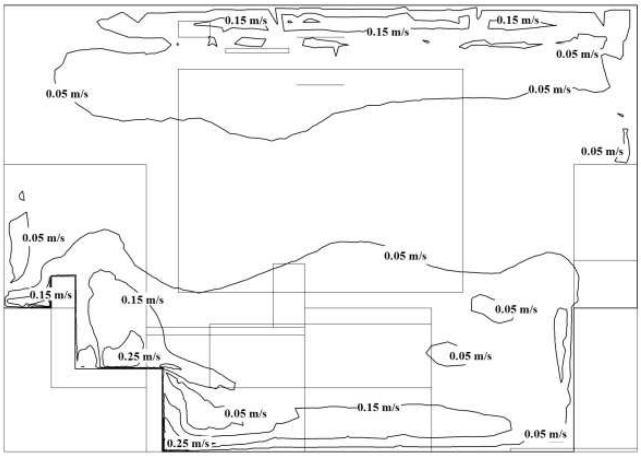

Fig. 2. Velocity isolines in plane x=1m, going through the resting person, for *t*=55s

After opening the air vent and air-exhaust, cold air of temperature -5°C began to flow inside. Relatively strong convection current in the plane of window, moving upwards, caused a turbulence of air close to the ceiling. Cold air, warmed after contacting the warmer convection current moved from the window vent towards the ceiling, towards the corner of the room on the left side of the window and further down the wall towards the sitting person or moved directly down along the window. The movement of air in the room had significant influence on the thermal comfort in the room.

Fig. 2. presents the velocity isolines in plane x=1 going through the resting person and parallel to the window. Although the plane was distanced from the window (where the air velocity reached 0.68m/s), an eddy flow close to the ceiling could be observed, caused by the convection current which in turn was caused by the radiator. The highest velocity – around 1.36m/s – was reached close to the air-exhaust. The air flow through the door crack reached 0.96m/s. In the area around the sitting person the air velocity equalled 0.05÷0.35m/s and in some places exceeded velocity acceptable in winter conditions, that is 0.2÷0.3m/s.

Draught Rating (predicted percentage of people dissatisfied with the draught) reached its highest value around the door crack – up to 40%. *DR* was around 10÷13% near the window, that is close to the strongest convective currents and close to window vent and air-exhaust. Fig. 3. presents the area of constant value of the *DR*=3%. In most areas of the room the *DR* value was much lower.

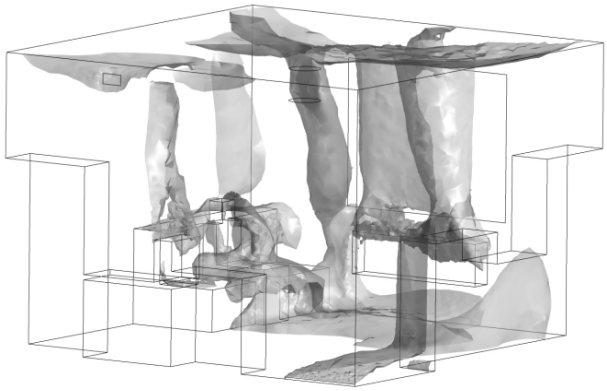

Fig. 3. Surface with constant indicator value *DR*=3% for *t*=55s

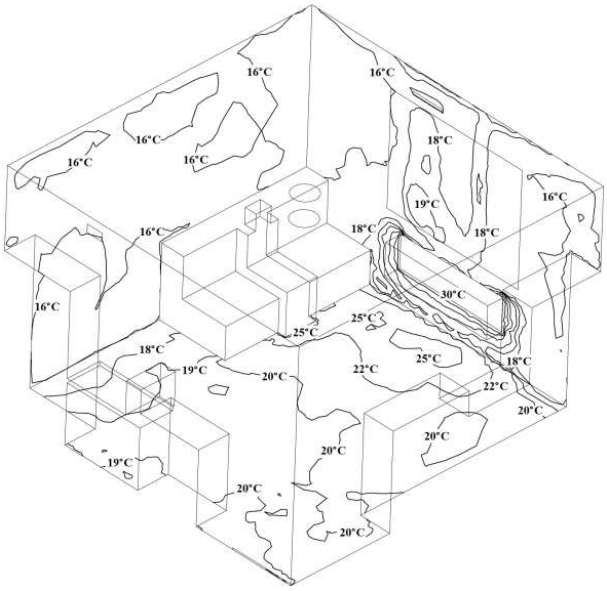

Fig. 4. Isotherms on the floor and external wall surface for *t*=55s

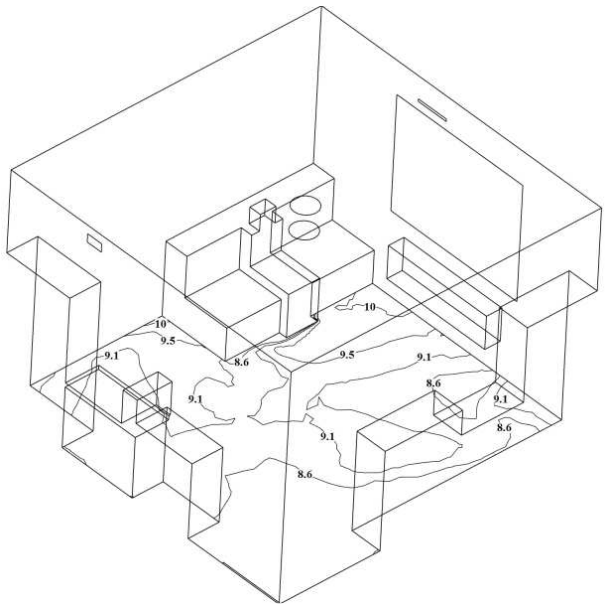

Fig. 5. Isolines of the *PDF* indicator (predicted percentage of people dissatisfied with floor temperature) for *t*=55s

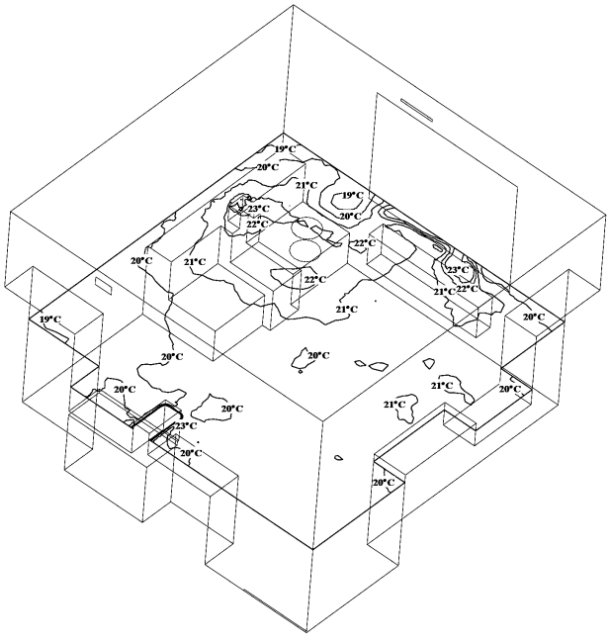

Fig. 6. *DRT* isotherms for a plane distanced by 1.1m for *t*=55s

The temperature of air in the room varied from -5°C on the surface of air vent up to 50°C on the radiator surface and 45°C on the chandelier's surface. Fig. 4. shows the isotherms on the floor and external walls of the analysed room. Because of the internal heat sources, the temperatures of window, external walls and floor around the radiator rose, which caused a rise in the predicted percentage of dissatisfied with floor temperature – *PDF* – Fig. 5. In the rest of the room this indicator was within the range of 8.5÷9.5%.

Fig.6. shows the isolines of *DRT* resultant temperature in plane parallel to the floor, distanced by 1.1m. This plane is located on the head level of a sitting person. Temperature felt for *t*=55s is slightly higher than the 20÷22°C recommended in winter conditions – this is caused mostly by the heat generated by the internal heat sources.

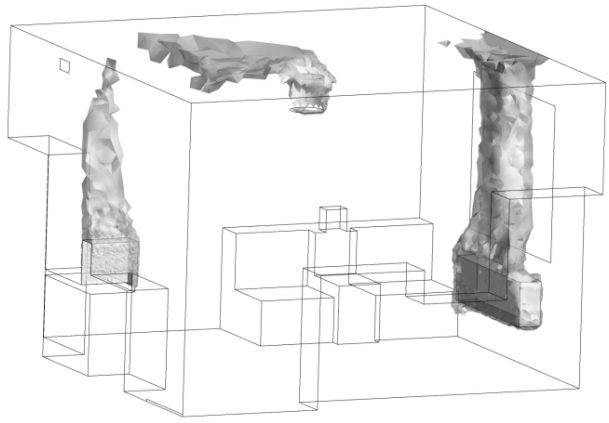

Fig. 7. Relative humidity *RH*≤40% for *t*=55s

Internal heat sources have tremendous effect on the thermal comfort conditions in a room. The effect of such sources is clearly visible in Fig. 7., which presents the part of the room with relative humidity lower than 40% – un-

comfortable for human. Observation of humidity distribution behaviour over time shows a growing area of uncomfortably low relative humidity *RH*, caused by internal heat sources and convection currents caused by them.

The predicted percentage of people dissatisfied with the difference of temperatures between head and ankles (*PDV*) was calculated for a seated person, presuming the ankle level to be 0.1m and head level 1.2m. The *PDV* factor distribution, presented in Fig. 8., shows that the *PDV* is low and for the majority of the room is lower than 1%. With passing time the value of the *PDV* indicator rises slightly in the vicinity of radiator and computer, that is in areas where human presence is physically impossible.

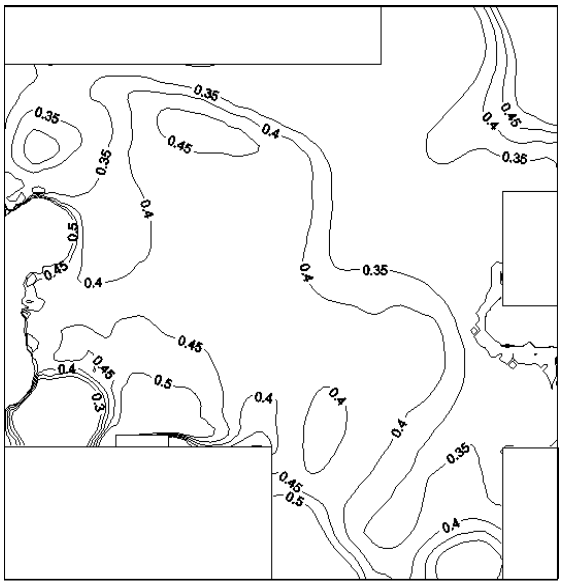

Fig. 8. Isolines of the *PDV* indicator (predicted percentage of people dissatisfied with the difference of temperatures between head and ankles) for *t*=55s

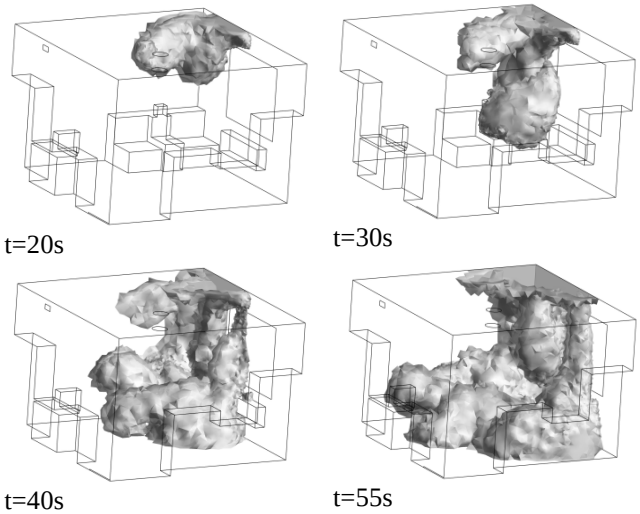

Fig. 9. Graphs of volume of air containing at least 0.01 mass fraction of fresh air after t=20, 30, 40 and 55s

Dividing the working fluid into two types: fresh air (outside) and old air (inside) in the physical model allowed visualising the inflow of outside air and observing its distribution in the room. Fig. 9. shows the graphs of volume of air containing at least 0.01 mass fraction of fresh air after *t*=20, 30, 40 and 55s. These graphs show the process of spreading of fresh air flowing from outside. The air flowing from the window vent moves towards the corners of the room, between the window and the sitting person, flows down, is partially lifted by the convection current from the radiator and moves up, towards the ceiling, along the window plane. Inside the room, after 55 seconds, 22% of the total area in room contains at least 0.01 mass fraction of fresh air.

Determining the global thermal comfort parameters *PMV* (1) and *PPD* (3) requires calculating the body temperature t_{cl}, which is achieved by solving a non-linear equation (2). This requires programming a calculation procedure in Fortran. Because of the lack of Fortran compiler compatible with ANSYS-CFX, this paper is limited to determining the average values of global thermal comfort parameters *PMV* and *PPD* for the whole room. For this purpose the calculator published on www.healthyheating.com/solutions.htm web-page was used.

The calculations assumed the following values: energy flux caused by a person in the room was equal 1 met (for a person resting in a seated position) and the thermal resistance coefficient of clothing was equal 0,6 clo. The following values were taken from the ANSYS-CFX postprocessor : the mean radiant temperature average in the room 20.91°C, the average relative humidity 44.41%, the average air velocity 0.075m/s and average air temperature 20,58°C. The calculations resulted in the following global thermal comfort parameters: *PMV*= - 1.3 , *PPD*=40.3%.

Based on these results it can be said that the conditions in the analysed room would not be comfortable for 40.3% of people staying in this room. The resulting average *PMV* means that a large group of people would describe their heat sensation as cold or relatively cold.

The goal of this paper was to determine the thermal comfort parameters in living quarters using numerical modelling. Numerical modelling allows for a quick analysis of the influence the type of ventilation has on thermal comfort conditions in living quarters. For this kind of calculations, very important is the creating of proper physical model of the fluid flow and heat transfer problem. The quality of the result is heavily influenced by the computational grid. In other words, in order to obtain good quality results, the calculations require dense computational grid and good computer equipment.

REFERENCES

1. **Abanto J., Barrero D., Reggio M., Ozell B.** (2004)**,** Airflow modeling in a computer room, *Building and Environment 39*, 1393-1402 ANSYS-CFX Release 11.0: Theory,2006.
2. **Ampofo F., Maidment G., Missenden J**. (2004), Underground railway environment in the UK Part 1: Review of thermalcomfort, *Applied Thermal Engineering 24*, 611–631.
3. **ANSYS-CFX** (2006) Release 11.0: Theory.
4. **Awbi H. B. (**2003), Ventilation of Buildings, *Taylor&Francis*.
5. **Bohojło A**. *(*2010), Wyznaczanie parametrów komfortu cieplnego w pomieszczeniu mieszkalnym, *Budownictwo i Inżynieria Środowiska Vol.1 No.1*.

6. **Bohojło A.** (2008)**,** *Modelowanie systemu wentylacji pomieszczeń z wykorzystaniem programu ANSYS-CFX*, praca dyplomowa, Politechnika Białostocka, Wydział Mechaniczny, TCiMPS.
7. **Bohojło A**., **Kołodziejczyk M.** (2009)**,** Modelowanie numeryczne parametrów lokalnych komfortu cieplnego, *Acta Mechanica et Automatica, Vol.3 No.1*.
8. **Evola G., Popov V.** (2006), Computational analysis of wind driven natural ventilation in buildings, *Energy and Buildings 38*, 491-501.
9. **Fanger O.,** (1974), Komfort cieplny, *Wyd. Arkady*, Warszawa.
10. **Heiselberg P., Murakami S., Roulet C.A.** (2008), Ventilation of Large Spaces in Buildings. Analysis and prediction technics, *Energy Conservation in Buildings and Community Systems, I EA Annex 26: Energy Efficient Ventilation of Large Enclosures.*
11. **Lin Z., Chow T. T., Tsang C. F.** (2007), Effect of door opening on the performance of displacement ventilation in a typical office building, *Building and Environment 42*,1335-1347.
12. **PN-EN ISO 7730:** 2006 (U*):* Ergonomia środowiska termicznego. Analityczne wyznaczanie i interpretacja komfortu termicznego z zastosowaniem obliczania wskaźników PMV i PPD oraz kryteriów lokalnego komfortu termicznego.
13. **Sorensen D. N., Voigt L. K.** (2003), Modelling flow and heat transfer around a seated human body by computantional fluid dynamics, *Building and Environment 38*,753-762.
14. **Stamou A., Katsiris I.** (2006), Verification of a CFD model for indoor airflow and heat transfer, *Building and Environment 41*,1171-1181.
15. **Tse W. L. , Chan W. L.** (2007), Real-time measurement of thermal comfort by using an open networking technology, *Measurement 40*, 654–664.
16. www.healthyheating.com/solutions.htm

The paper was supported by the Bialystok University of Technology under the research project No. W/WM/3/2011.

BEM APPROACH FOR THE ANTIPLANE SHEAR OF ANISOTROPIC SOLIDS CONTAINING THIN INHOMOGENEITIES

Viktor BOZHYDARNYK[*], Iaroslav PASTERNAK[*], Heorhiy SULYM[**], Nazar OLIYARNYK[***]

[*] Chair of Technical Mechanics, Lutsk National Technical University, Lvivska Str., 75, 43018 Lutsk, Ukraine
[**] Faculty of Mechanical Engineering, Bialystok University of Technology, Wiejska Str., 45C, 15-351 Bialystok, Poland
[***] Chair of Mechanics, Ivan Franko National University of L'viv, Universytets'ka Str., 1, 79000 L'viv, Ukraine

pasternak@ukrpost.ua, sulym@pb.edu.pl, nazar_oliyarnyk@ukr.net

Abstract: This paper considers a development of the boundary element approach for studying of the antiplane shear of elastic anisotropic solids containing cracks and thin inclusions. For modeling of thin defects the coupling principle for continua of different dimension is utilized, and the problem is decomposed onto two separate problems. The first is an external one, which considers solid containing lines of displacement and stress discontinuities and is solved using boundary element approach. The second is internal one, which considers deformation of a thin inhomogeneity under the applied load. Compatible solution of external and internal problems gives the solution of the target one. Stroh formalism is utilized to account the anisotropy of a solid and inclusion. Numerical example shows the efficiency and advantages of the proposed approach.

1. INTRODUCTION

Thin inclusions are often provided into materials for improving of their properties. Those are fibers and stringers in composite materials, glue connections, cavities and inclusions introduced for damping etc. However, thin inhomogeneities of material structure can also cause an undesirable effect. In particular, cracks, thin voids, foreign layers, thin inclusions etc. induce huge stress concentration, which can cause a failure or even mechanical fracture of the corresponding structural element.

The study of thin inhomogeneities in materials and structures mainly concerns defects of a type of thin void (crack). Application of different boundary element and boundary integral equation approaches for studying of cracks in anisotropic solids can be found in works by Ang et al. (1999), Denda and Marante (2004), Pan and Amadei (1996), Pan (1997), Sollero and Aliabadi (1995), Ting (1996) etc.

Less publications concern study of solids with thin inclusions. In modeling of thin inclusions, their influence on the main material is often replaced by the forces distributed with a certain density along a line, which lays at the median surface of inclusion (a mass forces method). Such approach is used in the BEM by Padron et al. (2007) for modeling of piles in a ground (beams bending model), by Riederer et al. (2009) for studying of anchor bolts screwed up in the rock (beam tension model), by Aliabadi and Saleh (2002) and Saleh and Aliabadi (1998) for modeling of rectilinear reinforcement of concrete. The most complete among mentioned is a model of Aliabadi and Saleh (2002) as it considers tension, shear and bending of thin inclusion. Nevertheless, the mass forces method is not suitable for modeling of the transverse deformation of inclusion, which is accompanied with displacement discontinuities at a median surface of thin inhomogeneity. Therefore, mentioned models of thin inhomogeneity require modification, which will take into account the transverse rigidity of inclusion's material.

Another approach in numerical modeling of thin inclusions is the analysis of solid with the inhomogeneity of real geometrical features and elastic properties (see Sulym and Pasternak (2008a), Sulym and Pasternak (2009)). However, in this case the thinness of inclusion should be addressed and special techniques developed by Sulym and Pasternak (2008b) are to be utilized.

The present paper develops the numerical-analytical approach for studying of the antiplane shear of anisotropic elastic solids based on the boundary element method and coupling principle for continuums of different dimension introduced by Sulym (2007).

2. PROBLEM FORMULATION

Consider a cylindrical elastic anisotropic solid, which contains a thin ribbon-like foreign inclusion. Assume that mechanical fields, which act in a solid and inclusion, and the applied load, do not depend on time and do not vary along the direction parallel to the generatrix of a solid. Consider that at the inclusion-solid interface the conditions of ideal mechanical contact are satisfied and a solid has a material symmetry plane perpendicular to the generatrix. These assumptions allow reducing spatial problem to consideration of 2D steady-state fields of a solid and inclusion acting at arbitrary plane, which is perpendicular to the solid's generatrix. The applied load is assumed to be parallel to the generatrix.

Based on the coupling principle for different dimension continua of Sulym (2007) (Fig. 1) the lined model of thin inhomogeneity can be developed. Due to the thinness of inhomogeneity its real geometrical features are with-

drawn, and contact tractions and displacements are transferred onto the inclusion's median surface Γ_C (accordingly onto its faces Γ_C^+ and Γ_C^-, see Fig. 1). Thus, the problem is reduced to determination of an elastic state of a solid containing the line of discontinuities of stress and displacement fields. After development of the interaction conditions for a thin inhomogeneity along with the integral equations concerning abovementioned field discontinuities for a solid, the elastic state of the latter can be determined.

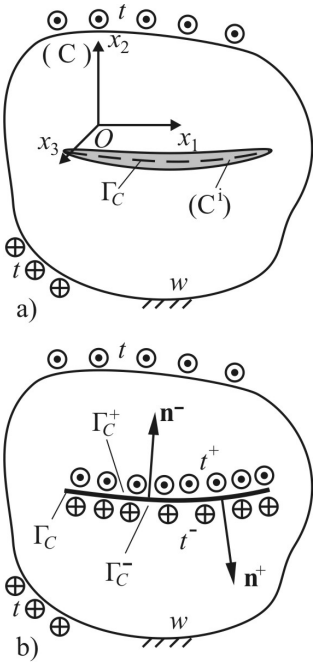

Fig. 1. Problem scheme (a) and modeling technique based on the coupling principle (b)

Consider a 2D domain S occupied by solid's median surface, which is perpendicular to the generatrix. Assume that a rectangular coordinate system $Ox_1x_2x_3$ origin is placed at this plane and Ox_3 axis is directed along the generatrix. Then, based on Ting (1996) the constitutive relations for antiplane shear of anisotropic solids can be written in the following compact form:

$$\sigma_{3j} = C_{jk} w_{,k} \quad (j,k = 1,2), \tag{1}$$

where σ_{3j} are the only nonzero components of stress tensor; $w \equiv u_3$ is the only nonzero component of displacement vector; $C_{11} = c_{55}$, $C_{12} = C_{21} = c_{45}$, $C_{22} = c_{44}$; c_{ij} are elastic moduli of the material. Here and further the Einstein summation convention is assumed.

The equilibrium equation (see Ting (1996)) for the case of antiplane shear can be reduced to:

$$\sigma_{3j,\,j} + f_3 = 0, \tag{2}$$

where f_3 is a body force applied to a solid. Substituting Eq. (1) into Eq. (2) one can obtain:

$$C_{jk} w_{,\,jk} + f_3 = 0. \tag{3}$$

The homogeneous solution $f_3 \equiv 0$ of Eq. (3) can be obtained using the Stroh formalism. Consider that:

$$w = aF\left(x_1 + px_2\right), \tag{4}$$

where a and p are complex constants to be determined, and $F(z)$ is an analytical function of z. Substituting Eq. (4) into Eq. (3) one obtains the following eigenrelation:

$$\left[Q + 2Rp + Tp^2\right]a = 0, \tag{5}$$

where $Q = C_{11}$, $T = C_{22}$, $R = C_{12} = C_{21}$ are numbers similar to the same-denoted Stroh matrices.

After differentiation of Eq. (4) and utilizing constitutive relations (1), stresses can be obtained in the form of Ting (1996):

$$\sigma_{31} = -\varphi_{,2}, \quad \sigma_{32} = \varphi_{,1}, \tag{6}$$

where $\varphi = bF(x_1 + px_2)$ is a stress function and

$$b = \left(R + pT\right)a = -\left(Q + pR\right)a/p. \tag{7}$$

Thus, for the solution of the problem it's more convenient to use the complex numbers a, b and p instead of elastic moduli C_{jk}. These complex numbers can be determined from the following eigenrelation of Ting (1996):

$$\mathbf{N} = \begin{bmatrix} N_1 & N_2 \\ N_3 & N_1 \end{bmatrix}, \quad \begin{matrix} \mathbf{N}\boldsymbol{\xi} = p\boldsymbol{\xi}, \\ \mathbf{N}^{\mathrm{T}}\boldsymbol{\eta} = p\boldsymbol{\eta}, \end{matrix} \tag{8}$$

where $N_1 = -R/T$, $N_2 = 1/T$, $N_3 = R^2/T - Q$; $\xi = [a, b]^T$ is a right eigenvector; $\eta = [b, a]^T$ is a left eigenvector of a matrix N; superscript "T" denotes matrix transpose. Vectors ξ_α and η_β obtained for the eigenvalues p_α and p_β are normalized using the relation:

$$\xi_\alpha^{\mathrm{T}} \boldsymbol{\eta}_\beta = \delta_{\alpha\beta}. \tag{9}$$

Therefore, the problem (8) gives two complex eigenvalues $p_1 = p$ and $p_2 = \bar{p}$, and corresponding eigenvectors $\xi_1 = \bar{\xi}_2$ are also complex conjugate. The variables w and φ are real, thus the general solution of the problem according to Ting (1996) is:

$$w = 2\,\mathrm{Re}\left[aF\left(x_1 + px_2\right)\right], \quad \varphi = 2\,\mathrm{Re}\left[bF\left(x_1 + px_2\right)\right], \tag{10}$$

Based on the Stroh formalism it is easy to obtain the Green function for a line force acting at a point $\xi(\xi_1, \xi_2)$ of infinite anisotropic medium (Ting, 1996):

$$W\left(\mathbf{x},\boldsymbol{\xi}\right) = \frac{1}{\pi}\,\mathrm{Im}\left[a^2 \ln Z\left(\mathbf{x},\boldsymbol{\xi}\right)\right],$$

$$T\left(\mathbf{x},\boldsymbol{\xi}\right) = \frac{1}{\pi}\,\mathrm{Im}\left[\frac{ab\left(n_2 - n_1 p\right)}{Z\left(\mathbf{x},\boldsymbol{\xi}\right)}\right], \tag{11}$$

where $Z(x,\xi) = x_1 + px_2 - (\xi_1, +p\xi_2)$. Displacements w along with tractions $t = \sigma_{3j}n_j$ at a point $x(x_1, x_2)$ of a solid at the surface with a normal $n(n_1, n_2)$ caused by the action of a concentrated factor $f_3\delta(\xi)$ at the point $\xi(\xi_1, \xi_2)$ can be determined within the following dependences:

$$w(\mathbf{x}) = W\left(\mathbf{x},\boldsymbol{\xi}\right) f_3, \quad t\left(\mathbf{x}\right) = T\left(\mathbf{x},\boldsymbol{\xi}\right) f_3. \tag{12}$$

Here $\delta(\boldsymbol{\xi})$ is the Dirac delta-function.

3. BOUNDARY INTEGRAL EQUATIONS OF EXTERNAL PROBLEM

Due to the symmetry of the elasticity tensor C_{jk} the following Betti type relation holds:

$$\int_{\partial S}\left[w^{(2)}t^{(1)}-t^{(2)}w^{(1)}\right]d\Gamma=\iint_{S}\left[f_3^{(2)}w^{(1)}-f_3^{(1)}w^{(2)}\right]dS \qquad (13)$$

for two different stress states of a solid. Choosing field (12) as one of the states of a solid, based on Eq. (13) one can obtain Somigliana type identity for antiplane shear of anisotropic solids:

$$\begin{aligned} w(\xi)=&\int_{\partial S}\left[W(\mathbf{x},\xi)t(\mathbf{x})-T(\mathbf{x},\xi)w(\mathbf{x})\right]d\Gamma(\mathbf{x})\\ &+\iint_{S}W(\mathbf{x},\xi)\,f_3(\mathbf{x})\,dS(\mathbf{x}). \end{aligned} \qquad (14)$$

Based on the method of Lin'kov (1999) of fictitious boundaries introduction and their further coupling, for a solid with a mathematical cut Γ_C one can receive the following integral representation for displacements:

$$\begin{aligned} w(\xi)=&\int_{\Gamma}\left[W(\mathbf{x},\xi)t(\mathbf{x})-T(\mathbf{x},\xi)w(\mathbf{x})\right]d\Gamma(\mathbf{x})\\ &+\int_{\Gamma_C^+}\left[W(\mathbf{x},\xi)\Sigma t(\mathbf{x})-T(\mathbf{x},\xi)\Delta w(\mathbf{x})\right]d\Gamma(\mathbf{x})\\ &+\iint_{S}W(\mathbf{x},\xi)\,f(\mathbf{x})\,dS(\mathbf{x}). \end{aligned} \qquad (15)$$

Here $\sum(\cdot)=(\cdot)^+ + (\cdot)^-$; $\Delta(\cdot)=(\cdot)^+ - (\cdot)^-$; $\Gamma=\partial S$ is a boundary of a domain S; $t^{\mp}=\sigma_{3j}^{\mp}n_j^{\mp}$ ($n_j^{\mp}$ are the components of normal vectors $\mathbf{n}^{\mp}$ of surfaces $\Gamma_C^{\mp}$); signs "+" and "–" denote variables concerned with faces Γ_C^+ and Γ_C^- of the mathematical cut Γ_C, respectively.

For simplification of further notations, consider that the solid is free of body forces, i.e. $f_3\equiv 0$. Thus, the last term in Eq. (15) vanishes.

Approaching the internal source point $\boldsymbol{\xi}$ to a boundary point $\mathbf{y}\in\Gamma$ and assuming that the curve Γ is smooth at the point $\mathbf{y}$, from Eq. (15) one can obtain displacement boundary integral equation:

$$\begin{aligned} \frac{1}{2}w(\mathbf{y})=&\int_{\Gamma_C^+}\left[W(\mathbf{x},\mathbf{y})\Sigma t(\mathbf{x})-T(\mathbf{x},\mathbf{y})\Delta w(\mathbf{x})\right]d\Gamma(\mathbf{x})\\ &+\mathrm{RPV}\int_{\Gamma}W(\mathbf{x},\mathbf{y})\,t(\mathbf{x})d\Gamma(\mathbf{x})\\ &-\mathrm{CPV}\int_{\Gamma}T(\mathbf{x},\mathbf{y})\,w(\mathbf{x})d\Gamma(\mathbf{x}), \end{aligned} \qquad (16)$$

where symbols "RPV" stand for the Riemann Principal Value, and "CPV" for Cauchy Principal Value of the integral. When a collocation point y lays at the smooth surface of the mathematical cut Γ_C, one can receive the following boundary integral equation:

$$\begin{aligned} \frac{1}{2}\Sigma w(\mathbf{y})=&\mathrm{RPV}\int_{\Gamma_C^+}W(\mathbf{x},\mathbf{y})\Sigma t(\mathbf{x})d\Gamma(\mathbf{x})\\ &-\mathrm{CPV}\int_{\Gamma_C^+}T(\mathbf{x},\mathbf{y})\Delta w(\mathbf{x})d\Gamma(\mathbf{x})\\ &+\int_{\Gamma}\left[W(\mathbf{x},\mathbf{y})t(\mathbf{x})-T(\mathbf{x},\mathbf{y})\,w(\mathbf{x})\right]d\Gamma(\mathbf{x}). \end{aligned} \qquad (17)$$

Eq. (17) can also be used when considering the crooked cuts or thin inclusions, however the requirement that the collocation point never coincides the crook point should be provided into the numerical procedure. Differentiating Eq. (17) for y_k and using constitutive relations (1) with the account of relation $n_i^+=-n_i^-$ one can obtain the stress boundary integral equation:

$$\begin{aligned} \frac{1}{2}\Delta t(\mathbf{y})=&n_j^+(\mathbf{y})\Big[\mathrm{CPV}\int_{\Gamma_C^+}D_j(\mathbf{x},\mathbf{y})\Sigma t(\mathbf{x})d\Gamma(\mathbf{x})\\ &-\mathrm{HPV}\int_{\Gamma_C^+}S_j(\mathbf{x},\mathbf{y})\Delta w(\mathbf{x})d\Gamma(\mathbf{x})\\ &+\int_{\Gamma}\left[D_j(\mathbf{x},\mathbf{y})t(\mathbf{x})-S_j(\mathbf{x},\mathbf{y})\,w(\mathbf{x})\right]d\Gamma(\mathbf{x})\Big], \end{aligned} \qquad (18)$$

where "HPV" stands for the Hadamard Principal Value (finite part) of an integral. The kernels of integrals in equation (18) are:

$$\begin{aligned} D_j(\mathbf{x},\mathbf{y})&=C_{jk}\frac{\partial W}{\partial y_k}=-\frac{1}{\pi}\mathrm{Im}\left[\left(\delta_{2j}-\delta_{1j}p\right)\frac{ab}{Z(\mathbf{x},\mathbf{y})}\right],\\ S_j(\mathbf{x},\mathbf{y})&=C_{jk}\frac{\partial T}{\partial y_k}=\frac{1}{\pi}\mathrm{Im}\left[\left(\delta_{2j}-\delta_{1j}p\right)\frac{b^2\left(n_2-n_1p\right)}{\left[Z(\mathbf{x},\mathbf{y})\right]^2}\right]. \end{aligned} \qquad (19)$$

The known expressions by Ang et al. (1999) or Pan and Amadei (1996) for kernels $D_j(\mathbf{x},\mathbf{y})$ and $S_j(\mathbf{x},\mathbf{y})$ additionally to complex numbers a and b contain constants C_{jk}, which compared to (19) complicates computational algorithms.

Assume that Γ_C is a median surface of thin inclusion. Without loss in generality, the interaction conditions between a solid and inhomogeneity, which is modeled using the coupling principle for different dimension continuums, according to Eqs. (17) and (18) is convenient to choose in the form of the following functional dependences:

$$\Sigma w(\mathbf{y})=F^w(\mathbf{y},\Sigma t,\Delta w),\quad \Delta t(\mathbf{y})=F^t(\mathbf{y},\Sigma t,\Delta w). \qquad (20)$$

Thus, when the collocation point y lays at a smooth boundary Γ of a solid one can use the only Eq. (16), and when the collocation point y lays at a smooth median surface Γ_C of the inhomogeneity two integral equations (17) and (18) along with the inclusion model (20) are used.

Thus, the formulated problem is reduced to determination from the system of boundary integral equations of unknown discontinuities of displacements Δw and stress:

$$\Delta\sigma_{3n}=\left(\sigma_{3j}^+-\sigma_{3j}^-\right)n_j^+=\sigma_{3j}^+n_j^+ +\sigma_{3j}^-n_j^-=\Sigma t$$

at the mathematical cut Γ_C and functions w or t, which are not set by the boundary conditions at the solid's boundary Γ. After all boundary functions are obtained, one can determine the field of displacements using the integral representation (15). After differentiation of Eq. (15), one can obtain stress field at arbitrary source point $\boldsymbol{\xi}$ of a solid by:

$$\begin{aligned} \sigma_{3j}(\xi)=&\int_{\Gamma}\left[D_j(\mathbf{x},\xi)t(\mathbf{x})-S_j(\mathbf{x},\xi)w(\mathbf{x})\right]d\Gamma(\mathbf{x})\\ &+\int_{\Gamma_C^+}\left[D_j(\mathbf{x},\xi)\Sigma t(\mathbf{x})-S_j(\mathbf{x},\xi)\Delta w(\mathbf{x})\right]d\Gamma(\mathbf{x}). \end{aligned} \qquad (21)$$

4. INCLUSION MODEL FOR THE INTERNAL PROBLEM

Consider mechanical fields acting at the certain cross-section y of a thin inclusion. Assume all quantities in the local coordinate system $Ox'_1x'_2x_3$, which axis Ox'_1 is directed along the normal vector $\mathbf{n}^+$. With the account of $\mathbf{n}^{\mp} = -\mathbf{n}^{i\mp}$ the conditions of a perfect mechanical contact of inclusion and a solid are $w^{\mp} = w^{i\mp}$, $t^{\mp} = -t^{i\mp}$. Here the non-italic superscript "i" denotes values concerned with the inclusion.

According to Eq. (1) stress inside the inclusion within the notations (5) equal:

$$\sigma_{31} = Q^{\mathrm{i}} w_{,1} + R^{\mathrm{i}} w_{,2}, \quad \sigma_{32} = R^{\mathrm{i}} w_{,1} + T^{\mathrm{i}} w_{,2}. \tag{22}$$

By integration of Eq. (22) over the thickness of inclusion one can obtain:

$$\begin{aligned} &\int_{-h}^{h} \sigma_{31} dh = Q^{\mathrm{i}} \left[w(h) - w(-h) \right] + R^{\mathrm{i}} \int_{-h}^{h} w_{,2} dh, \\ &\int_{-h}^{h} \sigma_{32} dh = R^{\mathrm{i}} \left[w(h) - w(-h) \right] + T^{\mathrm{i}} \int_{-h}^{h} w_{,2} dh. \end{aligned} \tag{23}$$

With the account of equilibrium equation (2) and contact conditions $t^{\mp} = -t^{i\mp}$ using the coupling principle for continuums of different dimension the following relations hold:

$$\int_{-h}^{h} \sigma_{32} dh = P(\mathbf{y}), \quad P(\mathbf{y}) = -P^0 + \int_{\mathbf{y}_0}^{\mathbf{y}} \Sigma t(s) ds, \tag{24}$$

where s is an arc coordinate of a mathematical cut Γ_C; P^0 is force applied at the left end of the inclusion, which position vector is defined by a point y_0. According to the mean value theorem:

$$\begin{aligned} &\int_{-h}^{h} \sigma_{31} dh = 2h\sigma_{31}^{\mathrm{avr}} \\ &\quad \approx h(\mathbf{y}) \left[t^{\mathrm{i}}(h) - t^{\mathrm{i}}(-h) \right] = h(\mathbf{y}) \Delta t(\mathbf{y}), \\ &\int_{-h}^{h} w_{,2} dh = 2h w_{,2}^{\mathrm{avr}} \\ &\quad \approx h(\mathbf{y}) \left[w_{,2}(h) + w_{,2}(-h) \right] = h(\mathbf{y}) \Sigma w_{,2}(\mathbf{y}). \end{aligned} \tag{25}$$

Withdrawing the interaction of mechanical fields acting in the directions normal and tangential to the median surface of the inhomogeneity (as in the model of the Winkler elastic foundation) and using Eqs. (24), (25) along with relations (23) one can obtain:

$$\begin{aligned} &\Delta t(\mathbf{y}) = -\frac{Q^{\mathrm{i}}(\mathbf{y})}{h(\mathbf{y})} \left[\Delta w(\mathbf{y}) + \Delta w^*(\mathbf{y}) \right], \\ &\Sigma w(\mathbf{y}) = 2w^0 + \int_{\mathbf{y}_0}^{\mathbf{y}} \frac{P(\mathbf{y}) + P^*(\mathbf{y})}{T^{\mathrm{i}}(\mathbf{y}) h(\mathbf{y})} ds. \end{aligned} \tag{26}$$

Considering assumptions made in Eq. (26) similar to Sulym (2007) the system of correcting functions Δw^*, P^* is introduced (in the theory of thin elastic defects by Sulym (2007) they are also called the end face forces and displacements). For thin defects, these functions are usually set using the aprioristic formulas. The latter are constructed under the assumption that the problem has the exact solution for three main cases of inclusion's material properties (a crack, a rigid line inclusion, and a continuous solid without inhomogeneity, i.e. inclusion material is similar to that of a medium). Considering the aprioristic formulas of Sulym (2007) the correcting functions for very thin inclusions can be assumed zero ones.

Mean value of displacement w^0 at the left end face of thin inclusion is determined using the inclusion's global equilibrium equation:

$$P^n + P^0 - \int_{\Gamma_C^+} \Sigma t(\mathbf{x}) d\Gamma(\mathbf{x}) = 0, \tag{27}$$

where P^n is a force applied at the right end of the thin inclusion.

5. BEM SOLUTION STRATEGY

System of integral equations (16)–(18) are solved simultaneously with Eqs. (26), (27) using the boundary element method proposed by Pasternak (2011). Curves Γ and Γ_C are approximated using respectively n and n_C rectilinear segments (boundary elements Γ_q). At each element, three nodal points are set: one at the centre, and two others at the distance of 1/3 of element length at both sides of central node (discontinuous three-node boundary element; if the polynomial shape functions are used it is called discontinuous quadratic boundary element, see Saleh and Aliabadi (1998)). Thus, the collocation point never coincides the corner points of the approximated boundary and the conditions assumed for the corresponding integral equations are provided. Boundary functions t, w, $\sum t$ and Δw are approximated at the element using their nodal values.

Using the abovementioned procedure, boundary integral equations (16)–(18) along with the model of the thin inclusion (26), (27) are reduced to the system of linear algebraic equations concerning the nodal values of boundary functions t, w, $\sum t$ and Δw.

Shape functions for the elements, which do not adjoin the inhomogeneity ends, are set in the form of Lagrange polynomials for the system of nodes $\xi_p = [-2/3; 0; 2/3]$ of three-node discontinuous boundary element.

To increase the accuracy of a method and for convenient determination of the generalized stress intensity factors (SIF) it is obvious to take an advantage of the special elements, which model near-tip parts of thin inclusion. According to Pasternak (2011) the following system of shape functions is introduced for displacement discontinuities:

$$\phi_p^{\Delta w} = \Phi_{p1}^{\Delta w} \sqrt{\rho} + \Phi_{p2}^{\Delta w} \rho + \Phi_{p3}^{\Delta w} \rho^{3/2} \quad (p = 1, 2, 3); \tag{28}$$

and for traction discontinuities:

$$\phi_p^{\Sigma t} = \Phi_{p1}^{\Sigma t} \rho^{-1/2} + \Phi_{p2}^{\Sigma t} + \Phi_{p3}^{\Sigma t} \sqrt{\rho} \quad (p = 1, 2, 3). \tag{29}$$

Here ρ is the normalized distance to the inclusion's tip; $\Phi_{pj}^{\Delta w}$ and $\Phi_{pj}^{\Sigma t}$ are constant matrices, which are determined the same as the factors of Lagrange polynomials.

Shape functions (28) and (29) allow direct determina-

tion of generalized SIF K_{31} and K_{32} through equations:

$$K_{31} = \lim_{s\to 0}\sqrt{\frac{\pi}{8s}}L\cdot\Delta w(s),\quad K_{32} = -\lim_{s\to 0}\sqrt{\frac{\pi s}{2}}\Sigma t(s), \qquad (30)$$

where $L = -2\sqrt{-1}b^2$ is a real number, which correspond in 2D anisotropic elasticity to the Barnett – Lothe tensor **L** (see Ting (1996)). In the case of a crack-like defect $K_{31} = K_{III}$ and $K_{32} = 0$, where K_{III} is the classical mode III stress intensity factor.

6. NUMERICAL EXAMPLE

To show the efficiency and accuracy of the proposed approach consider the problem of a thin elastic isotropic inclusion in the infinite anisotropic medium under the uniform shear at the infinity with $\sigma_{13}^{\infty} = \sigma_{23}^{\infty} = \tau$. The relative rigidity of inclusion is characterized by the ratio $k = G^i/c_{44}$, where G^i is a shear modulus of inclusion's material. The thickness of the inclusion is assumed to be 0.001 of its length ($h = 0{,}001a$). The correcting functions are assumed to be zero ones. The scheme of the problem is depicted in Fig. 2. Two cases of medium material properties are considered: isotropic (curve 1) and orthotropic with $c_{45} = 0$ and $c_{55}/c_{44} = 10$ (curve 2). The generalized SIF obtained using Eq. (30) (solid curves) are compared with the SIF obtained by the direct approach developed by Sulym and Pasternak (2008b) (dashed curves), which uses 311 quadratic boundary elements uniformly distributed at the inclusion's interface. The results are plotted in Fig. 2.

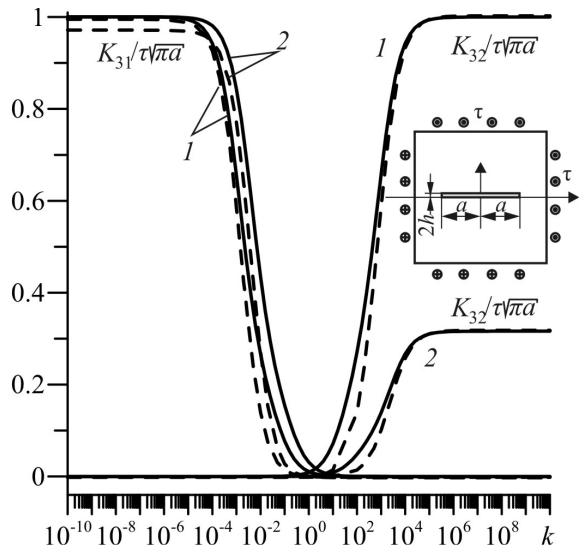

Fig. 2. Generalized SIF for a thin inclusion perfectly bonded into the isotropic (*1*) or anisotropic (*2*) medium

When the relative rigidity k of inclusion is extremely low (a cavity) or high (a rigid inclusion), the deviation of generalized SIF obtained with the proposed approach from the analytical solution of a crack or rigid line inclusion problems by Sulym (2007) is less than 0.04 % for both isotropic and anisotropic cases. The error of the direct approach is higher and about 1.5 % for isotropic and 3.5 % for anisotropic case.

For the intermediate values of the inclusion's relative rigidity the proposed approach gives a little higher values of the generalized SIF comparing to the direct one. This is explained by neglecting of correcting functions in inclusion model (26) during numerical computations. Nevertheless, higher values of generalized SIF can be treated as those, which already include safety factor.

The advantage of the proposed approach is the reduction of the general number of boundary elements (21 against 311) used for modeling of the problem. Besides, the proposed approach can be used for studying problems of very thin inclusions, which are challenging for the direct approach, even when the regularization procedure of Sulym and Pasternak (2008b) is applied.

7. CONCLUSION

Thin inhomogeneities of material structure induce considerable stress concentration at the vicinity of their tips. For thin inclusions in anisotropic elastic materials stress field near the tips of inhomogeneity possesses square root singularity. Therefore, for the numerical solution of the corresponding mathematical problem it is necessary to consider this behavior of boundary functions, in particular using special shape functions.

The stress field near the tip of thin inclusion in anisotropic elastic medium under antiplane shear can be defined within two real values, which are called generalized SIF. One of them stands for the displacement discontinuity, and in the case of a crack equal classical mode III SIF. Another stands for the stress discontinuity at the inhomogeneity.

The numerical analysis of a test problem shows high efficiency of the developed approach for modeling of different types of thin defects of anisotropic materials: cracks, thin elastic and rigid inclusions etc. It allows studying both bounded and infinite solids. The account of inclusion properties has essential influence on SIF of solids containing thin inhomogeneities.

REFERENCES

1. **Aliabadi M.H., Saleh A.L.** (2002), Fracture mechanics analysis of cracking in plain and reinforced concrete using the boundary element method, *Eng. Fract. Mech.*, 69, 267–280.
2. **Ang W.T., Clements D.L., Cooke T.** (1999), A hypersingular boundary integral equation for a class of antiplane multiple crack problems for inhomogeneous anisotropic elastic material, *Eng. Anal. Bound. Elem.*, 23, 567–572.
3. **Denda M., Marante M.E.** (2004), Mixed mode BEM analysis of multiple curvilinear cracks in the general anisotropic solids by the crack tip singular element, *Int. J. Sol. Struct.*, 41, 1473–1489.
4. **Lin'kov A.M.** (1999) *Kompleksnyj metod graničnyh elementov*, Nauka, Sankt-Peterburg.
5. **Padron L.A., Aznarez J.J., Maeso O.** (2007), BEM–FEM coupling model for the dynamic analysis of piles and pile groups, *Eng. Anal. Bound. Elem.*, 31, 473–484.
6. **Pan E., Amadei B.** (1996), Fracture mechanics analysis of 2D anisotropic media with a new formulation of the boundary element method, *Int. J. Fract.*, 77, 161–174.

7. **Pan E.** (1997), A general boundary element analysis of 2D linear elastic fracture mechanics, *Int. J. Fract.*, 88, 41–59.
8. **Pasternak Ia.** (2011) Coupled 2D electric and mechanical fields in piezoelectric solids containing cracks and thin inhomogeneities, *Eng. Anal. Bound. Elem.*, 35(4), 678–690.
9. **Riederer K., Duenser C., Beer G.** (2009), Simulation of linear inclusions with the BEM, *Eng. Anal. Bound. Elem.*, 33, 959–965.
10. **Saleh A.L., Aliabadi M.H.** (1998), Crack growth analysis in reinforced concrete using BEM, *J. Eng. Mech.*, 124(9), 949–958.
11. **Sollero P., Aliabadi M.H.** (1995), Anisotropic analysis of cracks in composite laminates using the dual boundary element method, *Composite Structures*, 31, 229–233.
12. **Sulym G.T.** (2007), *Osnovy matematyčnoj teorij termopružnoj rivnovagy deformivnyh til z tonkymy vklûčennâmy*, Dosl.-vydav. centr NTŠ, L'viv.
13. **Sulym G.T., Pasternak Ja.M.** (2008a), Vykorystannâ J-integrala dlâ doslidžennâ pozdovžn'ogo zsuvu anizotropnyh til is tonkostinnymy stričkovymy vklûčennâmy, *Visnyk Don. Univer. Ser. A.*, 1, 88–92.
14. **Sulym G.T., Pasternak Ja.M.** (2008b), Zastosuvannâ metodu granyčnyh elementiv do analizu antyploskoj deformacij anizotropnyh til iz tonkostinnymy strukturamy, *Mat. Met. Fiz.-Meh. Polya*, 51(4), 136–144.
15. **Sulym G.T., Pasternak Ja.M.** (2009), Vplyv rozmiriv anizotropnyh til zi stričkovymy pružnymy vklûčennâmy na parametry granyčnogo stanu za antyploskoj deformacij, *Metody rozv. prykl. zad. meh. deform. tverd. tila, Dnipropetrovs'k*, vyp. 10, 263–269.
16. **Ting T.C.T.** (1996), *Anisotropic elasticity: theory and applications*, Oxford University Press, New York.

STABILITY OF THE SECOND FORNASINI-MARCHESINI TYPE MODEL OF CONTINUOUS-DISCRETE LINEAR SYSTEMS

Mikołaj BUSŁOWICZ*

*Białystok University of Technology, Faculty of Electrical Engineering
ul. Wiejska 45D, 15-351 Białystok

busmiko@pb.edu.pl

Abstract: The problem of asymptotic stability of continuous-discrete linear systems is considered. Simple necessary conditions and two computer methods for investigation of asymptotic stability of the second Fornasini-Marchesini type model are given. The first method requires computation of the eigenvalue-loci of complex matrices, the second method requires computation of determinants of some matrices. Effectiveness of the methods is demonstrated on numerical example.

1. INTRODUCTION

In continuous-discrete systems both continuous-time and discrete-time components are relevant and interacting and these components can not be separated. Such systems are called the hybrid systems.

In this paper we consider the continuous-discrete linear systems whose models have structure similar to the models of 2D discrete-time linear systems. Such models, called the 2D continuous-discrete or 2D hybrid models, have been considered in Kaczorek (2002) in the case of positive systems.

The new general model of positive 2D hybrid linear systems has been introduced in Kaczorek (2007) for standard and in Kaczorek (2008a) for fractional systems. The realization, reachability and solvability problems of positive 2D hybrid linear systems have been considered in Kaczorek (2002, 2008b, 2011a), Kaczorek and Rogowski (2010), Kaczorek et al. (2008), Sajewski (2009).

The problems of stability and robust stability of 2D continuous-discrete linear systems have been investigated in Bistritz (2003, 2004), Busłowicz (2010a, b, 2011a, b), Busłowicz and Ruszewski (2011a, b), Guiver and Bose (1981) (see also Chapter 12 in Kaczorek (2011a)) for standard and in Kaczorek (2011a, b), Kaczorek and Sajewski (2011) for positive systems.

The main purpose of this paper is to present computational methods for investigation of asymptotic stability of the second Fornasini-Marchesini type model of continuous-discrete linear systems.

The following notation will be used: $\Re$ – the set of real numbers, $\Re_+ = [0, \infty]$, Z_+ – the set of non-negative integers, $\Re^{n\times m}$ – the set of $n \times m$ real matrices and $\Re^n = \Re^{n\times 1}$, $\| x(\cdot) \|$ – the norm of $x(\cdot)$, $\lambda_i(X)$ – i-th eigenvalue of matrix X.

2. PRELIMINARIES AND FORMULATION OF THE PROBLEM

Consider the state equation of the second Fornasini-Marchesini type model of a continuous-discrete linear system (Kaczorek, 2002) (for $i \in Z_+$ and $t \in \Re_+$):

$$\dot{x}(t,i+1) = A_1\dot{x}(t,i) + A_2x(t,i+1) + B_1\dot{u}(t,i) + B_2u(t,i+1), \quad (1)$$

where $\dot{x}(t,i) = \partial x(t,i)/\partial t$, $x(t,i) \in \Re^n$, $u(t,i) \in \Re^m$ and $A_1, A_2 \in \Re^{n\times n}$, $B_1, B_2 \in \Re^{n\times m}$.

Definition 1. The model (1) is called asymptotically stable (or Hurwitz-Schur stable) if for $u(t,i) \equiv 0$ (then also $\dot{u}(t,i) \equiv 0$) and bounded boundary conditions:

$$x(0,i), \quad i \geq 1, \quad i \in Z_+, \quad x(t,0), \quad \dot{x}(t,0), \quad t \in \Re_+, \quad (2)$$

the following condition holds:

$$\lim_{i,t\to\infty} \| x(t,i) \| = 0 \quad \text{for} \quad t, i \to \infty.$$

The characteristic matrix of the model (1) has the form:

$$H(s,z) = szI_n - sA_1 - zA_2. \quad (3)$$

The characteristic function of this model:

$$w(s,z) = \det H(s,z) = \det[szI_n - sA_1 - zA_2] \quad (4)$$

is a polynomial in two independent variables s and z, of the general form:

$$w(s,z) = \sum_{k=0}^{n}\sum_{j=0}^{n} a_{kj}s^k z^j, \quad a_{nn} = 1. \quad (5)$$

From Bistritz (2003, 2004) and Guiver and Bose (1981) we have the following theorem.

Theorem 1. The model (1) with characteristic function (4) is asymptotically stable if and only if the following condition holds:

$$w(s,z) \neq 0, \quad \text{Re}\, s \geq 0, \quad |z| \geq 1. \quad (6)$$

The polynomial $w(s,z)$ satisfying the condition (6) is called continuous-discrete stable (C-D stable) or Hurwitz-Schur stable (Bistritz (2003, 2004)).

The main purpose of this paper is to present computational methods for checking the condition (6) of asymptotic stability of the model (1) of continuous-discrete linear systems.

3. SOLUTION OF THE PROBLEM

Lemma 1. Simple necessary conditions for asymptotic stability of the model (1) are as follows:

$$\operatorname{Re}\lambda_i(A_2) < 0, \quad i = 1,2,...,n, \tag{7}$$

$$|\lambda_i(A_1)| < 1, \quad i = 1,2,...,n. \tag{8}$$

Proof. From (1) for $A_1 \equiv 0$ and $B_1 = B_2 \equiv 0$ one obtains the homogeneous state equation of the continuous-time linear system (for the fixed $i \in Z_+$):

$$\dot{x}(t,i+1) = A_2 x(t,i+1). \tag{9}$$

The system (9) is asymptotically stable if and only if the condition (7) holds, i.e. the matrix A_2 is Hurwitz stable (is a Hurwitz matrix).

Similarly, substitution of $A_2 \equiv 0$ and $B_1 = B_2 \equiv 0$ in (1) gives the equation:

$$\dot{x}(t,i+1) = A_1 \dot{x}(t,i), \tag{10}$$

which can be written in the form:

$$v(t,i+1) = A_1 v(t,i), \quad v(t,i) = \dot{x}(t,i). \tag{11}$$

The discrete-time linear system (11) is asymptotically stable if and only if the condition (8) holds, i.e. the matrix A_1 is Schur stable (is a Schur matrix). This completes the proof.

Theorem 2. The condition (6) is equivalent to the following two conditions:

$$w(s,e^{j\omega}) \neq 0, \quad \operatorname{Re} s \geq 0, \quad \forall \omega \in \Omega = [0, 2\pi], \tag{12}$$

and

$$w(jy,z) \neq 0, \quad |z| \geq 1, \quad \forall y \in [0, \infty). \tag{13}$$

Proof. From Bistritz (2003, 2004) and Guiver and Bose (1981) it follows that (6) is equivalent to the conditions:

$$w(s,z) \neq 0, \quad \operatorname{Re} s \geq 0, \quad |z| = 1, \tag{14}$$

and

$$w(s,z) \neq 0, \quad \operatorname{Re} s = 0, \quad |z| \geq 1. \tag{15}$$

It is easy to see that conditions (14) and (15) can be written in the forms (12) and (13), respectively.

The characteristic matrix (3) of the model (1) can be written in the following forms:

$$H(s,z) = [zI - A_1][sI - S_1(z)] = [sI - A_2][zI - S_2(s)], \tag{16}$$

where:

$$S_1(z) = (zI - A_1)^{-1}(zA_2), \tag{17}$$

$$S_2(s) = (sI - A_2)^{-1}(sA_1). \tag{18}$$

Hence,

$$w(s,z) = \det[zI - A_1]\det[sI - S_1(z)], \tag{19a}$$

$$w(s,z) = \det[sI - A_2]\det[zI - S_2(s)]. \tag{19b}$$

From (19a) and (17) for $z = e^{j\omega}$ we have:

$$w(s,e^{j\omega}) = \det[Ie^{j\omega} - A_1]\ \det[sI - S_1(e^{j\omega})], \tag{20}$$

where:

$$S_1(e^{j\omega}) = (Ie^{j\omega} - A_1)^{-1} A_2 e^{j\omega}. \tag{21}$$

Lemma 2. Let the necessary condition (8) be satisfied. The condition (12) holds if and only if all eigenvalues of the complex matrix (21) have negative real parts for all $\omega \in [0, 2\pi]$.

Proof. If (8) is satisfied then the matrix $Ie^{j\omega} - A_1$ is non-singular for all $\omega \in [0, 2\pi]$ and from (20) it follows that the condition (12) holds if and only if:

$$\det(sI - S_1(e^{j\omega})) \neq 0, \quad \operatorname{Re} s \geq 0, \quad \forall \omega \in \Omega = [0, 2\pi]. \tag{22}$$

Satisfaction of (22) means that all eigenvalues of (21) have negative real parts for all $\omega \in \Omega$.

The condition (22) holds if and only if the eigenvalue-loci of (21) with $\omega \in \Omega$ are located in the open left half-plane of the complex s plane. These eigenvalue-loci are the closed curves with endpoints (for $\omega = 0$ and $\omega = 2\pi$) in eigenvalues of $S_1(1) = (I - A_1)^{-1}A_2$.

From (19b) and (18) for $s = jy$ we have:

$$w(jy,z) = \det[jyI - A_2]\det[zI - S_2(jy)], \tag{23}$$

where:

$$S_2(jy) = (jyI - A_2)^{-1}(jyA_1). \tag{24}$$

Lemma 3. Let the necessary condition (7) be satisfied. The condition (13) holds if and only if all eigenvalues of the complex matrix (24) have absolute values less than one for all $y \geq 0$.

Proof. If (7) is satisfied then the matrix $jyI - A_2$ is non-singular for all $y \geq 0$ and from (23) we have that the condition (13) holds if and only if:

$$\det[zI - S_2(jy)] \neq 0, \quad |z| \geq 1, \quad \forall y \in [0, \infty), \tag{25}$$

i.e. all eigenvalues of (24) have absolute values less than one for all $y \geq 0$.

Satisfaction of (25) means that the eigenvalue-loci of (24) (eigenvalues of (24) for all $y \in [0, \infty)$) are located in the open unit circle of the complex z plane.

It is easy to check that:

$$\lim_{y\to\infty} S_2(jy) = \lim_{y\to\infty} \frac{jy \cdot \operatorname{adj}(jyI - A_2)}{\det(jyI - A_2)} A_1 = A_1, \tag{26}$$

where adj(.) denotes the adjoint matrix.

From the above and (24) it follows that the eigenvalue-loci of $S_2(jy)$ start for $y = 0$ in the origin of the complex plane and tend to the eigenvalues of A_1 for $y \to \infty$.

Theorem 3. The second Fornasini-Marchesini type model (1) is asymptotically stable if and only if the necessary conditions (7) and (8) are satisfied and the following conditions hold:

$$\mathrm{Re}\,\lambda_i\{S_1(e^{j\omega})\} < 0, \quad \forall \omega \in \Omega = [0, 2\pi], \quad i = 1,2,...,n, \tag{27}$$

and

$$|\lambda_i\{S_2(jy)\}| < 1, \quad \forall y \geq 0, \quad i = 1,2,...,n, \tag{28}$$

where the matrices $S_2(e^{j\omega})$ and $S_2(jy)$ have the forms (21) and (24), respectively.

Proof. It follows from Theorem 2 and Lemmas 1, 2 and 3.

Application of Theorem 3 requires computation of eigenvalues of complex matrices (21) and (24). This may be inconvenient from the computational reasons, particularly in the case of ill conditioned matrices.

Therefore, we present a new method for investigation of asymptotic stability of the model (1) which requires the computation of determinants of some matrices.

Consider the polynomial:

$$w_1(s, e^{j\omega}) = \det(sI - S_1(e^{j\omega})), \tag{29}$$

where $S_1(e^{j\omega})$ is defined by (21). From the classical Mikhailov theorem (see Busłowicz (2007), Keel and Bhattacharyya (2000)) it follows that the condition (27) holds if and only if for any fixed $\omega \in [0, 2\pi]$ plot of $w_1(jy, e^{j\omega})$ starts for $y = 0$ in the point $w_1(j0, e^{j\omega}) = \det(-S_1(e^{j\omega}))$ and runs in the positive direction by n quadrants of the complex plane (missing the origin of this plane) if y increases from 0 to +∞. This plot (called the Mikhailov hodograph) quickly tends to infinity as y grows to ∞. Therefore, direct application of the Mikhailov theorem to checking the condition (27) is not practically reliable.

To remove this difficulty, we introduce the rational function:

$$\phi_1(jy, e^{j\omega}) = \frac{w_1(jy, e^{j\omega})}{w_{10}(jy)}, \quad \omega \in \Omega = [0, 2\pi], \tag{30}$$

instead of $w_1(jy, e^{j\omega})$, where $w_{10}(s)$ is any Hurwitz stable reference polynomial of degree n.

Lemma 4. The condition (27) holds if and only if for all fixed $y \geq 0$ plot of (30) does not encircle or cross the origin of the complex plane.

Proof. If the reference polynomial $w_{10}(s)$ is Hurwitz stable then from the Argument Principle we have:

$$\Delta \arg_{y \in (-\infty, \infty)} w_{10}(jy) = n\pi.$$

From (30) it follows that for any fixed $\omega \in \Omega$:

$$\begin{aligned} &\Delta \arg_{y \in (-\infty, \infty)} \phi_1(jy, e^{j\omega}) = \\ &\quad = \Delta \arg_{y \in (-\infty, \infty)} w_1(jy, e^{j\omega}) - \Delta \arg_{y \in (-\infty, \infty)} w_{10}(jy). \end{aligned} \tag{31}$$

The condition (27) holds for any fixed $\omega \in \Omega$ if and only if:

$$\Delta \arg_{y \in (-\infty, \infty)} w_1(jy, e^{j\omega}) = \Delta \arg_{y \in (-\infty, \infty)} w_{10}(jy) = n\pi, \tag{32}$$

which holds if and only if $\Delta \arg_{y \in (-\infty, \infty)} \phi(jy, e^{j\omega}) = 0$.

Taking into account all $\omega \in \Omega$, we obtain that the above holds if and only if for all fixed $y \geq 0$ plot of (30) as a function of $\omega \in \Omega$ does not encircle or cross the origin of the complex plane.

The reference polynomial $w_{10}(s)$ can be chosen in the form:

$$w_1(s,1) = \det(sI - S_1(1)), \quad S_1(1) = (I - A_1)^{-1} A_2. \tag{33}$$

Hurwitz stability of the polynomial (33) is necessary for Hurwitz stability of the complex polynomial (29) for all $\omega \in \Omega$:

If $w_{10}(s) = w_1(s,1)$ then:

$$\phi_1(jy, e^{j\omega}) = \frac{w_1(jy, e^{j\omega})}{w_1(jy,1)}, \quad \omega \in \Omega. \tag{34}$$

Plot of (34) as a function of $\omega \in \Omega$ (with any fixed $y \geq 0$) is a closed curve. It begins with $\omega = 0$ and ends with $\omega = 2\pi$ in the point $(1, j0)$, because $\phi_1(jy, 1) = 1$. It is easy to check that if $y \to \infty$, then the closed curve (34) reduces to the point $(1, j0)$.

The plot of (34) is called the modified Mikhailov hodograph. From the above it follows that this hodograph is bounded for all $y \geq 0$.

Now, we consider the complex polynomial:

$$w_2(jy, z) = \det(zI - S_2(jy)), \tag{35}$$

where $S_2(jy)$ is defined by (24).

Let $w_{20}(z)$ be any Schur stable reference polynomial of degree n.

Similarly as for Lemma 4, we obtain the following lemma.

Lemma 5. The condition (28) holds if and only if for all fixed $y \geq 0$ plot of the function:

$$\phi_2(jy, e^{j\omega}) = \frac{w_2(jy, e^{j\omega})}{w_{20}(e^{j\omega})}, \quad \omega \in \Omega, \tag{36}$$

does not encircle or cross the origin of the complex plane, where $w_2(jy, e^{j\omega})$ has the form (35) for $z = e^{j\omega}$.

From (35) for $y = 0$ we have:

$$w_2(0, z) = \det(zI - S_2(0)) = z^n.$$

Therefore, the reference polynomial $w_{20}(z)$ can be chosen as $w_{20}(z) = w_2(0, z) = z^n$.

Schur stability of $w_2(0, z)$ is necessary for Schur stability of the complex polynomial (35) for all $y \geq 0$.

If $w_{20}(z) = z^n$ then:

$$\phi_2(jy, e^{j\omega}) = \frac{w_2(jy, e^{j\omega})}{e^{j\omega n}}, \quad \omega \in \Omega. \tag{37}$$

Plot of (37) as a function of $\omega \in \Omega$ with the fixed $y \geq 0$ is a closed curve. It begins with $\omega = 0$ and ends with $\omega = 2\pi$ in the point:

$$\phi_2(jy,1) = w_2(jy,1) = \det(I - S_2(jy)). \quad (38)$$

It is easy to see that $\phi_2(0,1) = 1$.

From (26) and (37) we have:

$$\phi_2(\infty, e^{j\omega}) = \lim_{y\to\infty} \phi_2(jy, e^{j\omega}) = \frac{\det(e^{j\omega}I - A_1)}{e^{j\omega n}}, \ \omega \in \Omega. \quad (39)$$

From the above it follows that if $y \to \infty$ then plot of (37) tends to the closed curve (39) with endpoints (for $\omega = 0$ and $\omega = 2\pi$) $\phi_2(\infty, 1) = \det(I - A_1)$.

From Theorem 3 and Lemmas 4 and 5 we have the following theorem.

Theorem 4. Assume that the necessary conditions (7) and (8) are satisfied. The model (1) is asymptotically stable if and only if the following two conditions hold:

1. plots of the function (34) do not encircle or cross the origin of the complex plane for all fixed $y \geq 0$;
2. plots of the function (37) do not encircle or cross the origin of the complex plane for all fixed $y \geq 0$.

Applying computational method given in Theorem 4 we can take into consideration the following remark.

Remark. The range $Y = [0, y_f]$ of values of the parameter y should be a suitable large, such that from plots of the functions (34) and (37) for $y \in Y$ we can affirm fulfilment (or not) the conditions of Theorem 4 for all $y \geq 0$. For any fixed $y \in Y$ determined with appropriately small step Δy, plots of the functions (34) and (37) should be draw separately digitizing the range $\Omega = [0, 2\pi]$ with a sufficiently small step $\Delta\omega$.

4. ILLUSTRATIVE EXAMPLE

Consider the second Fornasini-Marchesini type model (1) with the matrices:

$$A_1 = \begin{bmatrix} 0.4 & 0.1 & 0.3 \\ 0 & -0.8 & -0.4 \\ -0.3 & 0.2 & 0.4 \end{bmatrix}, \ A_2 = \begin{bmatrix} -1.4 & -1 & -0.1 \\ 0.8 & -0.4 & 0 \\ -1 & 0 & -0.7 \end{bmatrix}. \quad (40)$$

Computing eigenvalues of A_1 and A_2 one obtains:

– eigenvalues of A_1:

$$z_1 = -0.7247; \ \ z_{2,3} = 0.3624 \pm j0.2897$$

– eigenvalues of A_2:

$$s_1 = -0.7640; \ \ s_{2,3} = -0.8680 \pm j0.6635.$$

From the above it follows that the necessary conditions (7) and (8) hold.

Eigenvalue-loci of the matrices $S_1(e^{j\omega})$, $\omega \in [0, 2\pi]$ and $S_2(jy)$, $y \in [0, 50]$ are shown in Fig. 1 and 2, respectively. By 'o' in Fig. 2 are denoted points corresponding to eigenvalues of A_1. The eigenvalue-loci of $S_2(jy)$ tend to these points if $y \to \infty$.

From Fig. 1 and 2 it follows that the conditions (27) and (28) of Theorem 3 are satisfied and the system is asymptotically stable.

Plots of the functions (34) for $y \in [0, 40]$ and (37) for $y \in [0, 20]$ are shown in Fig. 3 and 4, respectively. The curve (39) is denoted by stars in Fig. 4.

From Fig. 3 and 4 it follows that the conditions of Theorem 4 are satisfied and the system is asymptotically stable.

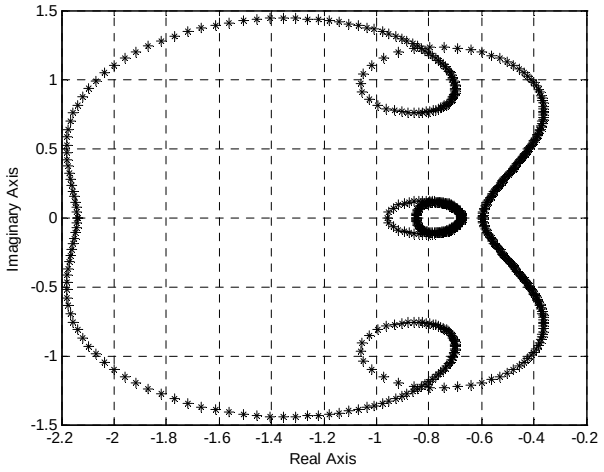

Fig. 1. Eigenvalue-loci of $S_1(e^{j\omega})$, $\omega \in \Omega = [0, 2\pi]$

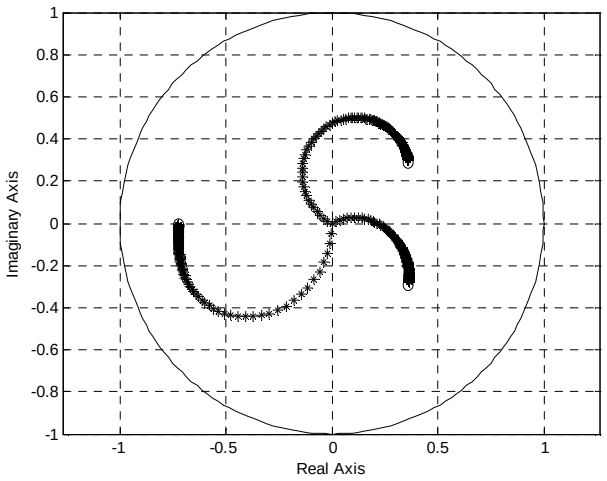

Fig. 2. Eigenvalue-loci of $S_2(jy)$, $y \in [0, 50]$

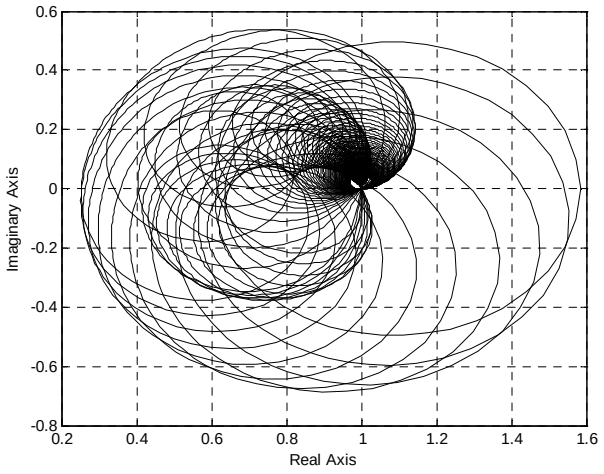

Fig. 3. Plot of (34) for $y \in [0, 40]$

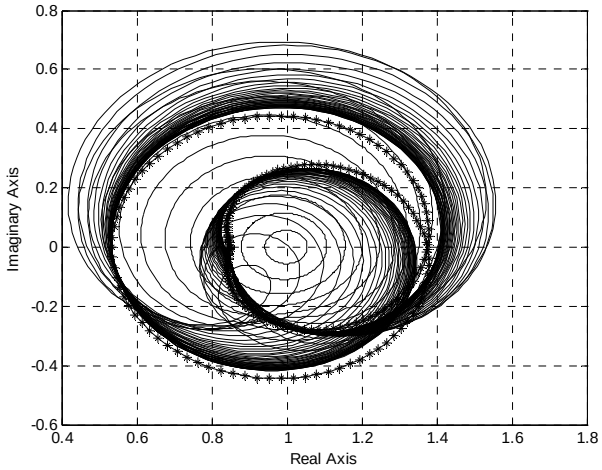

Fig. 4. Plot of (37) for $y \in [0, 20]$

5. CONCLUDING REMARKS

Simple necessary conditions and computational methods for analysis of asymptotic stability of the second Fornasini-Marchesini type model (1) of continuous-discrete linear systems have been given in Lemma 1 and Theorems 3 and 4, respectively. The method given in Theorem 3 requires computation of eigenvalue-loci of complex matrices (21) and (24). The method proposed in Theorem 4 requires computation of values of complex functions (34) and (37).

The method of Theorem 3 has been generalized in Busłowicz (2011b) for the first Fornasini-Marchesini type and the Roesser type models of continuous-discrete linear systems. The method of Theorem 4 has been applied in Busłowicz and Ruszewski (2011a) to asymptotic stability analysis of the first Fornasini-Marchesini type model.

Extension of the proposed methods for the new general type model of 2D continuous-discrete linear systems has been given in Busłowicz and Ruszewski (2011b).

REFERENCES

1. **Bistritz Y.** (2003), A stability test for continuous-discrete bivariate polynomials, *Proc. Int. Symp. on Circuits and Systems*, vol. 3, 682-685, Bangkok, Thailand.
2. **Bistritz Y.** (2004), Immittance and telepolation-based procedures to test stability of continuous-discrete bivariate polynomials, *Proc. IEEE Int. Symposium on Circuits and Systems*, vol. 3, 293-296, Vancouver, Canada.
3. **Busłowicz M.** (2007), *Stability of linear time-invariant systems with uncertain parameters*, Publishing Department of Technical University of Białystok, Białystok (in Polish)
4. **Busłowicz M.** (2010a), Robust stability of the new general 2D model of a class of continuous-discrete linear systems, *Bull. Pol. Ac. Techn. Sci.*, Vol. 57, No. 4, 561-565.
5. **Busłowicz M.** (2010b), Stability and robust stability conditions for general model of scalar continuous-discrete linear systems, *Measurement Automation and Monitoring*, Vol. 56, No. 2, 133-135.
6. **Busłowicz M.** (2011a), Improved stability and robust stability conditions for general model of scalar continuous-discrete linear systems, *Measurement Automation and Monitoring*, Vol. 57, No. 2, 188-189.
7. **Busłowicz M.** (2011b), Computational methods for investigation of stability of models of 2D continuous-discrete linear systems, *Journal of Automation, Mobile Robotics and Intelligent Systems*, Vol. 5, No. 1, 3-7.
8. **Busłowicz M.**, **Ruszewski A.** (2011a), Stability investigation of continuous-discrete linear systems, *Measurement Automation and Robotics*, No.2/2011, 566-575 (in Polish).
9. **Busłowicz M.**, **Ruszewski A.** (2011b), Computer methods for stability analysis of the Roesser type model of 2D continuous-discrete linear systems, *Int. J. Appl. Math. Comput. Sci.* (in press).
10. **Guiver J. P., Bose N. K.** (1981), On test for zero-sets of multivariate polynomials in noncompact polydomains, *Proc. of the IEEE*, Vol. 69, No. 4, 467-469.
11. **Kaczorek T.** (2002), *Positive 1D and 2D Systems*, Springer-Verlag, London.
12. **Kaczorek T.** (2007), Positive 2D hybrid linear systems, *Bull. Pol. Ac. Techn. Sci.*, Vol. 55, No. 4, 351-358.
13. **Kaczorek T.** (2008a), Positive fractional 2D hybrid linear systems, *Bull. Pol. Ac. Techn. Sci.*, Vol. 56, No. 3, 273-277.
14. **Kaczorek T.** (2008b), Realization problem for positive 2D hybrid systems, *COMPEL*, Vol. 27, No. 3, 613-623.
15. **Kaczorek T.** (2011a), *Selected Problems of Fractional Systems Theory*, Springer-Verlag, Berlin.
16. **Kaczorek T.** (2011b), New stability conditions for positive continuous-discrete 2D linear systems. *Int. J. Appl. Math. Comput. Sci.*, Vol. 21, No. 3, 521-524.
17. **Kaczorek T.**, **Rogowski K.** (2010), Reachability of linear hybrid systems described by the general model, *Archives of Control Sciences*, Vol. 20, No. 2, 199-2007.
18. **Kaczorek T. and Sajewski Ł.** (2011), Stability of continuous-discrete linear systems with delays in state vector, *Archives of Control Sciences*, Vol. 21, No. 1, 5-16.
19. **Kaczorek T., Marchenko V., Sajewski Ł.** (2008), Solvability of 2D hybrid linear systems - comparison of the different methods, *Acta Mechanica et Automatica*, Vol. 2, No. 2, 59-66.
20. **Keel L. H., Bhattacharyya S. P.** (2000), A generalization of Mikhailov's criterion with applications, *Proc. of American Control Conference*, Chicago, Vol. 6, 4311-4315.
21. **Sajewski Ł.** (2009), Solution of 2D singular hybrid linear systems, *Kybernetes*, Vol. 38, No. 7/8, 1079-1092.

Acknowledgement: The work was supported by the Ministry of Science and High Education of Poland under grant No. S/WE/1/2011.

STABILIZATION OF PENDULUM IN VARIOUS INCLINATIONS USING OPEN-LOOP CONTROL

Maciej CIĘŻKOWSKI*

*phD student, Department of Automatics and Robotics, Faculty of Mechanical Engineering, Bialystok University of Technology, ul. Wiejska 45 C, 15-351 Białystok

mciezkowski@gmail.com

Summary: The paper presents the stabilization method of physical pendulum in various inclinations. The theory of the motion in a rapidly oscillating field has been applied to explain the phenomenon of stabilization and to set conditions for the stability of the pendulum. The paper shows results of computer simulations which confirm that the position control of the pendulum in the open-loop is possible.

1. INTRODUCTION

The inverted pendulum, which is physical pendulum, whose center of mass lies above the point of suspension is very popular pendulum tested in automatics. It is an example of a nonlinear system characterized by high instability. Due to its properties it is a good object for testing different control algorithms. Beside the fact the system is interesting from a theoretical point of view, it has many practical applications: stabilization of a walking robot, rocket flight control (Astrom and Murray, 2008), or recently popular two-wheeled vehicle - "Segway".

Most of studies on inverted pendulum concern a closed-loop control. There is also a way to stabilize the pendulum in the open-loop control, where the pendulum suspension point performs fast oscillations in the vertical direction (Kapica, 1951; Siemieniako and Ciężkowski, 2011). Oscillations of the suspension point in the horizontal direction gives an interesting result, namely the possibility of stabilizing the pendulum between a horizontal and hanging position (Landau and Lifshitz, 2007; Siemieniako and Ciężkowski, 2011). It turns out that it is possible to generalize the problem and demonstrate the possibility of stabilization of the pendulum in various positions with oscillating point of suspension at the appropriate angle, which will be the subject of this paper.

2. MODEL OF PENDULUM

The perfectly rigid rod has been taken as the model of the pendulum, with mass m and length l. One end of the pendulum is the point of suspension. The system is placed in a gravitational field with a value of acceleration g. Fig. 1 shows the physical model of the pendulum. The system has been described by the Lagrange formalism.

The position of the suspension point of the pendulum describes vector:

$$\mathbf{r}_b = (A\cos(\Omega t)\sin(\beta), A\cos(\Omega t)\cos(\beta)) \tag{1}$$

where: A – amplitude vibrations of the suspension point, Ω – the frequency of the vibrations, β – angle, the direction of vibration of the suspension point.

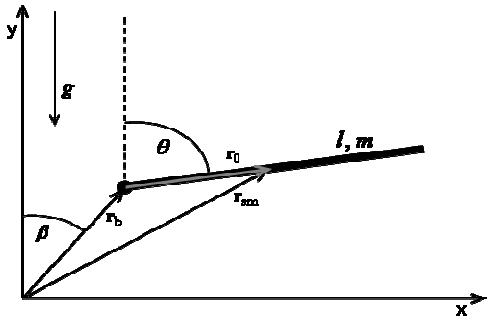

Fig. 1. Physical model of pendulum

The position of the mass center of the pendulum relative to the suspension is:

$$\mathbf{r}_0 = \frac{1}{2}l(\sin\theta, \cos\theta) \tag{2}$$

where: θ – the pendulum angle with respect to the y-axis.

Position of the mass center relative to the origin of the coordinate system is:

$$\mathbf{r}_{sm} = \mathbf{r}_b + \mathbf{r}_0 = (\frac{1}{2}l\sin\theta + A\cos(\Omega t)\sin(\beta), \frac{1}{2}l\cos\theta + A\cos(\Omega t)\cos(\beta)) \tag{3}$$

The kinetic energy is the sum of the translational kinetic energy of the mass center and the rotational kinetic energy of the pendulum relative to the mass center:

$$T = \frac{1}{2}m\dot{\mathbf{r}}_{sm}^{\ 2} + \frac{1}{2}\frac{1}{12}ml^2\dot{\theta}^2 = \frac{1}{6}m(3A^2\Omega^2\sin^2(\Omega t) + \dot{\theta}l(\dot{\theta}l - 3A\Omega\sin(\beta-\theta)\sin(\Omega t))) \tag{4}$$

The potential energy of system is:

$$V = gm(A\cos(\beta)\cos(t\Omega) + \frac{1}{2}l\cos(\theta)) \tag{5}$$

The Lagrangian has the form:

$$L = T - V \tag{6}$$

Substituting (4) and (5) into equation (6) then solving the Euler-Lagrange equation we get:

$$\frac{d}{dt}\frac{\partial L}{\partial \dot{\theta}} = \frac{\partial L}{\partial \theta} \Rightarrow \ddot{\theta} = \frac{3(A\Omega^2 \sin(\beta-\theta)\cos(t\Omega) + g\sin(\theta))}{2l} \tag{7}$$

The obtained equation is an equation of motion of the pendulum.

3. MOTION ANALYSIS OF PENDULUM AS THE MOTION IN A RAPIDLY OSCILLATING FIELD

Oscillating change of the suspension point's position realizes the pendulum's control. It is assumed that the frequency of these oscillations is large compared with the oscillation frequency of the system if the movement takes place only under the influence of the gravity. It is also assumed that the changes of the pendulum's position, caused by these vibrations, are small. Such an object can be regarded as an object moving in a rapidly oscillating field.

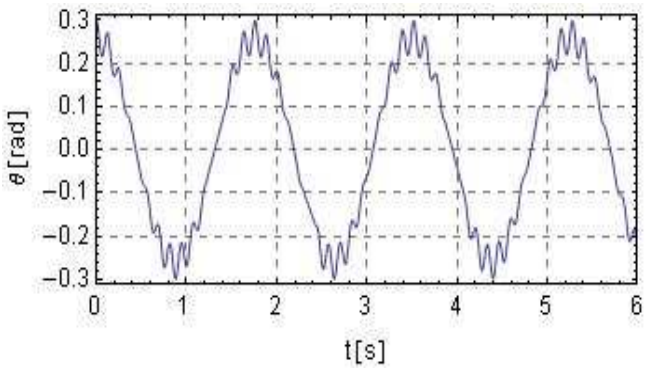

Fig. 2. Numerical simulation result

Fig. 2 (Siemieniako and Ciężkowski, 2011) shows the simulation results of the pendulum angle's time-variation. This is a solution of the equation (7) for values:

$$l = 1m,\ g = 9.81\frac{m}{s^2},\ A = 0.1m,\ \Omega = 50\frac{rad}{s},\ \beta = 0\,rad,$$

$$\theta(0) = 0.3\,rad,\ \dot{\theta}(0) = 0\frac{rad}{s}$$

It can be noted that the swing of the pendulum is composed of vibrations of high amplitude and low frequency (hereinafter referred to as $\Phi(t)$) and small oscillations of high frequency ($\xi(t)$). The presence of small oscillations appears to be consistent with the assumptions, if the movement takes place in a constant gravity field and rapidly oscillating field which enforces the oscillations of the suspension point. If the motion is a combination of two oscillations, the position of the pendulum can be written as:

$$\theta(t) = \Phi(t) + \xi(t) \tag{8}$$

where $\Phi(t)$ describes the "smooth" movement of the pendulum, averaged due to the rapid oscillations.

Substituting (8) to (7) and expanding the result in the first-order Taylor series because of the ξ (small oscillations) the following is obtained:

$$\ddot{\Phi} + \ddot{\xi} = -\frac{3A\xi\Omega^2\cos(\beta-\Phi)\cos(t\Omega)}{2l} + \frac{3A\Omega^2\sin(\beta-\Phi)\cos(t\Omega)}{2l} + \frac{3g\xi\cos(\Phi)}{2l} + \frac{3g\sin(\Phi)}{2l} \tag{9}$$

Acceleration of the suspension point is proportional to Ω^2 and changes quickly. It can be concluded that the ξ will meet the same relationship. Only the second term of the equation (9) satisfies these conditions (first term is proportional to ξ, so it is small). So you can write:

$$\ddot{\xi} = \frac{3A\Omega^2\sin(\beta-\Phi)\cos(t\Omega)}{2l} \tag{10}$$

The value of $\ddot{\Phi}$ is equal to the other terms of the equation (9):

$$\ddot{\Phi} = -\frac{3A\xi\Omega^2\cos(\beta-\Phi)\cos(t\Omega)}{2l} + \frac{3g\xi\cos(\Phi)}{2l} + \frac{3g\sin(\Phi)}{2l} \tag{11}$$

Double-integrating expression (10) under the assumption that Φ changes so slowly that we can consider them as constants, we get:

$$\xi = -\frac{3A\cos(t\Omega)\sin(\beta-\Phi)}{2l} \tag{12}$$

Substituting equation (12) to (11) and averaging the result due to the rapid oscillations ($\overline{\cos(t\Omega)} = \overline{0, \cos(t\Omega)^2} = 1/2$) we obtain the equation:

$$\ddot{\Phi} = \frac{9A^2\Omega^2\sin(2(\beta-\Phi))}{16l^2} + \frac{3g\sin(\Phi)}{2l} \tag{13}$$

To show why the pendulum is stable it has to be determined what the effective potential energy of the system is:

$$\frac{1}{3}ml^2\ddot{\Phi} = -\frac{dU_{ef}}{d\Phi} \Rightarrow U_{ef} = -\frac{1}{3}ml^2\int\ddot{\Phi}\,d\Phi \Rightarrow$$
$$U_{ef} = \frac{1}{2}glm\cos(\Phi) - \frac{3}{32}A^2m\Omega^2\cos(2(\beta-\Phi)) \tag{14}$$

Fig. 3 illustrates the graph of function (14) for different values of angle β, for fixed g, m, l, A, Ω equal to: $g = 9{,}81\ m/s^2$, $m = 0{,}8\ kg$, $l = 1m$, $A = 0{,}1\ m$, $\Omega = 70\ rad/s$.

The meaning of the line is as follows:

- solid line: $\beta = 0$;
- dotted line: $\beta = \pi/4$;
- "dot-dash" line: $\beta = \pi/2$;
- dashed line: $\beta = 3/4\pi$.

As shown in the Fig. 3 each plot has a minimum of the potential (and thus satisfies the condition of the stability), which for fixed parameters g, m, l, A, Ω is dependent on the

angle β. This relationship has been found, what will be the subject of the next chapter.

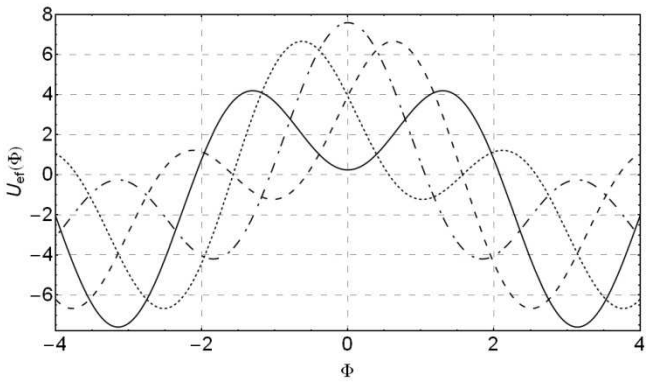

Fig. 3. Effective potential of the pendulum for various values of β

4. STABILITY CONDITIONS

Conditions for a minimum potential at a given point are: the first derivative U_{ef} is zero and the second derivative of the effective potential energy is positive at this point.

The first derivative of equation (14) is:

$$\frac{\partial U_{ef}}{\partial \Phi} = -\frac{3}{16} A^2 m \Omega^2 \sin(2(\beta - \Phi)) - \frac{1}{2} glm \sin(\Phi) \tag{15}$$

Denoting:

$$\lambda = \frac{3A^2\Omega^2}{4gl} \tag{16}$$

the extreme condition can be written as:

$$\frac{\partial U_{ef}}{\partial \Phi} = 0 \Leftrightarrow \sin(\Phi) + \frac{1}{2}\lambda \sin(2(\beta - \Phi)) = 0 \tag{17}$$

and can be solved for variable β. Solution of equation (17) gives the result:

$$\beta = \beta_{ext} = \frac{1}{2}(2\Phi - \arcsin(\frac{2\sin(\Phi)}{\lambda})) \tag{18}$$

The second derivative of the potential for $\beta = \beta_{ext}$ is:

$$\frac{\partial^2 U_{ef}}{\partial \Phi^2}|_{\beta=\beta_{ext}} = \frac{1}{8}(3A^2 m\Omega^2 \sqrt{1 - \frac{4\sin^2(\Phi)}{\lambda^2}} - 4glm\cos(\Phi)) \tag{19}$$

Requesting it to be greater than zero, conditions for the existence of a minimum of effective potential are:

I)

$$\lambda > \sqrt{4\sin^2(\Phi) + \cos^2(\Phi)} \qquad \text{for} \quad \Phi \in \langle 0, \frac{\pi}{2}) \tag{20}$$

II)

$$\lambda > 2 \qquad \text{for} \quad \Phi = \frac{\pi}{2} \tag{21}$$

III)

$$\lambda \geq 2\sin(\Phi) \qquad \text{for} \quad \Phi \in (\frac{\pi}{2}, \pi) \tag{22}$$

These conditions can be compared with the results for vertical and horizontal oscillations contained in the publication Siemieniako and Ciężkowski (2011): when the gle $\Phi = 0$ (the case of vertical oscillations) then according to (20) the stability condition is: $\lambda > 1$.

When $\Phi = \arccos(-1/\lambda)$ (the case of horizontal oscillations) then according to (22) the stability condition is: $\lambda > 1$.

In both cases, the stability conditions are the same as in the publication of the above mentioned authors.

4.1. Effective potential for a fixed parameter λ

The parameter λ, which determines the stability of the system is a function of variables describing the controlled object (this variable is the length of the pendulum) and variables controlling the pendulum (A, Ω). Equations (20), (21), (22) show that for any angle Φ within the range $< 0, \pi)$ the stability condition can be written: $\lambda > 2$.

This condition is satisfied for the example values: $l = 1m$, $g = 9{,}81\ m/s^2$, $A = 0{,}1\ m$, $\Omega = 70\ rad/s$, for which the parameter $\lambda = 3{,}74618$. The above-mentioned values and the pendulum mass $m = 0{,}1\ kg$ will be used in further analysis of the system.

Fig. 4 shows a graph of the pendulum effective potential energy as a function of the angle of oscillations the suspension point β and the angle Φ with the rest system parameters set above.

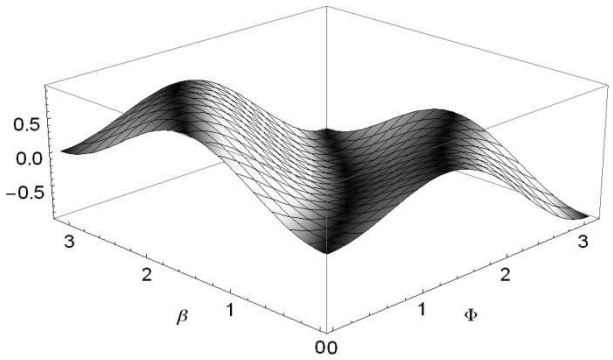

Fig. 4. Effective potential of the pendulum in function β and Φ

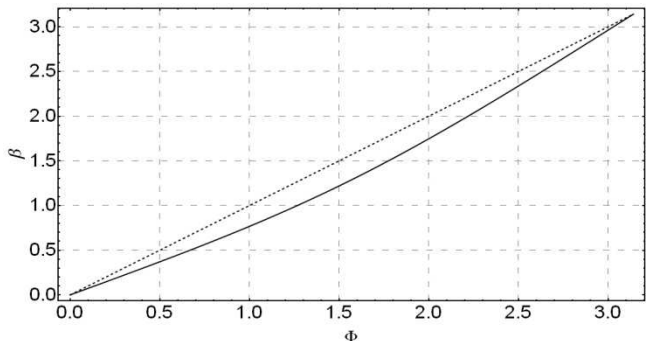

Fig. 5. The relationship between β and Φ, at which the pendulum is at a minimum of potential

The plot's colors reflect the absolute value of the first derivative of U_{ef} – the darker the color, the lower the value of the derivative. With these colors function extremes are

more visible. The longest dark bar at the graph represents the area where the potential has a minimum value. Drawing a relationship (18) one can show this curve as in Fig. 5.

The dashed line in Fig. 5 describes the relationship $\beta = \Phi$. The function (18) shows that with increasing λ, the function more and more „closes" to the relationship $\beta = \Phi$. This behavior becomes evident after analysis of the formula (14) describing the U_{ef}. The first term of this formula comes from the gravitational potential and the other from the oscillations. With increasing λ the second term begins to dominate over the gravity and takes the highest absolute value (for fixed λ), when $\beta = \Phi$.

5. NUMERICAL SIMULATION RESULTS

If the parameter λ does not change in the experiment (and of course satisfies the stability conditions), the only problem to solve is to determine the angle at which we want to set the pendulum and then, according to (18), determine the angle β_{ext} which will determine the direction of vibration of the pendulum suspension point. This chapter will be presenting numerical results for the specific values of the angle Φ. The parameters of the system (g, m, l, A, Ω) are the same as those listed in Section 4.1, the parameter $\lambda = 3{,}74618$. The simulation is the numerical solution of equation (7).

5.1. Example 1: $\boldsymbol{\Phi = \pi/4}$

The direction of oscillations according to (18): $\beta = 0{,}5918$.

Initial conditions: $\theta(0) = \pi/4 + 0{,}1\ rad$, $\dot{\theta}(0) = 0\ rad/s$.

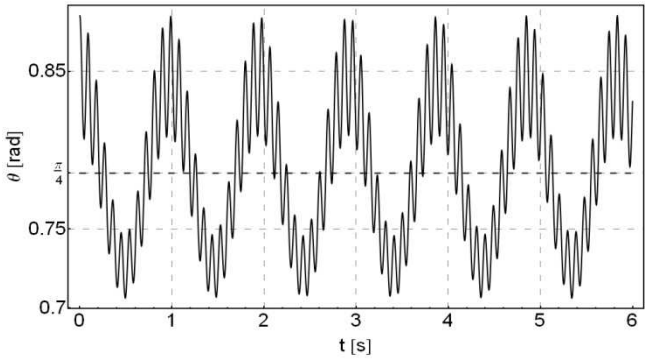

Fig. 6. Numerical simulation result of equation (7)

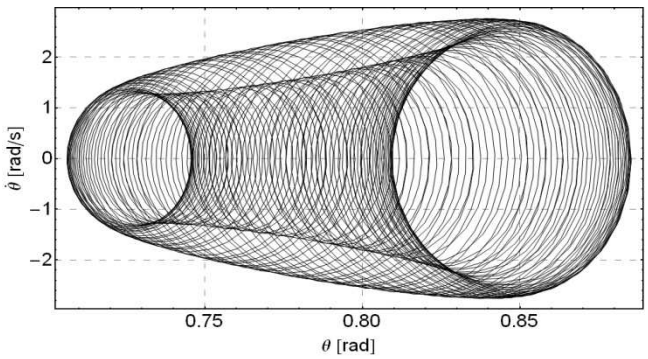

Fig. 7. Phase portrait of the simulation

Figs. 6 and 7 show the simulation results of the pendulum motion. As you can see the pendulum inclined to a certain angle starts to oscillate around the set point, in this case equal to $\pi/4$. Effective potential for this case has the form as shown:

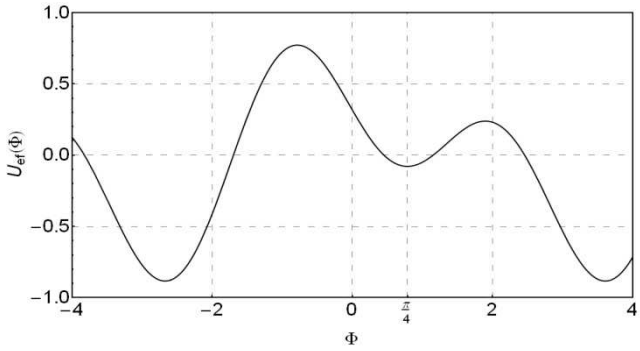

Fig. 8. Effective potential of the pendulum

As shown in Fig.8, the potential has a minimum for the desired angle.

5.2. Example 2: $\boldsymbol{\Phi = \pi/2}$

The direction of oscillations according to (18): $\beta = 1{,}289$.

Initial conditions: $\theta(0) = \pi/2 + 0{,}1\ rad$, $\dot{\theta}(0) = 0\ rad/s$.

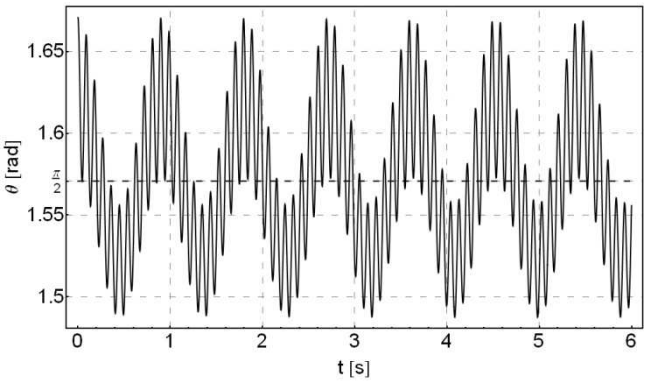

Fig. 9. Numerical simulation result of equation (7)

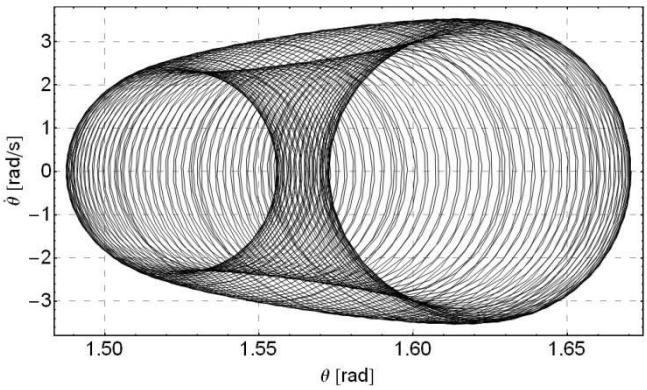

Fig. 10. Phase portrait of the simulation

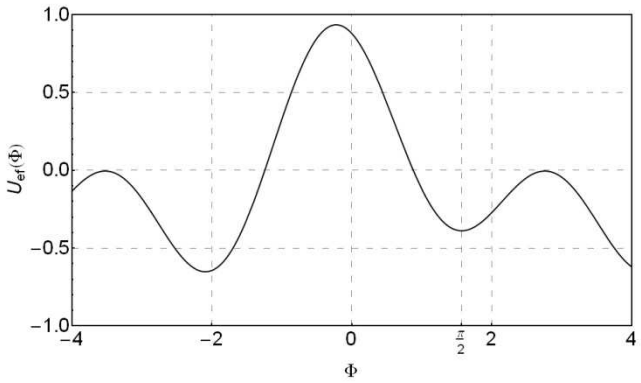

Fig. 11. Effective potential of the pendulum

These figures illustrate the results of the numerical simulation of the pendulum for $\Phi = \pi/2$. As you can see the system behaves as planned. In Fig. 9, and even better on the phase portrait can be seen increase of the speed of fast oscillations relative to the first example. The frequency of fast oscillations seems to be the same in both examples.

5.3. Example 3: $\Phi = 3/4\pi$

$\beta = 2{,}162$, $\theta(0) = 3/4\pi + 0{,}1\ rad$, $\dot{\theta}(0) = 0\ rad/s$.
The following figures show the simulation results.

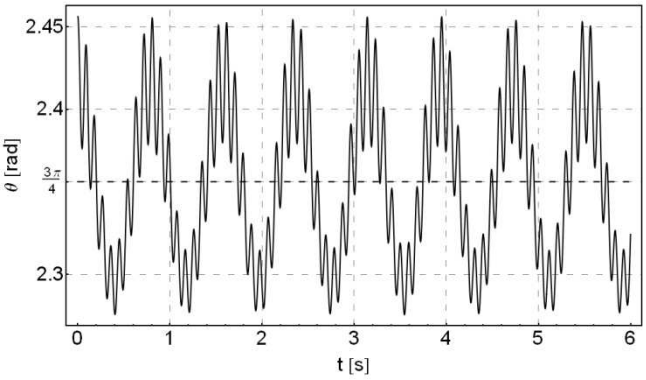

Fig. 12. Numerical simulation result of equation (7)

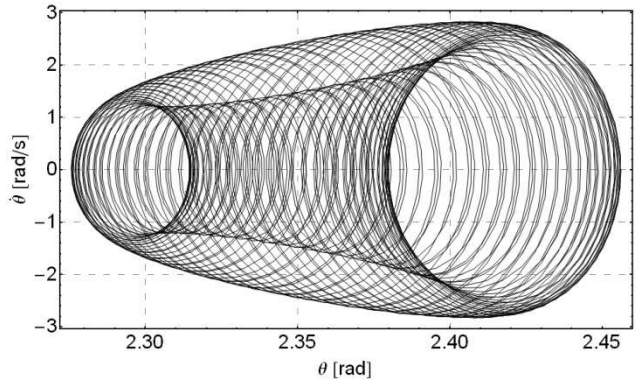

Fig. 13. Phase portrait of the simulation

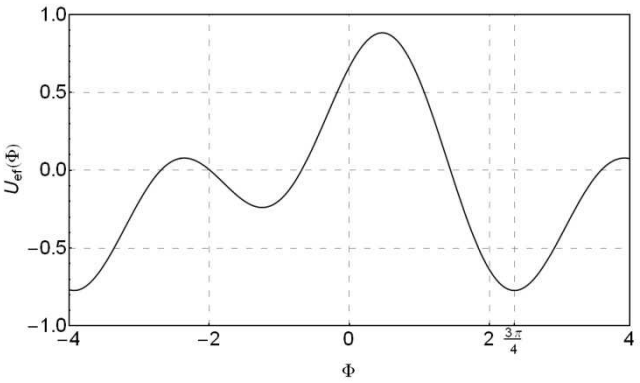

Fig. 14. Effective potential of the pendulum

The figures above illustrate the results of numerical simulation of the pendulum for $\Phi = 3/4\pi$.

6. NUMERICAL SIMULATION IN THE PRESENCE OF FRICTION FORCE AND RANDOM DISTURBANCES

The results presented in chapter five, illustrate behavior of the perfect system, that is, without energy dissipation and noise. In the real world, forces of friction and random disorders cannot be eliminated. To make the system more realistic, numerical simulation in presence of non-conservative forces was performed.

The Euler-Lagrange equation then takes the form:

$$\frac{d}{dt}\frac{\partial L}{\partial \dot{\theta}} - \frac{\partial L}{\partial \theta} = -k_1\dot{\theta} + k_2\varepsilon(t) \tag{23}$$

where: k_1 – viscous damping coefficient, k_2 – noise coefficient.

$\varepsilon(t)$ is a random disturbance and is assumed to obey normal distribution with density function: $\frac{1}{\sqrt{2\pi}} e^{\frac{-\varepsilon(t)^2}{2}}$.

The average value of $\varepsilon(t)$ is zero. The perturbation changes randomly at each simulation time step. Fig. 15 illustrates an example of the function $\varepsilon(t)$.

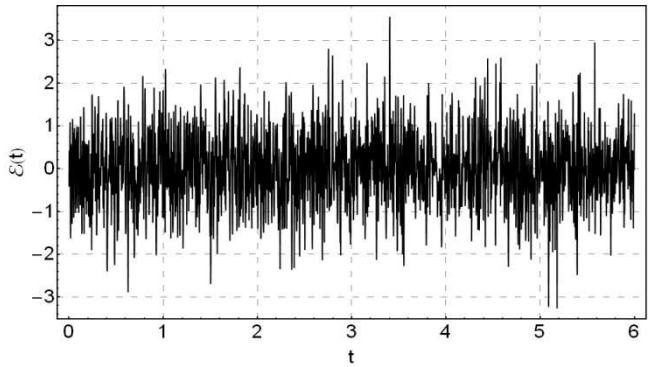

Fig. 15. Random perturbations of the system

Solution of the equation (23) gives the result:

$$\ddot{\theta} = \frac{3(A\Omega^2\sin(\beta-\theta)\cos(t\Omega)+g\sin(\theta))}{2l} - \frac{3k_1}{l^2m}\dot{\theta} + \frac{3k_2}{l^2m}\varepsilon(t) \tag{24}$$

The obtained equation is an equation of the pendulum's motion in the presence of friction force and random disturbances.

While the viscous friction should help to maintain the pendulum in the desired position, a random disturbance can cause loss of the system's stability. This will happen when the pendulum "jumps out" from an effective potential well on the result of existing disturbances. So the critical value of the parameter k_2 depends on the depth of potential well. The parameter $k_2 = 0{,}03Nm$ will be used in further analysis of the system. For such value of the coefficient k_2, some distortions have been noticed, but the system has still been stable. The adopted value of the damping factor is: $k_1 = 0{,}02Nm$. The initial conditions and the angle β values are the same as in the examples in chapter 5.

6.1. Example 1: $\Phi = \pi/4$

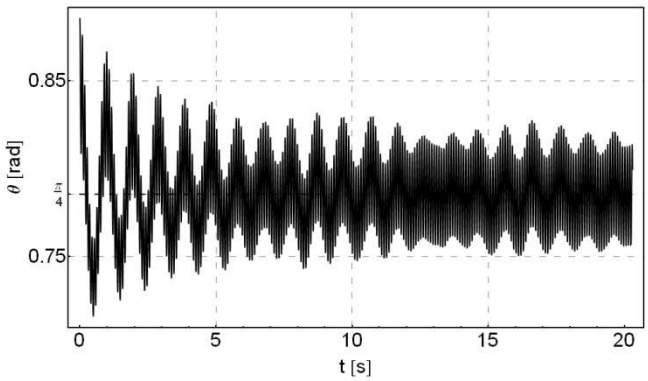

Fig. 16. Numerical simulation result of equation (24)

As shown in Fig. 16, high-amplitude oscillations are damped. Small amplitude and high frequency vibrations still occur. The presence of small oscillations is the result of the suspension point's vibrations. Force caused by these vibrations is so large that the friction is not able to dampen the pendulum. You can verify if the random disturbance force cause these small oscillations. Fig. 17 shows the result of the simulation, for the parameter$k_2 = 0Nm$.

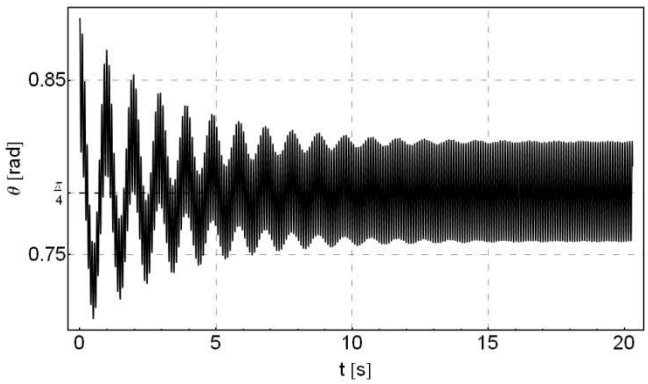

Fig. 17. Numerical simulation result of equation (24) for $k_2 = 0$

As shown in Fig. 17 the system still performs small vibrations. The simulations show that the random force introduces only a small disturbance to vibration.

To demonstrate the resistance of the system to disturbances, additional simulations were performed for the parameter $k_2 = 0{,}3Nm$ and $k_2 = 1{,}7Nm$. The results of these simulations are illustrated in Figs. 19 and 20.

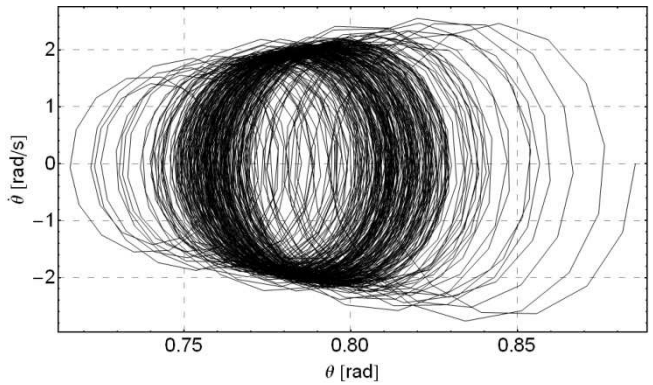

Fig. 18. Phase portrait of the simulation with random noise

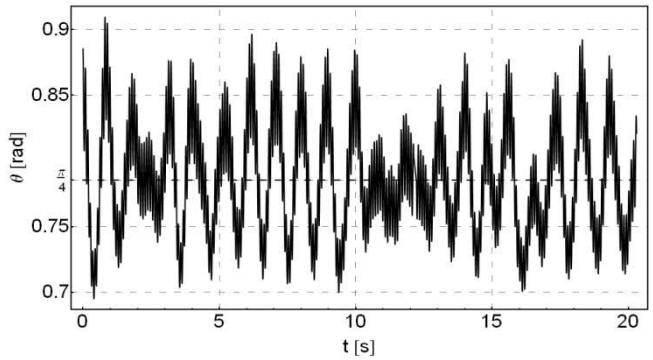

Fig. 19. Numerical simulation result of equation (24) for $k_2 = 0{,}3Nm$

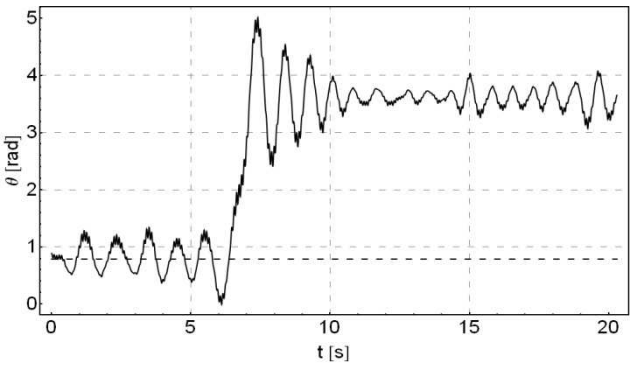

Fig. 20. Numerical simulation result of equation (24) for $k_2 = 1{,}7Nm$

Fig.19 shows that 10-times greater disturbance does not cause loss of stability. For $k_2 = 1{,}7Nm$ (Fig. 20) system is no longer stable and the pendulum "jumps" to the neighboring potential well (see Fig. 8).

6.2. Example 2: $\Phi = \pi/2$

As in the first example, the system performs small, rapid oscillations around the set point. Just as in the case without friction and disturbances, the speed of pendulum oscillations is greater than in example $\Phi = \pi/4$.

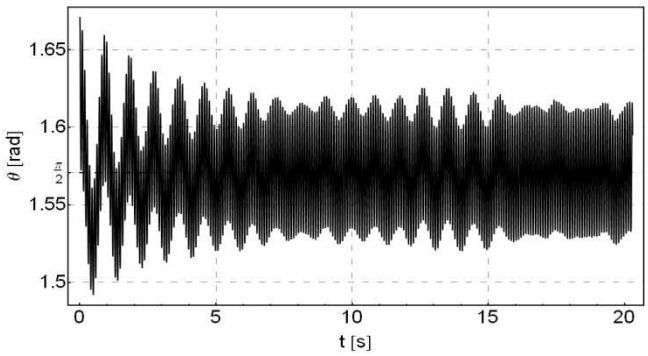

Fig. 21. Numerical simulation result of equation (24)

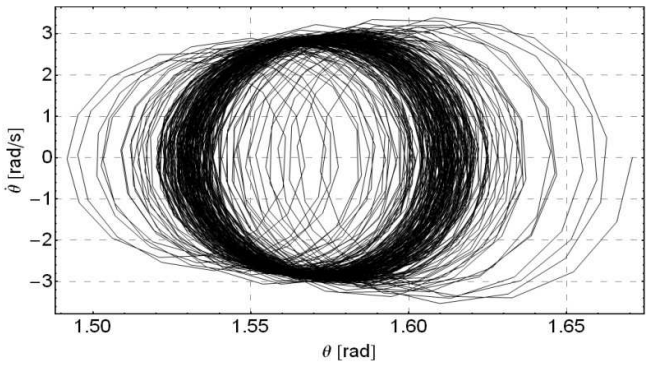

Fig. 22. Phase portrait of the simulation

6.3. Example 3: $\Phi = 3/4\pi$

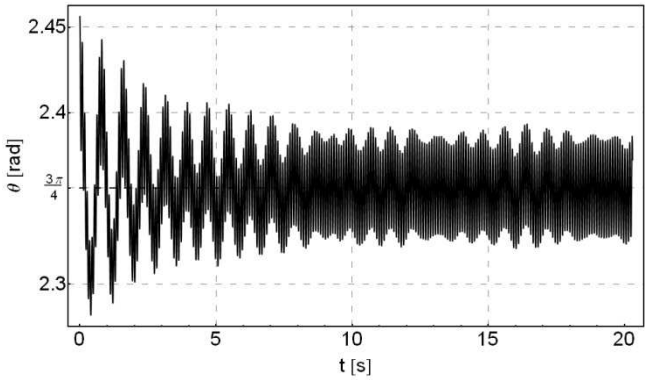

Fig. 23. Numerical simulation result of equation (24)

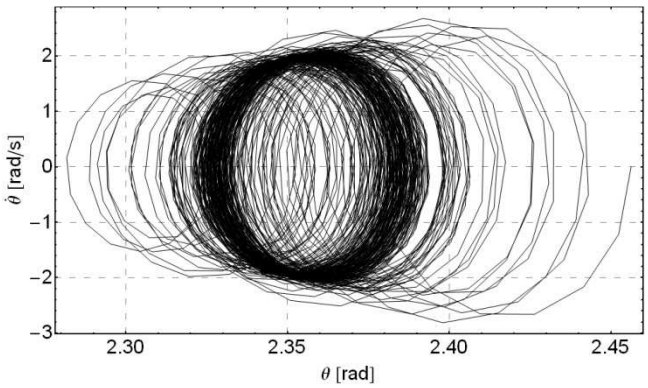

Fig. 24. Phase portrait of the simulation

The figures above illustrate the results of numerical simulation of the pendulum for $\Phi = 3/4\pi$.

7. SUMMARY

The results presented in this paper demonstrate the possibility of stabilizing the pendulum in various inclinations. The system is stable if its parameters satisfy the conditions that have been set in chapter four. In addition to solutions for the "ideal" system, the possibility of stabilizing the pendulum in the presence of friction force and random disturbances has been demonstrated. It is shown that the system is highly resistant to disturbances, which increases the chances of an experimental realization of the system.

REFERENCES

1. **Astrom K. J, Murray R. M.** (2008), *Feedback Systems: An Introduction for Scientists and Engineers*, Princeton Univ Pr.
2. **Kapitza P. L.** (1951), *Majatnik s vibrirujuwim podvesom*, Uspekhi Fizicheskikh Nauk.
3. **Landau L. D., Lifszyc J.M.** (2007), *Mechanika*, PWN, Warszawa.
4. **Siemieniako F., Ciężkowski M.** (2011), Sterowanie położeniem odwróconego wahadła w pętli otwartej, Wojciech Tarnowski, Tomasz Kiczkowiak (red.): *Polioptymalizacja i Komputerowe Wspomaganie Projektowania*, Mielno 2011, Wydawnictwo Uczelniane Politechniki Koszalińskiej, Koszalin 2011, str. 31-39.

MODELING OF MAGNETORHEOLOGICAL MOUNTS IN VARIOUS OPERATION MODES

Janusz GOŁDASZ[*], Bogdan SAPIŃSKI[**]

[*] Technical Center Kraków, BWI Group Poland, ul. Podgórki Tynieckie 2, 30-399 Kraków, Poland
[**] Department of Process Control, AGH University of Science and Technology, al. Mickiewicza 30, 30-059 Kraków, Poland

janusz.goldasz@bwigroup.com, deep@agh.edu.pl

Abstract: Recent advances in the research of magnetorheological/electrorheological (MR/ER) fluid based devices have indicated the opportunities for smart fluid based devices utilizing more than one operation mode. As such, the purpose of the present research is to draw attention to the existing models of magnetorheological (MR) mounts operating in two of the three fundamental operating modes, namely, the flow mode and the squeeze mode, and to highlight the potential applications of these modes in hydraulic mount applications. Therefore, in the paper the authors focus on recent applications of MR/ER fluids in that domain, and then proceed to summarizing the modeling principles for the two operation modes followed by a finite-element magnetostatic analysis of the mount's magnetic circuit, parameter sensitivity study and exemplary numerical simulations of each mode. The simulation results are converted into the frequency domain and presented in the form of dynamic stiffness and damping vs. frequency plots, respectively.

1. INTRODUCTION

Nearly all magnetorheological/electrorheological (MR/ER) devices can be classified as operating in at least one of the following three operation modes: flow mode, shear mode, and squeeze mode as shown in in Fig. 1. The devices operating in either flow mode or shear mode (linear/rotary shock absorbers, clutches, engine mounts) have been commercialized, and the theory well developed (Philips, 1969; Gavin et al., 1996a; Gavin et al., 1996b; Wiliams et al., 1993, Sproston et al., 1994).

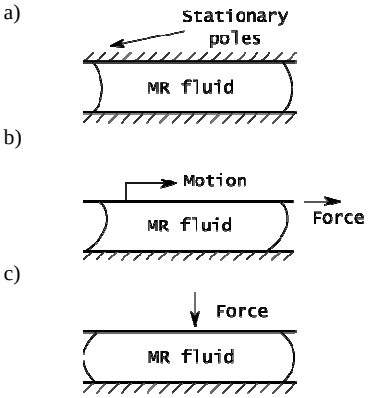

Fig. 1. Configurations of MR hardware: a) flow mode, b) shear mode, c) squeeze mode (Jolly et al., 1998)

For example, BWI Group (formerly the Chassis Division of Delphi Corp.) has developed and implemented an MR flow-mode based shock absorber (Hopkins et al., 2001; Kruckemeyer et al., 2001) (known under the commercial name of MagneRide) and an MR flow-mode based powertrain mount for the automotive industry (Baudendistel et al., 2002, Baudedistel et al., 2003). Also, Lord Corp. has been rather active in developing commercial applications of flow-mode MR dampers as well as shear-mode rotary MR dampers (brakes) (Carlson et al., 1994; Jolly, 1998). To the authors' best knowledge, no commercial applications of the squeeze-mode based hardware have been reported. There is, however, an ongoing engineering and research interest in the development of MR/ER fluid based hardware operating in the squeeze-mode (Wiliams et al., 1993; Sproston et al., 1994; Jolly and Carlson, 1996, Bolter and Janocha, 1998; Tang et al., 1998, Stanway et al., 2000, Farjoud et al., 2009). In the case of MR fluid, the devices employ a layer of MR fluid sandwiched between two magnetic poles of which at least one is subjected to vertical motion. As a result, the distance between the poles varies according to the displacement or force profile, and the fluid is forced out of the between them. The squeeze-mode seems very suitable for low-stroke (few millimeters or less) and high damping force MR/ER applications, namely powertrain mounts or general-purpose vibration isolators. As such, controllable squeeze-mode devices can be more compact when sized for same damping force requirements. Research challenges are due to the squeeze-mode model capable of predicting flow field, pressure distribution across squeezing plates and shear stresses (Farjoud et al., 2011), control schemes (Zhang et al., 2011). Manufacturing challenges may arise, though, due to the range of displacements required for effective operation.

However, ER fluids may not be suitable for implementing a real-world squeeze-mode device as one of the failure modes of such hardware is due to the contact of squeezing plates (and electrical short circuit). MR fluid squeeze-mode applications may be less problematic in that regard.

At the present moment, the most novel and promising squeeze-mode application seems a mixed-mode MR fluid-based damper or an MR mount (Brigley et al., 2007, Minh, 2009). Such a device might utilize the flow mode for large stroke motion damping, and make use of the squeeze flow

mode in order to enhance the primary flow mode in controlling small amplitude displacements. So far, several research studies have been conducted in that regard and a rather thorough summary of the recent research efforts was described by Minh (2009).

Therefore, the purpose of the research is to draw attention to the existing models of MR mounts operating in two of the above mentioned modes (flow, squeeze), and to highlight the potential applications of these modes in hydraulic mount applications (e.g. automotive powertrain mounts).

As such, the authors highlight some applications of MR/ER fluids in that domain, and then proceed to summarizing the modeling principles for the two operation modes followed by a finite-element magneto-static analysis of the mount's magnetic circuit, a parametric study and exemplary simulations of each mode.

2. MR HYDRAULIC MOUNT

The flow-mode MR damper is the smart-fluid based device that has been most commercialized over the years In a number of automotive vehicle platforms in particular (Alexandridis, 2007). The number of reported automotive MR damper applications well exceeds twenty in Europe, Asia, and US. Recent application areas also include military vehicle suspension applications (Lord Corp.). By a wide margin, it is the MR damper of the conventional deCarbon monotube design that is the most often implemented MR fluid based device. Apparently, another MR device under development is the MR hydraulic mount for powertrain applications (Baudendistel et al., 2002). The MR mount is claimed to operate in flow mode. Most ER fluid based mounts or MR fluid based ones follow the same design principle that conventional passive mounts are based upon, and with smart fluids the mount stiffness and damping characteristics can be controlled in real-time.

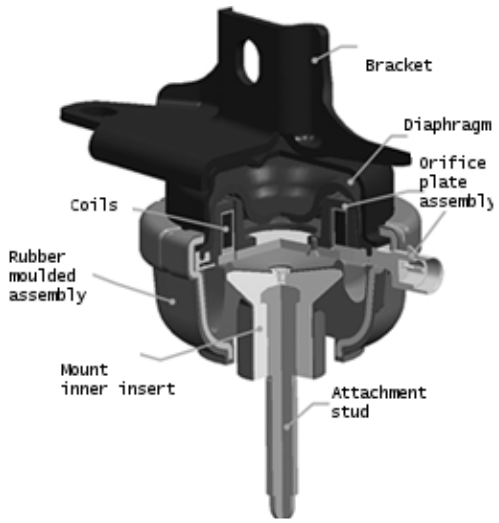

Fig. 2. MR hydraulic mount (courtesy of BWI Group)

As shown in Fig. 2, the components of each mount are rubber shells each constituting a fluid chamber filled with smart fluid and incorporating flow paths for the fluid. The upper volume is the pumping chamber, and the lower one is the so-called reservoir. In the case of MR mounts, the flow path is designed in such a way to be enveloped by the magnetic field generated in the circuit. With MR mounts, the presence of the magnetic field causes the smart fluid's yield stress to be altered according to the level of the magnetic field strength across the flow path height. As described by Baudendistel et al. (2002, 2003) two optional components of the MR mount are the so-called inertia track, and the decoupler. The decoupler is usually a partitioning plate located in a bypass flow path. With passive mounts it is a feature for providing means for enhancing the mount in isolating the low-displacement, high-frequen-cy inputs, whereas the inertia track (in the form of a long de-energized fluid channel) is used as an additional feature for controlling the fluid flow at low frequencies (Singh et al., 1992). These features have been widely used in passive conventional hydraulic mounts; however, their applications in MR mounts are none.

Active or semi-active mounts for have been of great interest for the automotive industry OEMs (Original Equipment Manufacturers) (Kowalczyk et al., 2004). Those mounts are capable of overcoming the conflicting design requirements of standard passive hydraulic mounts to deliver a device that is capable of providing a stiff support for the engine and good isolation at the same time.

3. MODELING OF MR MOUNTS

The following sections contain a brief summary of MR mount displacement-driven models operating in flow mode, squeeze mode, and the mixed mode (combined flow mode and squeeze mode), respectively.

3.1. Flow mode

The flow mode MR hydraulic mount exemplary configuration is shown in Fig. 3. The annular gap is contained In the stationary core. The magnetic field strength H is perpendicular to the surfaces of the annulus in the piston in order to restrict the fluid motion in the direction perpendicular to the surfaces of the annulus. A majority of the magnetic field strength H is generated in the circuit incorporating the core, the fluid volume contained in the annulus, and the outer ring of the core. The height of the annular gap is h, b is the mean radius of the annulus, and the cross-sectional area of the annular gap is $A_g=bh$. Also, the upper chamber cross-sectional area is A_p. The combined length of the active pole sections is L_a (the total length of the annular gap is L_g). The MR fluid is characterized by the bulk modulus β, the density ρ, the field-induced yield stress τ_0, and the field-invariant base viscosity μ. The top of the mount is driven by the known external displacement profile $x(t)$ (or the velocity $v(t)$), and the motion of the upper member forces the fluid to flow from one chamber to the other. The pressure drop across the stationary core is $\Delta P=P_1-P_2$, where P_1 and P_2 are pressures in the fluid chambers above and below the core assembly, respectively. The compliance of the upper chamber is C_1, and that of the lower one is C_2.

The volume flow rate through the annulus is Q. The geometry of the mount may contain a bypass path characterized by the hydraulic diameter H_b (the discharge coefficient C_b and the area A_b). The volume flow rate through the bypass is Q_b.

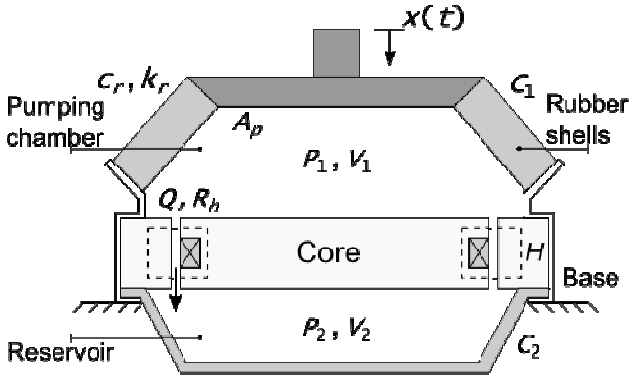

Fig. 3. Flow mode MR mount (Baudendistel et al., 2002); dashed lines show the magnetic field strength lines H

To arrive at the equations governing the behavior of the mount, the volumetric approach is used to describe pressure variations in each chamber. The method has been used In analyzing passive shock absorbers (Lee, 1997) and is common in engine mount analyses (Adiguna et al., 2003). Also, an inertia track model is implemented into the mount's model to account for the lumped mass of fluid in the annulus inertia (Singh et al., 1992, Kim and Singh, 1993, He and Singh, 2007). The hydraulic losses at the entry to the annulus (and the exit of the annular gap) and the effects of fluid flow development in the annulus are omitted, too. Then, the following set of equations can be drawn:

$$\begin{aligned}\frac{dP_1}{dt} &= \frac{A_p v - (Q+Q_b)}{C_1}\\ \frac{dP_2}{dt} &= \frac{Q+Q_b}{C_2}\\ \frac{dQ}{dt} &= \frac{A_g}{\rho L_g}(P_1 - P_2 - \Delta P_{MR})\end{aligned} \tag{1}$$

Briefly, Eq. 1 accounts for the pressure variations in each fluid chamber and the fluid mass inertia when bouncing on compliant fluid volumes. The pressure drop ΔP_{MR} across the annulus can be expressed as given by Gavin *et al.* (1996a, 1996b):

$$\Delta P_{MR} \approx 8\frac{\mu Q L_a}{bh^3}(1+3T)\left[\cos\left(\frac{1}{3}a\cos\left(1-54\left(\frac{T}{1+3T}\right)^3\right)\right)+\frac{1}{2}\right] \tag{2}$$

where T is the non-dimensional yield stress:

$$T = \frac{bh^2\tau_0}{12\mu Q} \tag{3}$$

Eq. 2 utilizes the solution of the Bingham model governing the quasi-steady-state relationship between the flow rate through the energized gap and the field-induced pressure drop in flow mode (Philips, 1969). The bypass flow rate Q_b is as follows:

$$Q_b = C_b A_b \sqrt{2\frac{|P_1 - P_2|}{\rho}}\operatorname{sign}(P_1 - P_2) \tag{4}$$

In the absence of magnetic field the laminar flow in the flow path is assumed. Therefore, the pressure drop at the de-energized (OFF) condition is:

$$\Delta P_{MR} = 12\frac{\mu L_g}{bh^3}Q \tag{5}$$

Moreover, assuming the mass M is attached to the upper base the equation governing the mass inertia can be derived as follows:

$$M\frac{dv}{dt} + c_r v + k_r x = A_p P_1 \tag{6}$$

where c_r and k_r are the rubber damping coefficient and the stiffness ratio, respectively. The equations represent a set of expressions governing the force of flow mode MR mounts.

3.2. Squeeze mode

The squeeze mode MR mount is shown in Fig. 4. In this configuration the lower pole is stationary, whereas the upper pole is driven by the displacement $x(t)$. Also, a planar plate is attached to the upper fixture. The initial gap across the upper plate and the upper surface of the core is h_0.

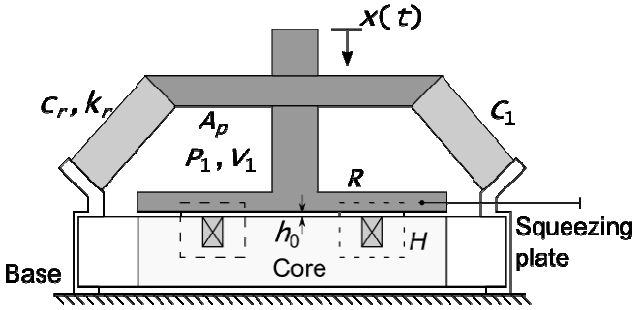

Fig. 4. Squeeze mode MR mount (Gołdasz and Sapiński, 2011); the magnetic field strength H shown with dashed lines

Then, the continuity equations and the MR squeeze mode expressions can be derived in the following manner (Kim et al., 1998, Stanway et al., 2000, Hong et al., 2002; Farjoud et al., 2009):

$$\begin{cases}\dfrac{dP_1}{dt} = \dfrac{A_p v}{C_1}\\ c_{Sq} = \dfrac{3\mu\pi R^3}{2(h_0+x)^3}\\ F_{Sq} = \tau_0\dfrac{3\pi R^3}{4(h_0+x)}\operatorname{sgn}(v)\end{cases} \tag{7}$$

Finally, the mass inertia can be described as follows:

$$M\frac{dv}{dt} + c_r v + c_{Sq} v + F_{Sq} + k_r x = A_p P_1 \tag{8}$$

where c_{Sq} is the viscous damping coefficient in the absence of magnetic field, F_{Sq} is the field induced force, and R is the outer radius of the upper plate. The first of the equa-

tions in the above set accounts for the compliance effects of the MR squeeze mode mount (chamber compliance). The above equations represent a set of expressions governing the output of squeeze mode MR mounts.

3.3. Mixed mode

The mixed mode mount shown in Fig. 5 include the pumping chamber, the reservoir chamber, and the stationary core incl. the annular gap. The magnetic field that is induced in the gap (upon the application of current in the primary coil) is perpendicular to the fluid flow (flow mode). The other coil faces the plate opposing the upper surface of the core.

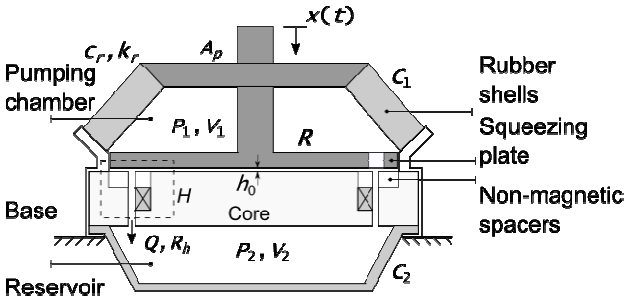

Fig. 5. Mixed-mode MR mount (Minh, 2009)

As a result of the plate displacement squeezing occurs. Both circuits can operate independently or in series. In this layout the flow-mode MR mount equations can be modified to include the squeeze mode circuit as follows (Minh, 2009):

$$\begin{aligned}\frac{dP_1}{dt} &= \frac{A_p v - (Q + Q_b)}{C_1} \\ \frac{dP_2}{dt} &= \frac{Q + Q_b}{C_2} \\ \frac{dQ}{dt} &= \frac{A_g}{\rho L_g}(P_1 - P_2 - \Delta P_{MR})\end{aligned} \tag{9}$$

$$M\frac{dv}{dt} + (c_r + c_{Sq})v + F_{Sq} + k_r x = A_p P_1 \tag{10}$$

where ΔP_{MR} is the field induced pressure drop defined In Section 3.1. Again, entry/exit effect are omitted in the analysis. Eqs. 9 and 10 reveal a set of expressions governing the dynamic output of mixed mode MR mounts. The equations may present a squeeze mode MR mount, a flow mode mount or a mixed mode mount. For instance, freezing the flow in the annulus by setting the yield stress In the flow path to a high level results in no-flow conditions and reduces the set of Eqs. 9 and 10 to the system of Eqs. 7 and 8. Also, setting the large initial gap between the squeezing plate and the core removes the squeeze mode contribution, and the flow mode can be studied on its own.

4. NUMERICAL SIMULATIONS

The numerical simulations include the development of a two-dimensional axi-symmetric model of the mixed mode MR mount of Fig. 5, the parameter sensitivity study as well as calculations of the complex transfer function of the MR mount when subjected to a sweep-sine constant amplitude displacement input.

The geometry and material properties of a mixed-mode mount virtual prototype are shown in Table 1. The data contained in the table represent the base configuration of the MR mount virtual prototype.

Tab. 1. Geometry and material properties of the MR mount

Symbol	Description	Value
A_p, mm^2	Mount effective area	2827
C_1, N/mm^5	Pumping chamber compliance	3100
C_2, N/mm^5	Reservoir chamber compliance	120000
L_g, mm	Annulus length	31
L_a, mm	Active length (flow mode)	13
h_1, mm	Annulus height (gap)	1.8
A_g, mm^2	Annulus cross-section area	281.6
R, mm	Plate radius (squeeze mode)	21
h_0, mm	Initial gap (squeeze mode)	{1, 3}
H_b, mm	Bypass size	0
ρ, g/cm^3	MR fluid density	3.1
μ, Ns/mm^2	MR fluid viscosity	0.00000003
k_r, N/mm	Rubber stiffness	200
c_r, Ns/mm	Rubber damping	0.1

4.1. Magnetostatic model

Two-dimensional axi-symmetric simulations (using the finite-element platform FEMM) were needed to optimize the geometry of the mount and to extract the flux density data for each gap that are necessary calculating the yield stress levels. Both coils were assumed to take on currents up to 500 ampere turns (AT). The *B–H* curve for the MR fluid is shown in Fig. 6 and SAE 1010 material properties were assumed for components in the magnetic circuit. The exemplary distributions of the magnetic field in the circuits at 500 ampere turns each are shown in Figs. 7 through 9.

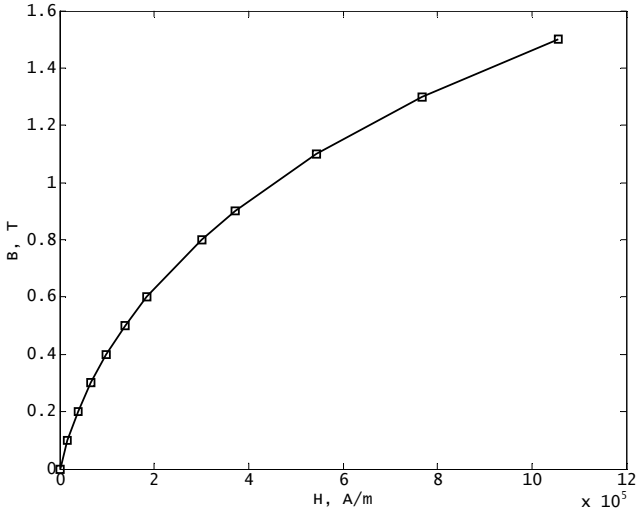

Fig. 6. MR fluid *B−H* curve (courtesy of BWI Group)

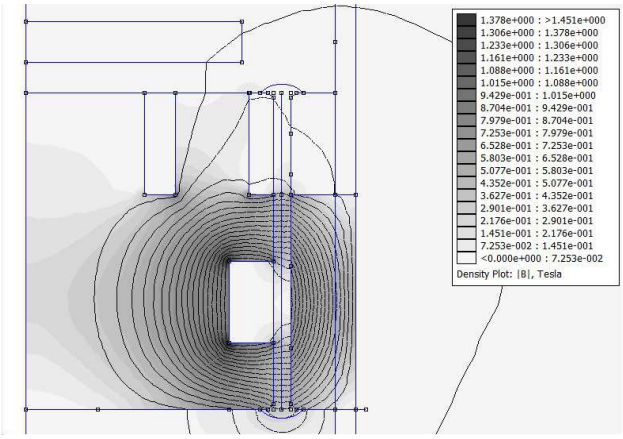

Fig. 7. Primary (flow-mode) coil; 500 AT

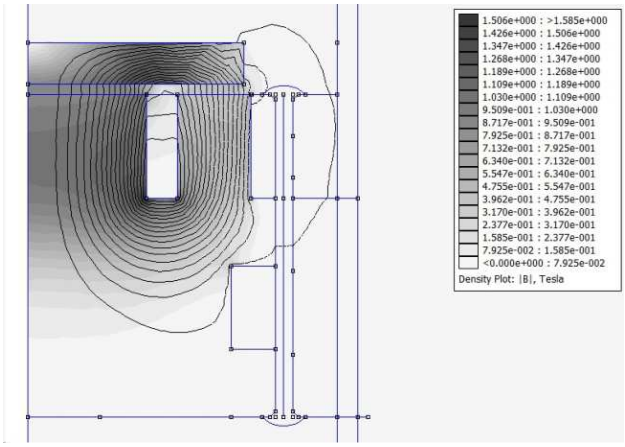

Fig. 8. Secondary (squeeze-mode) coil; -500 AT, h_0=1.0 mm

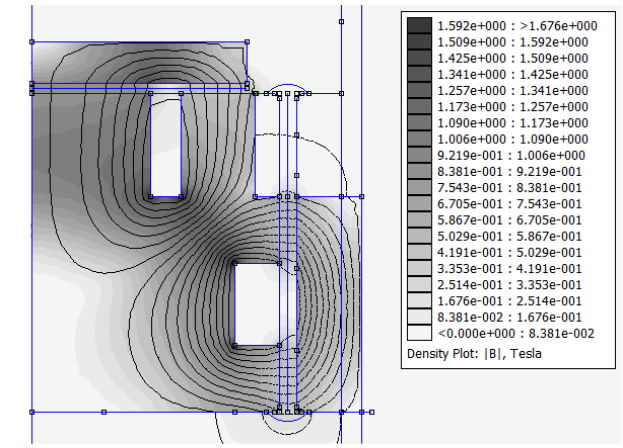

Fig. 9. Primary coil and secondary coil at ON condition

It is apparent from the illustrations both circuits can be operated independently with little influence of one mode on the other. For example, raising the coil current in the squeeze mode circuit even up to 500 ampere turns has little effect on the magnetic field strength in the switched off flow-mode annulus, and the calculated flux density level is less than 0.04 T.

The averaged flux density distribution (normal component) in the radial direction for the squeeze mode circuit AT the initial distance of 1.0 mm is revealed in Fig. 10, and the flux density vs. ampere turns vs. plate-to-core distance mapping is illustrated in Fig. 11. As shown in the images, the flux density in the squeeze mode gap is rather uniform; however, there is a significant difference in the flux density level across the inner and outer pole area, respectively. The results indicate there is some need for improvement and further optimization required in the squeeze mode circuit geometry.

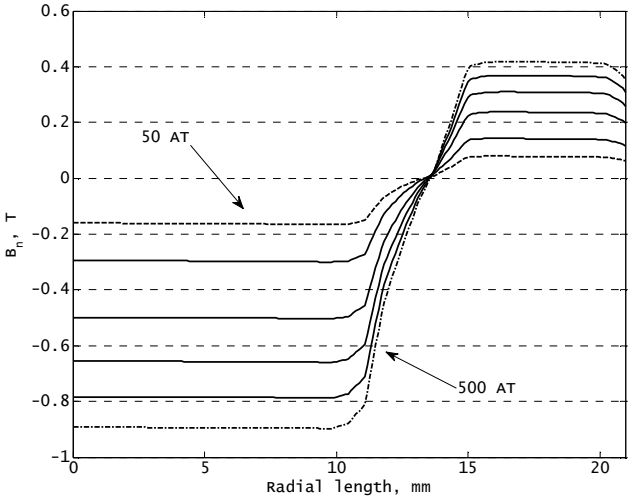

Fig. 10. Flux density distribution, squeeze mode; h_0=1.0 mm

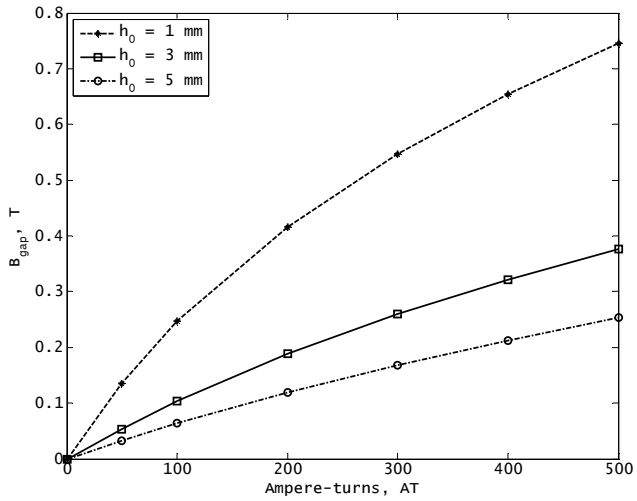

Fig. 11. Averaged flux density in the annulus, squeeze mode

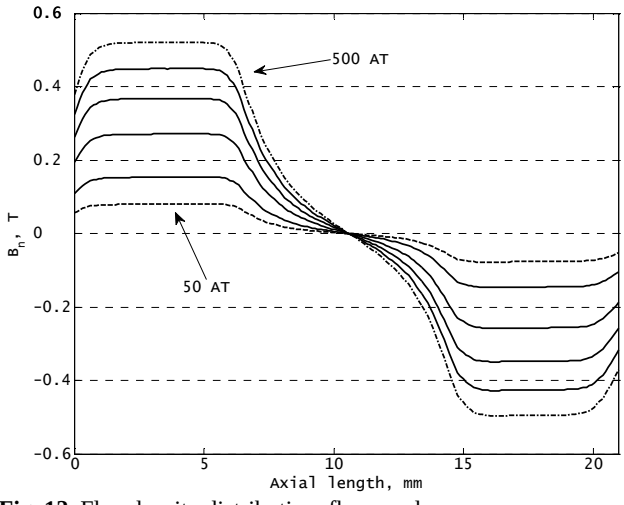

Fig. 12. Flux density distribution, flow mode

Similarly, the distribution of the averaged flux density normal component along the annulus (in the axial direction) and the flux density vs. ampere turns mapping for the flow mode circuit are shown in Figs. 12 and 13, respectively. The flux density distribution in the annulus is almost symmetrical across the two poles with little flux leakage to the other circuit.

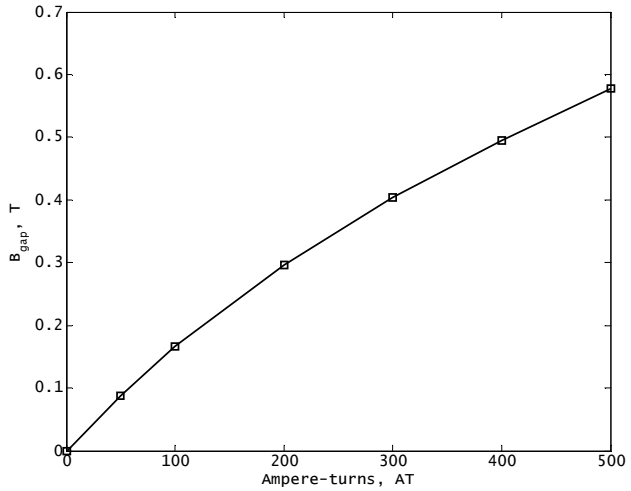

Fig. 13. Averaged flux density in the annulus, flow mode

4.2. Parameter sensitivity study

The parameter sensitivity study was required to understand the effect of material properties and geometric variables on the performance of the MR mount. To accomplish this, the mount model (at OFF condition) in Simulink was subjected to a sweep-sine constant amplitude displacement input. The results in time domain were the transmitted force and the input displacement. In all tests the input displacement amplitude was 2 mm, and the frequency varied from 0 to 300 Hz. The data were then converted into the frequency domain using FFT with Matlab – see Figs. 14−25. The MR mount performance metric of interest In the frequency domain is the so-called dynamic stiffness K_{dyn}. By definition, the dynamic stiffness is the ratio of the force to the displacement in frequency domain of the following form (Kim et al., 1993):

$$K_{dyn}(\omega)=\frac{F(\omega)}{X(\omega)} \tag{11}$$

where $F(\omega)$ and $X(\omega)$ are the frequency domain force and stroke, respectively. It is a complex variable from which the amplitude $|K_{dyn}|$ and phase ϕ can be calculated. Calculating the damping effects requires the calculation of the so-called dynamic damping C_{damp} in the following form:

$$C_{damp}(\omega)=\frac{K_{dyn}(\omega)\cdot\sin(\omega)}{\omega} \tag{12}$$

Both metrics are common when analyzing dynamic system data and have been used in the present study. At the OFF condition the contribution of squeeze mode is small, therefore, the study focused on the flow mode geometry and the material properties at this point. The parametric study involved the following flow mode parameters: annulus length L_g, gap size h, bypass size H_b, pumping chamber compliance C_1, base viscosity μ, and density ρ.

The influence of the annulus length L_g is shown in Figs. 14 and 15. Here, increasing the annulus length decreases the fluid resonant frequency. This effect is due to the larger mass of the fluid contained in the annulus.

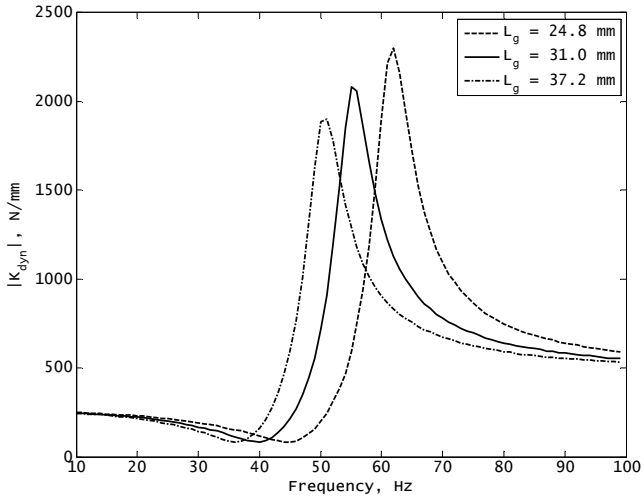

Fig. 14. Dynamic stiffness: influence of gap length, L_g

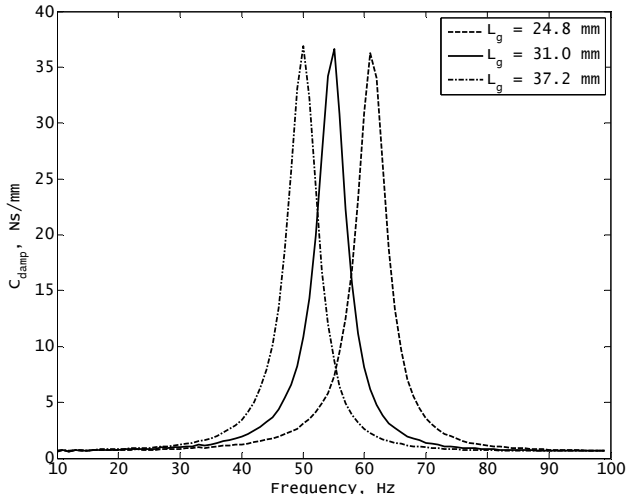

Fig. 15. Damping: influence of annular gap length, L_g

For comparison, increasing the gap size results in higher resonance frequencies of the fluid – see Figs. 16 and 17. Also, increasing the stiffness of the upper chamber (and decreasing the compliance C_1) shifts the resonant frequency towards higher frequencies as seen in Figs. 18 and 19. In addition to that, the respective effects of the bypass size and the viscosity lower the amplitude of the resonant frequency peaks as seen in Figs. 20 through 23. Also, increasing the density of the fluid results in an effect that is similar to the influence of the annulus length – see Figs. 24 and 25. It is due to the increased mass of the fluid in the annulus.

Also, it is interesting to note the reduction in the amplitude of the notch frequency (located below the fluid resonance) was achieved through varying the bypass flow path geometry, and changing the viscosity of the MR fluid.

Other parameters resulted in varying the location of the notch frequency (along with the resonance frequency) but not the amplitude.

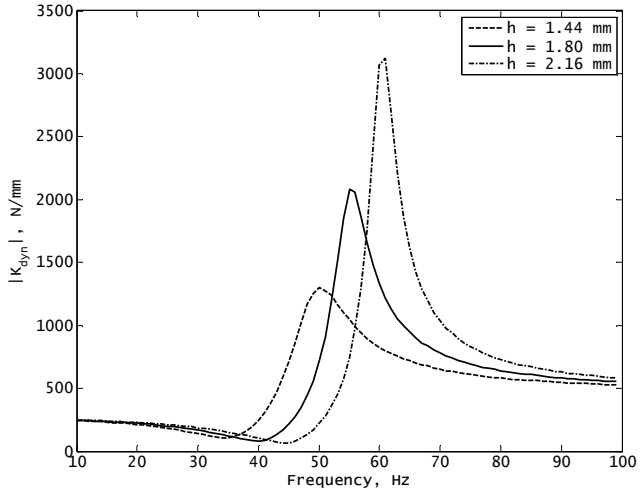

Fig. 16. Dynamic stiffness: influence of annular gap size, *h*

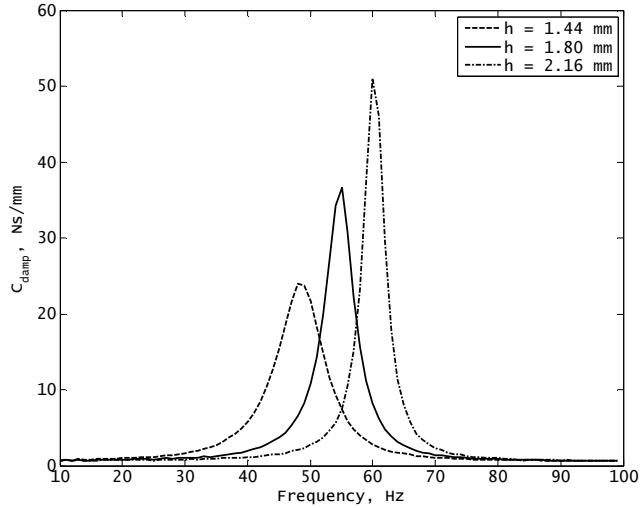

Fig. 17. Damping: influence of annular gap size, *h*

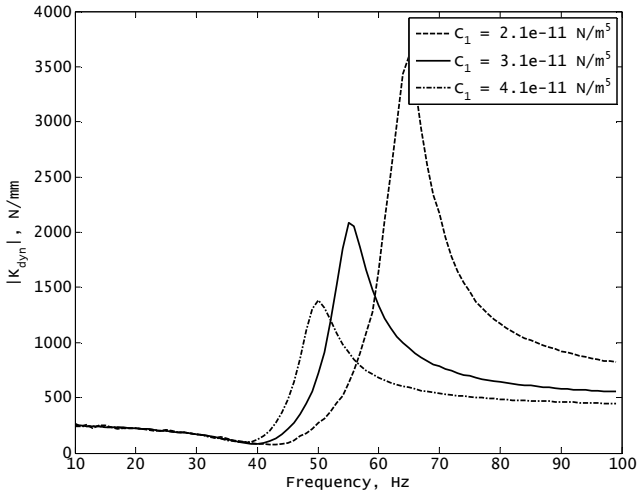

Fig. 18. Dynamic stiffness: pumping chamber compliance, C_1

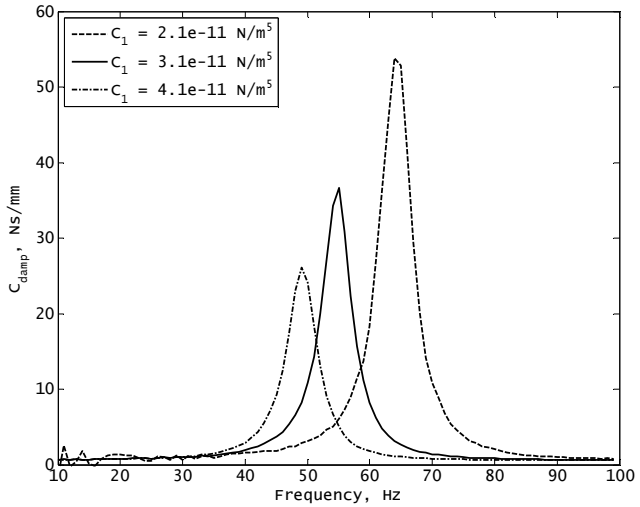

Fig. 19. Damping: pumping chamber compliance, C_1

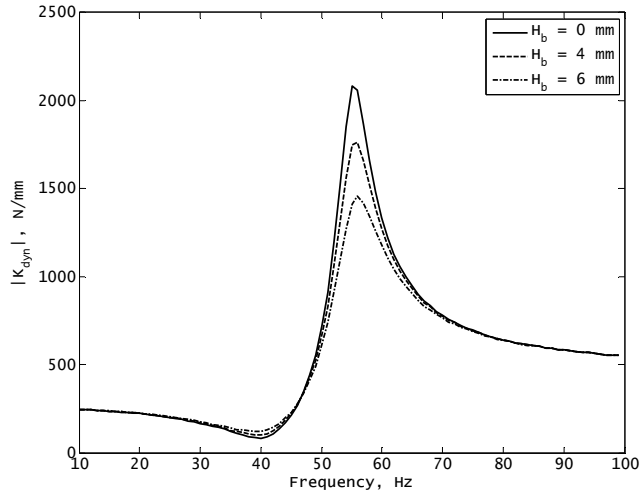

Fig. 20. Dynamic stiffness: influence of bypass path size, H_b

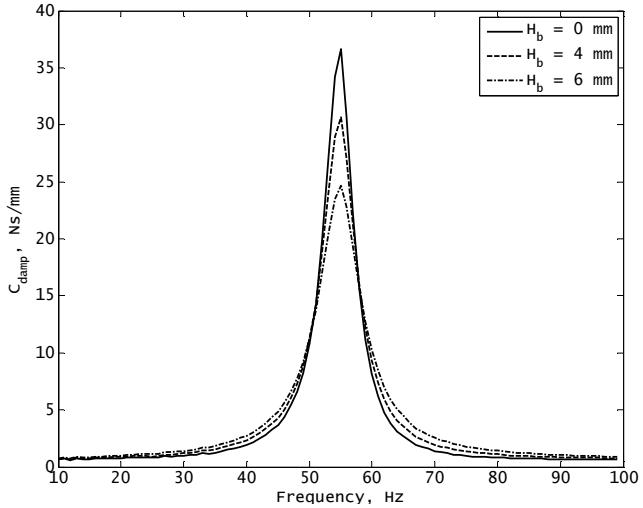

Fig. 21. Damping: influence of bypass path size, H_b

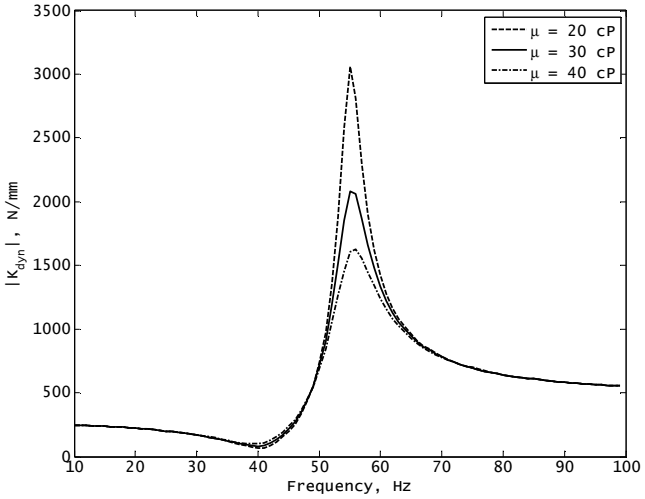

Fig. 22. Dynamic stiffness: influence of fluid base viscosity, μ

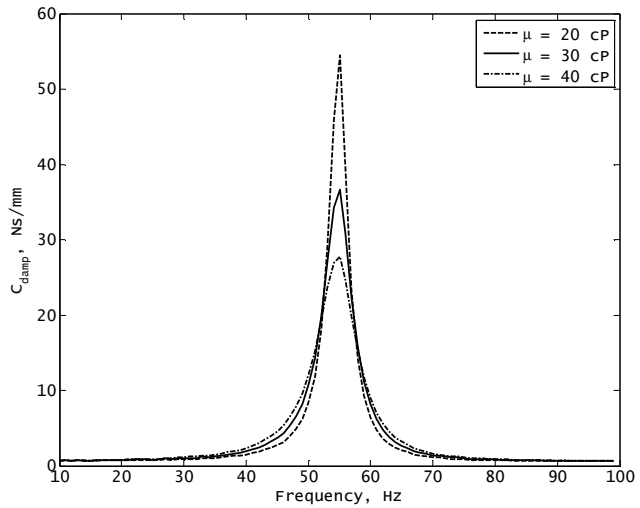

Fig. 23. Damping: influence of fluid base viscosity, μ

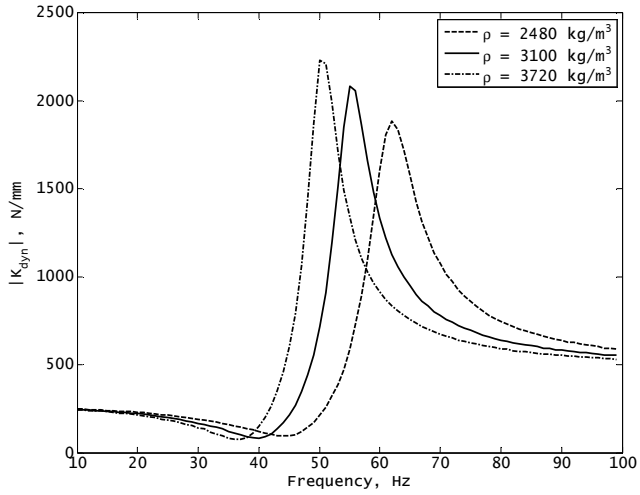

Fig. 24. Dynamic stiffness: influence of fluid density, ρ

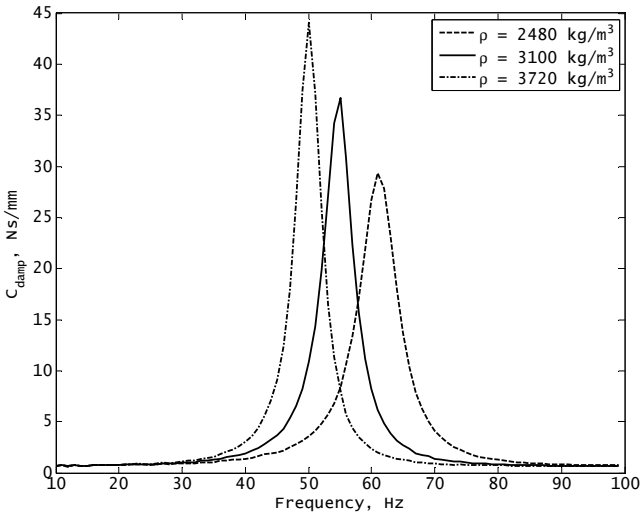

Fig. 25. Damping: influence of fluid density, ρ

4.3. Effect of magnetic field

The effect of magnetic field on the MR mount characteristics is illustrated in Figs. 26−33. Again, the data were obtained by running sweep-sine numerical tests on the mount model described by Eqs. 9 and 10. Each mode was first investigated on its own without the contribution of the other mode. For example, the flow mode tests were configured to minimize the contribution of the squeezing plate. As such, the initial gap between the core surface and the squeezing plate h_0 was set to 3 mm, and the stroking amplitude to 2 mm. Also, the squeeze mode coil was powered OFF. Then, the contribution from the viscous force in the squeeze mode gap is almost none, and squeezing of fluid does not interfere with flow mode. The results are shown In Figs. 26 and 27.

For comparison, the squeeze mode tests first involved cutting off the MR fluid flow in the annulus by setting the coil current level to a large value (above 200 ampere turns), and powering the squeeze mode coil circuit. As already mentioned, at this condition the MR mount model reduces to the configuration described in Section 3.2. Moreover, in order to observe the contribution of the squeeze mode on the flow mode performance the flow mode circuit was set to the OFF condition, and the squeeze mode coil current varied from 0 to 500 ampere turns. Also, the initial distance between the squeezing plate and the core surface was set down to 1 mm, and the stroking amplitude to 0.7 mm. The results are revealed in Figs. 28 and 29 (frozen annulus) as well as 30 and 31. At this condition, the pressure drop across the annulus is less than the field-induced yield stress, and the fluid flow is effectively eliminated so that there is no contribution of the fluid in the annulus to the damping, and the performance characteristics of the mount are solely controlled by the squeeze mode circuit and the mount rubber stiffness and damping, respectively.

The squeeze mode contribution modifies the stiffness (and the damping) rather uniformly across the frequency range. The squeeze mode effect is additive, and does not interact with the flow-mode directly. It is consistent with observations of other researchers (Minh, 2009). The effect

is related to the addition of a parallel spring (and a dashpot) of variable stiffness (and damping).

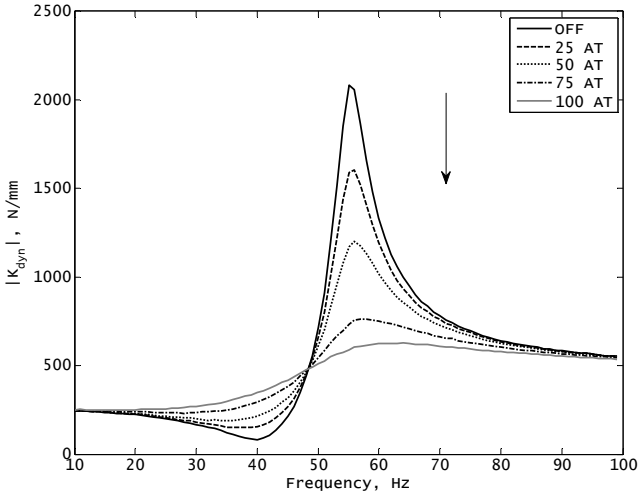

Fig. 26. Dynamic stiffness: magnetic field change; flow mode

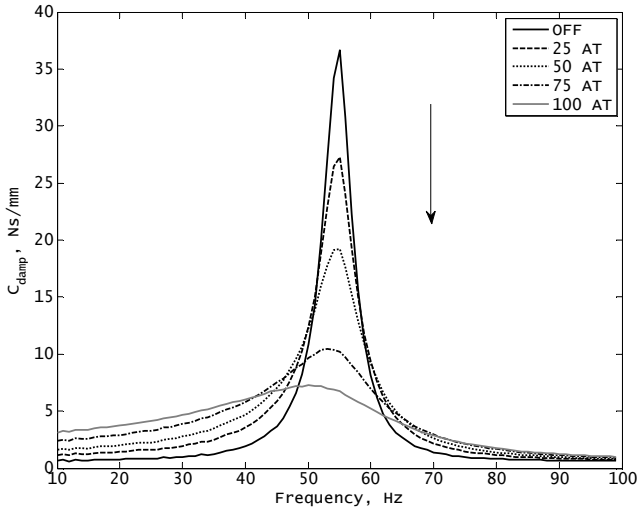

Fig. 27. Damping: magnetic field change; flow mode

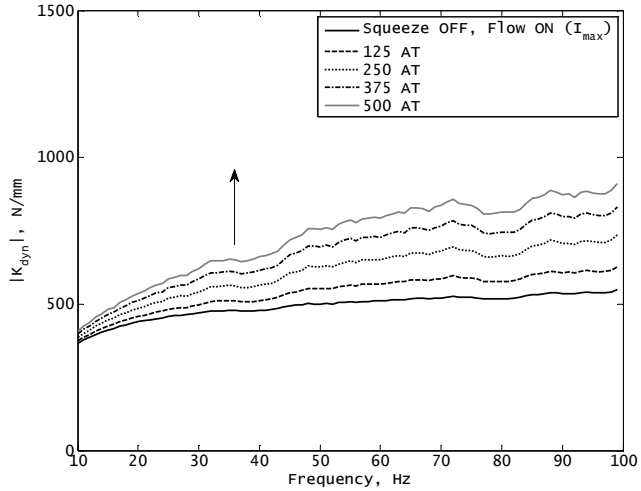

Fig. 28. Dynamic stiffness: magnetic field; squeeze mode

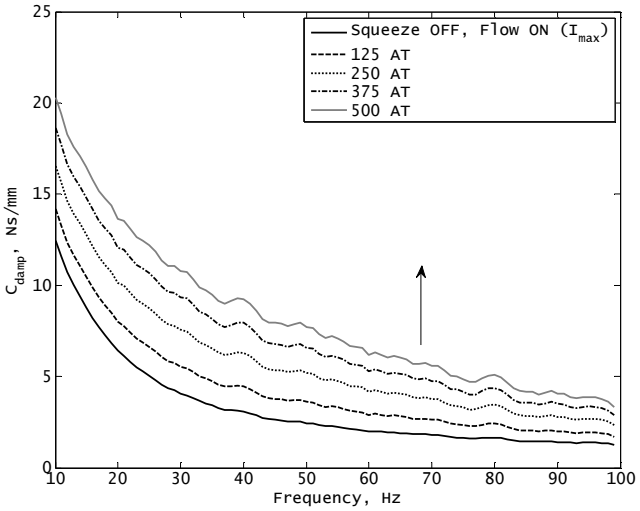

Fig. 29. Damping: influence of magnetic field; squeeze mode

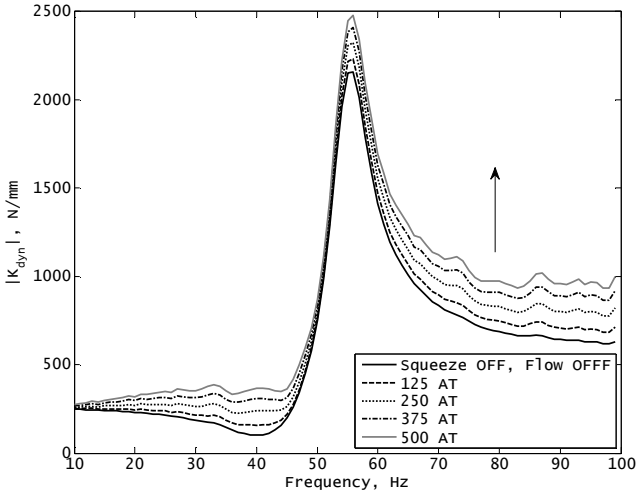

Fig. 30. Dynamic stiffness: magnetic field; squeeze mode

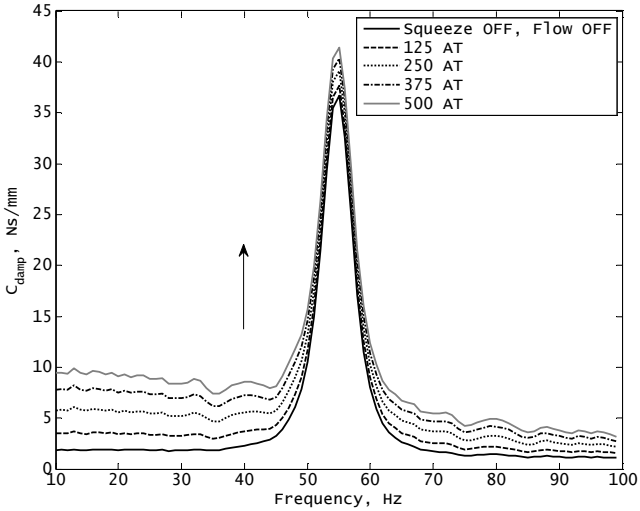

Fig. 31. Damping: squeeze mode (flow mode at OFF condition)

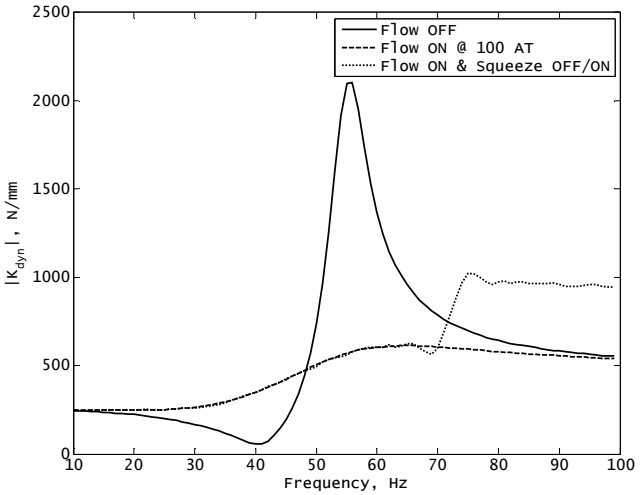

Fig. 32. Dynamic stiffness: simple control scheme

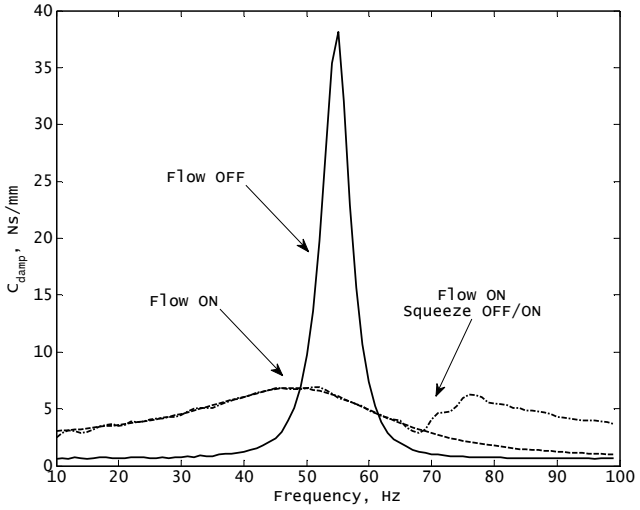

Fig. 33. Damping: simple control scheme

Finally, a simple control scheme was briefly analyzed In the present study. The tests involved exciting the mount with the sweep-sine displacement profile, powering the flow mode circuit, and switching the current on in the flow mode circuit above the resonance frequency. The effect is shown in Figs. 32 and 33. In a similar manner the effect can be controlled below the resonance frequency. The purpose of the test was to investigate the existing opportunities for controlling the MR mount performance characteristics.

5. SUMMARY

The purpose of the modeling study was to present a lumped parameter model of a mixed mode MR mount as well as to examine the opportunities for adapting the dynamic characteristics of the mount operating at one fundamental operation mode (flow or squeeze) or a combination of two modes (flow and squeeze). In addition to the MR effect that was introduced into the analysis by means of the Bingham plastic model the presented models capture the effects of rubber stiffness and damping, fluid chamber compliance and the fluid inertia. The effects of cavitation In fluid chambers were not examined in the study. When energized, both modes result in distinct performance characteristics. The effect of increasing the magnetic field In the annulus contribute to higher damping/stiffness (and amplitudes of the peak at the resonance), whereas the squeeze mode shows as a rather uniformly distributed superposition on the flow mode characteristics. With the squeeze mode the best effect can be achieved with small gaps between the core and the squeezing plate and small amplitude displacements. The squeeze mode effect is additive. Briefly, the results indicate the mixed mode potential for varying the stiffness and the damping of the mount AT any frequency region of interest. Shortly, the squeeze mode offers interesting engineering benefits; however, the device itself presents serious manufacturing challenges due to the low displacement amplitudes needed for achieving an optimum performance of the mount. Also, squeeze-mode fluid characterization study would need to be undertaken for further understanding of the material's rheology when operating in that mode and a suitable control scheme developed as well.

REFERENCES

1. BWI Group, http://www.bwigroup.com
2. FEMM, http://www.femm.info/wiki/HomePage
3. Lord Corp., http://www.lord.com
4. **Adiguna H., Tiwari M., Singh R., Tseng H., Hrovat D.** (2003), Transient response of a hydraulic engine mount, *J Sound and Vib*, Vol. 268, 217–248.
5. **Alexandridis A. A.** (2007), The MagneRide System, *In Proceedings of US Vehicle Dynamics Expo*, Novi, Michigan.
6. **Baudendistel T.A., Tewani S.G., Shores J.M., Long M.W., Longhouse R.E., Namuduri C.S., Alexandridis A.A.** (2003), Hydraulic mount with magnetorheological fluid, US Patent No. 6,622,995 B2.
7. **Baudendistel T.A., Tewani S.G., Long M.W, Dingle J. W.** (2002), Hybrid hydraulic mount with magnetorheological fluid chamber, US Patent No. 6,414,761 B1.
8. **Bolter, R., Janocha H.** (1998), Performance of long-stroke and low-stroke MR fluid dampers, *In Proceedings of the SPIE Conference of the International Society of Optical Engineers* (Ed. L. P. Davis), Washington, Vol. 3327, 303–313, Washington.
9. **Brigley M., Choi Y.–T., Wereley N., Choi S. B.** (2007), Magnetorheological isolators using multiple fluid modes, *J of Int Mater Sys and Struct*, Vol. 12, No 18, 1143–1148.
10. **Carlson D. J., Chrzan M, J.** (1994), Magnetorheological fluid dampers, US Patent No. 5277281.
11. **Farjoud A., Cavey R., Ahmadian M., Craft M.** (2009), Magneto-rheological fluid behavior in squeeze mode, *J Smart Mater and Struct*, Vol. 18, 095001.
12. **Farjoud A., Ahmadian M., Mahmoodi N., Zhang X., Craft M.** (2011), Non-linear modeling and testing of magneto-rheological fluids in low shear rate squeezing flows, *J Smart Mater and Struct*,, Vol. 20, 085013.
13. **Gavin H. P., Hanson R.D., Filisko F.E.** (1996a), Electrorheological dampers, Part 1: Analysis and design, *ASME J of Appl Mech*; Vol. 63, No 9, 669–75.
14. **Gavin H.P., Hanson R.D., Filisko F.E.,** (1996b), Electrorheological dampers, Part 2: Testing and modeling. *ASME J of Appl Mech*, Vol. 63, No 9, 676–82.

15. **Gopalswamy S., Linzell S. M., Jones G. L., Kruckemeyer W. C., Johnston G. L.** (1999), Magnetorheological fan clutch, US Patent No. 5,896,965.
16. **Gołdasz J., Sapiński B.** (2011), Model of a squeeze-mode magnetorheological mount, *Solid State Phenomena*, Vol. 177, 116–124.
17. **He S., Singh R.** (2007), Transient response of hydraulic engine mount to a realistic excitation: improved non-linear models and validation, *SAE Technical Paper*, 2007-01-2365.
18. **Hong S. R., Choi S. B., Jung W. J., Jeong W. B.** (2002), Vibration isolation using squeeze-mode ER mounts, *J of Int Mater Sys and Struct*, Vol. 7, No 13, 421–424.
19. **Hopkins P. N., Fehring J. D., Lisenker I., Longhouse R. E., Kruckemeyer W. C., Oliver M. L., Robinson F. M., Alexandridis A. A.** (2001), Magnetorheological fluid damper, US Patent N. 6,311,810 B1.
20. **Jolly M. R., Bender J. W., Carlson J. D.** (1998), Properties and applications of magnetorheological fluids, *In Proceedings of the SPIE Conference of the International Society of Optical Engineer*s (Ed. L. P. Davis), Washington, Vol. 3327, 262–275.
21. **Jolly M. R., Carlson J. D.** (1996), Controllable squeeze film damping using magnetorheological fluids, *In Proceedings of the 5th International Conference on New Actuators*, Bremen, 333–336.
22. **Kim G., Singh R.** (1993), Nonlinear analysis of automotive hydraulic engine mount, *Trans of the ASME*, Vol. 115, 482–487.
23. **Kim K.-J., Lee Ch.-W., Koo J.-H.** (2008), Design and modeling of semi-active squeeze film dampers using magnetorheological fluids, *J Smart Mater and Struct*, Vol. 17, doi: 10.1088/0964–1726/17/3/035006.
24. **Kowalczyk K., Svaricek F., Bohn C., Karkosch H.** (2004), An overview of recent automotive applications in active vibration control, *In Proceedings of the RTO AVT Symposium on Habitability of Combat and Transport Vehicles*, Prague, RTO-MP-AVT-110.
25. **Kruckemeyer W. C., Taeyoung H., Nehl T. W., Foister R. T.** (2001), Magnetorheological piston assembly and damper, US Patent Application No. 2006/0260891 A1.
26. **Lee K.** (1997), Numerical modelling for the hydraulic performance prediction of automotive monotube dampers, *J Veh Sys Dyn*, Vol. 28, 25–39.
27. **Minh N. T.** (2009), A novel semi-active magnetorheological mount for vibration isolation, Ph.D. Dissertation.
28. **Oliver M. L., Kruckemeyer W. C., Jensen E. L., Smith R. G.** (2003), Magnetorheological steering damper, US Patent No. 6,637,558 B2.
29. **Phillips R. W.** (1969), Engineering applications of fluids with a variable yield stress, Ph. D. Dissertation.
30. **Singh R., Kim G., Ravindra P.** (1992), Linear analysis of automotive hydromechanical mount with emphasis on decoupler characteristics, *J Sound and Vib*, Vol. 158, No. 2, 219–243.
31. **Sproston J. L., Rigby S. G., Wiliams E. W., Stanway R.** (1994), A numerical simulation of electrorheological fluids in oscillatory compressive squeeze-flow, *J. Phys D: Appl Phys*, Vol. 2, No 27, 338–340.
32. **Stanway R., Simms N.D., Johnson A.R.** (2000), Modelling and control of a magnetorheological vibration isolator, *In Proceedings of the SPIE Conference of the International Society of Optical Engineers*, Newport Beach, Vol. 3989, 184–193.
33. **Tang X., Wang X. J., Li W. H.** (1998), Testing and modeling of an MR damper in the squeeze flow mode, *In Proceedings of the 6th International Conference on ER Fluids, MR Suspensions and Their Applications* (Ed. M. Nakano and K. Koyama), Singapore, 870–878.
34. **Wiliams E., Rigby S. G., Sproston J., Stanway R.** (1993), Electorheological fluids applied to an automotive engine mount, *J Non-Newtonian Fluid Mech*, Vol. 47, 221−238.
35. **Zhang X., Zhang H., Ahmadian M., Guo K.** (2011), Study on squeeze-mode magnetorheological engine mount with robust H-infinite control, *SAE Technical Paper*, 2011-01-0757.

Acknowledegements: The study is completed under the AGH-UST's research program No 11.11.130.560 sponsored through statutory research funds.

MODELLING OF ADHESION EFFECT IN FRICTION OF VISCOELASTIC MATERIALS

Irina GORYACHEVA*, Yulia MAKHOVSKAYA*

*Institute for Problems in Mechanics, The Russian Academy of Sciences,
Vernadskogo prosp., 101/1, Moscow 119526, Russia

goryache@ipmnet.ru, makhovskaya@mail.ru

Abstract: A model is suggested for the analysis of the combined effect of viscoelastic properties of bodies and adhesive interaction between their surfaces in sliding. The model is based on the solution of the contact problem for a 3D wavy surface sliding on the boundary of a viscoelastic foundation taking into account the molecular attraction in the gap between the bodies. The influence of adhesion on the contact stress distribution, real contact area and hysteretic friction force is analyzed.

1. INTRODUCTION

According to the molecular-mechanical theory of friction (Kragelski, 1949), the friction force consists of two components. The deformation component arises due to deformation of materials by surface asperities. The adhesion component is due to molecular forces between surfaces.

The deformation component of the friction force of viscoelastic bodies can be determined by calculating the hysteretic losses as a result of cyclic deformation of surface layers by asperities of rough surfaces during their mutual sliding (Goryacheva, 1998).

Molecular forces appear in the gap between surfaces and act at a distance specified by the potential of molecular interaction (Deryagin et al., 1985). Molecular interaction between the surfaces leads not only to tangential traction giving the adhesion component of the friction force. At micro- and nano-scale levels of the surface roughness, at which the value of the gap is comparable with the radius of adhesive forces action, molecular forces acting in normal direction to contact surface can also influence the deformation component of the friction force. The influence of the adhesion attraction between surfaces on the hysteretic friction force was analyzed (Makhovskaya, 2005) for a separate asperity with a given shape of tip.

In what follows, the effect of adhesion on the friction In sliding of rough viscoelastic surfaces is modeled with taking into account the whole surface geometry - both tips of asperities and valleys between them for a 3D rough surface. Previously a similar approach was used for a 2D rough surface (Goryacheva and Makhovskaya, 2010).

2. DESCRIPTION OF THE MODEL

Consider a rigid wavy surface sliding with the velocity V along the x-axis on the viscoelastic foundation. The shape of the wavy surface is described by the periodic function:

$$f(x,y) = h - \frac{h}{4}\left(\cos\left(\frac{2\pi x}{l}\right)+1\right)\left(\cos\left(\frac{2\pi y}{l}\right)+1\right), \qquad (1)$$

where h and l are the height of asperities and distance between them, respectively, $h \ll l$ (Fig. 1).

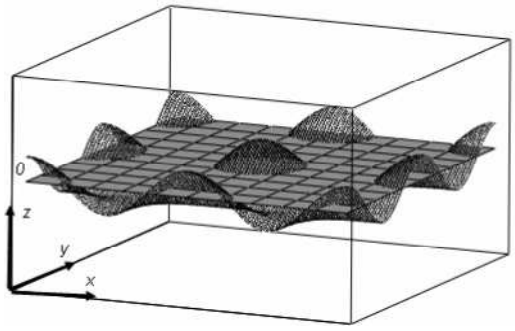

Fig. 1. Scheme of contact between a rigid wavy surface and a viscoelastic foundation

The mechanical properties of the viscoelastic foundation are described by the linear 1-D model:

$$w + T_\varepsilon \frac{\partial w}{\partial t} = \frac{(1-\nu^2)H}{E}\left(p + T_\sigma \frac{\partial p}{\partial t}\right) \qquad (2)$$

where p and w are the pressure and displacement on the boundary of the viscoelastic foundation, E is the Young modulus, ν is Poisson's ratio, H is the thickness of the viscoelastic layer, T_ε and T_σ are the retardation and relaxation times, respectively. Since $h \ll l$, we assume that $\partial w_z/\partial x \ll 1$ and then the quantities p and w are approximately equal to their projections on the z-axis, p_z and w_z, respectively.

Let the system of coordinates (x', y', z') be connected with the viscoelastic foundation, and the system of coordinates (x, y, z) with the sliding wavy surface so that:

$$x' = x + Vt, \quad y' = y, \quad z' = z \qquad (3)$$

In the moving system of coordinates *(x, y, z)* relation (2) has the form:

$$w - VT_{\varepsilon}\frac{\partial w}{\partial x} = \frac{(1-\nu^2)H}{E}\left(p - T_{\sigma}V\frac{\partial p}{\partial x}\right) \tag{4}$$

To take into account the adhesive (molecular) attraction between the surfaces, introduce the negative adhesive stress $p = -p_a(\delta)$ acting on the boundary of the viscoelastic foundation, where δ is the value of gap between the surfaces. We use the Maugis-Dugdale model in which the dependence of the adhesive stress on the gap between the surfaces has a form of one-step function (Maugis, 1991):

$$p_a(\delta) = \begin{cases} p_0, & 0 < \delta \le \delta_0 \\ 0, & \delta > \delta_0 \end{cases} \tag{5}$$

where δ_0 is the maximum value of gap for which the adhesive attraction acts. The surface energy γ is specified by the relation:

$$\gamma = \int_0^{+\infty} p_a(\delta)\, d\delta = p_0\delta_0 \tag{6}$$

Since the wavy surface is periodic with the period l, the contact problem can be considered in a square region $x \in (-l/2; l/2); y \in (-l/2; l/2)$. This square contains one asperity of the periodic wavy surface. The conditions of periodicity $p(x,y) = p(x+l,y)$ and $w(x,y) = w(x+l,y)$ must be satisfied. In the moving system of coordinates (*x, y, z*), the following boundary conditions for the stresses and displacements take place at the foundation surface ($z = 0$) in the square region region $x \in (-l/2; l/2); y \in (-l/2; l/2)$:

$$\begin{aligned} &w(x,y) = f(x,y) + D, && (x,y) \in \Omega^c; \\ &p(x,y) = -p_0, && (x,y) \in \Omega^a; \\ &p(x,y) = 0, && (x,y) \notin \Omega^c \cup \Omega^a; \end{aligned} \tag{7}$$

Here Ω^c is the contact region, Ω^a is the region in which adhesive stress $-p_0$ acts, and *D* is the penetration of the asperity into the foundation. The equilibrium condition is also satisfied:

$$P = \iint_{\Omega^c \cup \Omega^a} p(x,y)\, dxdy \tag{8}$$

where *P* is the normal load applied to each asperity of the wavy surface.

3. METHOD OF SOLUTION

The contact problem is solved by using the strip method (Kalker, 1990) which is an exact method for the case of 1D foundation. The square region $x \in (-l/2; l/2);\ y \in (-l/2; l/2)$ is divided into $2N$ strips of equal thickness Δ (Fig. 2). The normal displacement of the center of a strip *j* is:

$$D_j = \frac{h}{2}\left(\cos\left(\frac{2\pi\Delta j}{l}\right) - 1\right) + D \tag{9}$$

If the maximum normal penetration D of the wavy surface is prescribed, then for each strip, the maximum normal penetration is given by (9). The shape of rigid wavy surface in this strip is specified by:

$$f_j(x) = \frac{h_j}{2}\left(\cos\left(\frac{2\pi x}{l}\right) - 1\right), \quad h_j = \frac{h}{2}\left(\cos\left(\frac{2\pi\Delta j}{l}\right) + 1\right) \tag{10}$$

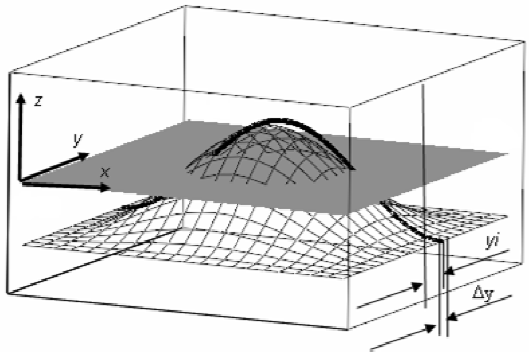

Fig. 2. The square $x \in (-l/2; l/2); y \in (-l/2; l/2)$ and its division into strips

In each strip, the contact problem is formulated and solved independently. For a *j*-th strip, the conditions for the displacement $w_j(x)$ and pressure $p_j(x)$ follow from (7) and they have the form:

$$\begin{aligned} &w_j(x) = f_j(x) + D_j, && x \in \Omega^c{}_j \\ &p_j(x) = -p_0, && x \in \Omega^a{}_j \\ &p_j(x) = 0, && x \notin \Omega^c{}_j \cup \Omega^a{}_j; \end{aligned} \tag{11}$$

When the contact problem is solved and the contact pressure $p_j(x)$ is calculated for each strip, the normal load acting on an asperity is calculated by the summation, which follows from (8):

$$P = 2\sum_{j=1}^{N} P_j, \quad P_j = \Delta \int_{-l/2}^{l/2} p_j(x)dx \tag{12}$$

If the maximum displacement *D* is unknown, while the load P is prescribed, then some initial values of *D* is set and the iteration procedure is applied to attain the prescribed value of the load *P*.

To determine the tangential stress applied to the rigid wavy surface from the viscoelastic foundation, we use the relation:

$$\tau_j(x) = p_j(x)\sin\left[\operatorname{arctg}\left(f_j'(x)\right)\right] \approx p_j(x)\, f_j'(x) \tag{13}$$

Then the tangential (friction) force acting on the asperity is calculated as:

$$T = 2\sum_{j=1}^{N} T_j, \quad T_j = \Delta \int_{l/2}^{l/2} \tau_j(x)dx \tag{14}$$

This force is different from zero because the pressure distribution is nonsymmetrical with respect to the axis of symmetry of the asperity due to hysteretic losses in the viscoelastic material. This force is called the hysteretic

or deformation component of the friction force. The corresponding friction coefficient is determined from the relation:

$$\mu = T / P \tag{15}$$

Thus, the problem is reduced to solving a 2-D contact problem for each strip to determine the contact pressure distribution $p_j(x)$ in the contact region $x \in \Omega_j$ and the boundary of the region of adhesive interaction Ω^a, after which the friction force can be calculated in accordance with Eqs. (12)-(15).

In order to write the boundary conditions for the contact pressures and displacements in a strip, we should take into account various regimes of the gap filling.

4. PROBLEM SOLUTION IN A STRIP FOR DIFFERENT REGIMES OF GAP FILLING

Three possible regimes of the gap filling are considered: saturated contact (Fig. 3a), discrete contact with saturated adhesive interaction (Fig. 3b), discrete contact with zones of adhesive interaction and zones of free boundary (Fig. 3c). In each *j*-th strip, one of these regimes is realized, depending on the displacement of the center D_j of this strip and values of the problem parameters (mechanical and geometric characteristics of the interacting bodies, load, and sliding velocity).

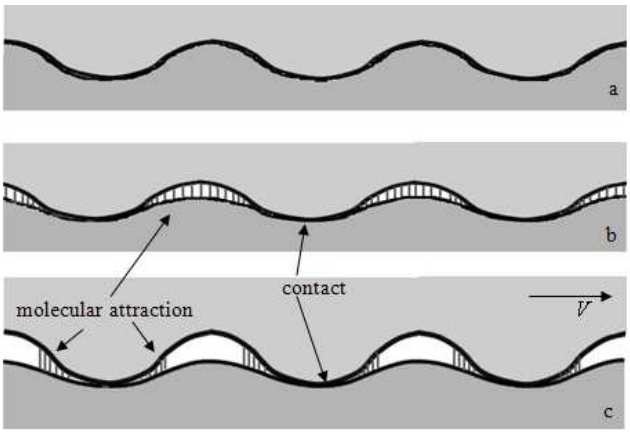

Fig. 3. Regimes og gap filling between the surfaces in the presence of adhesion

4.1. Saturated contact

In this case (Fig. 3,a), the displacement of the boundary $z = 0$ of the viscoelastic foundation $w_j(x)$ satisfies the first condition of (11) on the entire surface, i.e. over the whole length of the period $x \in (-l/2; l/2)$. By solving the differential equation (4) with the first condition of (11) and using the periodicity condition for the pressure $p_j(x - l/2) = p_j(x + l/2)$, we obtain the contact pressure in the form:

$$p_j(x) = \frac{E}{2H(l^2 + 4\pi^2 T_\sigma^2 V^2)}\left[h_j(l^2 + 4\pi^2 T_\varepsilon T_\sigma V^2)\cos\frac{2\pi x}{l} + \right.$$
$$\left. + 2\pi l h_j V(T_\varepsilon - T_\sigma)\sin\frac{2\pi x}{l} + (4\pi^2 T_\sigma^2 V^2 + l^2)\left(2D_j - h_j\right)\right] \tag{16}$$

where D_j and H_j are specified by relations (9) and (10). Normal force P_j acting on the j-th strip is determined by the relation:

$$P_j = \Delta \int_{-l/2}^{l/2} p(x)dx = \Delta \frac{El}{2Hl}(2D_j - h_j) \tag{17}$$

The saturated contact in the *j*-th strip is realized under the condition:

$$\min\left(p_j(x)\right) \geq -p_0 \tag{18}$$

Note that due to adhesion, the contact pressure can be negative but not smaller than the adhesive stress $-p_0$. If the minimum contact pressure in a *j*-th strip does not satisfy condition (18), then the saturated contact is not realized. In this case, the solution is sought for the discrete contact with saturated adhesive interaction.

4.2. Discrete contact with saturated adhesive interaction

In this case (Fig. 3,b), the problem solution is considered in the interval $x \in [-a_j, l - a_j]$. Two different boundary conditions take place for two zones of interaction. The differential equation (4) is solved in the zone of contact $-a_j < x < b_j$ for the contact pressure $p_j(x)$, the displacement $w_j(x)$ being specified by the first condition of (11). In the zone of adhesive interaction $b_j < x < l - a_j$, the differential equation (4) is solved for $w_j(x)$, the pressure $p_j(x)$ being prescribed by the second condition of (11). Thus two boundary conditions are necessary for the solution of these two differential equations. Also, two conditions are needed for the determination of the end points a_j and b_j of the contact region. As such conditions, the conditions of continuity of the functions $p_j(x)$ and $w_j(x)$ at the points $x = -a_j$ and $x = b_j$ and the periodicity condition are used. These conditions lead to two nonlinear equations for the numerical determination of the quantities a_j and b_j in the case where the penetration of interacting bodies D_j in the *j*-th strip is prescribed. The pressure $p_j(x)$ in the contact region $-a_j < x < b_j$ is calculated in accordance with the relation:

$$p_j(x) = -p_0 e^{(x-a_j)/\beta V} + \frac{Eh_j}{2H(l^2 + 4\pi^2\beta^2 V^2)}\left[(l^2 + 4\pi^2\alpha\beta V^2)\left(\cos\frac{2\pi x}{l} - \right.\right.$$
$$\left. - e^{(x-a_j)/\beta V}\cos\frac{2\pi a}{l}\right) - 2\pi l V(\alpha - \beta)\left(\sin\frac{2\pi x}{l} - e^{(x-a_j)/\beta V}\sin\frac{2\pi a}{l}\right) \tag{19}$$
$$\left. + 2D_j l^2 h\left(1 - e^{(x-a_j)/\beta V}\right)\right] + \frac{E}{2H}(2D_j - h_j)\left(1 - e^{(x-a_j)/\beta V}\right)$$

A similar relation is obtained for the determination of the unknown function of displacement $w_j(x)$ in the re-

gion of adhesive interaction $b_j < x < l - a_j$.

The normal and tangential forces acting in a strip in one period of the wavy surface are calculated as:

$$P_j = \Delta \int_{-a_j}^{l-a_j} p_j(x)dx, \quad T_j = \Delta \int_{-a_j}^{l-a_j} \tau_j(x)dx \tag{20}$$

Discrete contact with saturated adhesive interaction exists under the condition that in the solution obtained, the condition $b_j < l - a_j$ is satisfied. If in the solution obtained we have $b_j \geq l - a_j$, then the case of saturated contact is realized. The other condition of the existence of the discrete contact with saturated adhesive interaction follows from the adopted model of adhesion (5) and (6) – the maximum value of the gap between the surfaces $w_j(x) - f_j(x) - D_j$ should not exceed the prescribed value δ_0, i.e., we have:

$$\max\left(w_j(x) - f_j(x) - D_j\right) \leq \gamma / p_0 \tag{21}$$

If the function $w_j(x)$ in the interval $b_j < x < l - a_j$ does not satisfy condition (21), then in the *j*-th strip the discrete contact with saturated adhesion interaction is not realized. In this case, we should seek the solution for the discrete contact with zones of adhesive interaction and zones of free surface.

4.3. Discrete contact with zones of adhesive interaction

In this case (Fig 3,c), we have three different boundary conditions in three zones of interaction. The differential equation (4) is solved in the contact zone $-a_j < x < b_j$ for the contact pressure $p_j(x)$ and on the remaining intervals for the displacement $w_j(x)$. As additional conditions, the conditions of continuity for the pressure $p_j(x)$ and displacement $w_j(x)$ at the points $x = -a_{1j}$, $x = -a_j$ and $x = b_j$, $x = b_{1j}$ and the conditions of periodicity are used. Also, for the determination of the end points of the zones of adhesive interaction, a_{1j} and b_{1j}, we use the conditions following from (5) and (6), in accordance to which the value of gap between the surfaces at the points $x = -a_{1j}$ and $x = b_{1j}$ must be equal to δ_0. These conditions have the form:

$$\begin{aligned} &w(-a_1) - f(-a_1) - D = \gamma / p_0, \\ &w(b_1) - f(b_1) - D = \gamma / p_0 \end{aligned} \tag{22}$$

As a result, we obtain four nonlinear algebraic equations for numerical determination of the quantities a_j, b_j, a_{1j}, and b_{1j}, provided that the penetration of the bodies in the *j*-th strip D_j is prescribed. The pressure $p_j(x)$ in the contact zone $-a_j < x < b_j$ is specified by relation (19).

Note that the regimes of discrete contact with saturated adhesion and discrete contact with zones of adhesive interaction include also the cases, where there is no contact between the surfaces, and only adhesive interaction occurs over the entire surface or in separate zones of adhesive interaction. The solution for these cases can be easily obtained from Eq. (4) with the second condition of (11) imposed on the entire surface or in a periodical set of zones.

5. RESULTS OF CALCULATIONS

5.1. Solution for a 2-D wavy surface

Below the results of calculations are presented which illustrate the influence of viscoelastic properties, geometrical and adhesive parameters on the contact characteristics and sliding friction force for the case of two-dimensional contact problem. The shape of the wavy surface is described by the function $f(x) = h\,sin^2(\pi x/l)$.

In Fig. 4, the distribution of the normal stress $p(x)$ (curves 1) and tangential stress $\tau(x)$ (curves 2) is shown. Fig. 4,a corresponds to no adhesion and Fig. 4b to the case of adhesion.

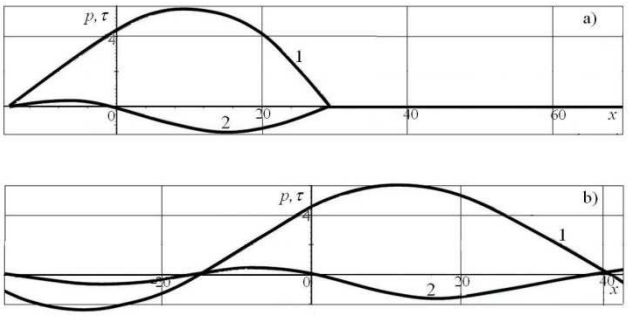

Fig. 4. Distribution of normal and tangential stresses in a period for the case of no adhesion (a) and with adhesion (b)

In Fig. 4, the stresses p and τ are measured in MPa, the *x*-coordinate in meters. These results are obtained for the material parameters $E/H = 2 \times 10^6$ Pa/m, $T_\sigma = 0{,}003$ s, $T_\varepsilon/T_\sigma = 1000$ load per unit length $P = 154$ N/m, sliding velocity $V = 0{,}1$ m/s, waviness parameters $l = 0{,}086$ mm, $h = 0{,}008$ mm, and adhesion parameters $\gamma = 0{,}05$ N/m, $p_0 = 5{,}5 \times 10^6$ Pa. The friction coefficient calculated for the case without adhesion (a) is $\mu = 0{,}139$, and for the case with adhesion (b) it is $\mu = 0{,}273$. The results indicate that taking into account adhesion not only leads to increase in the friction coefficient, but it also can change the regime of contact and lead from discrete contact (a) to saturated contact (b).

In Fig. 5, the contact width a + b (a) and the friction force T (b) versus load P are presented for the cases without adhesion (curves 1) and with adhesion (curves 2). The contact width is measured in meters, the forces per unit length T and P in N/m. The results are obtained for the material parameters $E/H = 2 \times 10^6$ Pa/m, $T_\sigma = 0{,}003$ s, $T_\varepsilon/T_\sigma = 1000$, sliding velocity $V = 0{,}1$ m/s, waviness parameters $l = 0{,}1$ mm, $h = 0{,}01$ mm, and adhesion parameters $\gamma = 0{,}01$ N/m, $p_0 = 5 \times 10^3$ Pa. As the load increases the contact width and friction force increase until they attain saturation which means that transition from discrete to saturated contact occurs. The behavior of the contact characteristics (contact width, shift of the contact region with respect to the symmetry axis, contact pressure distribution) differ significantly in the regimes of discrete and saturated contact.

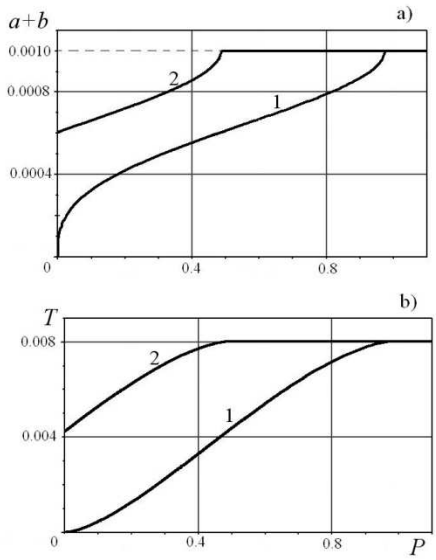

Fig. 5. The contact width (a) and friction force (b) vs normal load for the case with no adhesion (curves 1) and with adhesion (curves 2)

Comparison of curves 1 and 2 shows that taking into account adhesive interaction leads to a considerable increase in the real contact area and hysteretic component of the friction force in the case of discrete contact of the surfaces. Also, taking into account adhesion leads to appearance of negative pressure in the contact region. In the case of saturated contact, adhesion does not influence the contact area and friction force, but it may influence the contact pressure distribution. Results indicate also that with taking into account adhesion, transition from discrete to saturated contact occurs for lower load than without adhesion.

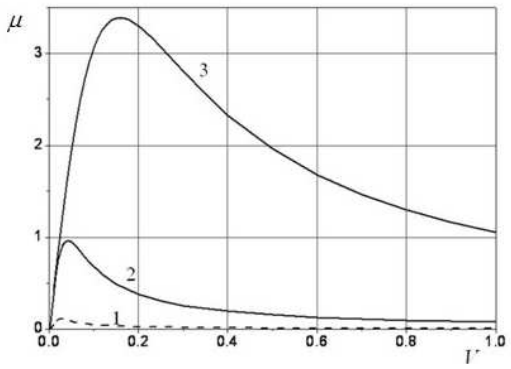

Fig. 6. The friction coefficient vs sliding velocity for different values of the adhesive stress

Figure 6 shows the friction coefficient vs sliding velocity [m/s] for various values of the adhesive stress. Dashed line corresponds to no adhesion (curve 1), curves 2 and 3 correspond to the cases with adhesion. The results are calculated for the mechanical parameters $E/H = 10^9$ Pa/m, $T_\sigma = 0{,}001$ s, $T_\varepsilon/T_\sigma = 10$, roughness parameters $l = 0{,}001$ mm, $h = 0{,}0001$ mm and adhesion parameters $\gamma = 0{,}01$ N/m, $\mathrm{p}_0 = 5 \times 10^4$ Pa (curve 2) and $\mathrm{p}_0 = 5 \times 10^5$ Pa (curve 3). In the presence of adhesion, the friction coefficient nonmonotonically depends on the velocity and tends to zero for large and small velocities, as it is the case without adhesion. Taking into account adhesion leads to the increase in the value of the friction coefficient, this increase is larger for higher p_0, provided that the surface energy γ is constant.

5.2. Solution for a 3-D wavy surface

Below the result of calculations for a 3D wavy surface (Fig. 1) are presented, the shape of which is described by the function (1).

In Fig. 7, the distributions of contact pressure $p(x,y)$ in the domain $x \in (-l/2; l/2)$; $y \in (0; l/2)$ are presented without adhesion (a) and in the presence of adhesion (b) for the same value of the load per one asperity (for one period) $P = 6{,}3561$ H. The results are obtained for $l = 0{,}005$ mm, $h = 0{,}0005$ mm, $E/H = 2 \times 10^9$ Pa/m, $T_\sigma = 0{,}0001$ s, $T_\varepsilon/T_\sigma = 10$, $V = 1$ m/s. Similarly to the 2D case, taking into account the adhesive interaction leads to an increase in the contact areas and, in some conditions, to their merging and passing to the regime of saturated contact (Fig. 2b).

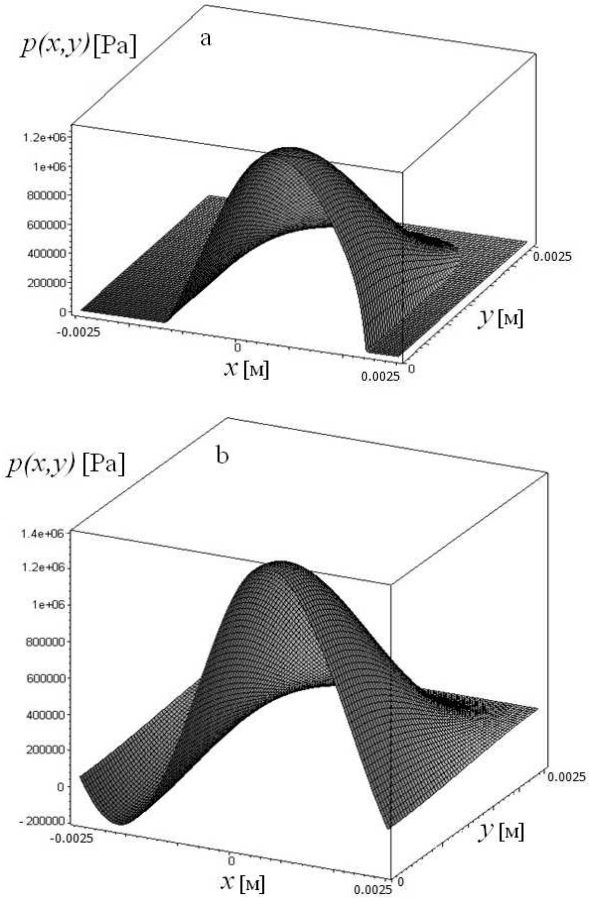

Fig. 7. Contact pressure distributions in a period of waviness without adhesion (a) and with adhesion (b)

The plots of the friction force vs load acting on one asperity are presented in Fig. 8 for the case without adhesion (dashed lines) and with adhesion (solid lines). The mechanical parameters of the material correspond to a kind of rubber. The sliding velocity is $V = 0{,}1$ m/s (Fig. 8a)

and $V = 1\ \mathrm{m/s}$ (Fig. 8b). The adhesion parameters are $\gamma = 0{,}01\ \mathrm{N/m}$ and $\mathrm{p}_0 = 5{,}5 \times 10^5$ Pa. The waviness parameters are $l = 0{,}010753$ mm and $h = 0{,}000971$ mm. The results show that increase in the friction force due to adhesion is smaller for higher velocity (i.e. for a material with higher effective compliance). The influence of adhesion on the friction force is significant for relatively small loads when the contact is not saturated. Due to adhesion, the friction force T is nonzero for zero load $P = 0$ and in some range of negative loads. Because of this fact, the friction coefficient $\mu = T/P$ becomes very high for very small loads. This allows us to make the conclusion, that for real rough surfaces, the effect of adhesion is especially significant for the asperities which are under small or negative load, and these asperities can contribute significantly into the total friction force.

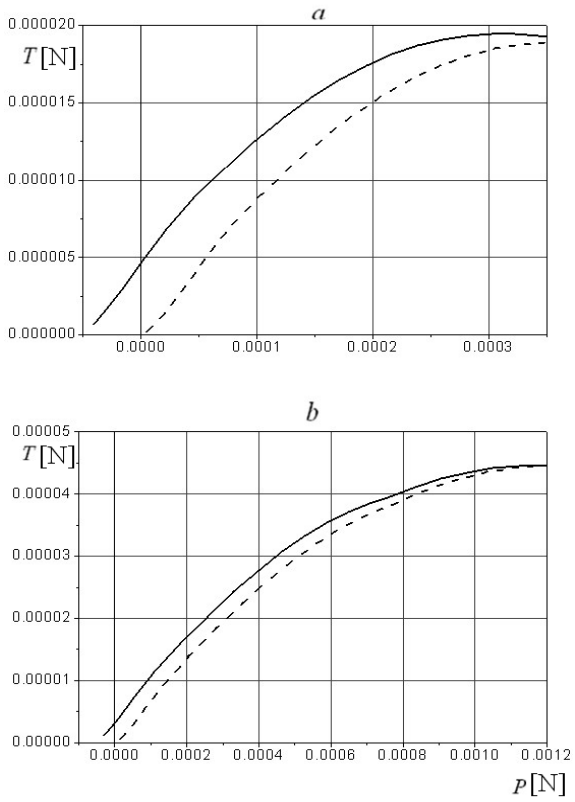

Fig. 8. The friction force vs normal load acting on one asperity with taking into account adhesion (solid lines) and without adhesion (dashed lines)

6. CONCLUSION

A model is suggested to study the adhesion effect on the hysteretic friction force in sliding of rough viscoelastic bodies. The model is based on the solution of a contact problem for a 3-D wavy rigid body sliding on the surface of the viscoelastic foundation taking into account the molecular attraction in the gap between the surfaces.

The results of calutions allow us to draw the following conclusion:

- taking into account the adhesive interaction leads to a significant increase in the real contact area and hysteretic friction forc;
- the transition from discrete to saturated contact in the presence of adhesion occurs at lower loads than without adhesion;
- due to adhesion, the contact between surfaces exists even for negative (tensile) loads;
- the effect of adhesion is especially significant for asperities which are under small or negative load;
- as the adhesion stress increases, the friction force increases, provided that the contact saturation is not attained.

The results obtained can be used for the analysis of the stress-strain state of surface layers and evaluation of the friction force at various scale levels of roughness in sliding of viscoelastic bodies. The mechanisms of fricrtion that were studied play a particular role for micro- and nano-scale levels for whith the size of the gap is close In order of magnitude to the radius of adhesive forces action.

REFERENCES

1. **Deryagin B. V., Churaev N. V., Muller V. M.** (1985), *Poverkhnostnye Sily*, Moscow, Nauka.
2. **Goryacheva I. G., Makhovskaya Yu. Yu.** (2010), Modeling of friction at different scale levels, *Mech. Solids.*, Vol. 45, No. 3, 390-398.
3. **Goryacheva, I. G.** (1998), *Contact Mechanics in Tribology* Kluwer Academic Publ., Dordercht.
4. **Kalker J.J.** (1990) *Three-Dimensional Elastic Bodies in Rolling Contact.* Series: Solid Mechanics and Its Applications, Kluwer Academic Publishers.
5. **Kragelski I.V.** (1949), Molekularno-mekhanicheskaya teoriya treniya, *Treniye i Iznos w Mashinakh*, T.III, Izd-vo AN SSSR, 178-183.
6. **Makhovskaya, Yu. Yu.** (2005), The sliding of viscoelastic bodies when there is adhesion**,** *J. Appl. Math and Mech*, Vol. 69, No. 2, 2005, 334-344.
7. **Maugis. D.** (1991), Adhesion of spheres: the JKR-DMT transition using a Dugdale model. *J. Colloid Interface Sci.*, Vol 150, 243-269.

The work was carried out under the financial support of Russian Foundation for Basic Research (grants No. 11-01-00650 and 11-01-90419)

INFLUENCE OF THERMOSENSITIVITY OF MATERIALS ON THE TEMPERATURE OF A PAD/DISC SYSTEM

Piotr GRZEŚ*

*PhD Student, Faculty of Mechanical Engineering, Bialystok University of Technology,
Wiejska 45 C, 15 351 Bialystok

p.grzes@doktoranci.pb.edu.pl

Abstract: A heat generation problem due to friction in a pad/disc brake system is studied. A linear problem is confronted and compared with a non-linear in which thermophysical properties of materials are temperature-dependent. To examine temperature of the pad and the disc during a single and a twofold braking process, axisymmetric FE contact model was used. The obtained results revel insignificant temperature differences at specified axial and radial positions of the components of the friction pair. It was remarked that the level of discrepancies between the constant and the thermosensitive materials correspond with the coefficient of thermal effusivity.

1. INTRODUCTION

Inherent heat generation during slipping of contacting bodies leads to an increase in temperature on the friction surfaces. Over the decades analytical and numerical models have been developed to improve the accuracy and repeatability of the obtained by their means solutions in application to various types of brake systems (Scieszka, 1998). Despite the fact that the analytical methods provide exact solutions on which numerical calculations are based, advantage of the latter is noticeable in application to complex objects with finite dimensions and non-linear problems (Yi et al., 2002; Scieszka and Zolnierz, 2007; Aderghal et al., 2011).

Parameters of braking operation such as a contact pressure, a sliding velocity, a coefficient of friction, cooling conditions are frequently brought to constant values aiming to distinguish markedly an impact of chosen factors. Adamowicz and Grzes (2011a) developed and compared axisymmetric two-dimensional and fully three-dimensional models of a disc rotor during a single emergency braking process. Braking operation with the constant as well as linearly decreasing velocity of a vehicle was studied to evaluate its influence on the temperature distributions of a disc. On the basis of that FE modelling technique the effects of cooling conditions during a period of braking with constantly rotating disc from adiabatic conditions to the firmly forced convection (100 W/(m^{2}K)) were studied in ref. (Adamowicz and Grzes, 2011b).

If the system operates markedly above a certain temperature, the friction materials can vary their thermophysical properties affecting the conditions of contact and in consequence a non-linear problem is apparent. Nonetheless only few numerical calculations deal with the temperature-dependent thermophysical properties of materials in application to brake systems (Lee and Barber, 1994; Thuresson, 2004; Sergienko 2009).

This study aims to examine an effect of thermosensitive materials on the thermal behaviour of a pad/disc tribosystem. The corresponding temperatures are confronted with the values of the model which operate within theirs constant equivalents. FE 2D contact model was used based on the author's previous study (Grzes, 2010). The properties of materials were adopted and approximated by using methodology with the three constants (Chichinadze et al., 1979).

2. STATEMENT OF THE PROBLEM

The frictional heat generation in a disc brake in actual is accompanied by its dissipation through the three known modes of heat transfer. The conduction absorbs energy from the pad/disc interface by the neighbouring parts of the brake assembly and hub. The convection exchanges heat from the exposed surfaces with the surrounding environment according to Newton's law of cooling. Typically disc brakes have vanes whose presence allows to enlarge the area of convective heat transfer, however evident advantages of such type of a rotor emerges during a long-lasting processes after disconnection of the sliding bodies or during a multiple brake application (Adamowicz and Grzes, 2011b). The remaining phenomenon that intensifies cooling of the brake is the thermal radiation. However its share in total heat dissipation is frequently ignored due to attained maximal temperatures and the duration of the analyzed process. Thereby in this study solely conduction and convection are taken into account.

The mechanisms of the pad operation through the caliper during brake application vary. However it is stated that the amount of heat generated during friction for certain dimensions of a rubbing path and assumed constant uniform contact pressure remains equal. The converted mechanical energy is assumed to be entirely used for the heat, whose magnitude expresses the capacity of friction power and in application to the rotating system has the following form:

$$q(t) = fr\omega(t)p_0 \tag{1}$$

where: f – friction coefficient, $\omega(t)$ – angular velocity, t – time, r – radial coordinate, p_0 – contact pressure.

The separation of heat between contacting bodies may be proceeded in two ways. One of frequently used approaches is a calculation of temperature fields by means of two individual bodies/models (a stator and a rotor) introducing a heat partition ratio (Grzes, 2009; 2011) and other is a use of contact model which is employed in this study (Bialecki and Wawrzonek, 2008). It is established that the separation of heat between the pad and the disc varies during the process satisfying two conditions of the perfect thermal contact on the corresponding friction surfaces:

$$T(r_i,0^+,t) = T(r_j,0^-,t),\ r_p \le r \le R_p,\ 0 \le t \le t_s, \tag{2}$$

$$K_d(T)\left.\frac{\partial T}{\partial z}\right|_{z=0^-} - K_p(T)\left.\frac{\partial T}{\partial z}\right|_{z=0^+} = q(r,t) \equiv fr\omega(t)p_0, \quad r_p \le r \le R_p,\ 0 \le t \le t_s, \tag{3}$$

where: +(–) denotes value obtained at the approach toward plane $z = 0$ from the +(–) side of the axis OZ, T – temperature, i, j – the pad and the disc corresponding radial locations on the contact surface, d, p – the disc and the pad, respectively, r, R – internal and external radius, respectively.

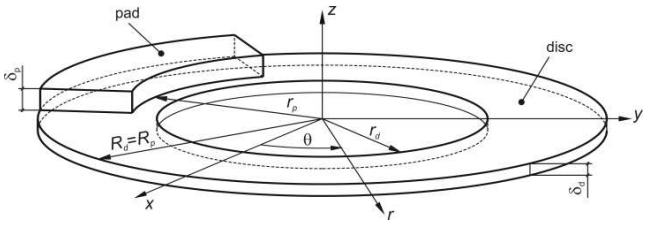

Fig. 1. Schematic diagram of half of a pad/disc brake system

Angular velocity of the rotor decreases linearly from the initial value ω_0 to full stop according to formula:

$$\omega(t) = \omega_0\left(1 - \frac{t}{t_s}\right),\ 0 \le t \le t_s, \tag{4}$$

where: t_s – braking time.

3. MATHEMATICAL FORMULATION

The governing equation for the heat conduction analysis was the parabolic heat conduction equation given in the cylindrical coordinate system (r, z):

$$\frac{\partial}{\partial r}\left(K_{d,p}(T)\frac{\partial T}{\partial r}\right) + \frac{K_{d,p}(T)}{r}\frac{\partial T}{\partial r} + \frac{\partial}{\partial z}\left(K_{d,p}(T)\frac{\partial T}{\partial z}\right) = \rho_{d,p}\, c_{d,p}(T)\frac{\partial T}{\partial t} \tag{5}$$

where: z – axial coordinate, $K(T)$ – thermal conductivity, ρ – density, $c(T)$ – specific heat.

In order to determine the transient temperature distributions in the brake components during frictional sliding process both analytical and numerical techniques were employed. Lack of the circumferential component in the above governing equation stems from the assumption that neither non-axisymmetric thermal load acting as the intensity of heat flux directed into the disc and the pad nor the resulting heat flow in the circumference, doesn't affect significantly an average temperature generated at the pad/disc interface above certain relative sliding velocity (Peclet number Pe).

The boundary and initial conditions (Fig. 2) are the following:

– on the free surfaces of the pad:

$$K_p(T)\left.\frac{\partial T}{\partial r}\right|_{r=r_p} = h[T(r_p,z,t) - T_a],\ 0 \le z \le \delta_p,\ 0 \le t \le t_s, \tag{6}$$

$$K_p(T)\left.\frac{\partial T}{\partial r}\right|_{r=R_p} = h[T_a - T(R_p,z,t)],\ 0 \le z \le \delta_p,\ 0 \le t \le t_s, \tag{7}$$

$$\left.\frac{\partial T}{\partial z}\right|_{z=\delta_p} = 0,\ r_p \le r \le R_p,\ 0 \le t \le t_s, \tag{8}$$

where: h – heat transfer coefficient, T_a – ambient temperature, T_0 – initial temperature, δ – thickness.

– and the free surfaces of the disc:

$$K_d(T)\left.\frac{\partial T}{\partial z}\right|_{z=0} = h[T_a - T(r,0,t)],\ r_d \le r \le r_p, 0 \le t \le t_s, \tag{9}$$

$$\left.\frac{\partial T}{\partial r}\right|_{r=r_d} = 0,\ -\delta_d \le z \le 0,\ 0 \le t \le t_s \tag{10}$$

$$K_d(T)\left.\frac{\partial T}{\partial r}\right|_{r=R_d} = h[T_a - T(R_d,z,t)],\ -\delta_d \le z \le 0,\ 0 \le t \le t_s \tag{11}$$

$$\left.\frac{\partial T}{\partial z}\right|_{z=-\delta_d} = 0,\ r_d \le r \le R_d,\ 0 \le t \le t_s \tag{12}$$

At the initial time moment $r = 0$ the pad and disc are heated to the same constant temperature:

$$T(r,z,0) = T_0,\ r_p \le r \le R_p,\ 0 \le z \le \delta_p, \tag{13}$$

$$T(r,z,0) = T_0, r_d \le r \le R_d, -\delta_d \le z \le 0. \tag{14}$$

where: T_0 – initial temperature.

4. NUMERICAL FORMULATION

The object of this section is to develop approximate time-stepping procedures for axisymmetric transient governing equations.

Using Galerkin's method the following matrix form of the Eq. (5) is formulated (Lewis et al., 2004)

$$[C(T)]\left\{\frac{dT}{dt}\right\} + [K(T)][T] = \{R\} \tag{15}$$

where: $[C(T)]$ is the heat capacity matrix, $[K(T)]$ is the heat conductivity matrix, and $\{R\}$ is the thermal force vector.

In order to solve the ordinary differential equation (15)

the direct integration method was used. Based on the assumption that temperature $\{T\}_t$ and $\{T\}_{t+\Delta t}$ at time t and $t+\Delta t$ respectively, the following relation is specified

$$\{T\}_{t+\Delta t} = \{T\}_t + \left[(1-\beta)\left\{\frac{dT}{dt}\right\}_t + \beta\left\{\frac{dT}{dt}\right\}_{t+\Delta t}\right]\Delta t \tag{16}$$

Substituting Eq. (16) to Eq. (15) we obtain the following implicit algebraic equation

$$\begin{aligned}&\left([C(T)] + \beta\Delta t[K(T)]\right)\{T\}_{t+\Delta t} = \\ &\left([C(T)] - (1-\beta)[K(T)]\Delta t\right)\{T\}_t + \\ &+ (1-\beta)\Delta t\{R\}_t + \beta\Delta t\{R\}_{t+\Delta t}\end{aligned} \tag{17}$$

where: β is the factor which ranges from 0,5 to 1 and is given to determine an integration accuracy and stable scheme.

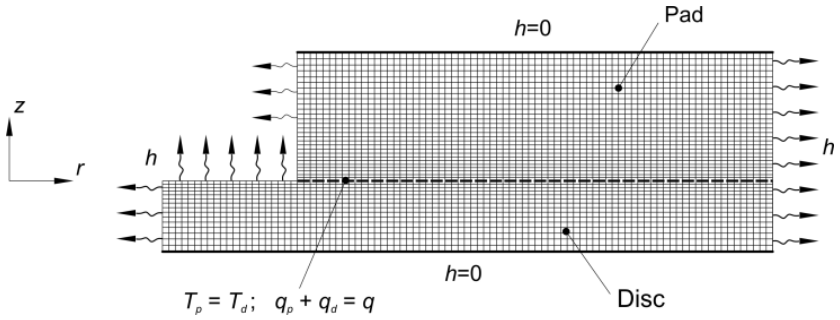

Fig. 2. Finite element mesh of a disc brake

FE axisymmetric 2D model is shown in Fig. 2. Four node quad type elements were used. Total number of elements of the brake model equals 3497, in which 1425 elements and 1536 nodes come to the disc, and 2072 elements and 2175 nodes come to the pad.

The heating of the friction surfaces was accomplished by means of the total intensity of heat flux directed into the pad. Furthermore by using 75 'multi point constraints' MPC at subsequent pairs of nodes of the friction surfaces of the pad and the disc separation according to boundary conditions Eqns. (2,3) during simulated slipping contact took place (constraint of the temperatures). Other surfaces (edges in the FE model) were either cooled or insulated satisfying Eqns. (6-14).

5. RESULTS AND DISCUSSION

In the study thermal finite element analysis of heat generation due to friction in a pad/disc brake system was carried out. The temperature evolutions at specified axial and radial positions obtained incorporating the temperature-independent thermophysical properties of materials are calculated and compared with the thermosensitive materials.

5.1. Operation parameters and dimensions of the pad/disc system

Operation parameters and dimensions of the brake are listed in Tab. 1. The single braking process proceeds during 3,96 s from the initial velocity of 100 km/h (ω_0 = 88,464 s^{-1}) to standstill with constant retardation (Talati and Jalalifar 2009). In order to develop twofold braking process the boundaries conditions after the disengagement of the braking components obviously had to be diverse. The total time of the twofold braking process equalled t_s = 40 s. The braking schema was as follows, after the moment of full stop a vehicle increased velocity with constant acceleration to the velocity of 100 km/h during 16.04 s. Then the cycle was repeated attaining 40 s of the total twofold braking operation. Despite the fact of change of the velocity the heat transfer coefficient remained constant (Tab. 2) which was due to the fact of its insignificant impact on the resulting temperature distributions.

Tab. 1. Operation parameters and dimensions of the disc and the pad (Talati and Jalalifar, 2009)

item	disc	pad
inner radius, r [m]	0,066	0,0765
outer radius, R [m]	0,1135	0,1135
thickness, δ [m]	0,0055	0,01
initial angular velocity of the rotor, ω_0 [s^{-1}]	88,464	
single/twofold braking time, t_s [s]	3,96/40	
heat transfer coefficient, h [W/(m^2K)]	60	
contact pressure, p_0 [Pa]	1.47×10^6	
coefficient of friction, f	0,5	
initial temperature, T_0 [°C]	20	
ambient temperature, T_a [°C]	20	

5.2. Thermophysical properties of materials

Behaviour of the material properties under the influence of temperature were derived from the measurements carried out in ref. (Chichinadze et al., 1979). To obtain mathematical formulas of variations of the essential in thermal analysis thermophysical properties of materials, the methodology proposed in that paper was used as well. Two of the three available crucial for the calculations properties were chosen having in mind possibly the smoothest temperature dependence. Thus despite the fact that the employed FE based

programme required specific heat *c* and thermal conductivity *K*, only the latter satisfied the criterions. The second parameter was the thermal diffusivity *k* whose value allowed to calculate required specific heat.

Below approximate formulas for the thermal conductivity and the thermal diffusivity of four different materials used in numerical computations are listed:

– for the pad materials:
  – FMK-845

$$K_p(T) = 9.806\left(1.171 + \frac{1.315}{1 + 7.32\cdot 10^{-7}\cdot T^2}\right) \tag{18}$$

$$k_p(T) = 10^{-6}\left(-0.823 + \frac{10.778}{1 + 1.487\cdot 10^{-6}\cdot T^2}\right) \tag{19}$$

  – FMK-11

$$K_p(T) = 9.806\left(4.017 + \frac{-2.282}{1 + 5.298\cdot 10^{-6}\cdot (T-900)^2}\right) \tag{20}$$

$$k_p(T) = 10^{-6}\left(-1.146 + \frac{17.207}{1 + 2.122\cdot 10^{-6}\cdot (T+100)^2}\right) \tag{21}$$

– and for the disc:
  – steel EI-696

$$K_d(T) = 0.014T + 15.727 \tag{22}$$

$$k_d(T) = -1.444\cdot 10^{-9}T + 5.502\cdot 10^{-6} \tag{23}$$

  – cast iron ChNMKh

$$K_d(T) = -0.028T + 52.727 \tag{24}$$

$$k_d(T) = 10^{-6}\left(5.557 + \frac{15.226}{1 + 8.018\cdot 10^{-6}(T+400)^2}\right) \tag{25}$$

The presented formulas for the thermal conductivity and the thermal diffusivity have their equivalent at approximately 20 °C which are shown in Tab. 2. As can be seen the major differences between temperature-independent thermophysical properties of materials of the disc (steel EI-696, cast iron ChNMKh) is encountered for the thermal conductivity *K*. Less distinct are the constant properties of the pad FMK-845, FMK-11). However for the thermosensitive materials together with the temperature their values vary in a different way (Figs. 3, 4) giving possibility to examine such a behaviour on the temperatures of the pad and the disc.

Tab. 2. Thermophysical properties of materials independent of temperature (Chichinadze et al., 1979)

material	K [W/(mK)]	k [m^2/s]	ρ [kg/m^3]
EI-696	16,3	$4{,}92\times10^{-6}$	7850
ChNMKh	51	$1{,}44\times10^{-5}$	7100
FMK-845	24,5	$1{,}04\times10^{-5}$	6000
FMK-11	34,3	$1{,}46\times10^{-5}$	4700

Using formulas 18-25 particular properties were calculated and set tabularly into the commercial finite element based programme (MSC.SOFTWARE). The step of the temperature was equal 0.1 °C giving consequently 8001 lines. Moreover it was established that the closest value of the given property from the table was selected during the calculations.

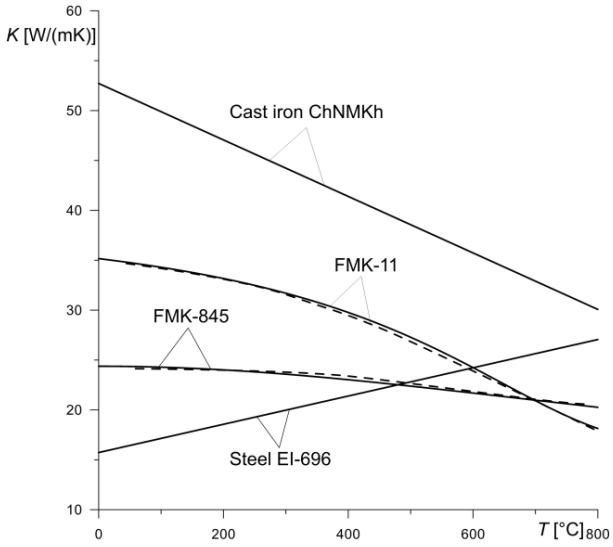

Fig. 3. Thermal conductivities of a disc and a pad versus temperature obtained from the measurements (solid curves) and their approximations (dashed curves) (Chichinadze et al., 1979)

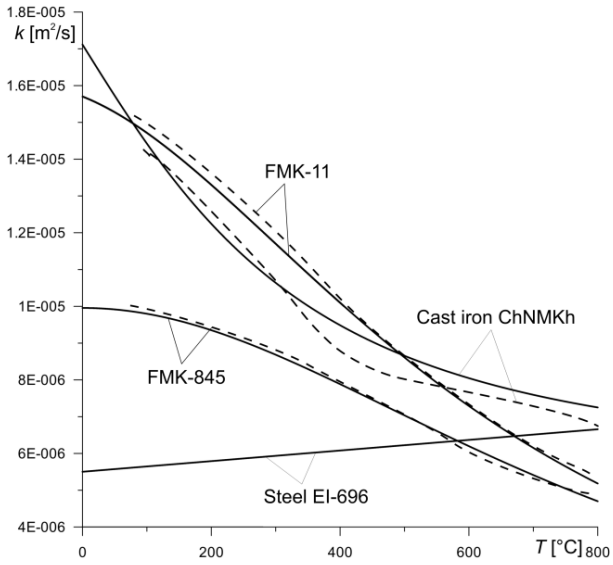

Fig. 4. Thermal diffusivities of a disc and a pad versus temperature obtained from the measurements (solid curves) and their approximations (dashed curves) (Chichinadze et al., 1979)

As a result of the carried out computations evolutions of temperature at the pad/disc interface (equal temperature on the pad and the disc friction surfaces at specified radial positions) are shown. In Fig. 5 the temperature evolutions are depicted for two braking couples, for the disc made of cast iron ChNMKh and two different pad materials FMK-845 (Fig. 5a) and FMK-11 (Fig. 5b).

As can be seen the temperatures on the friction surfaces are smooth not revealing any periods of interchangeable heating and cooling which stems from the main as-

sumptions of this study of axisymmetric heat flux distribution and perfect contact between the pad and the disc. Comparison of two- and three-dimensional axisymmetric models was shown is ref. (Adamowicz and Grzes, 2011a). Evolutions of temperature of the thermosensitive materials and their temperature-independent equivalents are marked with dashed and solid lines, respectively. All further plots will have the same denotation. The obtained results make evident that during the considered single braking operation, variations of the thermal conductivity and thermal diffusivity (Fig. 3, 4) do not allow to change firmly the contact temperatures of the disc brake at any of the radial positions. However the highest temperature difference between these two friction couplings is observable at the biggest distance from the axis of rotation *z*.

In Fig. 6 temperatures of the disc at different axial positions and constant radius r = 0,095 m are related to the braking time. Previous material compositions (Fig. 5) are confronted again. The distances between illustrated *z* positions are not constant to enable clear visualisation of the results. Since the disc is located under the radial coordinate axial values are plotted with minus. Obviously it can be seen that the temperatures are lower with the increase of *z* distance. Until half of the braking time t_s temperatures at each location in axial direction almost coincide (regarding thermosensitive and temperature-independent materials). After that time temperatures of the model with thermosensitive materials are slightly lower, however, revealing the same behaviour as materials with constant properties.

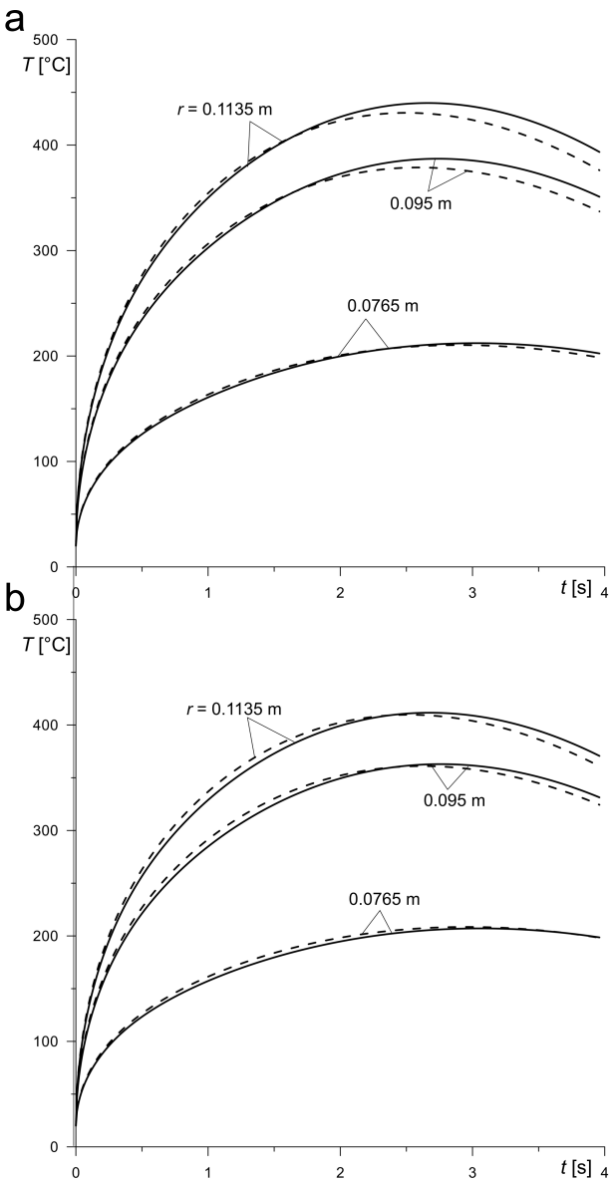

Fig. 5. Evolutions of temperature at the pad/disc interface for different radial positions, solid curves indicate temperature-independent thermophysical properties whereas dashed curves thermosensitive materials:
a) disc (cast iron ChNMKh)/pad (FMK-845)
b) disc (cast iron ChNMKh)/pad (FMK-11)

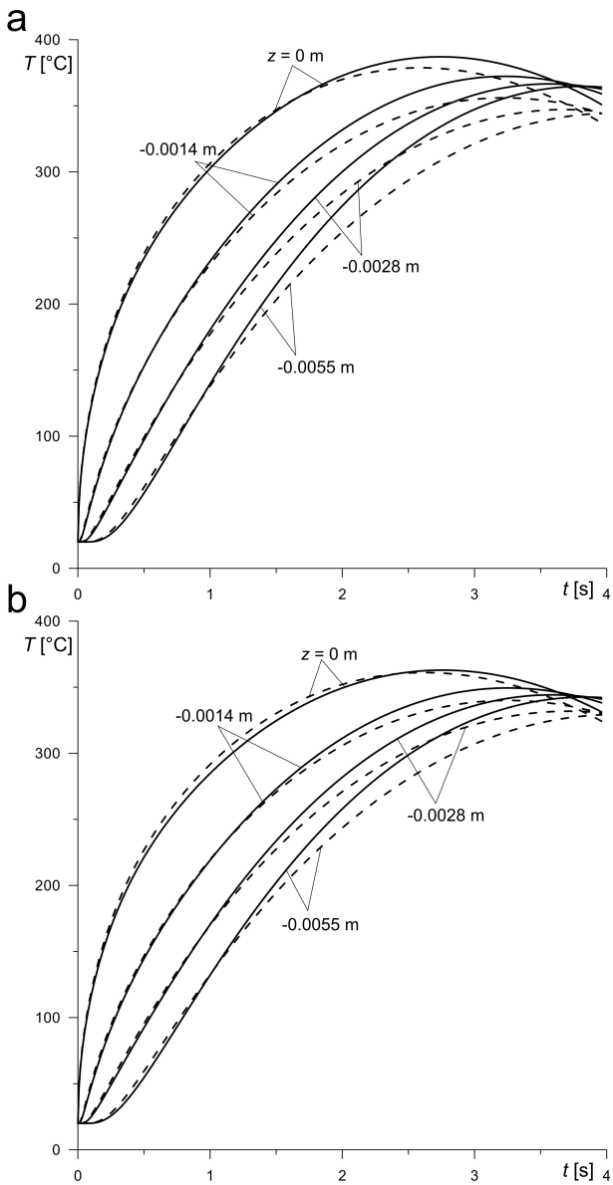

Fig. 6. Evolutions of temperature at different radial axial positions of a disc (r = 0.095 m), solid curves indicate temperature-independent thermophysical properties whereas dashed curves thermosensitive materials:
a) disc (cast iron ChNMKh)/pad (FMK-845)
b) disc (cast iron ChNMKh)/pad (FMK-11)

Temperature evolutions at the pad/disc interface for the disc made of steel EI-696 and two different pad materials (the same as in Fig. 5 and Fig. 6) are shown versus braking time in Fig. 7. It may be observed that unlike Fig. 5 and Fig. 6 the biggest temperature differences concentrate at about half of the braking time for both of the pad materials (Fig. 6a, b) and then decreases to equalize at the end of the process.

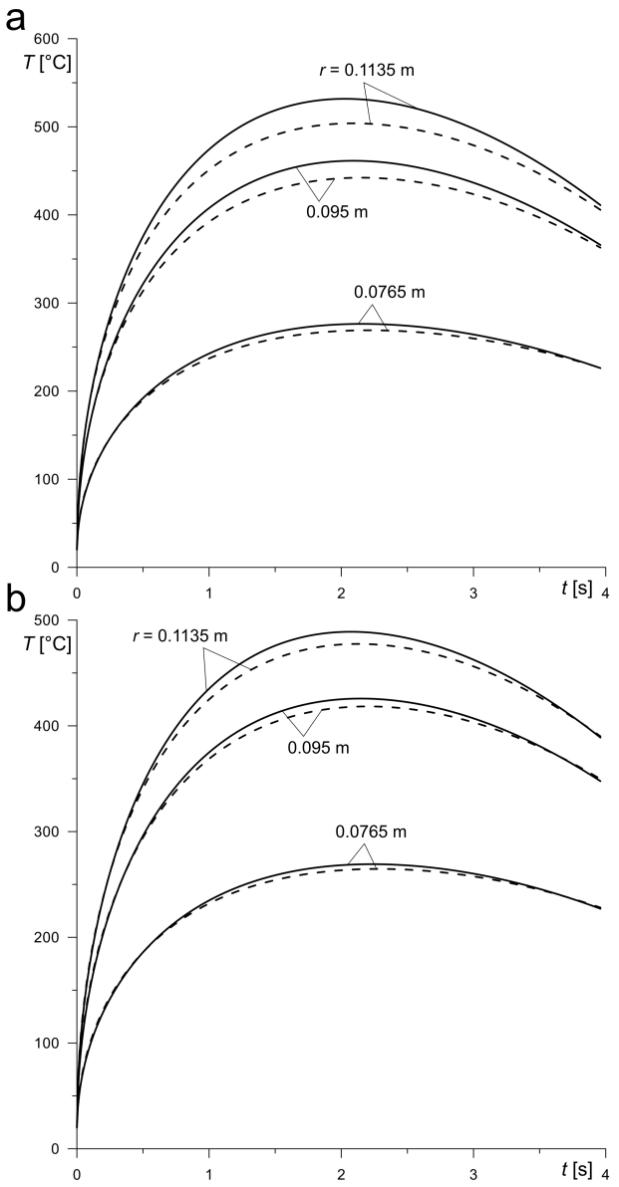

Fig. 7. Evolutions of temperature at the pad/disc interface for different radial positions, solid curves indicate temperature-independent thermophysical properties whereas dashed curves thermosensitive materials: a) disc (steel EI-696)/ pad (FMK-845) b) disc (steel EI-696)/pad (FMK-11)

Fig. 8 shows the temperature evolutions at specified axial locations (mean radius r = 0,095 mm) whose values correspond with Fig. 6. Spread of the subsequent temperatures at z = 0, -0,0014, -0,0028, -0,0055 m is clearly bigger than in Fig. 6 due to different material of the disc. In this case the disc made of steel EI-696 has the thermal conductivity about three times lower. Thereby the generated temperature is slower dissipated through conduction giving bigger temperature gradients. Even at the end of the process the temperature is not equal within the disc thickness both with the pad made of FMK-845 and FMK-11. However the highest temperature obtain during the process T = 461.4 °C occurs for the friction pair made of steel EI-696/FMK-845 (Fig. 8a). The same relationship took place for the disc made of cast iron ChNMKh (Fig. 6).

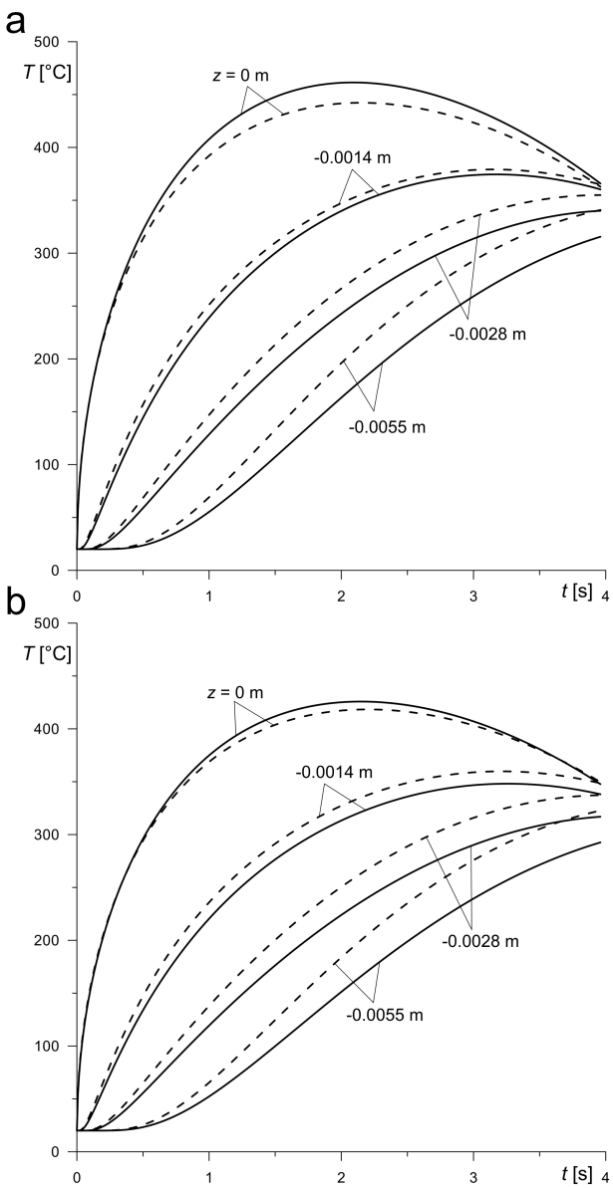

Fig. 8. Evolutions of temperature at selected axial positions of a disc (r = 0.095 m), solid curves indicate temperature-independent thermophysical properties, dashed curves thermosensitive materials: a) disc (steel EI-696)/pad (FMK-845) b) disc (steel EI-696)/pad (FMK-11)

The temperature evolutions on the contact surface at three different distances from the axis of rotation during twofold braking process t_s = 40 s are shown in Fig. 9. The disc made of steel EI-696 was combined with the pad made of FMK-845 (Fig. 9a) and FMK-11 (Fig. 9b). According to the braking schema time from 0 to 3.96 s corresponds to the braking with constant deceleration to standstill followed by the disengagement of the brake components and simultane-

ous acceleration of the vehicle to the prior velocity of 100 km/h. Then the process was repeated which clearly affected the temperature evolutions. Unlike the single braking in the analyzed cases of twofold braking the temperature of the model with thermosensitive materials was lower in all cases. The occurred phase of vehicle acceleration reveals opposite situation either for FMK-845 or FMK-11. This relation loses its meaning during the second acceleration introducing some inconsistency. However for the friction pair steel EI-696/FMK-11 the rule that the temperature is higher for constant properties of materials was remained.

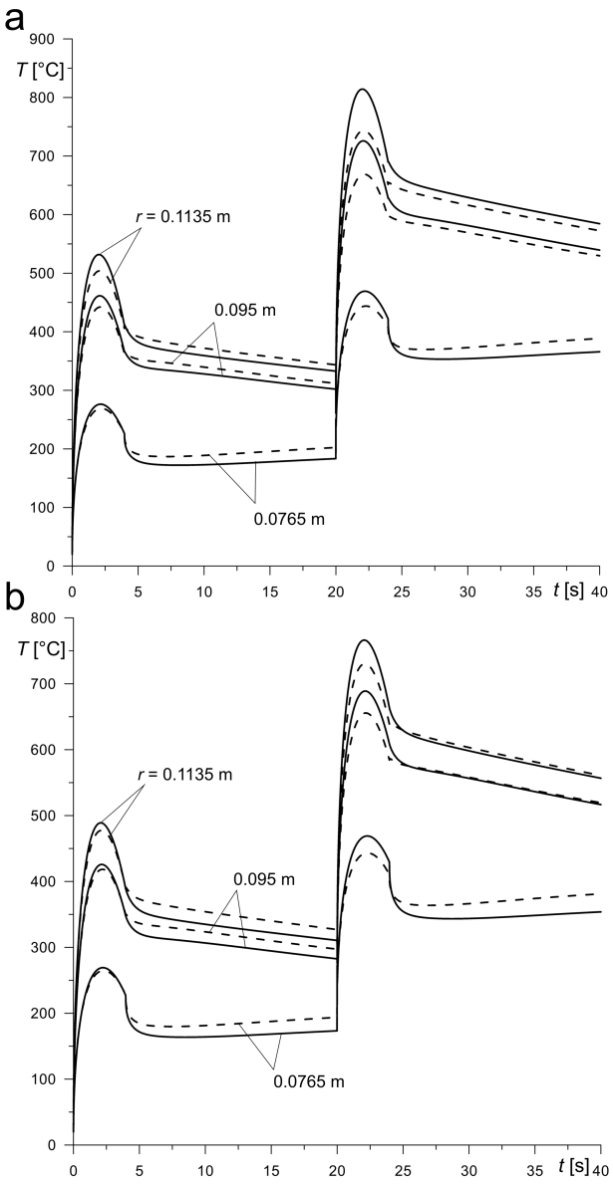

Fig. 9. Evolutions of temperature at the pad/disc interface during twofold braking process

Fig. 10 shows the temperature evolutions at selected axial positions z for the constant value of the radius r = 0,095 m. The process of the vehicle acceleration, just after the braking stage results in the temperature equalization (Fig. 10a, b) within the entire depth and its further linear decrease evoked by the cooling according to Newton's law. It may be observed that for both of friction pairs, the first and the second brake application doesn't generate the same behaviour of temperature regarding the case with temperature-dependent and independent material properties. In the figure solely disc temperature are shown. The noticeable jump of temperature after the coupling of the disc and the pad at time t = 20 s stems from the temperature difference between these components after their disconnection and cooling conditions (Fig. 10 a, b).

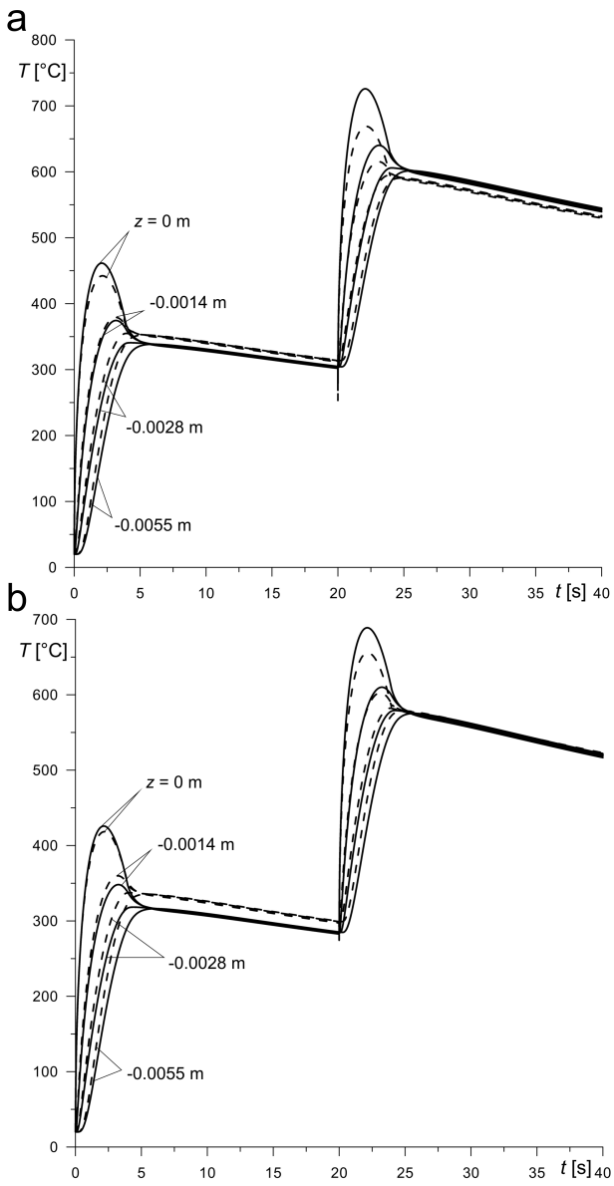

Fig. 10. Evolutions of temperature at different axial positions (r = 0,095 m) during twofold braking process

6. CONCLUSIONS

In this paper axisymmetric thermal analysis by using axisymmetric FE contact model was carried out to study an effect of the use of thermosensitive and temperature-independent thermophysical properties of materials on the temperatures of the pad/disc system during single and twofold braking. The calculated temperatures on the friction surfaces as well as values at the selected axial locations

were confronted and compared. The obtained results reveal that within the range of temperatures variations from 20 to 800 °C of the brake components, in spite of relatively marked fluctuations of the thermophysical properties the use of subsequent constant values corresponding to 20 °C is validated. Both single and twofold braking confirms that rule. However relationship between the resulting temperature values obtained during computations by means of thermosensitive properties and temperature-independent constants varies during the twofold braking. It was observed that direct relation between the thermal effusivity and the resulting temperature is evident.

REFERENCES

1. **Adamowicz A., Grzes P.** (2011a), Analysis of disc brake temperature distribution during single braking under non-axisymmetric load, *Applied Thermal Engineering*, Vol. 31, No. 6-7, 1003-1012.
2. **Adamowicz A., Grzes P.** (2011b), Influence of convective cooling on a disc brake temperature distribution during repetitive braking, *Applied Thermal Engineering*, Vol. 31, No. 14-15, 2177-2185.
3. **Aderghal N., Loulou T., Bouchoucha A., Rogeon P.** (2011), Analytical and numerical calculation of surface temperature and thermal constriction resistance in transient dynamic strip contact, *Applied Thermal Engineering*, Vol. 31, No. 8-9, 1527-1535.
4. **Chichinadze A. V., Braun E. D., Ginsburg A. G., et al.** (1979), *Calculation, test and selection of frictional couples*, Nauka, Moscow, (in Russian).
5. **Ginzburg A. H.** (1973), Theoretical and experimental bases for calculation of unitary process of braking by means of system of the equations of thermal dynamics of friction, In: *Optimum use of frictional material in units of friction of machines*, Nauka, Moscow, 93-105, (in Russian).
6. **Grzes P.** (2009), Finite element analysis of disc temperature during braking process, *Acta Mechanica et Automatica*, Vol. 3, No. 4., 36-42.
7. **Grzes P.** (2009), Finite element analysis of disc temperature during braking process, *Acta Mechanica et Automatica*, Vol. 3, No. 4., 36-42.
8. **Grzes P.** (2010), Finite element analysis of temperature distribution in axisymmetric model of disc brake, *Acta Mechanica et Automatica*, Vol. 4, No. 4., 3-28.
9. **Grzes P.** (2011), Partition of heat in 2D finite element model of a disc brake, *Acta Mechanica et Automatica*, Vol. 5, No. 2, 35-41.
10. **Lee K., Barber J. R.** (1994), An Experimental Investigation of Frictionally-Excited Thermoelastic Instability in Automotive Disk Brakes Under a Drag Brake Application, *Journal of Tribology*, Vol. 116, No. 3, 409-414.
11. **Nosko A. L., Belyakov N. S., Nosko A. P.** (2009), Application of the generalized boundary condition to solving thermal friction problems, *Journal of Friction and Wear*, Vol. 30, No. 6, 455-462.
12. **Scieszka S. F.**, (1998) *Hamulce cierne – zagadnienia materiałowe, konstrukcyjne i tribologiczne*, ITE, Radom.
13. **Scieszka S.**, **Zolnierz M.** (2007) The effect of the mine winder disc brake's design feature on its thermoelastic instability. Part I. Set-up for finite element modelling and numerical model verification, *Problems of Machines Operation and Maintenance* Vol. 42, No. 3, 111-124.
14. **Scieszka S.**, **Zolnierz M.** (2007), The effect of the mine winder disc brake's design feature on its thermoelastic instability. Part II. Finite element simulation, *Problems of Machines Operation and Maintenance* Vol. 42, No. 4, 183-193.
15. **Sergienko V. P., Tseluev M. Yu., Kupreev A. V.** (2009), Numerical simulation of operation heat modes of multidisc oil-cooled vehicle brake. Part 1. Heat problem solution, *Journal of Friction and Wear*, Vol. 30, No. 5, 341-349.
16. **Talati F., Jalalifar S.** (2009), Analysis of heat conduction in a disk brake system, *Heat and Mass Transfer*, Vol. 45, No. 8, 1047-1059.
17. **Thuresson D.** (2004), Influence of material properties on sliding contact braking applications, *Wear*, Vol. 257, No. 5-6, 451-460.
18. **Wawrzonek L.**, **Bialecki R.A**. (2008), Temperature in a disk brake, simulation and experimental verification, *International Journal of Numerical Methods for Heat & Fluid Flow*, Vol. 18, No. 3-4, 387-400.
19. **Yevtushenko A., Grzes P.** (2010), FEM-modeling of the frictional heating phenomenon in the pad/disc tribosystem (a review), *Numerical Heat Transfer Part A*, Vol. 58, No. 3, 207-226.
20. **Yevtushenko A., Grzes P.** (2011), Finite element analysis of heat partition in a pad/disc brake system, *Numerical Heat Transfer Part A*, Vol. 59, No. 7, 521-542.
21. **Yi Y.-B., Barber J. R., Hartsock D. L.** (2002), *Thermoelastic instabilities in automotive disc brakes-finite element analysis and experimental verification, in: J.A.C. Martins, D.P. Manuel, M. Marques (Eds.), Contact Mechanics*, Kluwer, Dordrecht, 187-202.
22. **Zhu Z.-C., Peng Y.-Z., Chen G.-A.** (2009), Three-dimensional transient temperature field of brake shoe during hoist's emergency braking, *Applied Thermal Engineering*, Vol. 29, No. 5-6, 932-937.

The paper was supported by the Bialystok University of Technology under the research project No. W/WM/11/2011

ASPECTS OF EXPLOITATION STABILITY OF SELECTED DENTAL PROSTHETIC BRIDGES

Marek JAŁBRZYKOWSKI[*], Joanna MYSTKOWSKA[*], Dariusz URBAN[**], Ewa KULESZA[*], Edyta ANDRYSEWICZ[*]

[*] Faculty of Mechanical Engineering, Bialystok University of Technology, Wiejska 45 C, 15-351 Bialystok
[**] Faculty of Medicine with the Division of Dentistry and Division of Medical Education in English, Medical University of Bialystok, Sklodowskiej 24A, 15-267 Bialystok

m.jalbrzykowski@pb.edu.pl, j.mystkowska@pb.edu.pl, darurb18@wp.pl, ewa.kulesza1@gmail.com, edchem@o2.pl

Abstract: The paper presents results of microscopic observations of selected porcelain bridges prepared on metallic base. The aim of microscopic observations was the identification of example wear types which have appeared during dental prosthetic bridges exploitation. The main attention was directed to wear forms that are quite often present in case of such prosthetic elements. The wear types comparative analysis was evaluated. The most frequent types of wear are: material's cracking, abrasive wear. Also, the metal corrosion and wear by dental plaque at prosthetic bridge surface were observed.

1. INTRODUCTION

Fixed prosthetic restorations such as crowns and bridges restore loss of human mastication organ functions. The main tasks of prosthetic dental bridges are: replenishment (restoration) of missing teeth with a simultaneous correction of speech disorders caused by loss of teeth, improvement of food mastication conditions and keep safe mastication organs and whole organism from harmful after-effects of loss a natural teeth. Total or partial defects in dentition do not cause only disorders in proper food chewing or speech disorders. Stomatognatic system disorders, loss of self-confidence and avoiding contact with other people are also of great importance. These aspects favour for the spread of mental complexes forming. Restoration of missing teeth and further rehabilitation proceedings partly eliminate disorders mentioned above (Maślanka, 2000; Shield, 1968).

Clinical investigations indicate that fixed prosthetic restorations, particularly bridges are exploited much longer than was previously thought. The mean clinical usefulness period of fixed prostheses ranges from 15 to 25 years (Maślanka, 2000). Only after such period of time, more than half of the originally deposited replenishment were lost, repaired or replaced by new constructions.

It can be assumed that the greatest impact on the durability and reliability of dental bridges have factors such as: material, manufacturing technology, design and service conditions. Particularly important is proper construction. However it is known from experience, that often only after the damage of dental bridge there is a possibility of verification the correctness of its implementation. On the other hand, in the manufacturing process of dental prosthetics components, many errors can be traced, but it seems that the most important are (Spiechowicz, 1980, 2010):

- improperly selected material,
- inappropriate design,
- improperly selected manufacturing parameters.

Also, abnormal service conditions in the oral cavity have a huge impact on shortening the time of use. The most negative exploitation factor is treatment the bridge with too high forces and pressures.

In a general context, the main exploitation conditions with more or less influence on the bridge condition, are (Shillingburg, 1994):

- occlusion,
- bruxism,
- mechanical stress,
- temperature factors,
- diet,
- oral hygiene.

Some of these factors have low-order effect on the bridges than others because of impact specificity. Fluctuations and temperature changes in the mouth are too small to have a significantly negatve impact on the durability of dental bridges. Similar situation is in case of the human diet. Materials for the construction of bridges are selected in this way that they show satisfactory resistance to environmental effects of saliva and food. This is rather individual matter, because literature reports are known, about the influence of biofilm on the stability of dentures (Estivill, 2011; Pusateri, 2009). Possible, rarely occurring corrosion centers of metal parts are mainly the result of negligence during the manufacturing stage. All mentioned above factors have an influence on exploitation durability of bridges. However, it seems that decisive are: occlusion, bruxism, and mechanical stresses.

2. MATERIALS AND METHODS OF INVESTIGATIONS

2.1. Materials

Ten dental prosthetic bridges in after-operational state were used for research. These bridges were obtained from

the Department of Prosthodontics, Medical University of Bialystok. Bridges exploitation history has been omitted because of general orientation of conducted research in range of forms and types of wear. Main emphasis in this work is general identification of the types of wear in exploited bridges removed from the mouth of patients.

2.2. Methods

Observations were carried out at macro and micro level. Macroobservations were made by the unaided eye and recorded by classic digital camera. Microobservations were performed using scanning electron microscope Hitachi S-3000N with an addition for chemical composition analysis from Thermo Noran-Quest (Fig. 1). Microscopic observations were used primarily for the appropriate surface selection for the chemical composition analysis.

Fig. 1. Scanning electron microscope Hitachi S-3000N

3. RESULTS

a)

b)

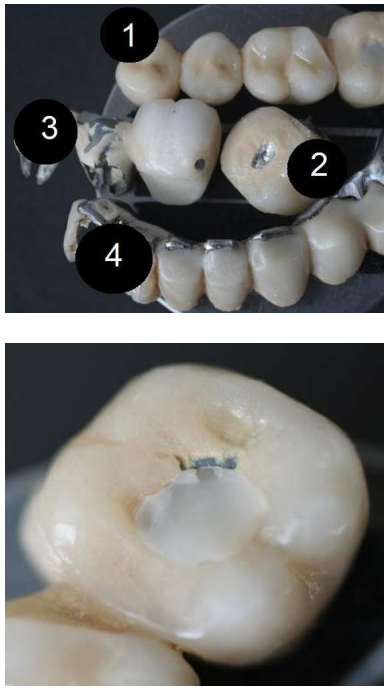

Fig. 2. Types of wear: 1,2 – abrasive, 3 – corrosive, 4 – microcracks; b) abrasive wear

a)

b)

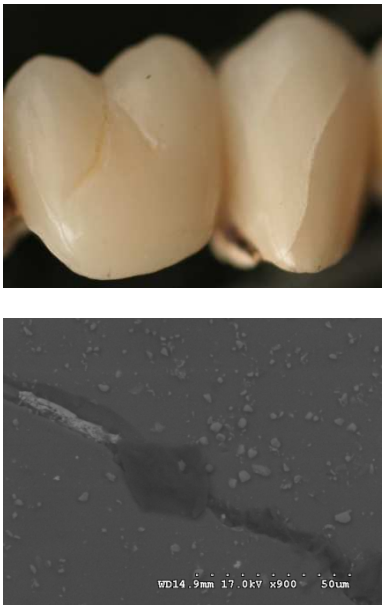

Fig. 3. Ceramic crack superstructure: a) macro- and b) microobservation (x900)

During the operational time dental bridges in patient's mouth are subjected to permanent loads. This follows directly from the process of chewing, crushing and chewing consumed foods. In addition, it comes to wear of dental prosthetics components due to mutual abrasion of these materials or their contact with the opposing teeth (Grosfeldowa, 1981). In Fig. 2 are presented examples of four dental bridges samples with distinct damage.

Both ceramic and acrylic veneers and metal parts are subject to abrasive wear. Fig. 2b shows selected macroobservation results of this kind of wear.

It is well known that the bridge in the oral cavity is exposed, among others on: normal and tangential loads, bending and stretching. These loads together with the moisture of the mouth lead to the initiation and spread of micro-and then macrocrevices in the elements of dental prosthetics. In case of prolonged use metal - ceramic bridges, the gaps within the veneers propagate only to the basic metal. After reaching this point, they connect round both sides of the cracks. However, this does not lead to detachment of ceramics, which is closely bounded to the metal carrier.

Fig. 3 shows an example of a ceramic cracked superstructure.

In relation to this form of wear, we can say that the size of range of gaps is dependent on plasticity - elastic material properties. It turns out that in materials, which are easy to form (metals), it is possible to retard and remove the gaps. On the other hand, in brittle materials - cracks propagate unhindered. It should be taken into account that microgaps and heterogeneity of the material are formed already at the firing process stage. They may be the result of, among others: the volume changes in ceramics during the firing, internal impurity and pores formation as a result of insufficient concentration of the material (Maślanka, 2000).

Both ceramics and metallic parts of dental bridges are failing by fatigue wear. Constructions between the bridge's constituents or tooth crown connection with the bridge span seem to be especially vulnerable points. These places are more vulnerable to fatigue due to cyclic loading during the

process of chewing. The result of volume fatigue wear is the fatigue crack. A good example of such cracking is destroyed bridge, which is shown in Fig. 4. On crack we see partially smooth surface, which is the result of the gradual increasing of gap in metal. This type of surface is typical for fatigue cracks.

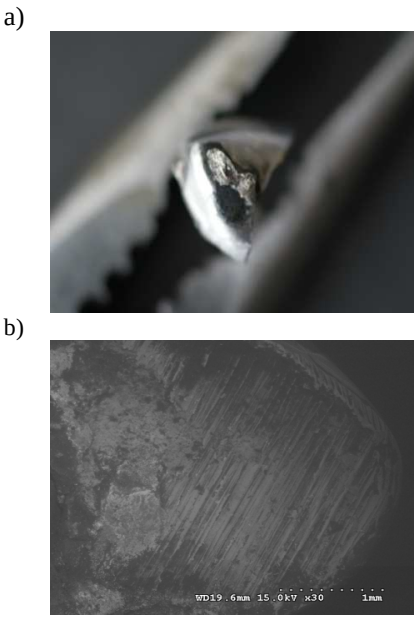

Fig. 4. Example of fatigue crack bridge span:
a) macro- and b) microobservation (x30)

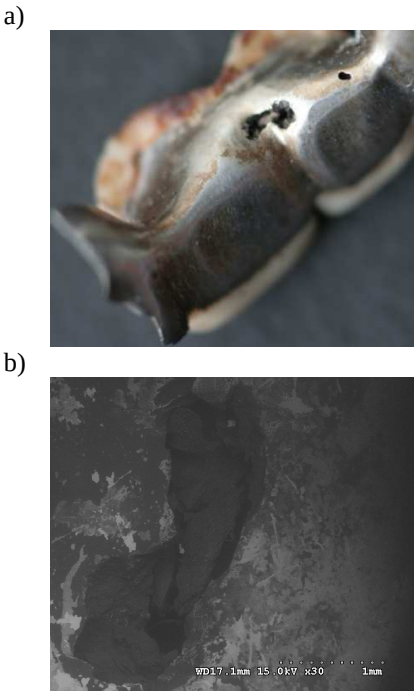

Fig. 5. Corrosive wear: a) macro- and b) microobservation (x30)

Inappropriate construction of bridges may be also the reason of bridges cracking. The elements most exposed to damage, as mentioned earlier, include connections of individual members. This possibly means that the connector in place of crack had too small cross section for transmitting applied load.

Another form of wear which could be seen in macroscopic observation is the corrosive wear. Corrosion is a common process in the group of nonfrictional causes of wear. Particularly vulnerable to corrosion are common metals and their alloys. Corrosive resistants are noble metals, such as gold or platinum and their alloys. In Fig. 5 we can see clear signs of corrosion and significant loss of material which is its consequence. Presence of corrosion could be the result of mistakes and negligences in the process of metal parts casting, poor material quality or the result of diet and oral hygiene.

In relation to oral hygiene and general care of the prosthesis, in Fig. 6 is showed example of dental bridge with a clearly visible layer of tooth scale. The reason of this dental bridge condition was inadequate oral hygiene. The bridge was removed from patient, because the tooth scale caused increased loss of tissue in the area of contact. This situation may leads to inflammation and a significant usage comfort reduction. The bridge structure is not without significance. It could have influence on tooth scale formation. It is possible that instead of saddle span, a self-cleaning span was used – it could eliminate retention area in which tooth scale deposition occurs. However, it is a individual matter of approach to the patient and the nature of his illness.

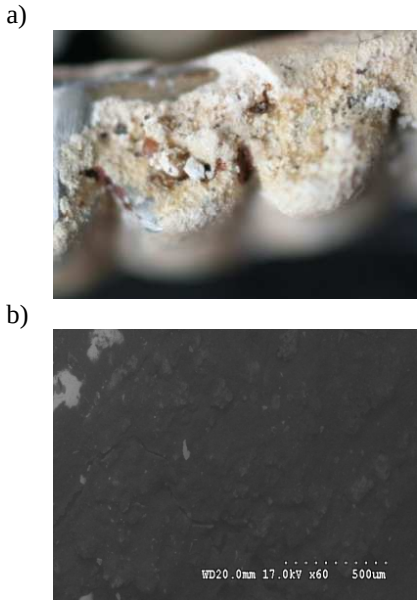

Fig. 6. Tooth scale in the lower part of dental bridges:
a) macro- and b) microobservation (x60)

Another cause of tooth scale deposition on the bridge surface is the inaccuracy in the quality of its surface forming. A full of meaning is influence of micro- roughness of surface.

Tooth scale is present in 80 - 100% of patients cases among adults. These are highly mineralized deposits accumulated on the tooth surface. The chemical composition of tooth scale is as follows: mineral salts 83 (%), including 76 (%) of calcium phosphate, 4 (%) magnesium phosphate and 3 (%) of calcium carbonate. Such elements as: K, Na, Cu, S, Cl, Sn and Fe are in trace amounts (Grosfeldowa, 1981).

Tooth scale visible on the bridge shown in Fig. 6 was put under chemical composition analysis by the scanning electron microscope with an attachment to the study of chemical composition. Example results of such chemical microanalysis of tooth scale are shown in Fig. 7.

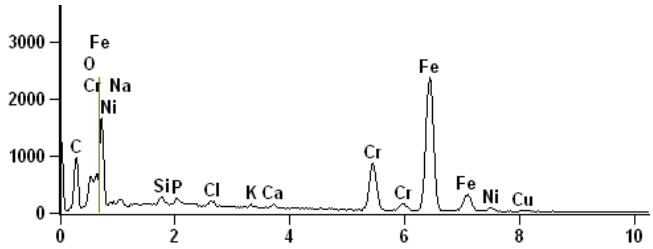

Fig. 7. Results of chemical microanalysis of tooth scale (Pietroczuk, 2008)

In Fig. 7 are shown results of the chemical composition, which indicate a presence of such elements as: Ca, P, Mg, C, F, Cl, Na. Thus, these results comply with the chemical composition of tooth scale visible on human enamel.

The next stage of research, the summarizing of the collected prosthetic bridges for the type of visible wear was evaluated. Fig. 8 shows the percentage fraction of identified damages in the inspected group of dental bridges.

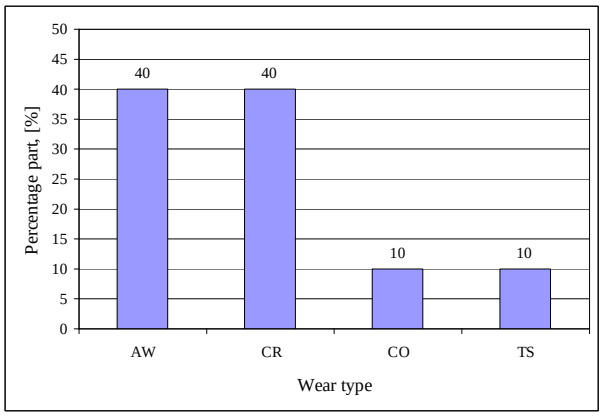

Fig. 8. Percentage damage fraction: AW – abrasive wear, CR – cracking, CO – corrosion, TS – tooth scale

The results of macro- and microscopic observations show that the largest participation in the examined group of dental prosthetic bridges have an abrasion wear and prosthetic bridge crackings caused by parameters of external forces in which bridges were used. In case of abrasive wear important is a friction combination, especially kind of materials which are in direct contact with each other. However, in the case of cracks significant are both, design, material and also a bridge production technology. Moreover, corrosive wear and presence of tooth scale are also very important.

4. SUMMARY AND CONCLUSIONS

Macroscopic and microscopic observations and chemical composition analysis of tooth scale on their surface (for the examined group of dental bridges), let to form the following general conclusions:

1. The most common types of wear are: fracture – 4 bridges and abrasion wear – 4 bridges. For 10 samples tested, one bridge has worn out due to corrosion, and there was one case of wear induced by accumulation of tooth scale.
2. Damage of all 10 bridges do not allow for their further exploitation. Actually, the only way to restore their functionality is to remake them, with paying particular attention to the causes of their primary wear.
3. After analyzing the causes of wear, depending on the type of damage in the manufacture of bridges, special attention should be focused on the following criteria: the construction of the bridge, material, manufacturing technology.
4. An important element is also properly occlusal surface design and fitting of the bridge at the oral cavity of opposite teeth in order to avoid wear due to inadequate occlusion.

Improper design, poorly selected material, wrong technology, improper fit of the bridge, wrong usage conditions and poor oral hygiene seem to be the most common causes of failure in healing with a prosthetic dental bridge.

REFERENCES

1. **Estivill D.**, Arias A., Torres-Lana A., Carrillo-Munoz A.J., Arevalo M.P. (2011), Biofilm formation by five species of Candida on three clinical materials, *J of Microbial Methods*, 86, 238-242.
2. **Grosfeldowa O.** (1981), *Fizjologia narządu żucia*, Państwowy Zakład Wydawnictw Lekarskich, Warszawa.
3. **Maślanka T.** (red) (2000), *Protetyka stomatologiczna. Korony i mosty*, Wydawnictwo Medyczne Urban & Partner, Wrocław.
4. **Pietrabissa R.**, Contro R., Quaglini V., Soucin M., Gionso L., Simion M. (2000), Experimental and computational approach for the evaluation of the biomechanical effects of dental bridge misfit, *Journal of Biomechanics*, 33, 1489-1495
5. **Pietroczuk M:** *Analiza rodzajów zużycia protetycznych mostów stomatologicznych*, Praca dyplomowa pod kier. dr inż. Marka Jałbrzykowskiego, Politechnika Białostocka, Wydział Mechaniczny, Białystok 2008.
6. **Pusateri C.**R., Monaco E.A., Edgerton M. (2009), Sensitivity of Candida albicans biofilm cells grown on denture acrylic to antifungal proteins and chlorhexidine, *Archives of Oral Biology*, 54, 588-594.
7. **Shield H. W.** (1968), The influence of bridge pontics on oral health, *J Milch Stale Dent Assoc*, 50:143.
8. **Shillingburg H.T., Hobo S., Whitsett L.D.** (1994), *Protezy stałe. Zarys postępowania klinicznego i laboratoryjnego*, Wyd. Kwintesencja, Warszawa.
9. **Spiechowicz E.** (1980), *Współczesne postępowanie laboratoryjne w protetyce stomatologicznej*, Państwowy Zakład Wydawnictw Lekarskich, Warszawa.
10. **Spiechowicz E.** (2010), *Protetyka stomatologiczna*, Państwowy Zakład Wydawnictw Lekarskich, Warszawa.

This work was financed by Polish Ministry of Science and Higher Education as a research project in 2010-2013 years (Grant No N N507 592938).

COMPRESSION OF TWO ROLLERS IN SHEET-FED OFFSET PRINTING MACHINE

Agnieszka JURKIEWICZ[*], Yuriy PYR'YEV[*]

[*]Warsaw University of Technology, Faculty of Production Engineering, Institute of Mechanics and Printing, Division of Graphic Art Technologies, ul. Konwiktorska 2, 00-217 Warsaw, Poland

agnieszka.jurkiewicz@wp.eu, y.pyryev@wip.pw.edu.pl

Abstract: The most important units of sheet-fed offset printing machine, like the ink and dampening systems as well as a printing unit, are composed, in the main, of contacting rollers of various sizes (in case of the printing unit they are named cylinders). Adequate setting of the said rollers is very important, because it has big influence on quality of print-outs. The settings are made experimentally by measuring the width of the contact area in the ink and dampening systems or by computing the clamp parameters – in the printing unit. This paper includes analysis of compression of two rollers depending on a width of the contact area, radiuses of the rollers as well as their Poisson's ratios and Young's modules.

1. INTRODUCTION

Printing unit, ink and dampening systems are composed mainly of rollers and cylinders (Fig. 1). A distinctive and extremely important element is the blanket cylinder which is located between the plate cylinder and the impression cylinder. There has been fixed a rubber blanket on a blanket cylinder for the purpose of better conveying the image from metal plate with ink on paper.

The printing unit includes 3 cylinders: plate cylinder, blanket cylinder and impression cylinder (Dejidas and Destree, 2007; Kipphan, 2001). In this part of machine there is a contact between a metal plate fixed onto the plate cylinder and a rubber blanket fixed onto the blanked cylinder as well as between the rubber blanket and the metal impression cylinder.

Plate cylinders are in contact with ink form rollers and with the dampening form roller. Soft – coated with rubber or other artificial materials and hard – metal rollers inside ink unit are in contact, thus being adequately adherent to each other. In the dampening unit, soft – coated with rubber, paper or fabric and hard – metal rollers are in contact alternately.

Setting an inadequate stress between cylinders of the printing unit and rollers of the ink and dampening systems affects 3 aspects of printings, namely: print-outs quality, wear and tear of machine elements and reduction in time of making the printing machines ready for operation. The elimination of printing errors which are observed on print-outs at the beginning and in the course of printing, extends time of making the printing machines ready for operation, increases consumption of waste paper and ink.

Uneven stress between rollers of ink and dampening systems may result in irregular ink and water transmission. Too big stress between ink rollers cause to excessive heat and rubber expansion.

Setting too big stress between ink form rollers and plate cylinder results in bouncing of rollers each from other while their conveying above the channel of the plate cylinder and stroking the front edge of plate. As a result, the ink thickness on plate is changed. It brings about generating smudges on print-outs, faster wear and tear of plate, too much tone value increase. Uneven setting of stress between ink form rollers can cause smudges as well.

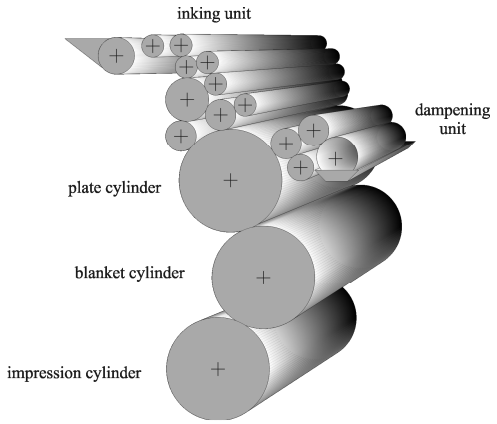

Fig. 1. An exemplary printing unit, ink and dampening systems

Too small stress in the dampening system results in transmission of too much amounts of water on plate. It can cause too much amount of water on plate and ink emulsification. It can involve problems as regards ink drying and ink adhering to ink rollers. In turn, too big stress makes water squeezed from the rollers and on the plate there is to small water film. In the dampening system, stress between the dampening form roller and the distributing roller as well as between the dampening form roller and the plate cylinder should be big enough to distribute water and to quicken the dampening form roller with the distribution roller.

For determining an adequate contact between the rollers and cylinders there is not measured or computed the stress. Printing operators check the stress in the ink and dampening systems regularly with foil stripes which they put in between the rollers and, next, take them out. In the ink

system they measure the width of the contact zone between the rollers. As regards the printing unit, a clamp is computed on the basis of height of the plate over bearer rings (hardened metal rings located at the ends of the two cylinders) of the plate cylinder and the height of rubber over bearer rings of the blanket cylinder.

2. STATEMENT OF THE PROBLEM

It becomes apparent that the most essential elements of sheet-fed offset printing machine are rollers which remain in mutual contact (Fig. 2). The contact of two cylinders, the axes of which were compressed to distance *d* due to unknown vertical compressing forces P, was considered. The contact area has a rectangular shape with unknown width *2a*. A contact stress *p(x)*, which takes place in the contact area $x \in (-a, a)$, is a symmetric, although unknown, function and $p(a) = p(-a) = 0$:

$$\int_{-a}^{a} p(x)dx = \mathrm{P} \tag{1}$$

We assume that in rollers a plane strain takes place which is independent on variable y.

Boundary condition for the contact of the two rollers is determined as follows (Jonson, 1985):

$$u_z^2 + u_z^1 = d_2 + d_1 - f_2(x) - f_1(x)\,,\ x \in (-a, a) \tag{2}$$

where: u_z^1, u_z^2 – displacement of the points located on the contact surfaces of, accordingly, body 2 and body 1 alongside with axis *z*, this displacement being assumed positive, d_2, d_1 – indentation of, accordingly, body 2 and body 1 under loading, $f_1(x) = 0{,}5x^2/R_1$, $f_2(x) = 0{,}5x^2/R_2$ – equations for surface of body 1 and body 2 before indentation.

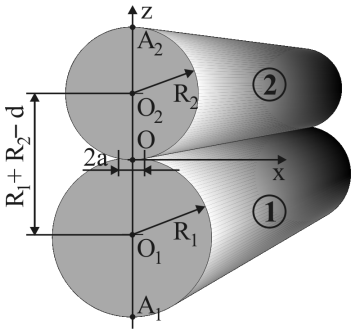

Fig. 2. Two contacting rollers

In the assumption of Herz's conditions (Timoshenko, Goodier, 1962), the problem is to solve the issue of half-space. Assuming that displacement does not depend on the direction *y*, the equation of the theory of elasticity for displacements (Lame) shall be as follows (Nowacki, 1970):

$$\begin{cases} (\lambda+2\mu)\dfrac{\partial^2 U_x(x,z)}{\partial x^2} + \mu\dfrac{\partial^2 U_x(x,z)}{\partial z^2} + (\lambda+\mu)\dfrac{\partial^2 U_z(x,z)}{\partial x \partial z} = 0 \\ (\lambda+2\mu)\dfrac{\partial^2 U_z(x,z)}{\partial z^2} + \mu\dfrac{\partial^2 U_z(x,z)}{\partial x^2} + (\lambda+\mu)\dfrac{\partial^2 U_x(x,z)}{\partial z \partial x} = 0 \end{cases} \tag{3}$$

where: λ, μ – Lame parameters, $U_z(x,z), U_x(x,z)$ – displacement alongside with axes *z* and *x*.

The boundary conditions for the considered problem are as follows:

$$\sigma_{zz}(x,z)\,|_{z=+0} = \begin{cases} -\,p(x), & |x| < a \\ 0, & |x| > a \end{cases} \tag{4}$$

$$\sigma_{xz}(x,0)\,|_{z=+0} = 0\,,\ -\infty < x < \infty \tag{5}$$

$$\sigma_{zz}(x,z)\,|_{z\to\infty} = 0\ ,\ \sigma_{xz}(x,0)\,|_{z\to\infty} = 0 \tag{6}$$

where: σ_{zz}, σ_{xz} – normal and shearing stresses:

$$\sigma_{zz} = (\lambda+2\mu)\frac{\partial u_z}{\partial z} + \lambda\frac{\partial u_x}{\partial x} \tag{7}$$

$$\sigma_{xz}(x,z) = \mu\left(\frac{\partial u_x}{\partial z} + \frac{\partial u_z}{\partial x}\right) \tag{8}$$

3. SOLUTION OF THE PROBLEM

The problem (3)-(6) is solved by using Fourier integral transform (Nowacki, 1970). For $U_x(x,z)$ and $U_z(x,z)$, the following equations are obtained:

$$U_x(x,z) = \frac{1}{\sqrt{2\pi}}\int_{-\infty}^{+\infty}\widetilde{U}_x(\xi,z)e^{-i\xi x}d\xi \tag{9}$$

$$U_z(x,z) = \frac{1}{\sqrt{2\pi}}\int_{-\infty}^{+\infty}\widetilde{U}_z(\xi,x)e^{-i\xi z}d\xi \tag{10}$$

$$\begin{aligned}\widetilde{U}_x = &-i\left[\left(\frac{(\lambda+3\mu)}{(\lambda+\mu)\xi} + z\frac{|\xi|}{\xi}\right)B + \frac{|\xi|}{\xi}A\right]e^{|\xi|z} - \\ &-i\left[\left(\frac{(\lambda+3\mu)}{(\lambda+\mu)\xi} - z\frac{|\xi|}{\xi}\right)D - \frac{|\xi|}{\xi}C\right]e^{-|\xi|z}\end{aligned} \tag{11}$$

$$\widetilde{U}_z = (A + zB)e^{|\xi|z} + (C + zD)e^{-|\xi|z} \tag{12}$$

where: $A(\xi), B(\xi), C(\xi), D(\xi)$ resulted from the four conditions namely (4)-(6).

The final solution of the problem (3)-(6) is as follows:

$$U_x(x,z) = \frac{1+\nu}{E\sqrt{2\pi}}\left(\frac{2xz}{r^2} - (1-2\nu)2arctg\frac{x}{z}\right) * p(x) \tag{13}$$

$$U_z(x,z) = -\frac{2(1-\nu^2)}{E\sqrt{2\pi}}\left(\frac{z^2}{(1-\nu)r^2} + \ln(e^{C_0}r^2)\right) * p(x) \tag{14}$$

where: $r^2 = x^2 + z^2$, ν – Poisson's ratio, E – Young's modulus, "*" – the convolution of function

$$g(x) * \varphi(x) = \int_{-a}^{a} g(x-s)\varphi(s)ds\,. \tag{15}$$

and the following relationships were taken into account:

$$\lambda = \frac{\nu E}{(1+\nu)(1-2\nu)}\,,\ \mu = \frac{E}{2(1+\nu)} \tag{16}$$

The constant C_0 is obtained from the condition $U_z(0,R)=0$. Substitution of normal displacement of half-space's edges $U_z^l(x,0)=u_z^l$, $l=1,2$ in the boundary condition (2) led to the integral equation for a contact stress function $p(x)$. The solution for the considered issue is as follows (Jonson, 1985):

$$p(x)=\frac{aE_0}{2R_0}\sqrt{1-\frac{x^2}{a^2}} \tag{17}$$

where:

$$\frac{1}{R_0}=\frac{1}{R_1}+\frac{1}{R_2},\ \frac{1}{E_0}=\eta_1+\eta_2,\ \eta_l=\frac{1-\nu_l^2}{E_l},\ l=1,2 \tag{18}$$

Substituting (17) in the equation (1) led to the equation of contact area width $2a$ (Jonson, 1985):

$$\mathrm{P}=\frac{\pi a^2 E_0}{4R_0} \tag{19}$$

The final equation for compression of the two rollers $d=d_1+d_2$ is as follows:

$$d=\frac{\mathrm{P}}{\pi}\left[\eta_1\ln\left(e^{m_1}\frac{4R_1^2}{a^2}\right)+\eta_2\ln\left(e^{m_2}\frac{4R_2^2}{a^2}\right)\right] \tag{20}$$

where: a – half of the contact zone width, R_1, R_2 – radius accordingly of upper roller and lower roller, ν_1, ν_2 – Poisson's ratio accordingly of upper and lower rollers, E_1, E_2 – Young's modulus accordingly of upper and lower rollers and

$$m_l=-\frac{\nu_l}{1-\nu_l}+\frac{1}{1-\nu_l}\frac{a^2}{4R_l^2},\ l=1,2 \tag{21}$$

Stresses placed near the contact area resulted from equations known from the literature (Jonson, 1985).

Analogical equation for contact of two spheres has been present in literature for quite a long time (Johnson, 1985; Popov, 2010; Timoshenko and Goodier, 1962).

4. NUMERICAL ANALYSIS AND DISCUSSION

The literature provides for various experimental researches and equations on compression of cylinders. Many divergences can be avoided if loading areas are defined accurately. Fig. 2 shows points O, O_1, O_2, A_1, A_2 where cylinders may be loaded. If cylinders are loaded in the points A_1, A_2 the coefficient m_l equals $m_l=\ln 4-1$ (Loo, 1958; Jonson, 1985; Zhuravlev, Karpenko, 2000). The last two of these authors used the solution consisting in compression of the cylinders by two forces (Muskhelishvili, 1963) and then they obtained compression for any radii. The papers (Birger, Panovko, 1968; Jarema, 2006) shows the coefficient $m_1=m_2=0{,}814$, which is most often used. But in reality this value of coefficients m_l takes place only for $\nu_1=\nu_2=0{,}3$. The authors (Zhuravlev, Karpenko, 2000) paid attention to this fact. Generally, the coefficient m_l equals $m_l=\ln 4-1+\nu_l(1-\nu_l)$.

If cylinders are loaded in the points O_1, O_2, coefficient m_l for $\eta_1=\eta_2$ equals $m_1=m_2=2/3$ (Chandrasekaran, 1987). The same coefficient m_l is given in the papers (Dinnik, 1952; Galin, 1976), where none of the said papers includes correct citation.

Using equations (19) and (20) we will come to dimensionless relation between compression of rollers $d_*=d/R_2$ and the contact area width $a_*=a/R_2$.

$$d_*=\frac{a_*^2}{2}\frac{R_*+1}{R_*(\eta_*+1)}\left[\eta_*\ln\left(e^{m_{1'/2}}\frac{2R_*}{a_*}\right)+\ln\left(e^{m_{2'/2}}\frac{2}{a_*}\right)\right] \tag{22}$$

where $\eta=\eta_1/\eta_2$, $R_*=R_1/R_2$, as well as to dimensionless relation between compression of rollers $d_*=d/R_2$ and the dimensionless radius $R_*=R_1/R_2$:

$$d_*=\frac{\mathrm{P}_*}{\pi}\left[\eta_*\ln\left(e^{m_1}\frac{\pi R_*(1+R_*)}{(1+\eta_*)\mathrm{P}_*}\right)+\ln\left(e^{m_2}\frac{\pi(1+R_*)}{(1+\eta_*)\mathrm{P}_*R_*}\right)\right] \tag{23}$$

where $P_*=P\eta_2R_2$.

Fig. 3 shows dependence (23) of dimensionless compression of the distance between axes of cylinders $d_*=d/R_2$, an indentation of lower cylinder $d_1=R_2$ and an indentation of upper cylinder $d_2=R_2$ on the dimensionless radius $R_*=R_1/R_2$ for steel cylinders $E_l=2{,}15\cdot 10^5$Mpa, $\nu_l=0{,}3$, $l=1{,}2$, $P=2{,}15\cdot 10^7$N/m ($P_*=0{,}84\cdot 10^{-2}, \eta_*=1$).

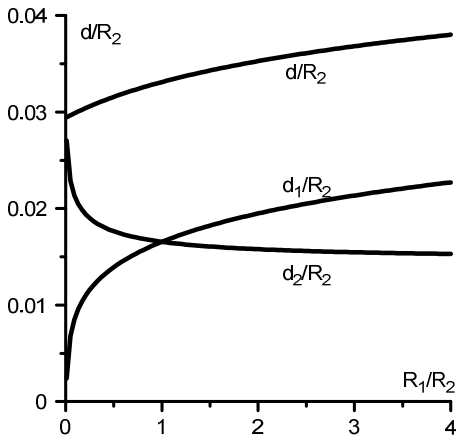

Fig. 3. Dependence of compression of cylinders' axes $\boldsymbol{d/R_2=d_1/R_2+d_2/R_2}$ and its components on $\boldsymbol{R_*=R_1/R_2}$

From Fig. 3 it can be seen that an increase of cylinder's indentation is on relation in increase of this cylinder's radius. The increase in radius of the bigger cylinder ($R_*>1$) causes the increase of compression $d_*=d/R_2$. The reduction in radius of the smaller cylinder ($R_*<1$) causes reduction of the cylinders' compression $d_*=d/R_2$, although an indentation of the bigger cylinder increases. Reduction in distance between the cylinders depends directly on an increase in the cylinders' loading.

Whenever contact takes place between the steel cylinder (body 1) and the rubber blanket (body 2), $\eta_*=0$ can be assumed. The equation (22) shall then take the following form:

$$d_* = \frac{a_*^2(R_*+1)}{2R_*}\ln\left(e^{m_{2/2}}\frac{2}{a_*}\right) \tag{24}$$

Fig. 4 shows the obtained dependence between dimensionless compression of cylinders' axes d/R_2 and the dimensionless contact area a/R_2 for various values $\boldsymbol{R_* = R_1/R_2}$.

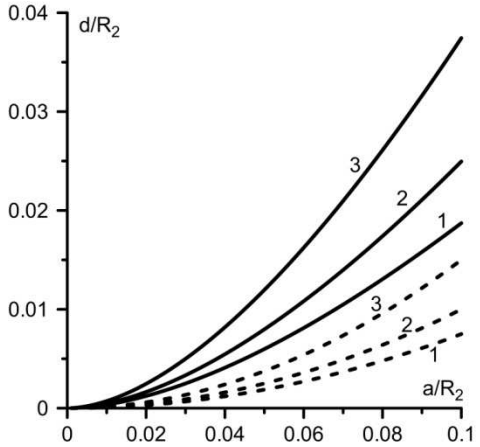

Fig. 4. Dependence of compression of cylinders' axes $\boldsymbol{d/R_2}$ on contact area $\boldsymbol{a/R_2}$. Curve $\boldsymbol{1 - R_* = 2}$, $\boldsymbol{2 - R_* = 1}$, $\boldsymbol{3 - R_* = 0,5}$

Analogical dependence which is used in the printing technical literature (Chehman i inni, 2005) $d/R_2 = 0{,}5a_*^2(R_*+1)/R_*$ is shown in the Fig. 4 as a dashed curve. A significant divergence of results can be seen.

5. CONCLUSSIONS

The obtained equation will be used in printing with the aim to calculate and verify the width of the contact area between the two rollers which remain in contact. Until now, in the printing industry the said contact area used to be determined only experimentally. The equation (20) allows for calculating the width of the contact zone depending on compression of the cylinders' axes, their radii as well as their Poisson's ratios and Young's modulus.

LITERATURE

1. **Belyaev N. M.** (1957), *Trudy po teorii uprugosti I plastichnosti* (*Works on Plasticity and Elasticity Theory*), Moscow, Gostekhteorizdat.
2. **Birger I. A., Panovko Y. G.** (eds) (1968), *Strength, stability, vibrations*. Mashinostroenie, Moscow, Vol. 2.
3. **Chandrasekaran N., Haisler W. E., Goforth R. E.** (1987), Finite Elrment Analysis of Problem Hertz Kontakt z Friction, *Finite Elements w Analysis and Design*, Vol. 3, 39-56.
4. **Chehman Y. I., Senkus V. T., Didych V. P., Bosak V. O.** (2005), *Printing equipment. Textbook*, Ukrainian Academy of Printing.
5. **Dejidas L. P., Jr., T. M. Destree** (2007), *Technologia offsetowego drukowania arkuszowego*, COBRPP, Warsaw.
6. **Destree T. M.** (2007), *Trudności w arkuszowym drukowaniu offsetowym*, COBRPP, Warsaw.
7. **Dinnik A. N.** (1952), *Impact and compression of elastic bodies*. *Selected Works*, Vol. 1, AN UkrSSR, Kiev.
8. **Galin L. A.**, Ed., (1976), *Development* of *Contact Problem Theory in the USSR*, Nauka, Moscow.
9. **Hoeprich M. R., Zantopulos H.** (1981), Line contact deformation: A cylinder between two flat plates. *ASME, Journal of Lubrication Tribology*, 103, 21-25.
10. **Jarema S. M.** (2006), *Mechanics of contact interaction of pairs of rolling friction of printing systems*, UAP, University of Ukraine, Kiev.
11. **Johnson K. I.** (1985), *Contact mechanic*s, Cambridge University Press, Cambridge.
12. **Kipphan H.** (2001), *Handbook of Print Media*, Springer-Verlag, Berlin Heidelberg.
13. **Loo T. T.** (1958), Effect of Curvature on the Hertz Theory for Two Cylinders in Contact, *J. Appl. Mech.*, 25, 122-124.
14. **Muskhelishvili N. I.** (1963*), Some Basic Problems of the Mathematical Theory of Elasticity*, Nordhoff, The Netherlands.
15. **Nowacki W.** (1970), *Teoria sprężystości*, PWN, Warszawa.
16. **Popov V. L.** (2010), *Contact Mechanics and Friction*, Springer-Verlag Berlin Heidelberg.
17. **Timoshenko S.** (1962), Goodier J. N., *Teoria sprężystości*, Arkady, Warszawa.
18. **Zhuravlev G. A., Karpenko V.A.** (2000*), Convergence of elastic bodies modeled by circular cylinders*, Machinery engineering. No. 6(28). 51–55.

REDUCTION AND DECOMPOSITION OF SINGULAR FRACTIONAL DISCRETE-TIME LINEAR SYSTEMS

Tadeusz KACZOREK*

*Faculty of Electrical Engineering, Białystok University of Technology, ul. Wiejska 45D, 15-351 Białystok

kaczorek@isep.pw.edu.pl

Abstract: Reduction of singular fractional systems to standard fractional systems and decomposition of singular fractional discrete-time linear systems into dynamic and static parts are addressed. It is shown that if the pencil of singular fractional linear discrete-time system is regular then the singular system can be reduced to standard one and it can be decomposed into dynamic and static parts The proposed procedures are based on modified version of the shuffle algorithm and illustrated by numerical examples.

1. INTRODUCTION

Singular (descriptor) linear systems have been addressed in many papers and books (Dodig and Stosic, 2009; Dai, 1989; Fahmy and O'Reill, 1989; Gantmacher, 1960; Kaczorek, 1992, 2007a; Kucera and Zagalak, 1988). The eigenvalues and invariants assignment by state and output feedbacks have been investigated in (Dodig and Stosic, 2009; Dai, 1989; Fahmy and O'Reill, 1989; Kucera and Zagalak, 1988; Kaczorek, 2004) and the realization problem for singular positive continuous-time systems with delays in Kaczorek (2007b). The computation of Kronecker's canonical form of a singular pencil has been analyzed in Van Dooren (1979). The fractional differential equations have been considered in the monograph (Podlubny, 1999). Fractional positive linear systems have been addressed in (Kaczorek, 2008, 2010) and in the monograph (Kaczorek, 2011). Luenberger in (Luenberger, 1978) has proposed the shuffle algorithm to analysis of the singular linear systems.

In this paper a modified version of the shuffle algorithm will be proposed for the reduction of the singular fractional system to equivalent standard fractional system and for decomposition of the singular fractional system into dynamic and static parts.

The paper is organized as follows. In section 2 it is shown that if the pencil of the singular system is regular then the singular system can be reduced to equivalent standard fractional system. The decomposition of singular fractional system into dynamic and static parts is addressed in section 4. Concluding remarks are given in section 5.

To the best of the author's knowledge the reduction and the decomposition of singular fractional linear discrete-time systems have not been considered yet.

The following notation be used in the paper.

The set of $n\times m$ real matrices will denoted by $\Re^{n\times m}$ and $\Re^{n} := \Re^{n\times 1}$. The set of $m\times n$ real matrices with nonnegative entries will be denoted by $\Re_{+}^{m\times n}$ and $\Re_{+}^{n} := \Re_{+}^{n\times 1}$. The set of nonnegative integers will be denoted by Z_+ and the $n\times n$ identity matrix by I_n.

2. REDUCTION OF SINGULAR FRACTIONAL SYSTEMS TO EQUIVALENT STANDARD FRACTIONAL SYSTEMS

Consider the singular fractional discrete-time linear system described by the state equation:

$$E\Delta^{\alpha} x_{i+1} = Ax_i + Bu_i\,,\ i\in Z_+ = \{0,1,...\} \tag{1}$$

where, $x_i \in \Re^n, u_i \in \Re^m$ are the state and input vectors, $A \in \Re^{n\times n}, E \in \Re^{n\times n}, B \in \Re^{n\times m}$ and the fractional difference of the order α is defined by:

$$\Delta^{\alpha} x_i = \sum_{k=0}^{i} (-1)^k \binom{\alpha}{k} x_{i-k}\,,\ 0<\alpha<1 \tag{2}$$

$$\binom{\alpha}{k} = \begin{cases} 1 & \text{for} \quad k=0 \\ \dfrac{\alpha(\alpha-1)...(\alpha-k+1)}{k!} & \text{for} \quad k=1,2,... \end{cases} \tag{3}$$

It is assumed that:

$$\det E = 0 \tag{4a}$$

and

$$\det[Ez - A] \neq 0 \tag{4b}$$

for some $z \in C$ (the field of complex numbers).

Substituting (2) into (1) we obtain:

$$\sum_{k=0}^{i+1} Ec_k x_{i-k+1} = Ax_i + Bu_i\,,\ i\in Z_+ \tag{5}$$

where:

$$c_k = (-1)^k \binom{\alpha}{k} \tag{6}$$

Applying the row elementary operations to (5) we obtain:

$$\sum_{k=0}^{i+1} \begin{bmatrix} E_1 \\ 0 \end{bmatrix} c_k x_{i-k+1} = \begin{bmatrix} A_1 \\ A_2 \end{bmatrix} x_i + \begin{bmatrix} B_1 \\ B_2 \end{bmatrix} u_i\,,\ i\in Z_+ \tag{7}$$

where $E_1 \in \Re^{n_1 \times n}$ is full row rank and $A_1 \in \Re^{n_1 \times n}$, $A_2 \in \Re^{(n-n_1) \times n}$, $B_1 \in \Re^{n_1 \times m}$, $B_2 \in \Re^{(n-n_1) \times m}$. The equation (7) can be rewritten as:

$$\sum_{k=0}^{i+1} E_1 c_k x_{i-k+1} = A_1 x_i + B_1 u_i \tag{8a}$$

and

$$0 = A_2 x_i + B_2 u_i \tag{8b}$$

Substituting in (8b) i by $i + 1$ we obtain:

$$A_2 x_{i+1} = -B_2 u_{i+1} \tag{9}$$

The equations (8a) and (9) can be written in the form:

$$\begin{bmatrix} E_1 \\ A_2 \end{bmatrix} x_{i+1} = \begin{bmatrix} A_1 - c_1 E_1 \\ 0 \end{bmatrix} x_i - \begin{bmatrix} c_2 E_1 \\ 0 \end{bmatrix} x_{i-1} - ... - \begin{bmatrix} c_{i+1} E_1 \\ 0 \end{bmatrix} x_0 + \begin{bmatrix} B_1 \\ 0 \end{bmatrix} u_i + \begin{bmatrix} 0 \\ -B_2 \end{bmatrix} u_{i+1} \tag{10}$$

If the matrix:

$$\begin{bmatrix} E_1 \\ A_2 \end{bmatrix} \tag{11}$$

is nonsingular then premultiplying the equation (10) by the inverse matrix $\begin{bmatrix} E_1 \\ A_2 \end{bmatrix}^{-1}$ we obtain the standard system:

$$x_{i+1} = \bar{A}_0 x_i + \bar{A}_1 x_{i-1} + ... + \bar{A}_i x_0 + \bar{B}_0 u_i + \bar{B}_1 u_{i+1} \tag{12}$$

where:

$$\bar{A}_0 = \begin{bmatrix} E_1 \\ A_2 \end{bmatrix}^{-1} \begin{bmatrix} A_1 - c_1 E_1 \\ 0 \end{bmatrix}, \quad \bar{A}_1 = -\begin{bmatrix} E_1 \\ A_2 \end{bmatrix}^{-1} \begin{bmatrix} c_2 E_1 \\ 0 \end{bmatrix}$$
$$..., \quad \bar{A}_i = -\begin{bmatrix} E_1 \\ A_2 \end{bmatrix}^{-1} \begin{bmatrix} c_{i+1} E_1 \\ 0 \end{bmatrix}, \tag{13}$$
$$\bar{B}_0 = \begin{bmatrix} E_1 \\ A_2 \end{bmatrix}^{-1} \begin{bmatrix} B_1 \\ 0 \end{bmatrix}, \quad \bar{B}_1 = \begin{bmatrix} E_1 \\ A_2 \end{bmatrix}^{-1} \begin{bmatrix} 0 \\ -B_2 \end{bmatrix}.$$

If the matrix (11) is singular then applying the row elementary operations to (10) we obtain:

$$\begin{bmatrix} E_2 \\ 0 \end{bmatrix} x_{i+1} = \begin{bmatrix} A_{20} \\ \bar{A}_{20} \end{bmatrix} x_i + \begin{bmatrix} A_{21} \\ \bar{A}_{21} \end{bmatrix} x_{i-1} + ... + \begin{bmatrix} A_{2,i} \\ \bar{A}_{2,i} \end{bmatrix} x_0 + \begin{bmatrix} B_{20} \\ \bar{B}_{20} \end{bmatrix} u_i + \begin{bmatrix} B_{21} \\ \bar{B}_{21} \end{bmatrix} u_{i+1} \tag{14}$$

where $E_2 \in \Re^{n_2 \times n}$ is full row rank with $n_2 \geq n_1$ and $A_{2,j} \in \Re^{n_2 \times n}$, $\bar{A}_{2,j} \in \Re^{(n-n_2) \times n}$, $j = 0,1, ..., i$, $B_{2,k} \in \Re^{n_2 \times m}$, $\bar{A}_{2,k} \in \Re^{(n-n_2) \times m}$, $k = 0,1$.

From (14) we have:

$$0 = \bar{A}_{20} x_i + \bar{A}_{21} x_{i-1} + ... + \bar{A}_{2,i} x_0 + \bar{B}_{20} u_i + \bar{B}_{21} u_{i+1} \tag{15}$$

Substituting in (15) i by $i + 1$ (in state vector x and in input u) we obtain:

$$\bar{A}_{20} x_{i+1} = -\bar{A}_{21} x_i - ... - \bar{A}_{2,i} x_1 - \bar{B}_{20} u_{i+1} - \bar{B}_{21} u_{i+2} \tag{16}$$

From (2.14) and (2.16) we have:

$$\begin{bmatrix} E_2 \\ \bar{A}_{20} \end{bmatrix} x_{i+1} = \begin{bmatrix} A_{20} \\ -\bar{A}_{21} \end{bmatrix} x_i + \begin{bmatrix} A_{21} \\ -\bar{A}_{22} \end{bmatrix} x_{i-1} + ... + \begin{bmatrix} A_{2,i} \\ 0 \end{bmatrix} x_0 + \begin{bmatrix} B_{20} \\ 0 \end{bmatrix} u_i + \begin{bmatrix} B_{21} \\ -\bar{B}_{20} \end{bmatrix} u_{i+1} + \begin{bmatrix} 0 \\ -\bar{B}_{21} \end{bmatrix} u_{i+2} \tag{17}$$

If the matrix:

$$\begin{bmatrix} E_2 \\ \bar{A}_{20} \end{bmatrix} \tag{18}$$

is nonsingular then premultiplying the equation (17) by its inverse we obtain the standard system:

$$x_{i+1} = \hat{A}_0 x_i + \hat{A}_1 x_{i-1} + ... + \hat{A}_i x_0 + \hat{B}_0 u_i + \hat{B}_1 u_{i+1} + \hat{B}_2 u_{i+2} \tag{19}$$

where:

$$\hat{A}_0 = \begin{bmatrix} E_2 \\ \bar{A}_{20} \end{bmatrix}^{-1} \begin{bmatrix} A_{20} \\ -\bar{A}_{21} \end{bmatrix}, \quad \hat{A}_1 = \begin{bmatrix} E_2 \\ \bar{A}_{20} \end{bmatrix}^{-1} \begin{bmatrix} A_{21} \\ -\bar{A}_{22} \end{bmatrix}$$
$$..., \quad \hat{A}_i = \begin{bmatrix} E_2 \\ \bar{A}_{20} \end{bmatrix}^{-1} \begin{bmatrix} A_{2,i} \\ 0 \end{bmatrix}, \tag{20}$$
$$\hat{B}_0 = \begin{bmatrix} E_2 \\ \bar{A}_{20} \end{bmatrix}^{-1} \begin{bmatrix} B_{20} \\ 0 \end{bmatrix}, \quad \hat{B}_1 = \begin{bmatrix} E_2 \\ \bar{A}_{20} \end{bmatrix}^{-1} \begin{bmatrix} B_{21} \\ -\bar{B}_{20} \end{bmatrix},$$
$$\hat{B}_2 = \begin{bmatrix} E_2 \\ \bar{A}_{20} \end{bmatrix}^{-1} \begin{bmatrix} 0 \\ -\bar{B}_{21} \end{bmatrix}$$

If the matrix (18) is singular we repeat the procedure. Continuing this procedure after at most n steps we finally obtain a nonsingular matrix and the desired fractional system. The procedure can be justified as follows. The elementary row operations do not change the rank of the matrix $[Ez - A]$. The substitution in the equations (8b) and (15) i by $i + 1$ also does not change the rank of the matrix $[Ez - A]$ since it is equivalent to multiplication of tits lower rows by z and by assumption (4b) holds. Therefore, the following theorem has been proved.

Theorem 1. The singular fractional linear system (5) satisfying the assumption (4) can be reduced to the standard fractional linear system

$$x_{i+1} = \tilde{A}_0 x_i + \tilde{A}_1 x_{i-1} + ... + \tilde{A}_i x_0 + \tilde{B}_0 u_i + \tilde{B}_1 u_{i+1} + ... + \tilde{B}_p u_{i+p} \tag{21}$$

where $\tilde{A}_j \in \Re^{n \times n}$, $j = 0,1, ..., i$, $\tilde{B}_k \in \Re^{n \times m}$, $k = 0,1, ..., p < n$ whose dynamics depends on the future inputs $u_{i+1}, ..., u_{i+p}$.

Example 1. Consider the singular fractional linear system (1) for $\alpha = 0{,}5$ with:

$$E = \begin{bmatrix} 5 & 0 & 2 \\ 2 & 0 & 1 \\ 1 & 0 & 0 \end{bmatrix}, \quad A = \begin{bmatrix} 0.2 & 2 & -2 \\ 2 & 1 & 0 \\ -1.8 & 0 & -1 \end{bmatrix}, \quad B = \begin{bmatrix} 1 & 2 \\ -1 & 2 \\ 2 & -1 \end{bmatrix}. \tag{22}$$

In this case the conditions (4) are satisfied since: $\det E = 0$ and

$$\det[Ez-A]=\begin{vmatrix}5z-0.2 & -2 & 2z+2\\ 2z-2 & -1 & z\\ z+1.8 & 0 & 1\end{vmatrix}=z-0.2$$

Applying to the matrices (22) the following elementary row operations $L[1+2\times(-2)]$, $L[3+1\times(-1)]$ we obtain:

$$[E\quad A\quad B]=\begin{bmatrix}5 & 0 & 2 & 0.2 & 2 & -2 & 1 & 2\\ 2 & 0 & 1 & 2 & 1 & 0 & -1 & 2\\ 1 & 0 & 0 & -1.8 & 0 & -1 & 2 & -1\end{bmatrix}$$

$$\rightarrow\begin{bmatrix}1 & 0 & 0 & -3.8 & 0 & -2 & 3 & -2\\ 2 & 0 & 1 & 2 & 1 & 0 & -1 & 2\\ 0 & 0 & 0 & 2 & 0 & 1 & -1 & 1\end{bmatrix}=\begin{bmatrix}E_1 & A_1 & B_1\\ 0 & A_2 & B_2\end{bmatrix} \tag{23}$$

and the equations (8) have the form:

$$\sum_{k=0}^{i+1}c_k\begin{bmatrix}1 & 0 & 0\\ 2 & 0 & 1\end{bmatrix}x_{i-k+1}=\begin{bmatrix}-3.8 & 0 & -2\\ 2 & 1 & 0\end{bmatrix}x_i+\begin{bmatrix}3 & -2\\ -1 & 2\end{bmatrix}u_i \tag{24a}$$

and

$$0=[2\quad 0\quad 1]x_i+[-1\quad 1]u_i \tag{24b}$$

Using (6) we obtain:

$$c_1=-\binom{\alpha}{1}=-\alpha=-0.5,\ c_2=(-1)^2\binom{\alpha}{2}=\frac{\alpha(\alpha-1)}{2!}=-\frac{1}{8},$$

$$\ldots,\ c_{i+1}=(-1)^{i-1}\frac{\alpha(\alpha-1)\ldots(\alpha-i)}{(i+1)!}\Big|_{\alpha=0.5}$$

and the equation (10) has the form:

$$\begin{bmatrix}1 & 0 & 0\\ 2 & 0 & 1\\ 2 & 0 & 1\end{bmatrix}x_{i+1}=\begin{bmatrix}-3.3 & 0 & -2\\ 3 & 1 & 0.5\\ 0 & 0 & 0\end{bmatrix}x_i+\frac{1}{8}\begin{bmatrix}1 & 0 & 0\\ 2 & 0 & 1\\ 0 & 0 & 0\end{bmatrix}x_{i-1}$$
$$-\ldots-c_{i+1}\begin{bmatrix}1 & 0 & 0\\ 2 & 0 & 1\\ 0 & 0 & 0\end{bmatrix}x_0+\begin{bmatrix}3 & -2\\ -1 & 2\\ 0 & 0\end{bmatrix}u_i+\begin{bmatrix}0 & 0\\ 0 & 0\\ 1 & -1\end{bmatrix}u_{i+1} \tag{25}$$

The matrix $\begin{bmatrix}1 & 0 & 0\\ 2 & 0 & 1\\ 2 & 0 & 1\end{bmatrix}$ is singular and we perform the elementary row operation $L[3+2\times(-1)]$ on (25) obtaining the following:

$$\begin{bmatrix}1 & 0 & 0\\ 2 & 0 & 1\\ 0 & 0 & 0\end{bmatrix}x_{i+1}=\begin{bmatrix}-3.3 & 0 & -2\\ 3 & 1 & 0.5\\ -3 & -1 & -0.5\end{bmatrix}x_i+\frac{1}{8}\begin{bmatrix}1 & 0 & 0\\ 2 & 0 & 1\\ -2 & 0 & -1\end{bmatrix}x_{i-1}$$
$$-\ldots-c_{i+1}\begin{bmatrix}1 & 0 & 0\\ 2 & 0 & 1\\ -2 & 0 & -1\end{bmatrix}x_0+\begin{bmatrix}3 & -2\\ -1 & 2\\ 1 & -2\end{bmatrix}u_i+\begin{bmatrix}0 & 0\\ 0 & 0\\ 1 & -1\end{bmatrix}u_{i+1} \tag{26}$$

The matrix:

$$\begin{bmatrix}E_2\\ \bar{A}_{20}\end{bmatrix}=\begin{bmatrix}1 & 0 & 0\\ 2 & 0 & 1\\ -3 & -1 & -0.5\end{bmatrix} \tag{27}$$

is nonsingular and we obtain the equation (19) with the matrices:

$$\hat{A}_0=\begin{bmatrix}E_2\\ \bar{A}_{20}\end{bmatrix}^{-1}\begin{bmatrix}A_{20}\\ -\bar{A}_{21}\end{bmatrix}=\begin{bmatrix}1 & 0 & 0\\ 2 & 0 & 1\\ -3 & -1 & -0.5\end{bmatrix}^{-1}\begin{bmatrix}-3.3 & 0 & -2\\ 3 & 1 & 0.5\\ 0.25 & 0 & 0.125\end{bmatrix}$$
$$=\begin{bmatrix}-3.3 & 0 & -2\\ 4.85 & -0.5 & 3.625\\ 9.6 & 1 & 4.5\end{bmatrix}$$

$$\vdots$$

$$\hat{A}_i=\begin{bmatrix}E_2\\ \bar{A}_{20}\end{bmatrix}^{-1}\begin{bmatrix}-A_{2,i}\\ 0\end{bmatrix}=\begin{bmatrix}1 & 0 & 0\\ 2 & 0 & 1\\ -3 & -1 & -0.5\end{bmatrix}^{-1}\begin{bmatrix}1 & 0 & 0\\ 2 & 0 & 1\\ 0 & 0 & 0\end{bmatrix}$$
$$=\begin{bmatrix}1 & 0 & 0\\ -3 & 0 & -0.5\\ 0 & 0 & 1\end{bmatrix},$$

$$\hat{B}_0=\begin{bmatrix}E_2\\ \bar{A}_{20}\end{bmatrix}^{-1}\begin{bmatrix}B_{20}\\ 0\end{bmatrix}=\begin{bmatrix}1 & 0 & 0\\ 2 & 0 & 1\\ -3 & -1 & -0.5\end{bmatrix}^{-1}\begin{bmatrix}3 & -2\\ -1 & 2\\ 0 & 0\end{bmatrix}$$
$$=\begin{bmatrix}3 & -2\\ -5.5 & 3\\ -7 & 6\end{bmatrix}$$

$$\hat{B}_1=\begin{bmatrix}E_2\\ \bar{A}_{20}\end{bmatrix}^{-1}\begin{bmatrix}B_{21}\\ -\bar{B}_{20}\end{bmatrix}=\begin{bmatrix}1 & 0 & 0\\ 2 & 0 & 1\\ -3 & -1 & -0.5\end{bmatrix}^{-1}\begin{bmatrix}0 & 0\\ 0 & 0\\ -1 & 2\end{bmatrix}$$
$$=\begin{bmatrix}0 & 0\\ 1 & -2\\ 0 & 0\end{bmatrix}$$

$$\hat{B}_2=\begin{bmatrix}E_2\\ \bar{A}_{20}\end{bmatrix}^{-1}\begin{bmatrix}0\\ -\bar{B}_{21}\end{bmatrix}=\begin{bmatrix}1 & 0 & 0\\ 2 & 0 & 1\\ -3 & -1 & -0.5\end{bmatrix}^{-1}\begin{bmatrix}0 & 0\\ 0 & 0\\ -1 & 1\end{bmatrix}$$
$$=\begin{bmatrix}0 & 0\\ 1 & -1\\ 0 & 0\end{bmatrix} \tag{28}$$

3. DECOMPOSITION OF SINGULAR FRACTIONAL SYSTEM INTO DYNAMIC AND STATIC PARTS

Consider the singular fractional system (5) satisfying the assumptions (4). Applying the procedure presented in section 2 after p steps we obtain:

$$\begin{bmatrix} E_p \\ 0 \end{bmatrix} x_{i+1} = \begin{bmatrix} A_{p,0} \\ \overline{A}_{p,0} \end{bmatrix} x_i + \begin{bmatrix} A_{p,1} \\ \overline{A}_{p,2} \end{bmatrix} x_{i-1} + ... + \begin{bmatrix} A_{pi} \\ \overline{A}_{pi} \end{bmatrix} x_0 + \begin{bmatrix} B_{p,0} \\ \overline{B}_{p,0} \end{bmatrix} u_i + \begin{bmatrix} B_{p,1} \\ \overline{B}_{p,1} \end{bmatrix} u_{i+1} + ... + \begin{bmatrix} B_{p,p-1} \\ \overline{B}_{p,p-1} \end{bmatrix} u_{i+p-1} \tag{29}$$

where $E_p \in \Re^{n_p \times n}$ is full row rank, $A_{pj} \in \Re^{n_p \times n}$, $\bar{A}_{pj} \in \Re^{(n-n_p)\times n}$, $j = 0,1,...,p$ and $B_{pk} \in \Re^{n_p \times m}$, $\bar{B}_{pk} \in \Re^{(n-n_p)\times m}$, $k = 0,1,...,p-1$ with nonsingular matrix:

$$\begin{bmatrix} E_p \\ \overline{A}_{p,0} \end{bmatrix} \in \Re^{n \times n} \tag{30}$$

Using the elementary column operations we may reduce the matrix (30) to the form:

$$\begin{bmatrix} I_{n_p} & 0 \\ A_{21} & I_{n-n_p} \end{bmatrix}, \quad A_{21} \in \Re^{(n-n_p)\times n_p} \tag{31}$$

and performing the same elementary operations on the matrix I_n we can find the matrix $Q \in \Re^{n \times n}$ such that:

$$\begin{bmatrix} E_p \\ \overline{A}_{p,0} \end{bmatrix} Q = \begin{bmatrix} I_{n_p} & 0 \\ A_{21} & I_{n-n_p} \end{bmatrix} \tag{32}$$

Taking into account (32) and defining the new sate vector:

$$\tilde{x}_i = Q^{-1} x_i = \begin{bmatrix} \tilde{x}_i^{(1)} \\ \tilde{x}_i^{(2)} \end{bmatrix}, \quad \tilde{x}_i^{(1)} \in \Re^{n_p}, \quad \tilde{x}_i^{(2)} \in \Re^{n-n_p}, \quad i \in Z_+ \tag{33}$$

from (29) we obtain:

$$\begin{aligned} \tilde{x}_{i+1}^{(1)} &= E_p x_{i+1} = E_p Q Q^{-1} x_{i+1} = A_{p,0} Q Q^{-1} x_i + A_{p,1} Q Q^{-1} x_{i-1} \\ &+ ... + A_{pi} Q Q^{-1} x_0 + B_{p,0} u_i + B_{p,1} u_{i+1} + ... + B_{p,p-1} u_{i+p-1} \\ &= [A_{p,0}^{(1)} \quad A_{p,0}^{(2)}] \begin{bmatrix} \tilde{x}_i^{(1)} \\ \tilde{x}_i^{(2)} \end{bmatrix} + [A_{p,1}^{(1)} \quad A_{p,1}^{(2)}] \begin{bmatrix} \tilde{x}_{i-1}^{(1)} \\ \tilde{x}_{i-1}^{(2)} \end{bmatrix} \\ &+ ... + [A_{pi}^{(1)} \quad A_{pi}^{(2)}] \begin{bmatrix} \tilde{x}_0^{(1)} \\ \tilde{x}_0^{(2)} \end{bmatrix} + B_{p,0} u_i + B_{p,1} u_{i+1} \\ &+ ... + B_{p,p-1} u_{i+p-1} \\ &= A_{p,0}^{(1)} \tilde{x}_i^{(1)} + A_{p,0}^{(2)} \tilde{x}_i^{(2)} + ... + A_{pi}^{(1)} \tilde{x}_0^{(1)} + A_{pi}^{(2)} \tilde{x}_0^{(2)} \\ &+ B_{p,0} u_i + B_{p,1} u_{i+1} + ... + B_{p,p-1} u_{i+p-1}, \quad i \in Z_+ \end{aligned} \tag{34}$$

and

$$\begin{aligned} \tilde{x}_i^{(2)} &= -A_{21} \tilde{x}_i^{(1)} - \overline{A}_{p,1}^{(1)} \tilde{x}_{i-1}^{(1)} - \overline{A}_{p,1}^{(2)} \tilde{x}_{i-1}^{(2)} - ... - \overline{A}_{pi}^{(1)} \tilde{x}_0^{(1)} - \overline{A}_{pi}^{(2)} \tilde{x}_0^{(2)} \\ &- \overline{B}_{p,0} u_i - ... - \overline{B}_{p,p-1} u_{i+p-1}, \quad i \in Z_+ \end{aligned} \tag{35}$$

where:

$$A_{pj} Q = [A_{pj}^{(1)} \quad A_{pj}^{(2)}], \quad \overline{A}_{pj} = [\overline{A}_{pj}^{(1)} \quad \overline{A}_{pj}^{(2)}], \quad j = 0,1,...,i \tag{36}$$

Substitution of (34) into (35) yields:

$$\begin{aligned} \tilde{x}_{i+1}^{(1)} &= \tilde{A}_{p,0} \tilde{x}_i^{(1)} + ... + \tilde{A}_{pi} \tilde{x}_0^{(1)} + \tilde{B}_{p,0} u_i \\ &+ ... + \tilde{B}_{p,p-1} u_{i+p-1}, \quad i \in Z_+ \end{aligned} \tag{37}$$

where

$$\begin{aligned} \tilde{A}_{p,0} &= A_{p,0}^{(1)} - A_{p,0}^{(2)} A_{21}, ..., \tilde{A}_{pi} = A_{pi}^{(1)} - A_{p,0}^{(2)} A_{pi}^{(1)} \\ \tilde{B}_{p,0} &= B_{p,0} - A_{p,0}^{(2)} \overline{B}_{p,0}, ..., \tilde{B}_{p,p-1} = B_{p,p-1} - A_{p,0}^{(2)} \overline{B}_{p,p-1} \end{aligned} \tag{38}$$

The standard system described by the equation (37) is called the dynamic part of the system (5) and the system described by the equation (35) is called the static part of the system (5).

Therefore, the following theorem has been proved.

Theorem 2. The singular fractional linear system (5) satisfying the assumption (4) can be decomposed into the dynamical part (37) and static part (35) whose dynamics depend on the future inputs $u_{i+1}, ..., u_{i+p-1}$.

Example 2. Consider the singular fractional system (1) for $\alpha = 0{,}5$ with the matrices (22). The matrix (27) is nonsingular. To reduce this matrix to the form (31) we perform the elementary operations $R[1+3\times(-2)]$, $R[2\times(-1)]$, $R[2,3]$. The matrix Q has the form:

$$Q = \begin{bmatrix} 1 & 0 & 0 \\ 0 & 0 & -1 \\ -2 & 1 & 0 \end{bmatrix}$$

and

$$\begin{bmatrix} E_2 \\ \overline{A}_{20} \end{bmatrix} Q = \begin{bmatrix} 1 & 0 & 0 \\ 2 & 0 & 1 \\ -3 & -1 & -0.5 \end{bmatrix} \begin{bmatrix} 1 & 0 & 0 \\ 0 & 0 & -1 \\ -2 & 1 & 0 \end{bmatrix} = \begin{bmatrix} 1 & 0 & 0 \\ 0 & 1 & 0 \\ -2 & -0.5 & 1 \end{bmatrix},$$

$A_{21} = [-2 \quad -0.5]$, $n_2 = 2$.

The new state vector (33) is:

$$\tilde{x}_i = Q^{-1} x_i = \begin{bmatrix} 1 & 0 & 0 \\ 2 & 0 & 1 \\ 0 & -1 & 0 \end{bmatrix} \begin{bmatrix} x_{1,i} \\ x_{2,i} \\ x_{3,i} \end{bmatrix} = \begin{bmatrix} \tilde{x}_i^{(1)} \\ \tilde{x}_i^{(2)} \end{bmatrix}, \quad \tilde{x}_i^{(1)} = \begin{bmatrix} x_{1,i} \\ 2x_{1,i} + x_{3,i} \end{bmatrix}, \quad \tilde{x}_i^{(2)} = -x_{2,i}. \tag{39}$$

In this case the equations (34) and (35) have the forms:

$$\begin{aligned} \tilde{x}_{i+1}^{(1)} &= \begin{bmatrix} 0.7 & -2 \\ 2 & 0.5 \end{bmatrix} \tilde{x}_i^{(1)} + \begin{bmatrix} 0 \\ -1 \end{bmatrix} \tilde{x}_i^{(2)} + \frac{1}{8} \tilde{x}_{i-1}^{(1)} \\ &- ... - c_{i+1} \tilde{x}_0^{(1)} + \begin{bmatrix} 3 & -2 \\ -1 & 2 \end{bmatrix} u_i \end{aligned} \tag{40}$$

and

$$\begin{aligned} \tilde{x}_i^{(2)} &= [2 \quad 0.5] \tilde{x}_i^{(1)} + [0.25 \quad 0] \tilde{x}_{i-1}^{(1)} \\ &+ ... + c_{i+1} [-2 \quad 0] \tilde{x}_0^{(1)} - [1 \quad -2] u_i - [1 \quad -1] u_{i+1} \end{aligned} \tag{41}$$

Substituting (41) into (40) we obtain:

$$\begin{aligned}\tilde{x}_{i+1}^{(1)} &= \begin{bmatrix} 0.7 & -2 \\ 0 & 0 \end{bmatrix}\tilde{x}_i^{(1)} + \frac{1}{8}\begin{bmatrix} 1 & 0 \\ 0 & -1 \end{bmatrix}\tilde{x}_{i-1}^{(1)} \\ &-\ldots - c_{i+1}\begin{bmatrix} 1 & 0 \\ -2 & 1 \end{bmatrix}\tilde{x}_0^{(1)} + \begin{bmatrix} 3 & -2 \\ 0 & 0 \end{bmatrix}u_i + \begin{bmatrix} 0 & 0 \\ 1 & -1 \end{bmatrix}u_{i+1}\end{aligned} \tag{42}$$

The dynamic part of the system is described by (42) and the static part by (41).

4. CONCLUDING REMARKS

The singular fractional linear discrete-time systems with regular pencil have been addressed. It has been shown that if the assumption (4) are satisfied then: 1) the singular fractional linear system can be reduced to equivalent standard fractional system (Theorem 1), 2) the singular fractional linear system can be decomposed into dynamic and static parts (Theorem 2). The proposed procedures have been illustrated by numerical examples. The considerations can be easily extended to singular fractional linear continuous-time systems.

REFERENCES

1. **Dai L.** (1989), *Singular Control Systems*, Lectures Notes in Control and Information Sciences, Springer-Verlag, Berlin.
2. **Dodig M., Stosic M.** (2009), Singular systems state feedbacks problems, *Linear Algebra and its Applications*, Vol. 431, No. 8, 1267-1292.
3. **Fahmy M.H, O'Reill J.** (1989), Matrix pencil of closed-loop descriptor systems: infinite-eigenvalues assignment, *Int. J. Control*, Vol. 49, No. 4, 1421-1431.
4. **Gantmacher F. R.** (1960), *The Theory of Matrices*, Chelsea Publishing Co., New York.
5. **Kaczorek T.** (2004), Infinite eigenvalue assignment by output-feedbacks for singular systems, *Int. J. Appl. Math. Comput. Sci.*, Vol. 14, No. 1, 19-23.
6. **Kaczorek T.** (2007a), *Polynomial and Rational Matrices. Applications in Dynamical Systems Theory*, Springer-Verlag, London.
7. **Kaczorek T.** (2007b), Realization problem for singular positive continuous-time systems with delays, *Control and Cybernetics*, Vol. 36, No. 1, 47-57.
8. **Kaczorek T.** (2008), Fractional positive continuous-time linear systems and their reachability, *Int. J. Appl. Math. Comput. Sci.*, Vol. 18, No. 2, 223-228.
9. **Kaczorek T.** (2010), Positive linear systems with different fractional orders, *Bull. Pol. Ac. Sci. Techn.*, Vol. 58, No. 3, 453-458.
10. **Kaczorek T.** (2011), *Selected Problems of Fractional Systems Theory*, Springer-Verlag, Berlin.
11. **Kaczorek T.** York (1992), *Linear Control Systems*, Vol. 1, Research Studies Press J. Wiley, New.
12. **Kucera V., Zagalak P.** (1988), Fundamental theorem of state feedback for singular systems, *Automatica*, Vol. 24, No. 5, 653-658.
13. **Luenberger D.G.** (1978), Time-invariant descriptor systems, *Automatica*, Vol.14, 473-480.
14. **Podlubny I.** (1999), *Fractional Differential Equations*, Academic Press, New York.
15. **Van Dooren P.** (1979), The computation of Kronecker's canonical form of a singular pencil, *Linear Algebra and Its Applications*, Vol. 27, 103-140,

Acknowledgments: This work was supported by National Centre of Sciences in Poland under work N N514 6389 40.

NUMERICAL ANALYSIS OF CROSSWISE HETEROGENEOUS COVERING STRUCTURES IN 3D CLASS STRUCTURE CONDITIONS

Janusz KRENTOWSKI[*], Rościsław TRIBIŁŁO[*]

[*]Katedra Mechaniki Konstrukcji, Wydział Budownictwa i Inżynierii Środowiska,
Politechnika Białostocka, ul. Wiejska 45, 15-351 Białystok

janusz@delta-av.com.pl

Summary: The following paper presents the results of analyses of multi-layered elements and thick constructions, as well as simplifications used for solving structures of 2D class models published in specialist literature, and compares them with a different approach involving generalization of pertinent problems into 3D classes. An error estimation method was proposed, together with a procedure of shaping grid's density ensuring necessary computing precision. Solving huge sets of equations allowed for practically continuous values of complex functions of stress states. Several of the presented typical examples indicate the possibility of applying the algorithms, among others, to heterogeneous structures of reinforced concrete constructions.

1. JUSTIFICATION FOR THE PROCESSES OF CHANGES IN THE ANALYSIS OF TYPICAL 2D STRUCTURES

The authors of the present paper aim at presenting an algorithm that could be practically applied in the analysis of complex engineering constructions, or their untypical integral parts. The analysis processes can be useful for studying rigidity and effort in constructing crosswise heterogeneous coverings, as well as for examination of changes in physical properties and mass of materials, and shape of coverings of any given architectural forms. An algorithm for coverings of considerable thickness, for instance thick slabs, turns out to be analogous to another algorithm used to describe multilayered surface coverings with small or huge rises. The problem of approximation of multilayered sandwich-type coatings was only painstakingly solved in Marcinkowski, (2003), despite assumed simplifications such as crosswise symmetry of structure (Fig. 1). By deforming normal, multi-node regular elements, new elements in curvilinear coordinate system were obtained.

It seems that this operation could yield desirable results only for thin-layered coverings of small elevation; but overall, practical value of the solution is evaluated as dissatisfactory. For instance, it is by no means practical nor justified to analyze and design covers of thickness t = 0,635mm with core thickness h_r = 11,430 mm, taking into account production process measurement toleration of any construction materials, as well as their thickness regulation methods.

Moreover, the accepted assumption that thickness of the layers in the covering surface can be achieved with tolerance t = ±0,0001mm is purely academic. Be that as it may, the methods employed for analyzing architectural forms of elevated coverings, such as multi-curve covering of a large spread shown in Fig. 2, based on (Noor and Kim, 1996), are indeed worthwhile and call for further investigation. A covering of any given thickness can be thus studied with well-founded claims for practical applicability of the achieved solutions, even in the cases where variable mass of construction material is an essential and indispensable factor. The authors of the present paper wish to present the analysis algorithms proving positive aspects of analyzing constructions freely heterogeneous in their structure by changing the discretization class from 2D to 3D.

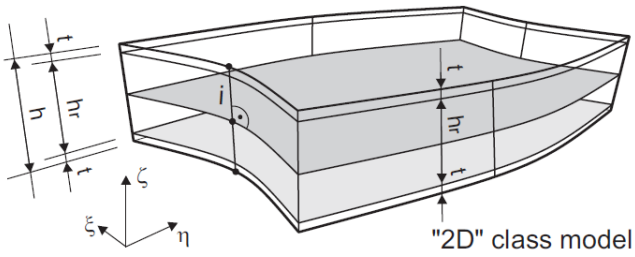

Fig. 1. Scientific interpretation of symmetrically layered sandwich type coating

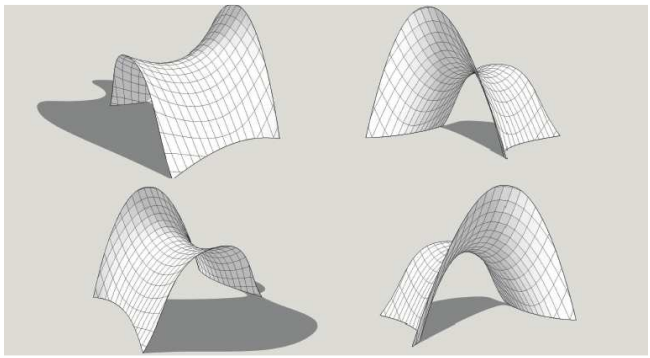

Fig. 2. An elevated covering of a large spread

2. CROSSWISE DISCRETIZATION OF ELEMENTS IN THE PERSPECTIVE OF VARIABLE ANALYSIS PARAMETERS

While the problem of developing methods for analysis of spatial elements remains still relevant, the number of publications offering practically applicable solutions and algorithms is relatively small. Among others, the issue of spatial analysis was addressed in Michalczuk and Tribiłło, (2002). The crucial factor determining the value of results obtained for crosswise heterogeneous structures is the node density in the grid discretizing thickness $h(z)$ of an element. It seems reasonable to generate the grid with constant node distance h_i; accordingly, relying on the fact that $h(z) = h_i \cdot s$, the tests could be created to estimate the discretization error of, among others, a circular slab freely supported along its circumference (Fig. 3). By acting on the middle surface in the layer $h(z) = h_i \cdot (s/2)$ with the load q, a classical closed solution is obtained and the acceptable error margin Δw_d can be established during the discretization to suit the practical applicability of the expected results (Vilberg and Abdulwahab, 1997). For the established error $\Delta w_d \leq 0{,}01 \cdot (gb^4)(64D^2)$, the satisfactory precision is achieved with the thickness parameter $s = 20$, which is proved by the results in Tab.1, and illustrated by the function drawn in Fig. 4.

Essentially, a faultless solution is obtained with the parameter s = 40, which is illustrated by the following results:

$\Delta w(\xi{=}0{,}000) = 0{,}001 \cdot (qb^4)/64D << \Delta w_d$,

$\Delta w(\xi{=}0{,}133) = 0{,}001 \cdot (qb^4)/64D << \Delta w_d$,

$\Delta w(\xi{=}0{,}583) = 0{,}000 \cdot (qb^4)/64D << \Delta w_d$,

$\Delta w(\xi{=}0{,}917) = 0{,}000 \cdot (qb^4)/64D << \Delta w_d$.

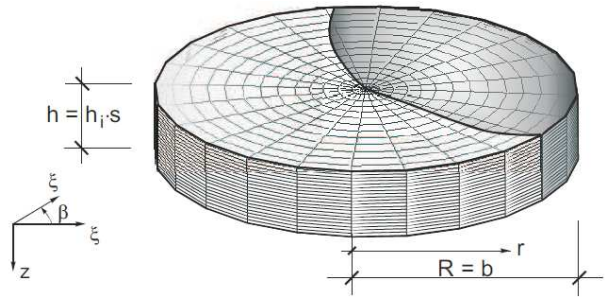

Fig. 3. Discrete model of a circular slab

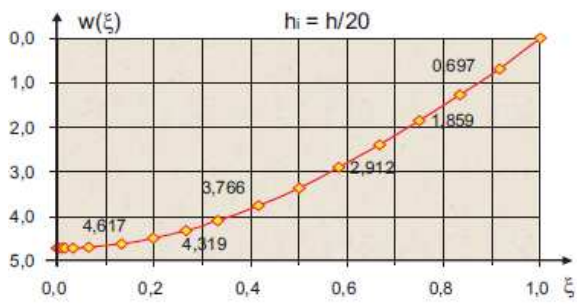

Fig. 4. Results of the solution for the circular slab with the grid density s = 20

Tab. 1. Results of the solution for the circular slab with the grid density $s = 20$

ξ = r / R	0,00000	0,00500	0,01000
w (ξ) ·(qb^4)/64D	4,720285	4,720138	4,719698
ξ = r / R	0,01667	0,03333	0,06667
w (ξ) ·(qb^4)/64D	4,718677	4,713799	4,694335
ξ = r / R	0,13333	0,20000	0,26667
w (ξ) ·(qb^4)/64D	4,616848	4,491538	4,318911
ξ = r / R	0,33333	0,41667	0,50000
w (ξ) ·(qb^4)/64D	4,100396	3,765554	3,367379
ξ = r / R	0,58333	0,66667	0,75000
w (ξ) ·(qb^4)/64D	2,911802	2,406222	1,859450
ξ = r / R	0,83333	0,91667	1,00000
w (ξ) ·(qb^4)/64D	1,280466	0,696812	0,00000

3. GENERALIZATION OF A CROSSWISE HETEROGENEOUS STRUCTURE

The principal idea of the generalization involves analyzing a crosswise heterogeneous covering structure made of various materials M_j, j = 1, 2, 3, …, each of them having different density, elasticity, and boundary conditions "BC". This kind of approach is graphically presented in Fig. 5.

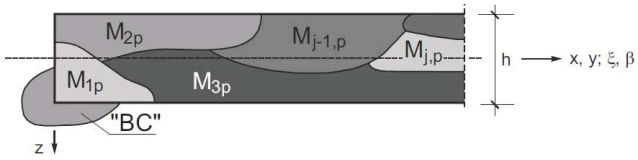

Fig. 5. Generalized structure of a crosswise heterogeneous covering "p" composed of materials M_j

When performing the discretization of a spatial figure of a covering, its construction materials can be interpreted as functions:

$$M_{vj} = M_j(\rho, g, E, \nu)_j \tag{1}$$

of the parameters: ρ_j – material's density; g_z – acceleration resulting from the inertia field in the Z-axis direction, E_j – material's modulus of elasticity, ν_j – Poisson number.

For static problems, the force-balance equations in the nodes consider also gravitational forces, represented by the product of density ρ and acceleration g_z, and marked with the $\mathbf{M_S}$ vector. The elastic features of masses can be expressed by a complex function which takes into account, for instance, material's strength. This is shown by the relation

$$E = F(f_c), \tag{2}$$

f_c denoting here material's compressive stress resistance.

The relation (2) has not been widely studied, but for its interpretation the formula

$$F(f_c) = 9{,}5(f_{ck} + 8)^{1/3} = E_{cm}, \tag{3}$$

can be accepted; incidentally, the formula describes the average secant modulus of elasticity of concrete often used in designing processes. Such relationships from the field of concrete mechanics can be employed in numerical analysis algorithms. The value of function (2) can be constant for a wide range of materials. As an example of unchangeable modulus of elasticity E_S, steel of classes A-0, A-I, A-II, A-III, A-IIIN produced in Poland can be mentioned.

Algorithms of numerical analysis of 3D elements formulated in (Michalczuk and Tribiłło, 2002) are used in a generalized form, specifying the approximate norm criteria allowing construction design, usually taking values of generalized *M*, *N*, *Q* type forces or the criteria justified by the stress conditions σ_i = 1, 2, 3, in the three-dimensional space.

Empirical and hypothetical norm stress distribution used to determine cross-section load-bearing capacity can be eliminated by solving the mathematical model taking into account function (1) only. From among several analyzed models, the results of the analysis for the slab shown in Fig. 3 are presented, taking advantage of the previously documented calculations of grid density which would allow for elimination of discretization errors.

The algorithm used with the model is similar for any given coordinate system, and the problem is solved by interpreting stresses in a mixed coordinate system (ξ, β, z). A discretized model of the slab is formed as shown in Fig. 3, with the stress $q(\xi, \beta)$ applied to surfaces of discrete elements of upper layer as can be seen in Fig. 6. The properties of construction materials of the crosswise heterogeneous structure can be expressed for j = 2 as:

$$M_{1p} = M_p(\rho_1, g, E_1, \nu_1), \tag{4}$$

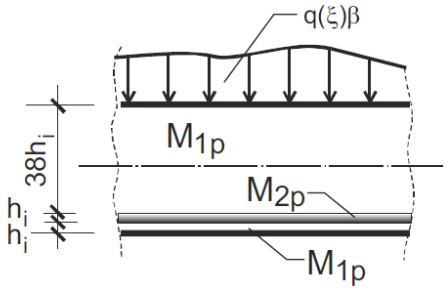

Fig. 6. Section of a crosswise heterogeneous slab with $j = 2$

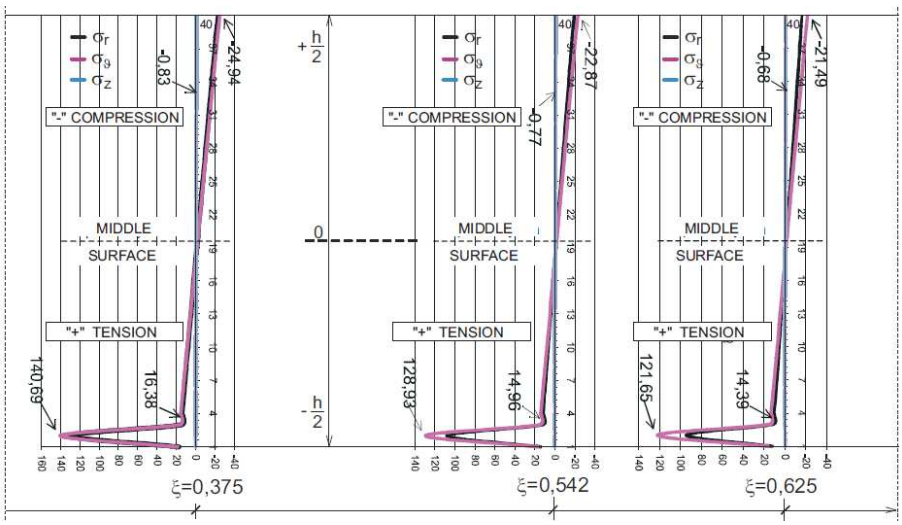

Fig. 7. Stress analysis results $\sigma_r(\xi)$, $\sigma_v(\xi)$, $\sigma_z(\xi)$ in the parameter structure (4) with $j = 2$

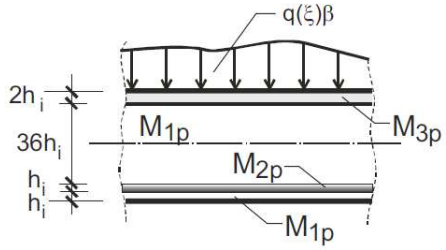

Fig. 8. Crosswise heterogeneous slab with $j = 3$

The equations are solved by calculating stresses σ_r, σ_v, σ_z, in units (q), and the solution is found within $0 \le \xi \le 1$ interval for any given value of R. It is assumed that g = 10m/s^2; $\nu_1 = \nu$ =0,2; k = 1; $E_1 = E$; c = 8; a = 3; $\rho_1 = \rho$; $\rho_2 = 3\rho$; $q(\xi, \beta) = q$.

The actual stress distribution seems to be different from the empirical norm assumptions in reinforced concrete constructions; this conclusion is further substantiated by the stress functions as drawn in Fig. 7.

From the technological point of view, there is a common problem of designing layered-concrete slabs which are constrained by concerns related to use of erected constructions and not infrequently to transport systems. The mathematical model for the parameter j = 3 clearly justifies nonlinear stress distributions in a crosswise heterogeneous structure (Jing Liu and Forster, 2000). Accordingly, the slab presented in Fig. 6 can be augmented with the material $M_{3p} = M_p$ (1,5ρ_j,g,2E,ν) as illustrated in Fig. 8. Practical aspects of the model construction and the parameters M_{3p} are formulated following contemporary, realistic criteria of development of materials technology. The curves of non-

linear functions of local stress distributions have increased; values of the function are shown in Fig. 9. The models generated with a grid density s = 40 ensure the positive evaluation of discretization criteria for j = 3, and the grids with higher density are proper for solving problems where $j > 3$.

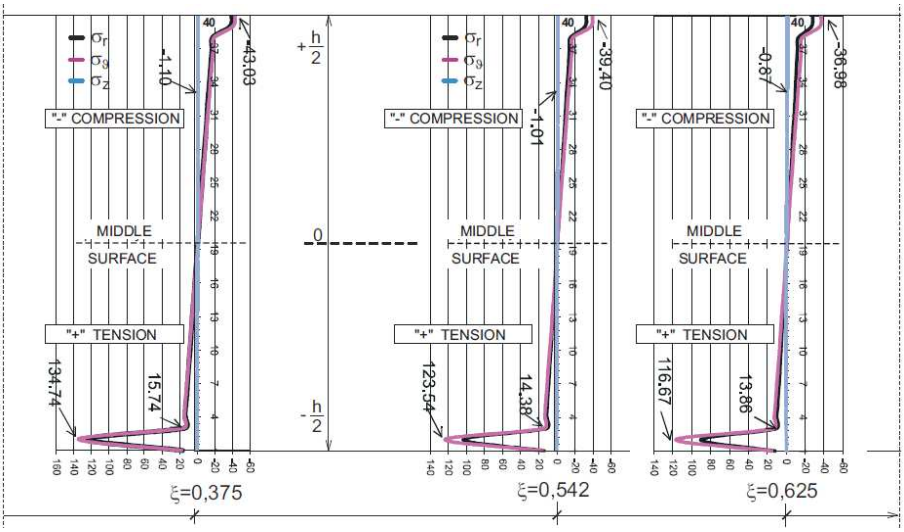

Fig. 9. Stress analysis results $\sigma_r(\xi)$, $\sigma_v(\xi)$, $\sigma_z(\xi)$ in structure (4) augmented with parameters M_{3p}, j = 3

The properly-designed and dense enough grid constitutes a practical justification for the inseparability of deformation and tension, and ensuring the force-balancing conditions in several thousands of the spatial grid nodes is, in engineering, a strong basis for practical interpretation of results in terms of continuous functions (Lo, 1985, 1988).

4. SUMMING-UP

The results published in the present paper confirm the claim that analysis of layered elements by changing the 2D class models into the appropriate 3D class models can be effective. The authors have backed up their assumptions with convincing calculations conducted for crosswise heterogeneous structures. The most crucial aspect of the analysis involved obtaining correct and sufficiently precise stress distribution functions in materials of various parameters and elastic properties, also accounting for density of the medium and characteristics of gravitational field. These non-linear functions can lay mathematical foundations for determining of limited load-bearing capacity of the analyzed section, which is often contradictory with empirical criteria used ,for instance, in analysis of atypical, reinforced concrete elements, particularly under complex stress conditions. Contemporary progress in computer technology justifies the change in the point of view on reduction of the model class. The generalizations allowing for conducting of both synthesis and analysis processes with algorithms of transition from 2D into 3D classes involve employing algorithms for solving huge sets of equations.

REFERENCES

1. **Jing Liu, Forster S. J.** (2000), A three-dimensional finite element model for confined concrete structures, *Computer and Structures*, No 77.
2. **Lo S. H.** (1985), A new mesh generation for arbitrary planar domains, *International Journal for Numeric Methods in Engineering*, Vol. 21.
3. **Lo S.H.** (1988), Finite elements generation over curved surface. *Computer and Structures*, Vol. 29, No 5.
4. **Marcinkowski J.** (2003), Geometrically nonlinear static analysis of sandwich plates and shells. *Journal of Theoretical and Applied Mechanics*, Vol. 41, No 3.
5. **Michalczuk P., Tribiłło R.** (2002), Spatial models of solid buildings. *Scientific Brochures – Bialystok University of Technology*, No 22, (in Polish).
6. **Noor A. K., Kim Y. H.** (1996), Buckling and postbuckling of composite panels with cutouts subjected to combined edge shear and temperature change, *Computer and Structures*, Vol. 60, No 2.
7. **Vilberg N.E., Abdulwahab F.** (1997), Terror estimation with postprocessed finite elements solutions. *Computer and Structures*, Vol. 64, No 1.

ANALIZA STRUKTUR POPRZECZNIE NIEJEDNORODNYCH W WARUNKACH ZMIENNYCH PARAMETRÓW MATERIAŁÓW KONSTRUKCYJNYCH

Streszczenie: Na tle analizowanych w literaturze technicznej elementów warstwowych a także konstrukcji grubych i wykorzystania uproszczeń umożliwiających rozwiązanie struktur modeli klas 2D, opublikowano wyniki rozwiązań uzyskiwanych odmiennie przez uogólnienie problemów do klas 3D. Wskazano na technikę szacowania błędu i kształtowania gęstości siatki umożliwiającej uzyskanie żądanej, uzasadnionej technicznie dokładności obliczeń. W publikowanych kryteriach rozwiązanie wielkich układów równań umożliwiło uzyskanie praktycznie ciągłych wartości funkcji złożonych stanów naprężeń. Zamieszczone niektóre charakterystyczne przykłady wskazują na możliwość wykorzystania algorytmów na przykład w niejednorodnych strukturach konstrukcji żelbetowych.

GENERATION OF FRICTIONAL HEAT DURING UNIFORM SLIDING OF TWO PLANE-PARALLEL STRIPS

Michał KUCIEJ*

*Faculty of Mechanical Engineering, Bialystok University of Technology, 45C Wiejska Street, Bialystok, 15-351, Poland

m.kuciej@pb.edu.pl

Abstract: The thermal problem of friction for a tribosystem consisting of two plane-parallel strips is studied. It is assumed that the relative sliding speed is constant. The convective cooling on free surfaces of strips and the heat transfer through a contact surface are considered, too. The evolution of the contact temperature and its spatial distribution in materials of frictional pair such as aluminum/steel, was investigated.

1. INTRODUCTION

The evolution and distribution of temperature in a plane-parallel strip/the semi-space tribosystem, at sliding with a constant speed have been investigated in articles (Yevtushenko and Kuciej, 2009a; Yevtushenko et al., 2009), and with a constant deceleration – in articles (Yevtushenko and Kuciej, 2009b, 2010a). The corresponding solution with a time-dependent contact pressure has been obtained in article (Yevtushenko et al., 2011). The influence of the duration of increase in pressure from zero (at the initial moment of time) to nominal value (at the moment of stop) on the temperature for a friction pair metal-ceramic strip/cast iron semi-space has been studied in article (Yevtushenko et al., 2010). The distribution of the thermal stresses for the same friction couple has been investigated in article (Yevtushenko and Kuciej, 2010b). The analytical solution of the contact problem with frictional heat generation for a two-element tribosystem – the composite strip sliding on a surface of the homogeneous semi-space – have been obtained in article (Kuciej, 2011a, 2011b).

In the present article we investigate the transient temperature distribution in tribosystem consisting of two plane-parallel strips. We assumed that the heat contact of the strips is imperfect, and on its outer surfaces there are convective heat exchange with environment, according to the Newton's law. The exact solution of the problem is obtained by method of separation of variables.

2. STATEMENT OF THE PROBLEM

The problem of contact interaction of plane-parallel strips of thickness $d_i, i = 1,2$ is under consideration. The scheme of contacting bodies is shown in Fig. 1. The strips are compressed by the normal pressure p_0, applied to their outer surfaces. In the initial time moment $t = 0$ the relative sliding of the strips begins with constant speed V_0 in the direction of y-axis of a Cartesian coordinate system $Oxyz$. The sliding is accompanied by frictional heat generation on a contact plane $z = 0$. The sum of the intensities of the frictional heat fluxes directed into each component of friction pair is equal to the specific friction power $q_0 = fV_0p_0$ (f is a frictional coefficient) and the thermal contact of the strips is imperfect – the heat transfer between the contact surfaces of the strips takes place. On the outer surfaces $z = d_1$ and $z = -d_2$ of the strips the convective heat exchange with the environment occurs. It is assumed that the contact heat transfer coefficient h and the coefficients of the heat exchange $h_i, i = 1,2$ are constant. All the values and parameters which refer to strips in the further considerations will have bottom indexes $i = 1,2$.

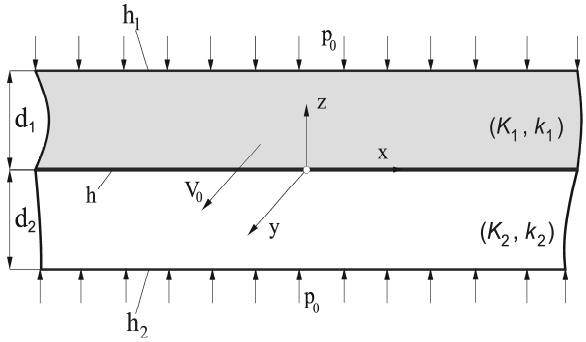

Fig. 1. Scheme of the contact problem

In such statement, the transient temperature $T_i(z,t)$, $i = 1,2$ fields in strips can be found, from the solution of a boundary-value problem of heat conduction:

$$\frac{\partial^2 T_1^*(\zeta,\tau)}{\partial \zeta^2} = \frac{\partial T_1^*(\zeta,\tau)}{\partial \tau}, \quad 0 < \zeta < 1, \tau > 0, \tag{1}$$

$$\frac{\partial^2 T_2^*(\zeta,\tau)}{\partial \zeta^2} = \frac{1}{k^*}\frac{\partial T_2^*(\zeta,\tau)}{\partial \tau}, -d^* < \zeta < 0, \tau > 0, \tag{2}$$

$$K^* \frac{\partial T_2^*}{\partial \zeta}\bigg|_{\zeta=0-} - \frac{\partial T_1^*}{\partial \zeta}\bigg|_{\zeta=0+} = 1, \quad \tau > 0, \tag{3}$$

$$K^*\left.\frac{\partial T_2^*}{\partial\zeta}\right|_{\zeta=0-}+\left.\frac{\partial T_1^*}{\partial\zeta}\right|_{\zeta=0+}+ \\ +\mathrm{Bi}[T_2^*(0,\tau)-T_1^*(0,\tau)]=0,\ \tau>0, \tag{4}$$

$$\left.\frac{\partial T_1^*}{\partial\zeta}\right|_{\zeta=1}+\mathrm{Bi}_1T_1^*(1,\tau)=0,\quad \tau>0, \tag{5}$$

$$K^*\left.\frac{\partial T_2^*}{\partial\zeta}\right|_{\zeta=-d^*}-\mathrm{Bi}_2T_2^*(-d^*,\tau)=0,\quad \tau>0, \tag{6}$$

$$T_1^*(\zeta,0)=0,\ 0\le\zeta\le1,\ T_2^*(\zeta,0)=0,\ -d^*\le\zeta\le0\,. \tag{7}$$

$$\zeta=\frac{z}{d_1},\ \tau=\frac{k_1t}{d_1^2},\ d^*=\frac{d_2}{d_1},\ K^*=\frac{K_2}{K_1},\ k^*=\frac{k_2}{k_1}, \tag{8}$$

$$T_0=\frac{q_0d_1}{K_1},\ \mathrm{Bi}=\frac{\mathrm{h}d_1}{K_1},\ \mathrm{Bi}_i=\frac{\mathrm{h}_id_1}{K_1},\ T_i^*=\frac{T_i-T_s}{T_0},\ i=1,2\,,$$

where K is a coefficient of thermal conductivity and k is a coefficient of thermal diffusivity.

3. SOLUTION TO THE PROBLEM

The complete solution to a boundary-value problem of heat conduction (1)–(7) we shall present in the form:

$$T_1^*(\zeta,\tau)=\theta_1(\zeta)+\Theta_1(\zeta,\tau)\,,\ 0\le\zeta\le1\,,\ \tau\ge0\,, \tag{9}$$

$$T_2^*(\zeta,\tau)=\theta_2(\zeta)+\Theta_2(\zeta,\tau)\,,\ -d^*\le\zeta\le0\,,\ \tau\ge0\,, \tag{10}$$

where the stationary components $\theta_i(\xi),\ i=1,2$ are given as:

$$\theta_1(\zeta)=a_1\zeta+b_1,\ 0\le\zeta\le1, \\ \theta_2(\zeta)=a_2\zeta+b_2,\ -d^*\le\zeta\le0, \tag{11}$$

$$a_i=\frac{\hat a_i}{a}\,,\ b_1=-\left(1+\frac{1}{\mathrm{Bi}_1}\right)a_1\,,\ b_2=\left(d^*+\frac{K^*}{\mathrm{Bi}_2}\right)a_2\,, \tag{12}$$

$$\hat a_1=-\mathrm{Bi}_1[K^*\mathrm{Bi}_2+(K^*+d^*\mathrm{Bi}_2)\mathrm{Bi}], \\ \hat a_2=\mathrm{Bi}_2[\mathrm{Bi}_1+(1+\mathrm{Bi}_1)\mathrm{Bi}], \tag{13}$$

$$a=2K^*\mathrm{Bi}_1\mathrm{Bi}_2+[K^*(\mathrm{Bi}_1+\mathrm{Bi}_2)+ \\ +(K^*+d^*)\mathrm{Bi}_1\mathrm{Bi}_2]\mathrm{Bi}, \tag{14}$$

and the dimensionless transient temperatures $\Theta_i(\xi,\tau),\ i=1,2$ are taken as the solution of the following homogeneous boundary-value problem:

$$\frac{\partial^2\Theta_1^*(\zeta,\tau)}{\partial\zeta^2}=\frac{\partial\Theta_1^*(\zeta,\tau)}{\partial\tau},\quad 0<\zeta<1,\ \tau>0, \tag{15}$$

$$\frac{\partial^2\Theta_2^*(\zeta,\tau)}{\partial\zeta^2}=\frac{1}{k^*}\frac{\partial\Theta_2^*(\zeta,\tau)}{\partial\tau},\ -d^*<\zeta<0,\ \tau>0, \tag{16}$$

$$K^*\left.\frac{\partial\Theta_2^*}{\partial\zeta}\right|_{\zeta=0-}-\left.\frac{\partial\Theta_1^*}{\partial\zeta}\right|_{\zeta=0+}=0,\quad \tau>0, \tag{17}$$

$$K^*\left.\frac{\partial\Theta_2^*}{\partial\zeta}\right|_{\zeta=0-}+\left.\frac{\partial\Theta_1^*}{\partial\zeta}\right|_{\zeta=0+}+ \\ +\mathrm{Bi}[\Theta_2^*(0,\tau)-\Theta_1^*(0,\tau)]=0,\ \tau>0, \tag{18}$$

$$\left.\frac{\partial\Theta_1^*}{\partial\zeta}\right|_{\zeta=1}+\mathrm{Bi}_1\Theta_1^*(1,\tau)=0,\quad \tau>0, \tag{19}$$

$$K^*\left.\frac{\partial\Theta_2^*}{\partial\zeta}\right|_{\zeta=-d^*}-\mathrm{Bi}_2\Theta_2^*(-d^*,\tau)=0,\quad \tau>0, \tag{20}$$

$$\Theta_1^*(\zeta,0)=-\theta_1(\zeta),\quad 0\le\zeta\le1, \\ \Theta_2^*(\zeta,0)=-\theta_2(\zeta),\quad -d^*\le\zeta\le0. \tag{21}$$

The solution of the transient heat conduction problem (15)–(21) is constructed by method of separation of variables as (Ozisik, 1980):

$$\Theta_1(\zeta,\tau)=\sum_{n=1}^{\infty}C_n\Phi_{1,n}(\zeta)e^{-\lambda_n^2\tau}\,,\ 0\le\zeta\le1\,,\ \tau\ge0\,, \tag{22}$$

$$\Theta_2(\zeta,\tau)=\sum_{n=1}^{\infty}C_n\Phi_{2,n}(\zeta)e^{-\lambda_n^2\tau}\,,\ -d^*\le\zeta\le0\,,\ \tau\ge0\,, \tag{23}$$

where:

$$\Phi_{1,n}(\zeta)=A_{1,n}^*\sin(\lambda_n\zeta)+B_{1,n}^*\cos(\lambda_n\zeta)\,, \tag{24}$$

$$\Phi_{2,n}(\zeta)=A_{2,n}^*\sin\left(\frac{\lambda_n}{\sqrt{k^*}}\zeta\right)+B_{2,n}^*\cos\left(\frac{\lambda_n}{\sqrt{k^*}}\zeta\right), \tag{25}$$

$$A_{1,n}^*=(\mathrm{Bi}_1\cos\lambda_n-\lambda_n\sin\lambda_n)\times \\ \times\left\{\varepsilon\lambda_n\left[\varepsilon\lambda_n\sin\left(\frac{d^*\lambda_n}{\sqrt{k^*}}\right)-\mathrm{Bi}_2\cos\left(\frac{d^*\lambda_n}{\sqrt{k^*}}\right)\right]-\right. \\ \left.-\mathrm{Bi}\left[\varepsilon\lambda_n\cos\left(\frac{d^*\lambda_n}{\sqrt{k^*}}\right)+\mathrm{Bi}_2\sin\left(\frac{d^*\lambda_n}{\sqrt{k^*}}\right)\right]\right\}, \tag{26}$$

$$A_{2,n}^*=[\lambda_n(\lambda_n\sin\lambda_n-\mathrm{Bi}_1\cos\lambda_n)- \\ -\mathrm{Bi}(\lambda_n\cos\lambda_n+\mathrm{Bi}_1\sin\lambda_n)]\times \\ \times\left[\varepsilon\lambda_n\sin\left(\frac{d^*\lambda_n}{\sqrt{k^*}}\right)-\mathrm{Bi}_2\cos\left(\frac{d^*\lambda_n}{\sqrt{k^*}}\right)\right], \tag{27}$$

$$B^*_{1,n} = (\lambda_n \cos\lambda_n + \mathrm{Bi}_1 \sin\lambda_n)\times$$
$$\times\left\{\varepsilon\lambda_n\left[\mathrm{Bi}_2\cos\left(\frac{d^*\lambda_n}{\sqrt{k^*}}\right)-\varepsilon\lambda_n\sin\left(\frac{d^*\lambda_n}{\sqrt{k^*}}\right)\right]\right. \quad (28)$$
$$\left.+\,\mathrm{Bi}\left[\varepsilon\lambda_n\cos\left(\frac{d^*\lambda_n}{\sqrt{k^*}}\right)+\mathrm{Bi}_2\sin\left(\frac{d^*\lambda_n}{\sqrt{k^*}}\right)\right]\right\},$$

$$B^*_{2,n} = [\lambda_n(\mathrm{Bi}_1\cos\lambda_n - \lambda_n\sin\lambda_n)+$$
$$+\,\mathrm{Bi}(\lambda_n\cos\lambda_n + \mathrm{Bi}_1\sin\lambda_n)]\times \quad (29)$$
$$\times\left[\varepsilon\lambda_n\cos\left(\frac{d^*\lambda_n}{\sqrt{k^*}}\right)+\mathrm{Bi}_2\sin\left(\frac{d^*\lambda_n}{\sqrt{k^*}}\right)\right],$$

$$C_n = -\frac{r_n}{R_n},\ n = 1,2,\ldots, \quad (30)$$

$$r_n = k^* r_{1,n} + K^* r_{2,n},\ R_n = 0.5(k^* R_{1,n} + K^* R_{2,n}), \quad (31)$$

$$r_{i,n} = a_i I_{i,n} + b_i J_{i,n}, i = 1,2, \quad (32)$$

$$I_{1,n} = A^*_{1,n}(\lambda_n^{-1}\sin\lambda_n - \cos\lambda_n)+$$
$$+\,B^*_{1,n}[\sin\lambda_n - \lambda_n^{-1}(1-\cos\lambda_n)], \quad (33)$$

$$I_{2,n} = A^*_{2,n}\left[\frac{\sqrt{k^*}}{\lambda_n}\sin\left(\frac{d^*\lambda_n}{\sqrt{k^*}}\right)-d^*\cos\left(\frac{d^*\lambda_n}{\sqrt{k^*}}\right)\right]+$$
$$+\,B^*_{2,n}\left\{\frac{\sqrt{k^*}}{\lambda_n}\left[1-\cos\left(\frac{d^*\lambda_n}{\sqrt{k^*}}\right)\right]-d^*\sin\left(\frac{d^*\lambda_n}{\sqrt{k^*}}\right)\right\}, \quad (34)$$

$$R_{1,n} = {A^*_{1,n}}^2(\lambda_n - \sin\lambda_n\cos\lambda_n)+$$
$$+\,2A^*_{1,n}B^*_{1,n}\sin^2\lambda_n + {B^*_{1,n}}^2(\lambda_n + \sin\lambda_n\cos\lambda_n), \quad (35)$$

$$R_{2,n} = {A^*_{2,n}}^2\left[\frac{d^*\lambda_n}{\sqrt{k^*}}-\sin\left(\frac{d^*\lambda_n}{\sqrt{k^*}}\right)\cos\left(\frac{d^*\lambda_n}{\sqrt{k^*}}\right)\right]-$$
$$-\,2A^*_{2,n}B^*_{2,n}\sin^2\left(\frac{d^*\lambda_n}{\sqrt{k^*}}\right)+ \quad (36)$$
$$+\,{B^*_{2,n}}^2\left[\frac{d^*\lambda_n}{\sqrt{k^*}}+\sin\left(\frac{d^*\lambda_n}{\sqrt{k^*}}\right)\cos\left(\frac{d^*\lambda_n}{\sqrt{k^*}}\right)\right],$$

$$J_{1,n} = A^*_{1,n}(1-\cos\lambda_n) + B^*_{1,n}\lambda_n^{-1}\sin\lambda_n, \quad (37)$$

$$J_{2,n} = A^*_{2,n}\left[\cos\left(\frac{d^*\lambda_n}{\sqrt{k^*}}\right)-1\right]+B^*_{2,n}\sin\left(\frac{d^*\lambda_n}{\sqrt{k^*}}\right), \quad (38)$$

and $\lambda_1, \lambda_2, \ldots, \lambda_n, \ldots$ are the real roots of the characteristic equation:

$$\Delta(\lambda) = \varepsilon[2\lambda(\lambda\sin\lambda - \mathrm{Bi}_1\cos\lambda)-$$
$$-\,\mathrm{Bi}(\lambda\cos\lambda + \mathrm{Bi}_1\sin\lambda)]\times$$
$$\times\left[\varepsilon\lambda\sin\left(\frac{d^*\lambda}{\sqrt{k^*}}\right)-\mathrm{Bi}_2\cos\left(\frac{d^*\lambda}{\sqrt{k^*}}\right)\right]- \quad (39)$$
$$-\,\mathrm{Bi}(\lambda\sin\lambda - \mathrm{Bi}_1\cos\lambda)\times$$
$$\times\left[\varepsilon\lambda\cos\left(\frac{d^*\lambda}{\sqrt{k^*}}\right)+\mathrm{Bi}_2\sin\left(\frac{d^*\lambda}{\sqrt{k^*}}\right)\right]=0,$$

where:

$$\varepsilon = \frac{K^*}{\sqrt{k^*}}. \quad (40)$$

4. SOLUTION TO THE PROBLEM

The numerical results have been obtained for the friction couple an first strip – aluminum ($K_1 = 209\mathrm{Wm^{-1}K^{-1}}$, $k_1 = 8{,}6\cdot10^{-5}\mathrm{m^2s^{-1}}$) and a second strip – steel ($K_2 = 22\mathrm{Wm^{-1}K^{-1}}$, $k = 1{,}1\cdot10^{-5}\mathrm{m^2s^{-1}}$). The friction conditions are: $p_0 = 1\mathrm{MPa}$, $V_0 = 10\mathrm{ms^{-1}}$, $f = 0{,}45$ and $d_1 = 5$ mm. The choice of materials above were taken from the article (Yevtushenko and Kuciej, 2009a), in which the solution was obtained to the heat conduction problem of friction, where the strip is sliding with the constant speed on the surface of the semi-space.

The results, presented in Figs. 2–4 have been obtained in the case of the perfect thermal contact of strips at $h \to \infty$ ($\mathrm{Bi} \to \infty$) for two variants of boundary conditions on the outer surface $z = d_1$ of the aluminum strip: a) thermal isolation at $h_1 \to \infty$ ($\mathrm{Bi}_1 \to \infty$) or b) maintaining initial temperature at $h_1 \to \infty$ ($\mathrm{Bi}_1 \to \infty$).

Evolutions of temperature (22)–(25), (30) on the contact surface $z = 0$ for two strips and for three values of steel strip thickness d_2 are presented in the Fig. 2. Thermal isolation on the outer surface of aluminum strip causes increase of the contact surface temperature, nearly 2.5 times in relation to the temperature obtained in the case of maintenance of the initial temperature at the same surface $z = d_1$. At the beginning of sliding temperature increases rapidly at the contact surface, and after some time it reaches a steady state. Time to reach the steady state temperature increases with increase of the steel strip thickness. After exceeding value $d_2 = 20$ mm, the contact temperature and duration of reaching the steady state temperature do not change.

Influence of the coefficient of heat exchange on the contact surfaces h(Bi) on the contact surface temperature of the aluminum and steel strips is shown in Fig. 3. It should be noted that the parameter h is the value inversely proportional to the thermal resistance of the contact area. The highest jump of temperature on the contact surface is observed when $h \to 0$ (thermal resistance is greatest). The value of the temperatures difference is also influenced by the boundary conditions on the outer surface of the strips i. e. Bi_1. Reducing the thermal resistance of the contact surface causes the alignment of the contact temperature between strips. For $\mathrm{Bi} > 15$, the thermal contact

between the strips becomes perfect. The value of the temperatures difference at the contact surface depends also on the boundary conditions on the outer surface of aluminum strip: maximum difference is about 250℃ at $\mathrm{Bi}_1 \to 0$ (Fig. 3a) and 180℃ (Fig. 3b) at $\mathrm{Bi}_1 \to \infty$). The largest temperature changes are noticeable for the steel strip. However, in the case of the aluminum strip after increase of the initial temperature, together with a slight increase Biot number Bi, the temperature gets a steady state.

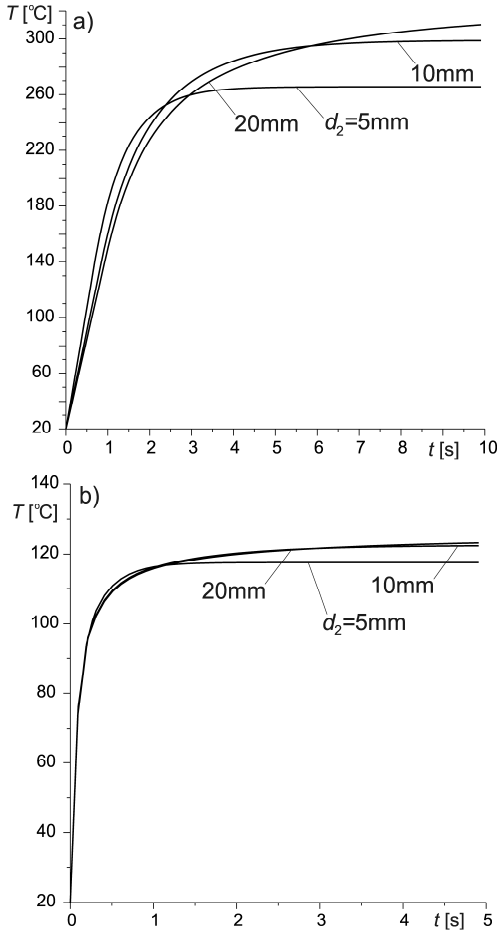

Fig. 2. Evolution of the temperature $T(0,t)$ on the contact surface at $d_1 = 5\mathrm{mm}$, $\mathrm{Bi} \to \infty$, $\mathrm{Bi}_2 \to \infty$, for three values $d_2 = 5\mathrm{mm}, 10\mathrm{mm}, 15\mathrm{mm}$; a) $\mathrm{Bi}_1 \to 0$; b) $\mathrm{Bi}_1 \to \infty$

To verify exactly the presented solutions for the strip/strip system, analysis of the evolution of dimensionless temperature $T^*(0,\tau)$ for four values d^* of relative thickness of strips, calculations were carried out for two tribosystems aluminum /steel and steel /aluminum (Fig. 4). In the case when the first strip is made of aluminum, the contact temperature decreases while thickness of the steel strip increases. However, in other case, when the first strip is made of steel, the temperature on the contact surface increases while thickness of the aluminum strip increases, too. For the first aluminum strip at $d^* \geq 2$ and steel strip at $d^* \geq 4$ as was established above (in dimension form), one of the strip (the second one), can be replaced with the semi-space (Fig. 4). The presented curves for $d^* = 4$ in Fig. 5 corresponds closely with the results shown in Fig. 4 in the article (Yevtushenko and Kuciej, 2009a) for the strip/semi-space tribosystem.

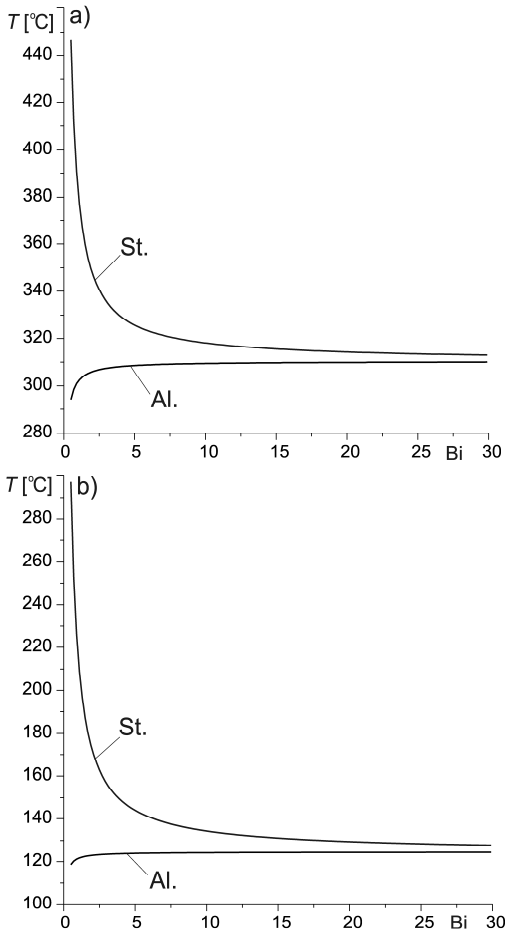

Fig. 3. Dependence of the temperatures $T_i(0,t), i = 1,2$ on the contact surfaces on Biot number Bi at $d_1 = 5\mathrm{mm}$, $d_2 = 20\mathrm{mm}$, $\mathrm{Bi} \to \infty$, $\mathrm{Bi}_2 \to \infty$, $t = 10\mathrm{s}$: a) $\mathrm{Bi}_1 \to 0$; b) $\mathrm{Bi}_1 \to \infty$

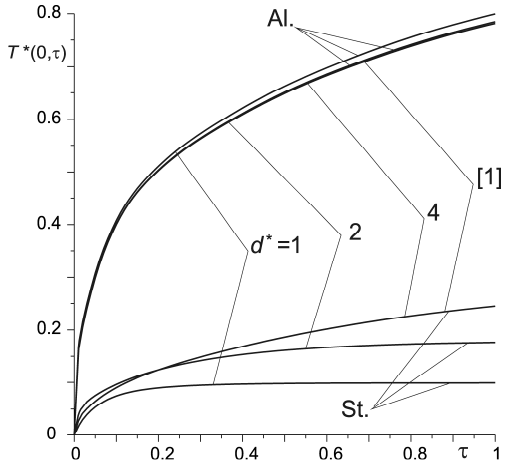

Fig. 4. Evolution of the dimensionless contact temperature $T^*(0,\tau)$ for four values d^* at $\mathrm{Bi} \to \infty$, $\mathrm{Bi}_1 = 10$, $\mathrm{Bi}_1 \to \infty$

5. CONCLUSIONS

We obtained the analytical solution to the heat conduction problem of friction for the two-element tribosystem. The heat exchange through the contact surfaces of strips and convective cooling on their outer surfaces are taken into account.

We carried out the numerical analysis for the aluminum /steel tribosystem, where one strip is sliding on the surface of the other strip with the constant velocity. We investigated the influence of strip thickness, the contact conductivity and the type of boundary conditions on the evolution of the temperature on the contact surface. This allowed us to determine the limits of the thickness of the strip, at which the solution may be replaced with a suitable solution for the strip /semi-space tribosystem (Yevtushenko and Kuciej, 2009a). For the relative thickness strip $d^* \geq 3$ we can calculate temperature from the solution obtained for strip /semi-space, but for smaller values of d^* calculation of temperature should be carried out using the solution for the strip /strip system.

REFERENCES

1. **Kuciej M.** (2011a), Nonstationary frictional heat production in the course of sliding of a composite layer over the surface of a half space, *Materials Science*, Vol. 47, 52-60.
2. **Kuciej M.** (2011b), Investigation of the temperature field induced in the process of friction of a composite pad and a homogeneous disc, *Int. Comm. Heat Mass Transfer*, Vol. 38, 16-24.
3. **Ozisik M .N.** (1980), *Heat conduction*, J. Wiley and Sons, New York.
4. **Yevtushenko A., Kuciej M.** (2010b), Temperature and thermal stresses in a pad/disc during braking, *Applied Thermal Engineering*, Vol. 30, 354-359.
5. **Yevtushenko A. A., Kuciej M.** (2009a), Influence of convective cooling on the temperature in a frictionally heated strip and foundation, *Int. Comm. Heat Mass Transfer*, Vol. 36, 129-136.
6. **Yevtushenko A. A., Kuciej M.** (2009b), Temperature in a frictionally-heated ceramic-metal patch and cast iron disc during braking, *Num. Heat Transfer, Part A*, Vol. 56, 97-108.
7. **Yevtushenko A. A., Kuciej M.** (2010a), Influence of the convective cooling and the thermal resistance on the temperature of the pad/disc tribosystem, *Int. Comm. Heat Mass Transfer*, Vol. 37, 337-342.
8. **Yevtushenko A. A., Kuciej M., Rozniakowska M.** (2009), The contact heat transfer between the plane-parallel strip and the semi-infinite foundation, *Int. Comm. Heat Mass Transfer*, Vol. 36, 787-793.
9. **Yevtushenko A. A., Kuciej M., Yevtushenko O.O.** (2010), Influence of the pressure fluctuations on the temperature in pad/disc tribosystem, *Int. Comm. Heat Mass Transfer*, Vol. 37, 978-983.
10. **Yevtushenko A. A., Kuciej M., Yevtushenko O.O.** (2011), Influence of the temporal profile of the contact pressure on the maximal temperature in pad/disc tribosystem, *Heat Mass Transfer*, Vol. 47, 1113-1120.

Acknowledgement: The present paper is financially supported by the National Science Centre of Poland (project No 2011/01/B/ST8/07446).

STICK-SLIP CONTACT PROBLEM OF TWO HALF PLANES WITH A LOCAL RECESS

Nataliya MALANCHUK[*], Andrzej KACZYŃSKI[**]

[*]Pidstryhach Institute for Applied Problems of Mechanics and Mathematics, Naukova Str. 3-b, 79060 Lviv, Ukraine
[**]Faculty of Mathematics and Information Science, Warsaw University of Technology, Plac Politechniki 1, 00-061 Warsaw

natamalanchuk@gmail.com, akacz@mini.pw.edu.pl

Abstract: A plane problem of frictional contact interaction between two elastic isotropic half planes one of which possesses a single shallow recess (depression) is examined in the case of successive application of remote constant normal and shear forces. The loads steps (compression, and next monotonically increasing shear loads) lead to the main contact problem with an unknown stick-slip boundary determined by the Amonton-Coulomb law. It is reduced to a Cauchy-type singular integral equation for the tangential displacement jump in the unknown sliding region. Its size is derived from an additional condition of finiteness of shear stresses at the edges of the slip zone. Considerations are carried out for some general shape of the recess. Analytical results with the characterization of the considered contact are given and illustrated for the certain form of the initial recess.

1. INTRODUCTION

The frictional effects during contact of elastic solids are the subject of the investigation of many authors. Interest to such problems is stimulated by applied requests of engineering, tribology, geophysics, bulding industry and biomechanics. Amonton-Coulomb's classical friction law is used widely in engineering applications involving contact (Kragelsky et al.; 1982). In this law, it is assumed that two contacting bodies either stick ($|s| < fp$) or slip ($|s| = fp$) to each other, where f is the constant coefficient of friction, s and p are the magnitudes of tangential and normal traction due to friction. If the equality $|s| = fp$ is valid for the whole contact region, then we have the case of sliding friction. Realistic frictional contact problems reduce to finding the correct size and location of the stick-slip boundary depending on given loading conditions.

In literature dealing with contact problems (Barber and Ciavarella; 2000) the overwhelming majority of works consider the contact of bodies with non-conforming boundaries (see classification by Johnson; 1985). The problem to be considered is referred to contact frictional problems involving interactions of bodies with conformable boundaries. Such a kind of the interaction taking into account the absence of local contact caused by the presence of local small geometric perturbations of initial boundaries is less investigated although it is quite typical for many contacting joints. In this field basic research regarding frictionless contact has been carried on and documented (see, for example, Shvets et al., 1996; Kaczyński and Monastyrskyy, 2002; Monastyrskyy and Kaczyński, 2010; and references therein). Similar problems involving friction were considered by Martynyak and Kryshtafovych (2000), Kryshtafovych and Matysiak (2001) and in a series of papers by Martynyak et al. (2005, 2006).

The present paper is devoted to analyze the behavior of a complete contact couple formed by two semi-infinite elastic planes with the presence of a small surface recess under the combination of remote normal and shear forces. This is achieved in two steps: first, by solving the full stick contact problem and next, using it to pose and solve the stick-slip problem with an unknown slip zone defined by the Amonton-Coulomb law. Research is performed for some general shape of the recess. The final results are given and illustrated in particular case.

2. FORMULATION OF THE PROBLEM

The problem under study involves the investigation of frictional contact between two homogeneous elastic half-planes D_2 (upper) and D_1 (lower) made of the same isotropic material. Referring to the Cartesian coordinate system Oxy the boundary of D_2 is rectilinear whereas the boundary of D_1 has a small deviation in the form of the sloping recess located in a segment $x \in [-b, b]$ as shown in Fig. 1a. Accordingly, the shape of the lower half-plane boundary is described by the smooth function $r(x)$ given by the formula:

$$r(x) = \begin{cases} -r_0\left(1 - x^2/b^2\right)^{n+1/2}, & |x| \le b, \\ 0, & |x| > b, \end{cases} \tag{1}$$

where r_0 and $2b$ are maximal depth and length of the recess, $n = 1,2,...$ is a natural parameter, and the assumption $0 < r_0/b \ll 1$ is made.

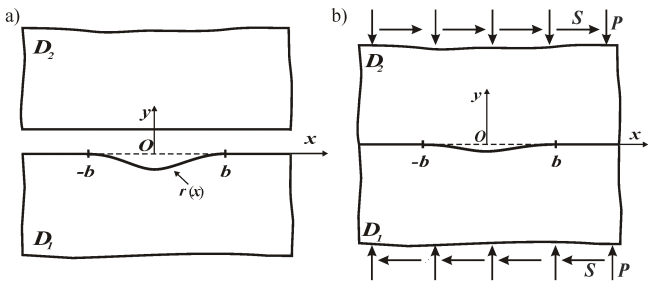

Fig. 1. Sketch of interaction of half-planes:
a) before contact; *b*) in full contact

The following phases of constant loading at infinity are considered: first, normal compressive forces P leading to full contact and subsequently, monotonically increasing shear forces S giving rise to partial sliding.

Similar to the well-known Cattaneo procedure used in partial slip contact under combined normal and tangential loading (Ciavarella; 1998), the full stick contact problem is solved and analyzed first in order to establish correctly the conditions in formulation of the main stick-slip contact problem of interest.

3. FULL-STICK CONTACT PROBLEM

Consider the problem of full-stick contact of the half-planes without slip (Fig. 1b) characterized by the boundary conditions at the interface $y = 0$, $|x| < \infty$:

$$\begin{aligned} &\sigma_y^-(x,0) = \sigma_y^+(x,0), \qquad \tau_{xy}^-(x,0) = \tau_{xy}^+(x,0), \\ &u^-(x,0) - u^+(x,0) = 0, \;\; v^-(x,0) - v^+(x,0) = -r(x), \end{aligned} \tag{2}$$

and at infinity:

$$\begin{aligned} &\sigma_y(x,\pm\infty) = -P, \quad \tau_{xy}(x,\pm\infty) = S, \\ &\sigma_x(\pm\infty, y) = 0, \qquad \tau_{xy}(\pm\infty, y) = S. \end{aligned} \tag{3}$$

Here and subsequently, σ_y, σ_x, τ_{xy} – the components of stresses; u, v – the components of the displacement vector; superscripts "–" and "+" denote the limit values of functions at the interface of the half planes D_1 and D_2.

Additionally, the requirement of the non-negativity constraint of the contact pressure:

$$p(x) = -\sigma_y^-(x,0) \ge 0\,, \;\; |x| < \infty \tag{4}$$

has to be used to determine a condition for the complete contact.

Following the solution of the above problem employing the well-known technique of analytical continuation (Muskhelishvili; 1953) and given in Martynyak et al. (2005 a, b), the stresses and displacements in the bodies are expressed by means of the derivative of the function r(x) as follows:

$$\begin{aligned} &\sigma_x(x,y) + \sigma_y(x,y) = 4\,\mathrm{Re}\left[\Phi_l(z)\right] - P, \\ &\sigma_y(x,y) - i\,\tau_{xy}(x,y) = \Phi_l(z) - \Phi_l(\overline{z}) + \\ &\qquad\qquad - (z-\overline{z})\overline{\Phi_l'(z)} - P - i\,S, \\ &2G\frac{\partial}{\partial x}\left[u(x,y) + iv(x,y)\right] = \kappa\Phi_l(z) + \Phi_l(\overline{z}) + \\ &\qquad\qquad - (z-\overline{z})\overline{\Phi_l'(z)} + \frac{3-\kappa}{4}P, \end{aligned} \tag{5}$$

in which:

$$\begin{aligned} &\Phi_1(z) = -\Phi_2(z) = \frac{(-1)^{l+1}G}{\pi(1+\kappa)}\int_{-b}^{b}\frac{r'(t)\,dt}{t-z}, \\ &z = x + iy \in D_l, \;\; l = 1,2, \end{aligned} \tag{6}$$

and G is the shear modulus, v is Poisson's ratio, $\kappa = 3 - 4v$ is Kolosov's constant.

Inserting (1) into (6) and using (5) gives the normal stresses on the contact surface for $|x| \le b$:

$$\sigma_y^{\pm}(x,0) = \frac{2Gr_0(2n+1)}{(1+\kappa)b}\left(\frac{(2n-1)!!}{2^n n!} + \mathrm{P}^{(a)}(x)\right) - P \tag{7}$$

and for $|x| > b$:

$$\begin{aligned} &\sigma_y^{\pm}(x,0) = \frac{2Gr_0(2n+1)}{(1+\kappa)b}\times \\ &\times\left(\frac{(2n-1)!!}{2^n n!} + (-1)^{n+1}\left|\frac{x}{b}\right|\left(\frac{x^2}{b^2}-1\right)^{n-\frac{1}{2}} + \mathrm{P}^{(a)}(x)\right) - P, \end{aligned} \tag{8}$$

where:

$$\mathrm{P}^{(a)}(x) = a_2\left(\frac{x}{b}\right)^2 + a_4\left(\frac{x}{b}\right)^4 + \ldots + a_{2n}\left(\frac{x}{b}\right)^{2n},$$

$$a_{2(j+1)} = \sum_{k=j+1}^{n}\frac{(-1)^k n!}{k!(n-k)!}\cdot\frac{(2k-2j-3)!!}{(2k-2j-2)!!},$$

$$j = 0,1,2,\ldots,n-1, \;\; (-1)!! = 1, \;\; 0!! = 1.$$

Accordingly, the shear stresses are:

$$\tau_{xy}^{\pm}(x,0) = S\,, \;\; x \in (-\infty, +\infty). \tag{9}$$

By observing that the global maximum of RHS in relation (7) is achieved at $x = 0$, we obtain from (4) the inequality for the value of the normal pressure P that satisfies full contact of the bodies

$$P \ge \frac{Gr_0(2n+1)(2n-1)!!}{2^{n-1}n!(1+\kappa)b}. \tag{10}$$

According to the Amonton-Coulomb law, the increase in the shear forces S does not affect in sliding if the contact stresses satisfy the condition $|\tau_{xy}| < f|\sigma_y|$, i. e.

$$S < f\left(P - \frac{Gr_0(2n+1)(2n-1)!!}{2^{n-1}n!(1+\kappa)b}\right). \tag{11}$$

Thus, the slip occurs when this condition is violated.

4. STICK-SLIP CONTACT PROBLEM

Let us consider now the case opposite to (11):

$$S \ge f\left(P - \frac{Gr_0(2n+1)(2n-1)!!}{2^{n-1}n!(1+\kappa)b}\right) \tag{12}$$

that is the condition of sliding in the vicinity of the point $x = 0$. So we are faced with the stick-slip problem in which we assume from the loading and geometry symmetry that there exists a region of local sliding $|x| < c$ (see Fig. 2). Note that the half-length of the slip zone c is unknown.

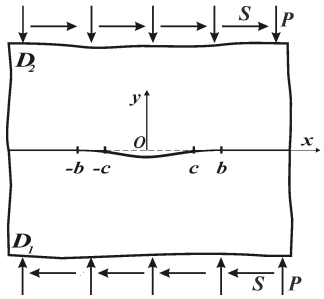

Fig. 2. Interaction of half-planes in stick-slip contact

For the present non-trivial problem we have the same boundary conditions at infinity given by (3) and the following contact condition on $y = 0$:

$$\sigma_y^-(x,0) = \sigma_y^+(x,0),\ \ |x| < \infty,$$
$$\tau_{xy}^-(x,0) = \tau_{xy}^+(x,0),\ \ |x| < \infty,$$
$$\left|\tau_{xy}^-(x,0)\right| = f\left|\sigma_y^-(x,0)\right|,\ \ |x| < c, \tag{13}$$
$$u^-(x,0) - u^+(x,0) = 0,\ \ |x| \ge c\,,$$
$$v^-(x,0) - v^+(x,0) = -r(x),\ \ |x| < \infty.$$

Moreover, $sign\left(\tau_{xy}^-\right) = signS$ is chosen from the slip behavior.

To determine an unknown coordinate c of the stick-slip boundary, we will use the condition ensuring finiteness of the contact shear stresses at the edges of the slip zone:

$$\lim_{x\to\pm c}\left|\tau_{xy}(x,0)\right| < +\infty\,. \tag{14}$$

In dealing with solution to the above posed problem we use the commonly employed method of intercontact gap functions, devised by Martynyak (1985).

First we solve an auxiliary problem with the same boundary conditions of the original problem but instead of $(13)_3$ we set:

$$u^-(x,0) - u^+(x,0) = U(x),\quad |x| \le c. \tag{15}$$

Results for the normal and tangential stresses at the nominal interface are expressed as (Martynyak et al.; 2005b):

$$\sigma_y^-(x,0) = \frac{2G}{\pi(1+\kappa)}\int_{-b}^{b}\frac{r'(t)dt}{t-x} - P,$$
$$\tau_{xy}^-(x,0) = -\frac{2G}{\pi(1+\kappa)}\int_{-c}^{c}\frac{U'(t)dt}{t-x} + S \tag{16}$$

and comparing with the solution of stick problem we see that the formula for normal stresses doesn't change. Now substitution (16) into relationships $(13)_3$ yields a singular integral equation for the unknown derivative of function $U'(x)$:

$$\frac{1}{\pi}\int_{-c}^{c}\frac{U'(t)dt}{t-x} = \frac{1+\kappa}{2G}(S - fP) + \frac{(2n+1)r_0 f}{b}\left(\frac{(2n-1)!!}{2^n n!} + \mathrm{P}^{(a)}(x)\right),\ \ |x| < c \tag{17}$$

By utilizing the theory of singular equations with Cauchy kernels (Muskhelishvili; 1953), it is possible to obtain the solution of this equation in the class of functions with the natural conditions of continuity of the relative tangential shift $U(\mp c) = 0$. Omitting details, we focus only on the expressions for the tangential stresses at the interface boundary:

$$\tau_{xy}^-(x,0) = fP - \frac{2G(2n+1)\,r_0 f}{(1+\kappa)b}\left(\frac{(2n-1)!!}{2^n n!} - \mathrm{P}^{(w)}(x)\right),\ \ |x| \le c,$$
$$\tau_{xy}^-(x,0) = fP - \frac{2G(2n+1)\,r_0 f}{(1+\kappa)b}\left(\frac{(2n-1)!!}{2^n n!} - \mathrm{P}^{(w)}(x)\right) + \left[S - fP + \frac{2G(2n+1)r_0 f}{(1+\kappa)b}\left(\frac{(2n-1)!!}{2^n n!} - \mathrm{P}^{(d)}(x)\right)\right]\times$$
$$\times\frac{|x|}{\sqrt{x^2 - c^2}},\quad |x| > c, \tag{18}$$

where:

$$\mathrm{P}^{(d)}(x) = d_0 + d_2(x/c)^2 + d_4(x/c)^4 + \ldots + d_{2n}(x/c)^{2n},$$
$$d_0 = \sum_{k=1}^{n}\frac{(2k-3)!!}{(2k)!!}a_{2k}(c/b)^{2k},$$
$$d_{2j} = -a_{2j}\left(\frac{c}{b}\right)^{2j} + \sum_{k=j+1}^{n}\frac{(2k-2j-3)!!}{(2k-2j)!!}a_{2k}\left(\frac{c}{b}\right)^{2k},\ j = 1,2,\ldots,n-1,$$
$$d_{2n} = -a_{2n}(c/b)^{2n},$$
$$\mathrm{P}^{(w)}(x) = w_0 + w_2(x/c)^2 + w_4(x/c)^4 + \ldots + w_{2n}(x/c)^{2n},$$
$$w_{2j} = \sum_{m=j}^{n}\frac{d_{2m}(2m-2j-1)!!}{(2m-2j)!!},\quad j = 0,1,2,\ldots,n.$$

In order to close the problem in hand, we have to modify the above expressions to guarantee their finiteness in the vicinity of the point $\mp c$ according to the condition (14). By analyzing relation (18), it is sufficient to fulfil the equation:

$$S - fP + \frac{(2n+1)Gr_0 f(2n-1)!!}{2^{n-1}n!b(1+\kappa)} - \frac{2G(2n+1)r_0 f}{(1+\kappa)b}\mathrm{P}^{(d)}(c) = 0\,. \tag{19}$$

In point of fact, this equation determines the unknown location c of the stick-slip boundary.

5. RESULTS

To analyze and illustrate the behavior of the contact couple on the basis of the obtained analytic solution to the considered problem, calculations are performed for the special form of the recess given by the formula (1) for $n = 3$.

Considering first the stick contact problem, we find the normal contact stresses from relations (7) and (8):

$$\sigma_y^{\pm}(x,0)=\frac{14Gr_0}{(1+\kappa)b}\left(\frac{5}{16}-\frac{15}{8}\frac{x^2}{b^2}+\frac{5}{2}\frac{x^4}{b^4}-\frac{x^6}{b^6}\right)-P,\quad |x|\le b,$$

$$\sigma_y^{\pm}(x,0)=\frac{14Gr_0}{(1+\kappa)b}\times$$

$$\times\left(\frac{5}{16}+\left|\frac{x}{b}\right|\left(\frac{x^2}{b^2}-1\right)^{\frac{5}{2}}-\frac{15}{8}\frac{x^2}{b^2}+\frac{5}{2}\frac{x^4}{b^4}-\frac{x^6}{b^6}\right)-P,\ |x|>b. \quad (20)$$

Graphs of contact stresses are given in Fig. 3. The solid line corresponds to $f|\bar{\sigma}_y|(\bar{\sigma}_y=\sigma_y/G)$ and the dashed lines 1, 2, 3 – to tangential stresses $\bar{\tau}_{xy}(\bar{\tau}_{xy}=\tau_{xy}/G)$ over the contact line $\bar{x}=x/b$ under pressure $\bar{P}=2\cdot10^{-4}$ $(\bar{P}=P/G)$, friction coefficient $f=0{,}1$, maximal depth of the recess $\bar{r}_0=r_0/b=10^{-4}$ and Poisson's ratio $\nu=0{,}2$ for some values of shear stresses $\bar{S}$ $(\bar{S}=S/G)$: $1-\bar{S}=2\cdot10^{-6}$; $2-\bar{S}=6{,}328\cdot10^{-6}$; $3-\bar{S}=15\cdot10^{-6}$.

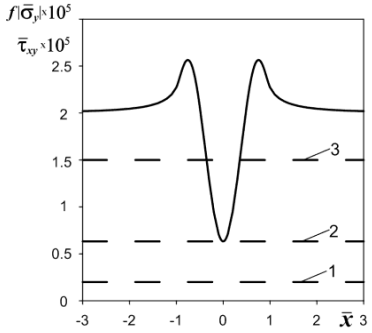

Fig. 3. Distributions of the contact stresses

In view of (11), if $P\ge\frac{35Gr_0}{8b(1+\kappa)}$, then the half planes are in full contact. By analyzing the relations (7) and (8) we see that the increase of the shear forces S does not in sliding if $S<\frac{35Gr_0}{8b(1+\kappa)}$ that follows from the condition $|\bar{\tau}_{xy}<f|\sigma_y|$. This shows the dashed line 1. However, according to the Amonton-Coulomb law, for $S\ge f(P-\frac{35Gr_0}{8b(1+\kappa)})$ sliding starts in the vicinity of the point $\bar{x}=0$ (see the dashed lines 2, 3).

Now we pass to the main contact problem involving sliding in the unknown region $|x|\le c$ for loads:

$$S\ge f\left(P-\frac{35Gr_0}{8(1+\kappa)b}\right).$$

The governing singular integral equation (17) for the unknown derivative of function $U'(x)$ has the form:

$$\frac{1}{\pi}\int_{-c}^{c}\frac{U'(t)dt}{t-x}=\frac{1+\kappa}{2G}(S-fP)+$$
$$+\frac{7r_0f}{b}\left(\frac{5}{16}-\frac{15}{8}\frac{x^2}{b^2}+\frac{5}{2}\frac{x^4}{b^4}-\frac{x^6}{b^6}\right),|x|<c. \quad (21)$$

The desired solution is:

$$U(x)=\sqrt{c^2-x^2}\left[-\frac{1+\kappa}{2G}(S-fP)+\frac{fr_0}{b}\left(\frac{5}{16}\frac{c^6}{b^6}-\frac{21}{16}\frac{c^4}{b^4}+\right.\right.$$
$$+\frac{35}{16}\frac{c^2}{b^2}-\frac{35}{16}++\frac{3}{8}\frac{c^4}{b^4}\frac{x^2}{b^2}+\frac{1}{2}\frac{c^2}{b^2}\frac{x^4}{b^4}+\frac{x^6}{b^6}-\frac{7}{4}\frac{c^2}{b^2}\frac{x^2}{b^2}+$$
$$\left.\left.+\frac{35}{8}\frac{x^2}{b^2}-\frac{7}{2}\frac{x^4}{b^4}\right)\right],\ |x|<c. \quad (22)$$

From the equation (19), having now the form:

$$S-fP+\frac{35Gr_0f}{8b(1+\kappa)}-\frac{14Gr_0f}{(1+\kappa)b}\left(\frac{15}{16}\frac{c^2}{b^2}-\frac{15}{16}\frac{c^4}{b^4}+\frac{5}{16}\frac{c^6}{b^6}\right)=0,$$

we find the half-length of the slip zone – parameter c:

$$c=b\sqrt{1-\sqrt[3]{\frac{8(1+\kappa)b}{35Gfr_0}(fP-S)}} \quad (23)$$

and then the tangential contact stresses are:

$$\tau_{xy}^{-}(x,0)=fP+\frac{14Gr_0f}{(1+\kappa)b}\left(-\frac{5}{16}+\frac{15}{8}\frac{x^2}{b^2}-\frac{5}{2}\frac{x^4}{b^4}+\frac{x^6}{b^6}\right),\quad |x|\le c,$$

$$\tau_{xy}^{-}(x,0)=fP+\frac{14Gr_0f}{(1+\kappa)b}\left(-\frac{5}{16}+\frac{15}{8}\frac{x^2}{b^2}-\frac{5}{2}\frac{x^4}{b^4}+\frac{x^6}{b^6}\right)+$$
$$-\frac{7Gr_0f}{(1+\kappa)b}\left(\frac{15}{4}-\frac{5}{2}\frac{c^2}{b^2}-5\frac{x^2}{b^2}+\frac{3}{4}\frac{c^4}{b^4}+\frac{c^2}{b^2}\frac{x^2}{b^2}+2\frac{x^4}{c^4}\right)\times$$
$$\times\left|\frac{x}{b}\right|\sqrt{\frac{x^2}{b^2}-\frac{c^2}{b^2}},\quad |x|>c. \quad (24)$$

By assuming the threshold value $S=fP$ we have $c=b$ and the shear contact stresses become:

$$\tau_{xy}^{\pm}(x,0)=fP+\frac{14Gfr_0}{(1+\kappa)b}\left(\frac{x^6}{b^6}-\frac{5}{2}\frac{x^4}{b^4}+\frac{15}{8}\frac{x^2}{b^2}-\frac{5}{16}\right),\quad |x|\le b,$$

$$\tau_{xy}^{\pm}(x,0)=fP+\frac{14Gfr_0}{(1+\kappa)b}\left(\frac{x^6}{b^6}-\frac{5}{2}\frac{x^4}{b^4}+\frac{15}{8}\frac{x^2}{b^2}-\frac{5}{16}+\right.$$
$$\left.-\left|\frac{x}{b}\right|\left(\frac{x^2}{b^2}-1\right)^{5/2}\right),\quad |x|>b. \quad (25)$$

Since the condition $\tau_{xy}=f|\sigma_y|$ is satisfied at any point of the contact region, we have the case of sliding friction.

The results of numerical calculations are performed for the following dimensionless parameters:

$\bar{x}=x/b$, $\bar{r}_0=r_0/b$, $\bar{c}=c/b$, $\bar{U}=U/b$, $\bar{\sigma}_y=\sigma_y/G$, $\bar{\tau}_{xy}=\tau_{xy}/G$, $\bar{P}=P/G$, $\bar{S}=S/G$ and $f=0.1$, $\bar{r}_0=10^{-4}$, $\nu=0.2$.

Fig. 4 shows the distributions of the relative tangential shift of bodies boundaries $\bar{U}$ in the slip zone under the pressure $\bar{P}=2\cdot10^{-4}$ for the following values of the shear tractions $\bar{S}$:$1-\bar{S}=10^{-5}$; $2-\bar{S}=1{,}4\cdot10^{-5}$; $3-\bar{S}=1{,}8\cdot10^{-5}$; $4-\bar{S}=2\cdot10^{-5}$. The maximum value of the modulus of the relative tangential shift of boundaries increases with the shear tractions and reaches in the centre of the recess.

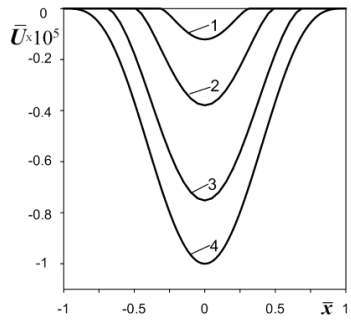

Fig. 4. Distributions of the relative tangential shift of bodies boundaries

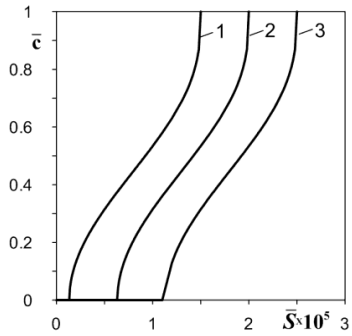

Fig. 5. Half-length of the slip zone versus the external shear forces

The nonlinear dependence of the half length of the slip size $\bar{c}$ on the shear forces $\bar{S}$ for some values of the pressure $\bar{P}$: $1-\bar{P}=1{,}5\cdot10^{-4}$; $2-\bar{P}=2\cdot10^{-4}$; $3-\bar{P}=2{,}5\cdot10^{-4}$ is shown in Fig. 5. The horizontal straight lines of the plots correspond to the case of the stick contact of the bodies. We can see that the zone of sliding becomes greater with increasing shear forces.

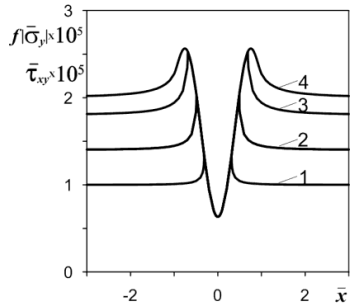

Fig. 6. Contact stresses in the stick-slip problem

Symmetric distributions of stresses for illustrating the behavior of the slip-stick contact are demonstrated in Fig. 6. A graph of $f|\bar{\sigma}_y|$ (curve 4) and graphs of tangential stresses $\bar{\tau}_{xy}$ (curves 1, 2, 3) versus $\bar{x}=x/b$ are given under the pressure $\bar{P}=2\cdot10^{-4}$ for the following values of the shear forces $\bar{S}$:1 – $\bar{S}=10^{-5}$; 2 – $\bar{S}=1{,}4\cdot10^{-5}$; 3 – $\bar{S}=1{,}8\cdot10^{-5}$. It is seen that the normal stresses have a global maximum near the edges of the recess at the points $\bar{x}=\mp0{,}76$. The maximum of tangential stresses is reached at the ends of the region of sliding. Moreover, the curves coincide in the slip zone $(-\bar{c},\bar{c})$. Outside this interval, the tangential stresses $\bar{\tau}_{xy}$ are less than $f|\bar{\sigma}_y|$ and monotonically decrease to the limiting values at infinity.

6. CONCLUSIONS

In the paper we have investigated the complete frictional contact of two half-planes containing local geometric perturbation of boundaries accounting for frictional slip under sequential remote normal and shear forces. The formulated stick-slip contact problem is reduced to the singular integral equation for the function of the relative tangential shift of bodies boundaries which is next solved with the determination of the size of sliding. On the basis of the analytical solution to the above-mentioned problem the dependences of slip zone length and contact stresses on applied loadings are analyzed.

REFERENCES

1. **Barber J.R., Ciavarella M.** (2000), Contact mechanics, *Int. J. Solids Struct.*, Vol. 37, No 1-2, 29-43.
2. **Ciavarella M.** (1998), The generalized Cattaneo partial slip plane contact problem. I – Theory, II – Examples, *Int. J. Solids Struct.*, Vol. 35, 2349-2378.
3. **Johnson K.L.** (1985), *Contact mechanics*, Cambridge University Press, Cambridge.
4. **Kaczyński A., Monastyrskyy B.** (2002), Contact problem for periodically stratified half-space and rigid foundation possessing geometrical surface defect, *J. Theor. Appl. Mech.*, Vol. 40, No. 4, 985-999.
5. **Kragelsky I.V., Dobychin M.N., Kombalov V.S.** (1982), *Friction and wear. Calculation methods*, Pergamon Press, Oxford.
6. **Kryshtafovych A.A,, Matysiak S.J.** (2001), Frictional contact of laminated elastic half-spaces allowing interface cavities. Part 1: Analytical treatment. Part 2: Numerical results, *Int. J. Numer. Anal. Meth. Geomech.*, Vol. 25, 1077–1099.
7. **Martynyak R. M.** (1985), Interaction of elastic bodies provided imperfect mechanical contact (in Ukrainian), *Mathematical Methods and Physicomechanical Fields*, Vol. 22, 89-92.
8. **Martynyak R.**, **Kryshtafovych A.** (2000), Friction contact of two elastic semiplanes with local surface depressions, *Friction and Wear*, Vol. 21, No. 4, 6-15.
9. **Martynyak R.**, **Malanchuk N., Monastyrskyy B.** (2005a), Elastic interaction of two half-planes provided partial slipping at the region of intersurface gap, *Mathematical Methods and Physicomechanical Fields*, Vol. 48, No. 3, 101-109.
10. **Martynyak R.**, **Malanchuk N., Monastyrskyy B.** (2005b), Shear of two half planes pressed to each other and containing a surface groove. Part 1. Full contact, *Materials Science*, Vol. 41, No. 2, 178-185.
11. **Martynyak R.**, **Malanchuk N., Monastyrskyy B.** (2006), Shear of two half planes pressed to each other and containing a surface groove. Part 2. Incomplete contact, *Materials Science*, Vol. 42, No. 4, 551-559.
12. **Monastyrskyy B., Kaczyński A.** (2010), Contact interaction of two elastic half spaces with circular groove, *Materials Science*, Vol. 46, No. 3, 336-347.
13. **Muskhelishvili N.I.** (1953), *Some basic problems of the mathematical theory of elasticity*, Noordhoff, Groningen.
14. **Shvets R.M., Martynyak R.M., Kryshtafovych A.A.** (1996), Discontinuous contact of an anisotropic half-plane and rigid base with disturbed surface, *Int. J. Engng. Sci.*, Vol. 34, No. 2, 183-200.

GRAIN SIZE DEPENDENCE OF CREEP LIFETIME MODELED BY MEANS OF CELLULAR AUTOMATA

Krzysztof NOWAK*

*Zakład Wytrzymałości Materiałów, Wydział Inżynierii Lądowej,
Politechnika Krakowska, ul. Warszawska 24, 31-155 Kraków

kn@limba.wil.pk.edu.pl

Abstract: Grain size dependence of creep is a complex relation. It can be increasing, decreasing or constant function accordingly to current conditions and material. It is a consequence of complex nature of microscopic mechanisms affecting creep. Some of them are analyzed in current paper by means of multiscale model, using simulation of damage development done by cellular automata technique. It was shown that enlarged sizes of grains, which promote development of intergranular microcracks, are compensated by reduced density of voids forming vacancies. Obtained in simulations grain size dependency follows experimentally observed dependency for small grains in dislocation creep range.

1. INTRODUCTION

1.1. Grain size dependency of creep rate

The phenomenon of creep of polycrystalline materials depends on number of parameters describing their microstructure. One of the most important is grain size. The dependency of steady-state creep rate (or minimum creep rate) on grain size was already largely studied. However, no unambiguous formula for this relation was obtained. It appears that many factors like material structure, temperature, loading level and also environment influence this relation (Boettner and Robertson, 1961).

It is known that for dislocation creep of pure metals rate of secondary creep does not depend on grain size (Dobrzański, 1996), but the majority of alloys exhibits minimum for that relation (Wilshire and Palmer, 2002). If the minimum creep rate is described by equation:

$$\dot{\varepsilon}_{\min} = B\sigma^n \left(\frac{1}{d}\right)^p \exp\left(\frac{-Q_C}{RT}\right), \tag{1}$$

where σ is applied stress, T is temperature, d is grain diameter, Q_c is creep activation energy, B, n, p are material constants, R is gas constant, then the grain size dependency is characterized by parameter p. It is equal to about -2 for large grains, i.e. if the grain is larger then the creep rate is larger, too. The grain boundaries form obstacles for dislocation motion therefore large grains (less borders less obstacles) allow for faster creep rate. For small grains p=1, so the dependency is reverse. The grain boundaries are sources of dislocations and vacancies. If the grains are smaller then there are more borders and more dislocations. The dependency is stronger (p=2) for diffusional creep at small loading level (Wilshire and Palmer, 2002).

The alloys exhibit also the dependency of creep index n (Eq. (1)) on grain size: for larger grains the creep rate dependency upon stress is stronger, and the value of n is larger (Wilshire and Palmer, 2002). Accurate tests showed that similar dependency comes out also for copper. E.g. for dislocation creep at temperature about 0,55 T_m (melting temperature) and for stresses larger than 20 MPa the value of index n is larger for larger grain sizes (see Tab. 1).

Tab. 1. Dependency of creep index n on grain size for copper

grain size [μm]	**temperature** [K]	**creep index** n	**reference**
30	723	4.17	Feltham and Meakin, 1959
40	723	4.48	Wilshire and Battenbough, 2007
100	728	5.24	Evans and Wilshire, 1993
450	723	5.84	Pahutova and others, 1971

These results cannot be used for setting the precise relation, as there are differences among laboratories and test conditions, but the tendency is obvious. Additionally, it can be noticed that the creep rate does not depend on grain size for the stress of about 50 MPa, whereas for smaller stress the smaller grain is the larger creep rate occurs.

1.2. Grain size dependency of time and strain to failure

There is much less experimental data for grain size relation of damage development in creep conditions. But, using the Monkman-Grant relation in form (Evans, 1984):

$$\dot{\varepsilon}_{\min}^{\beta} t_f = C, \tag{2}$$

where t_f is time to failure, β and C are material constants, the time to failure can be approximately evaluated. The relation (2) is very well experimentally confirmed, e.g. for copper in large temperature range (Feltham and Meakin, 1959, Wilshire and Battenbough, 2007). The value of β is changing from 0,8 to 1, and C from 0,003 to 0,6. On this basis it can be assumed that the grain size dependency of time to failure is reverse to the grain size dependency of creep rate.

More experimental data are available for the analysis of the strain to failure value. It is influenced to a greater extent by mechanisms of tertiary creep. According to Fleck and others (1970) a critical crack length (Griffith-Orowan) in comparison to grain size is crucial in determination of strain to failure for large grains. A crack can easily develop along one grain facet, but it is more difficult for this crack to pass from one facet to another. Therefore, if grain size is larger than critical size of crack the failure starts at the beginning of third period of creep and strain to failure is small. The mechanism of voids development is more important in determination of strain to failure for small grains (e.g. lesser than 100 μm in 700 K for copper, Fleck and others, 1970). As the participation of grain boundaries in the whole volume is greater for smaller grains and as grain boundaries are main sources of vacancies the volume fraction of voids is greater for them and thus the strain to failure is smaller.

2. MULTISCALE MODEL OF DAMAGE IN CREEP CONDITIONS

Analysis of grain size dependency of time to failure should include a number of mechanisms occurring in microstructure of material and influencing creep rate and damage development. Taking into account even the most important of these like dislocation climbing, pile-ups, annihilations, grain boundary sliding, nucleation and growth of cavities, crack development leads to very complex model and the analysis of it can be very cumbersome. Every mechanism has its own scale relevant to its subject. The size of single dislocation is about 10^{-10} m, void is about 10^{-6} m, grain - 10^{-4} m, and the size of crack can be comparable to size of construction. The proper analysis of grain size dependency requires multiscale modeling: connection of smaller models appropriate for particular scales (Ostoja-Starzewski, 2007). An example of such procedure is CAFE model of creep damage presented by Chrzanowski and Nowak (2009), Nowak (2011) and used in this analysis. This model consists of deformation model in macroscale, defined by Finite Element (FE) method, and damage model in microscale built using Cellular Automata (CA) technique.

Damage development process is the only one modeled here in microscale. As damage is discontinuous, discrete Cellular Automata are chosen as an appropriate tool for this process (Chrzanowski and Nowak, 2010). They allow for simulation in discrete manner of many processes progressing in material structure.

2.1. Microstructure of material

Microscopic processes are modeled within Representative Volume Element (RVE). It is very difficult to define RVE for damage process. According to Lemaitre and Dufailly (1987) it should be from 50 to 500 μm for metals and it is connected with sizes of defects. On the other side it is connected with material structure (e.g. RVE size is equal to 6-7 grains diameters after Hayhurst, 2005). The model analyzing different grain sizes should keep constant size of RVE with varying number of grains.

The polycrystalline structure of material is built in CA mesh using discrete Voronoi tessellation. First, the n_{seed} number of seed points is randomly distributed over RVE. Every seed point has its own state value allowing for differentiate the grains. Next, the grains growing procedure is applied until whole RVE is covered by cells belonging to particular grains. If the linear size of planar RVE is N_0 then mean grain diameter is:

$$d = N_0 \Big/ \sqrt{n_{seed}} \,. \tag{3}$$

Important state of cell to be distinguished by CA is *damage*. *Damaged cells* can move freely like vacancies or can aggregate into voids. Initial number of *damaged cells* is specified in relation to whole volume by parameter f_{v0}. At the beginning the *damaged cells* are distributed randomly over all RVE.

2.2. Damage model

Two main mechanisms of voids growth are implemented: diffusion of vacancies and deformation of material surrounding voids. Diffusional motion of vacancies is modeled by free moves of *damaged cells*. It is implemented In block neighborhood. All cells are divided into 2x2 blocks and *damaged cells* can change its position inside block randomly. In consecutive CA iteration the position of blocks is shifted so the *damaged cells* can move in any direction. If a *damaged cell* reaches another *damaged cell* especially at grain border they may coalescence into void. The process is controlled by surface energy criterion. The diffusion movement is possible only when it does not contribute to the growth of the value of J, defined as:

$$J = w_{d-m} l_{d-m} + w_{g-g} l_{g-g} \,, \tag{4}$$

where $l_{d\text{-}m}$, $l_{g\text{-}g}$ are lengths of borders between *damaged* and *undamaged* cells, and between two neighboring grains, respectively; $w_{d\text{-}m}$, $w_{g\text{-}g}$ are weight coefficients for these kinds of borders. To promote stability of the method the lengths are calculating in blocks enlarged by one cell in all directions (4x4). The diffusion rate is changed by T_{step} parameter. It is time period (in seconds) equivalent for one diffusion iteration.

The size of RVE is changed according to applied deformation. At beginning of every CA iteration this external deformation is compared with current size of RVE. If deformation exceeds the current size then dimensions of RVE measured in cells are changed accordingly. The deforma-

tion is stretched over cells according to procedure proposed by Matic and Geltmacher (2001) adapted to grain structure (Chrzanowski and Nowak, 2007). The grain boundaries are considered as weaker than grain interior stimulating development of intergranular cracks. Another mechanism connected with deformation is introduced by control of voids volume fraction. Precise density measurements show that it is decreasing with increasing creep strains (Boettner and Robertson, 1961). It is due to development of oids and changes of void volume fraction can be calculated from relative density changes. The strain dependency of void volume fraction (Eq. 5) proposed by Belloni and others (1977) is used in current model to control the number of *damaged cells* during deformation of RVE:

$$\rho = \rho_0\left(1 - H\varepsilon^{\gamma}\right), \tag{5}$$

where ρ, ρ_0 are mass density and initial mass density, ε is strain, H and γ are material parameters. The number of *damaged cells* related to deformation is very important for damage development process. When there are too little *damaged cells* then the effect of inhibited void growth is reached, but when there are lots of *damaged cells* the void growth is enhanced by deformation. In that way it simulates the real material behavior.

The aim of CA model is to determine the value of damage parameter (ω) as homogenized value for RVE. It is calculated as the maximum ratio of linear size of connected path of *damaged cells* to current size of RVE. The RVE is consider as fully damaged when damage parameter is equal to 1 and path of *damaged cells* joins two opposite sides of RVE.

2.3. Deformation model

Macroscopic strains are sum of instantaneous strains and creep strains. Creep strains are obtained numerically by FE method for constitutive equation (Nowak K., 2011):

$$\dot{\varepsilon}_c = B_1\varepsilon_c^{-2}\left(\frac{\sigma\left(1-\omega_0\right)}{1-\omega}\right)^{n_1}, \tag{6}$$

where ε_c is creep strain, σ is stress, B_1, n_1, ω_0 are parameters of deformation model. Damage parameter ω is obtained from CA model running in every Gauss point of FE mesh. Strains calculated according to Eq. (6) are used to determine current size of RVE in CA model. Parameters B_1, n_1 are fitted to primary period of creep curve, where damage can be neglected for real material. Parameter ω_0 in Eq. (6) compensates non-zero initial value of damage for CA model. It was necessary because non-zero initial value of f_{v0} parameter and large instantaneous (plastic) strain produce significant value of damage parameter already in early stages of simulation. The final failure is assumed when damage parameter reaches 1 in any Gauss point.

3. RESULTS

Analysis of grain size dependency has been performed using model described above. The model parameters have been suited to the results of creep experiment for copper in 823 K for grain size of 30 μm (Feltham and Meakin, 1959). The deformation model parameters were as follows: B_1=7.57E-24 (MPa)^{n_1}s^{-1}, n_1=9.76, ω_0=0.15. They were calculated from values of β parameter of primary strain equation reported by Feltham and Meakin (1959):

$$\varepsilon_c = \beta t^{1/3}, \tag{7}$$

where t is time.

The model uses structure described by N_0=641, n_{seed}=10. According to Eq. (3) it gives mean grain diameter d=202.7 cells. By comparison to experimental grain size (30 μm) the size of single cell can be estimated as 0.15 μm and RVE size as nearly 100 μm. The size of single cell can be regarded as size of smallest recognized void. The model of intergranular failure is implemented and voids can develop only along grain boundaries: $w_{d\text{-}m}$=0, $w_{g\text{-}g}$=1. Parameters of Eq. (5) were set to H=1.17 and γ=2.3. They were obtained by regression analysis of data for copper in temperatures 673 K - 823 K and stress range 21 MPa - 34 MPa (Boettner and Robertson, 1961). Remaining parameters of damage model were suited to secondary creep data: f_{v0}=0.006, T_{step}=0.25 s (see Fig. 1). The agreement of times to failure and strains to failure with experimental data was obtained.

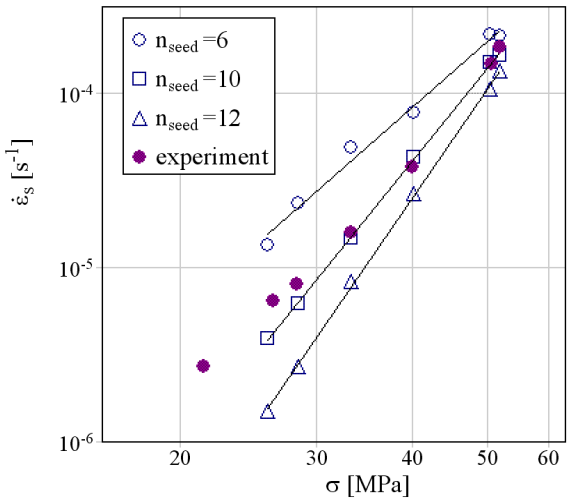

Fig. 1. Dependency of stationary creep rate on parameter n_{seed} – simulation results in comparison with experimental results (Cu at 823 K 30 μm mean grain size, Feltham and Meakin, 1959)

Next, the influence of parameter n_{seed} was examined. The simulations were performed for n_{seed}=6, 10 and 12, keeping other parameters constant (see Fig. 1). It corresponds to grain sizes: 39, 30, 27 μm. The creep rates are decreasing for decreasing grain sizes and the creep indexes n (Eq. 1) calculated as tangent of regression line at Fig. 1 are increasing (3.89, 5.49, 6.45, accordingly).

Results for time to failure are compatible with experimental relation (2). Times to failure are larger for smaller grains and the difference is greater for smaller stresses. This behavior is typical for large grain sizes as damage is growing faster for larger grains. The diffusion mechanism

of void growth is prevailing for small stresses and number of *damaged cells* in relation to lengths of all borders in RVE becomes deciding parameters in damage development simulation.

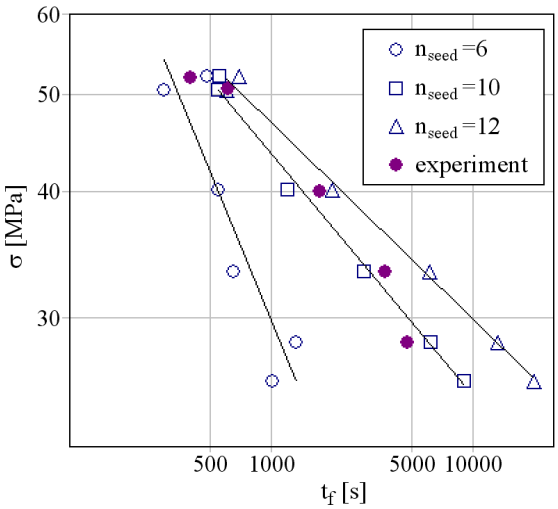

Fig. 2. Dependency of time to failure on parameter n_{seed} – simulation results in comparison with experimental results (Cu at 823 K 30 μm mean grain size, Feltham and Meakin, 1959)

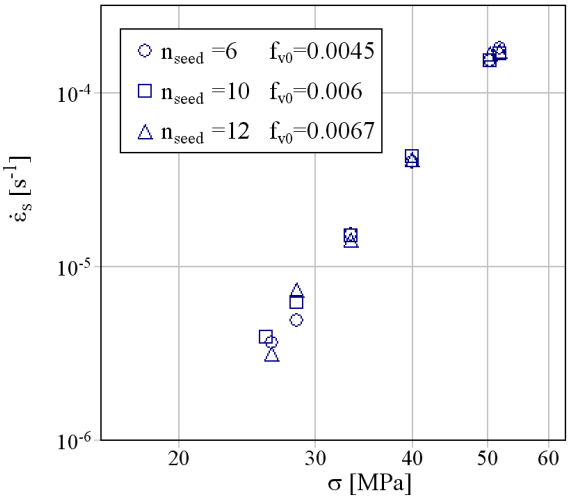

Fig. 3. Dependency of stationary creep rate on parameters n_{seed} and f_{v0} – simulation results

In real materials number of vacancies is connected with surfaces of grain boundaries as grain boundaries are ideal sources of vacancies (Evans, 1984). Therefore, smaller grains have increased number of vacancies. To reflect this effect the initial density of *damaged cells* f_{v0} has to be corrected. For 3D model of constant RVE size, number of grains is changing like $\sim d^{-3}$, surface of single grain boundaries is like $\sim d^{2}$, so surface of all grains in RVE is $\sim d^{-1}$. Similarly for 2D model: number of grains is changing like $\sim d^{-2}$, length of single grain boundaries is like $\sim d$, so length of all grains borders in RVE is $\sim d^{-1}$. In all cases, to keep the value of f_{v0} proportional to the length (or surface) of grain boundaries it should be $\sim d^{-1}$. The value of parameter H (Eq. 5) is changed in the same proportion, too.

Results of simulations with corrected values of f_{v0} are presented on Figs 3 and 4. Obtained creep rates coincide very well, showing that there is no dependency of creep rate on grain size. The larger value of f_{v0} fully compensates the smaller size of grains. This is consistent with general relation for metals in dislocation creep range. The results for time to failure exhibit more scatter, but there is also no apparent dependency on grain size. The results of simulation comply with the Monkman-Grant rule (2).

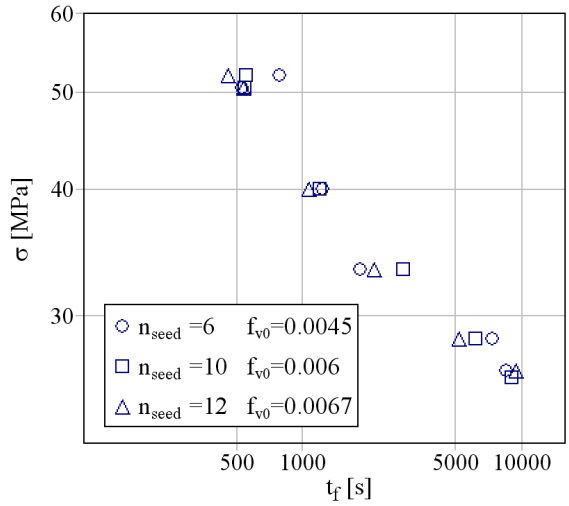

Fig. 4. Dependency of time to failure on parameters n_{seed} and f_{v0} – simulation results

4. CONCLUSIONS

The simulations of damage development in creep conditions by means of Cellular Automata show that the simple enlargement of grains is not sufficient to explain observed experimentally dependency on grain size. Besides grain size also initial density of *damaged cells* is important to properly simulate this dependency. But comparison with the experiments for copper (see Tab. 1) shows that not all mechanisms connected with grain size are taken into account and thus further investigation has to be performed.

REFERENCES

1. **Abedrabbo N., Pourboghrat F., Carsley J.** (2006), Forming of AA5182-O and AA5754-O at elevated temperatures using coupled thermo-mechanical finite element models, *International Journal of Plasticity*, 23, 841–875.
2. **Bolkowski S., Stabrowski M., Skoczylas J., Sroka J., Sikora J., Wincenciak S.** (1993), *Komputerowe metody analizy pola elektromagnetycznego*, WNT, Warszawa.
3. **Goshima T., Hanson M.T., Keer L.M.** (1990), Three-dimensional analysis of thermal effects on surface crack propagation in rolling contact, *Journal of Thermal Stresses*, Vol. 13, 237-261.
4. **Grześ P.** (2009), Finite element analysis of disc temperature during braking process, *Acta Mechanica et Automatica*, Vol. 3, No. 4, 36-42.

5. **Kaczorek T.** (2002), *Positive 1D and 2D Systems*, Springer Verlag, London.
6. **Malinin N. N, Rżysko J.** (1981), *Mechanika materiałów*, PWN, Warszawa.
7. **Belloni G., Bernasconi G., Piatti G.** (1977), Creep damage and rupture in AISI 310 austenitic steel, *Meccanica*, Vol. 12, 84-96.
8. **Boettner R.C., Robertson W.D.** (1961), A Study of the Growth of Voids in Copper During the Creep Process by Measurement of the Accompanying Change in Density, *Trans. Metall. Soc. AIME*, Vol. 221, 613-622.
9. **Chrzanowski M., Nowak K.** (2007), Cellular Automata in Damage Mechanics: Brittle Creep Rupture Case, *Arch. Mech.*, Vol. 59, 329-339.
10. **Chrzanowski M., Nowak K. (**2009), On Multiscale Modelling of Creep Damage by Means of Cellular Automata, *Journal of Multiscale Modelling*, Vol. 1, 389-402.
11. **Chrzanowski M., Nowak K. (**2010), Opis zniszczenia mieszanego w warunkach pełzania przy pomocy automatów komórkowych, *Acta Mechanica et Automatica*, Vol. 4, 29-36.
12. **Dobrzański L.A. (**1996), *Metaloznawstwo z podstawami nauki o materiałach*, Wydawnictwa Naukowo-Techniczne, Warszawa.
13. **Evans H.E. (**1984), *Mechanisms of Creep Fracture*, Elsevier Applied Science Publishers, London, New York.
14. **Evans R.W., Wilshire B. (**1993), *Introduction to Creep*, The Institute of Materials, London.
15. **Feltham P., Meakin J.D. (**1959), Creep in Face-Centred Cubic Metals with Special Reference to Copper, *Acta Metall*., Vol. 7, 614-627.
16. **Fleck R.G., Cocks A.C.F., Taplin D.M.R. (**1970), The Influence of Polycrystal Grain Size upon the Creep Ductility of Copper, *Metall. Mater. Trans.*, Vol. 1B, 3415-3420.
17. **Hayhurst D.R.** (2005), CDM mechanisms-based modelling of tertiary creep: ability to predict the life of engineering components, *Arch. Mech.*, Vol. 57, 2-3.
18. **Johnson W. R., Barrett C.R., Nix W.D. (**1972), The effect of environment and grain size on the creep behavior of a Ni-6 pct W solid solution, *Metall. Mater. Trans.*, Vol. 3B, 695-698.
19. **Lemaitre J., Dufailly J.** (1987), Damage measurements, *Eng. Fract. Mech.*, Vol. 28, 643-661.
20. **Matic P., Geltmacher A.B.** (2001), A cellular automaton-based technique for modeling mesoscale damage evolution, *Comp. Mat. Sci.*, Vol. 20, 120-141.
21. **Nowak K. (**2011), Uncertainty of lifetime for CAFE creep damage model, *Computer Methods in Materials Science*, Vol. 11, 315-323.
22. **Ostoja-Starzewski M. (**2007), *Microstructural Randomness and Scaling in Mechanics of Materials*, Chapman and Hall/CRC.
23. **Pahutova M., Cadek J., Rys P. (**1971), High temperature creep in copper, *Phil. Mag.*, Vol. 22, 509-517.
24. **Wilshire B., Battenbough A.J. (**2007), Creep and creep fracture of polycrystalline copper, *Mater. Sci. Eng.*, Vol. 443A, 156-166.
25. **Wilshire B., Palmer C.J. (**2002), Grain size effects during creep of copper, *Scripta Mater.*, Vol. 46, 483-488.

EXACT SOLUTION OF A DIELECTRIC CRACK OF MODE III IN MAGNETO-ELECTRO-ELASTIC HALF-SPACE

Bogdan ROGOWSKI*

*Department of Mechanics of Materials, Technical University of Lodz,
Al. Politechniki 6, 93-590 Lodz, Poland

bogdan.rogowski@p.lodz.pl

Abstract: This paper investigated the fracture behaviour of a piezo-electro-magneto-elastic material subjected to electro-magneto-mechanical loads. The PEMO-elastic medium contains a straight-line crack which is parallel to its poling direction and loaded surface of the half-space. Fourier transform technique is used to reduce the problem to the solution of one Fredholm integral equation. This equation is solved exactly. The semi-permeable crack-face magneto-electric boundary conditions are utilized. Field intensity factors of stress, electric displacement, magnetic induction, crack displacement, electric and magnetic potentials, and the energy release rate are determined. The electric displacement and magnetic induction of crack interior are discussed. Strong coupling between stress and electric and magnetic field near the crack tips has been found.

1. INTRODUCTION

Due to the growth in applications as smart devices, the mechanical and fracture properties of two-phase magnetostrictive/piezoelectric composites are becoming more and more important, see: Huang and Kuo (1997), Pan (2001), Buchanan (2004), Chen et al. (2005), Annigeri et al. (2006), Lee and Ma (2007), Calas et al. (2008) and Hou et al. (2009), among other, have been published the papers on this field. The fracture mechanics of PEMO-elastic materials also have attracted much attention and many research papers have been published; see e.g. Liu et al. (2001), Sih and Song (2003), Gao et al. (2003), Zhou et al. (2004), Hu and Li (2005), Wang and Mai (2006b), Li and Kardomateas (2007), Feng et al. (2007), Tian and Rajapakse (2008), Zhan and Fan (2008); among others.

For the fracture analysis of a magneto-electro-elastic solid of much interest are the effects of magneto-electric boundary conditions at the crack surfaces on the crack growth as well as the choosing of fracture criteria (Wang and Mai, 2006b, Wang et al., 2006a). As an approximation to a real crack, the magneto-electrically permeable and impermeable crack face boundary conditions are prevail in the above stated-works. However these two ideal crack models are only the limiting cases of real dielectric crack (Wang and Mai; 2006b; Rogowski, 2007). However, the above-mentioned works associated with semi-permeable crack problems are only limited to an infinite magneto-electro-elastic solid with cracks. Additionally, the numerical procedures are used to obtain the results. Motivated by this consideration this paper investigates a PEMO-elastic half-space with an electrically and magnetically conducting crack under anti-plane mechanical and in-plane electromagnetic loadings to shown exact solution in simple analytical form.

2. BASIC EQUATIONS

For a linearly magneto-electro-elastic medium under anti-plane shear coupled with in-plane electric and magnetic fields there are only the non-trivial anti-plane displacement w:

$$u_x = 0\,,\ u_y = 0\,,\ u_z = w(x,y) \tag{1}$$

strain components γ_{xz} and γ_{yz}:

$$\gamma_{xz} = \frac{\partial w}{\partial x}\,,\ \gamma_{yz} = \frac{\partial w}{\partial y} \tag{2}$$

stress components τ_{xz} and τ_{yz}, in-plane electrical and magnetic potentials ϕ and ψ, which define electrical and magnetic field components E_x, E_y, H_x and H_y:

$$E_x = -\frac{\partial \phi}{\partial x}\,,\ E_y = -\frac{\partial \phi}{\partial y}\,,\ H_x = -\frac{\partial \psi}{\partial x}\,,\ H_y = -\frac{\partial \psi}{\partial y} \tag{3}$$

and electrical displacement components D_x, D_y and magnetic induction components B_x, B_y with all field quantities being the functions of coordinates x and y.

The generalized strain-displacement relations (2) and (3) have the form:

$$\gamma_{\alpha z} = w_{,\alpha}\,,\ E_\alpha = -\phi_{,\alpha}\,,\ H_\alpha = -\psi_{,\alpha} \tag{4}$$

where $\alpha = x, y$ and $w_{,\alpha} = \partial w/\partial \alpha$.

For linearly magneto-electro-elastic medium the coupled constitutive relations can be written in the matrix form

$$[\tau_{\alpha z}, D_\alpha, B_\alpha]^T = \mathbf{C}[\gamma_{\alpha z}, -E_\alpha, -H_\alpha]^T \tag{5}$$

where the superscript T denotes the transpose of a matrix and:

$$\mathbf{C}=\begin{bmatrix} c_{44} & e_{15} & q_{15} \\ e_{15} & -\varepsilon_{11} & -d_{11} \\ q_{15} & -d_{11} & -\mu_{11} \end{bmatrix} \tag{6}$$

where c_{44} is the shear modulus along the z-direction, which is direction of poling and is perpendicular to the isotropic plane (x, y), ε_{11} and μ_{11} are dielectric permittivity and magnetic permeability coefficients, ε_{15}, q_{15} and d_{11} are piezoelectric, piezo-magnetic and magneto – electric coefficients, respectively.

The mechanical equilibrium equation (called as Euler equation), the charge and current conservation equations (called as Maxwell equations), in the absence of the body force electric and magnetic charge densities, can be written as:

$$\tau_{z\alpha,\alpha}=0\,;\quad D_{\alpha,\alpha}=0\,;\quad B_{\alpha,\alpha}=0\,;\quad \alpha=x,y \tag{7}$$

Subsequently, the Euler and Maxwell equations take the form:

$$\mathbf{C}\left[\nabla^2 w,\nabla^2\phi,\nabla^2\psi\right]^T=[0,0,0]^T \tag{8}$$

where $\nabla^2=\frac{\partial^2}{\partial x^2}+\partial^2/\partial y^2$ is the two-dimensional Laplace operator.

Since $|\mathbf{C}|\neq 0$ one can decouple the equations (8):

$$\nabla^2 w=0\,;\quad \nabla^2\phi=0\,;\quad \nabla^2\psi=0 \tag{9}$$

If we introduce, for convenience of mathematics in some boundary value problems, two unknown functions:

$$\left[\chi-e_{15}w,\eta-q_{15}w\right]^T=\mathbf{C}_0[\phi,\psi]^T \tag{10}$$

where:

$$\mathbf{C}_0=\begin{bmatrix} -\varepsilon_{11} & -d_{11} \\ -d_{11} & -\mu_{11} \end{bmatrix} \tag{11}$$

Then:

$$[\phi,\psi]^T=\mathbf{C}_0{}^{-1}\left[\chi-e_{15}w,\eta-q_{15}w\right]^T \tag{12}$$

where:

$$\mathbf{C}_0{}^{-1}=\frac{1}{\varepsilon_{11}\mu_{11}-d_{11}^2}\begin{bmatrix} -\mu_{11} & d_{11} \\ d_{11} & -\varepsilon_{11} \end{bmatrix}=\begin{bmatrix} e_1 & e_2 \\ e_2 & e_3 \end{bmatrix} \tag{13}$$

The governing field variables are:

$$\begin{aligned} &\tau_{zk}=\tilde{c}_{44}w_{,k}-\alpha D_k-\beta B_k \\ &\phi=\alpha w+e_1\chi+e_2\eta \\ &\psi=\beta w+e_2\chi+e_3\eta \\ &D_k=\chi_{,k} \\ &B_k=\eta_{,k}\,;\quad k=x,y \end{aligned} \tag{14}$$

$$\nabla^2 w=0\,;\quad \nabla^2\chi=0\,;\quad \nabla^2\eta=0 \tag{15}$$

where:

$$\begin{aligned} &\tilde{c}_{44}=c_{44}+\alpha e_{15}+\beta q_{15} \\ &\alpha=\frac{\mu_{11}e_{15}-d_{11}q_{15}}{\varepsilon_{11}\mu_{11}-d_{11}^2}=-\left(e_1e_{15}+e_2q_{15}\right) \\ &\beta=\frac{\varepsilon_{11}q_{15}-d_{11}e_{15}}{\varepsilon_{11}\mu_{11}-d_{11}^2}=-\left(e_3q_{15}+e_2e_{15}\right) \end{aligned} \tag{16}$$

Note that $\tilde{c}_{44}$ is the piezo-electro-magnetically stiffened elastic constant.

Note also that:

$$\mathbf{C}^{-1}=\frac{1}{\tilde{c}_{44}}\begin{bmatrix} 1 & \alpha & \beta \\ \alpha & \alpha^2+\tilde{c}_{44}e_1 & \alpha\beta+\tilde{c}_{44}e_2 \\ \beta & \alpha\beta+\tilde{c}_{44}e_2 & \beta^2+\tilde{c}_{44}e_3 \end{bmatrix} \tag{17}$$

These material parameters will appear in our solutions.

3. FORMULATION OF THE CRACK PROBLEM

Consider a PEMO-elastic half-space containing straight-line crack of length $2a$, parallel to the surface of a half-space which is subjected to electric, magnetic and mechanical loads. The crack is located along the x-axis from $-a$ to a at a depth h from the loaded surface with a rectangular coordinate system, as shown in Fig. 1. The PEMO-elastic half-space is poled in the z-direction.

To solve the crack problem in linear elastic solids, the superposition technique is usually used. Thus we first solve the magneto-electro-elastic field problem without the cracks in the medium under electric, magnetic and mechanical loads. This elementary solution is:

$$\begin{aligned} &\tau_{yz}=\tau_0 \\ &D_y=D=\begin{cases} D_0, & case\ I \\ \dfrac{e_{15}}{c_{44}}\tau_0+\left(\varepsilon_{11}+\dfrac{e_{15}^2}{c_{44}}\right)E_0+\left(d_{11}+\dfrac{e_{15}q_{15}}{c_{44}}\right)H_0, & case\ II \end{cases} \\ &B_y=B=\begin{cases} B_0, & case\ I \\ \dfrac{q_{15}}{c_{44}}\tau_0+\left(d_{11}+\dfrac{e_{15}q_{15}}{c_{44}}\right)E_0+\left(\mu_{11}+\dfrac{q_{15}^2}{c_{44}}\right)H_0, & case\ II \end{cases} \end{aligned} \tag{18}$$

Then, we use equal and opposite values as the crack surface traction and utilize the unknowns d_0 and b_0 in the crack region. Thus, in this study, $-\tau_0$; $-(D-d_0)$, $-(B-b_0)$ are, respectively, mechanical, electrical and magnetic loadings applied on the crack surfaces (the so called perturbation problem).

The boundary conditions can be written as:

$$\begin{aligned} &\tau_{zy}(x,h\pm)=-\tau_0\,,\ D_y(x,h\pm)=-D+d_0\,, \\ &B_y(x,h\pm)=-B+b_0\,;\quad |x|<a \end{aligned} \tag{19}$$

$$\left\|\tau_{zy}\right\|=0\,,\ \left\|D_y\right\|=0\,,\ \left\|B_y\right\|=0\,,\ |x|<\infty\,,\ y=h \tag{20}$$

$$\left[\!\left[w\right]\!\right]=0\,,\ \left[\!\left[\phi\right]\!\right]=0\,,\ \left[\!\left[\psi\right]\!\right]=0\,,\ |x|\geq a,\ y=h \tag{21}$$

$$\tau_{zy}(x,0)=0\,,\ D_y(x,0)=0\,,\ B_y(x,0)=0\,;\ |x|<\infty \tag{22}$$

where the notation $[|f|] = f^+ - f^-$ and f^+ denotes the values for $h+$ while f^- for $h-$.

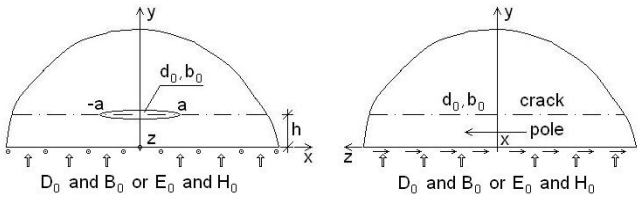

Fig. 1. The PEMO-elastic half-space with a crack parallel to its surface under an anti-plane mechanical and in-plane electric and magnetic loads. Inside the crack the unknown electromagnetic field appears (d_0 and b_0 are unknown to be determined)

Of course, in perturbation problem the surface of the half-space is free. The electric displacement d_0 and magnetic induction b_0 inside the crack are obtained from semi-permeable crack face boundary conditions (Rogowski (2007)). For two different magneto-electric media: PEMO-material and notch space we have continuity condition of electric and magnetic potential in both materials at interface. The semi-permeable crack-face magneto-electric boundary conditions are expressed as follows:

$$d_0 = -\varepsilon_c \frac{[\![\phi]\!]}{2\delta(x)}, \quad b_0 = -\mu_c \frac{[\![\psi]\!]}{2\delta(x)} \tag{23}$$

where $\delta(x)$ describes the shape of the notch and ε_c, μ_c are the dielectric permittivity and magnetic permeability of crack interior. If we assume the elliptic notch profile such that:

$$\delta(x) = (\delta_0/a)\sqrt{a^2 - x^2} \tag{24}$$

where δ_0 is the half-thickness of the notch at $x = 0$, we obtain:

$$\begin{aligned} 2d_0(\delta_0/\varepsilon_c)\sqrt{a^2 - x^2} &= -[\![\phi]\!] \\ 2b_0(\delta_0/\mu_c)\sqrt{a^2 - x^2} &= -[\![\psi]\!] \end{aligned} \tag{25}$$

Eqs (25) form two coupling linear equations with respect to d_0 and b_0 since $[|\phi|]$ and $[|\psi|]$ depends linearly on these quantities as show boundary conditions (19) and (21).

4. THE SOLUTION FOR HALF-SPACE WITH DISCONTINUITY AT y = h

Define the Fourier transform pair by equations:

$$\hat{f}(s) = \int_0^\infty f(x)\cos(sx)dx, \quad f(x) = \frac{2}{\pi}\int_0^\infty \hat{f}(s)\cos(sx)ds \tag{26}$$

Considering the symmetry about y-axis the Fourier cosine transform is only applied in Eqs (15) resulting in ordinary differential equations and their solutions:

$$\hat{w}(s,y) = A_1(s)e^{-sy} \tag{26a}$$

$$\begin{aligned} &\hat{\chi}(s,y) = B_1(s)e^{-sy} && y > h \\ &\hat{\eta}(s,y) = C_1(s)e^{-sy} \\ &\hat{w}(s,y) = A_2(s)e^{-sy} + A_3(s)e^{sy} \\ &\hat{\chi}(s,y) = B_2(s)e^{-sy} + B_3(s)e^{sy} && 0 \le y < h \\ &\hat{\eta}(s,y) = C_2(s)e^{-sy} + C_3(s)e^{sy} \end{aligned} \tag{26b}$$

In the domain $y > h$ the solution has the form (26a) to ensure the regularity conditions at infinity.

The transforms of Eqs (14) yield:

$$\begin{aligned} &\hat{\varphi}(s,y) = e_1\hat{\chi}(s,y) + e_2\hat{\eta}(s,y) + \alpha\hat{w}(s,y) \\ &\hat{\psi}(s,y) = e_2\hat{\chi}(s,y) + e_3\hat{\eta}(s,y) + \beta\hat{w}(s,y) \\ &\hat{\tau}_{zy}(s,y) = \tilde{c}_{44}\hat{w}_{,y} - \alpha\hat{D}_y - \beta\hat{B}_y \\ &\hat{D}_y = \hat{\chi}_{,y}, \quad \hat{B}_y = \hat{\eta}_{,y} \end{aligned} \tag{27}$$

The unknown functions $A_i(s), B_i(s)$ and $C_i(s)$, $i = 1, 2, 3$, are obtained from the boundary conditions (20) and (22), which in transform domain are:

$$\begin{aligned} &[\![\hat{\tau}_{zy}]\!] = 0; \quad [\![\hat{D}_y]\!] = 0; \quad [\![\hat{B}_y]\!] = 0 \\ &\hat{\tau}_{zy} = 0; \quad \hat{D}_y = 0; \quad \hat{B}_y = 0; \quad y = 0 \end{aligned} \tag{28}$$

where $[|\hat{f}] = \hat{f}(s, h+) - \hat{f}(s, h-)$.

The result is:

$$\begin{aligned} A_1(s) &= \hat{f}(s)\left(e^{-sh} - e^{sh}\right) \\ B_1(s) &= \hat{g}(s)\left(e^{-sh} - e^{sh}\right) \\ C_1(s) &= \hat{h}(s)\left(e^{-sh} - e^{sh}\right) \\ A_2(s) = A_3(s) &= \hat{f}(s)\,e^{-sh} \\ B_2(s) = B_3(s) &= \hat{g}(s)\,e^{-sh} \\ C_2(s) = C_3(s) &= \hat{h}(s)\,e^{-sh} \end{aligned} \tag{29}$$

Finally, the solution for the half-space with dislocation density functions $f(s)$, $g(s)$ and $h(s)$ in the domain $y \ge 0$ $|x| < \infty$ is given by:

$$\begin{aligned} w(x,y) &= -\frac{2}{\pi}\int_0^\infty \hat{f}(s)\left[sgn(y-h)e^{-s|(y-h)|} - e^{-s(y+h)}\right]\cos(sx)ds \\ \chi(x,y) &= -\frac{2}{\pi}\int_0^\infty \hat{g}(s)\left[sgn(y-h)e^{-s|(y-h)|} - e^{-s(y+h)}\right]\cos(sx)ds \\ \eta(x,y) &= -\frac{2}{\pi}\int_0^\infty \hat{h}(s)\left[sgn(y-h)e^{-s|(y-h)|} - e^{-s(y+h)}\right]\cos(sx)ds \end{aligned} \tag{30}$$

$$\tau_{zy}(x,y)=\frac{2}{\pi}\tilde{c}_{44}\int_0^\infty s\hat{f}(s)\left[e^{-s|(y-h)|}-e^{-s(y+h)}\right]cos(sx)ds+$$

$$-\frac{2}{\pi}\int_0^\infty s\left[\alpha\hat{g}(s)+\beta\hat{h}(s)\right]\left[e^{-s|(y-h)|}-e^{-s(y+h)}\right]cos(sx)ds$$

$$D_y(x,y)=\frac{2}{\pi}\int_0^\infty s\hat{g}(s)\left[e^{-s|(y-h)|}-e^{-s(y+h)}\right]cos(sx)ds$$

$$B_y(x,y)=\frac{2}{\pi}\int_0^\infty s\hat{h}(s)\left[e^{-s|(y-h)|}-e^{-s(y+h)}\right]cos(sx)ds$$

where $sgn(y-h)=+1$ or $y>h$ or $y<h$, respectively.

The potentials $\varphi(x,y)$ and $\psi(x,y)$ are obtained from Eqs (14).

5. FREDHOLM INTEGRAL EQUATION OF THE SECOND KIND

The unknown functions $f(s)$, $g(s)$ and $h(s)$ can be obtained from the mixed boundary conditions (19) and (21)which yield:

$$\frac{2}{\pi}\int_0^\infty s\hat{f}(s)\left[1-e^{-2sh}\right]\cos(sx)ds=-\frac{\tau_0+(D-d_0)\alpha+(B-b_0)\beta}{\tilde{c}_{44}}$$

$$\frac{2}{\pi}\int_0^\infty s\hat{g}(s)\left[1-e^{-2sh}\right]\cos(sx)ds=-(D-d_0)$$

$$\frac{2}{\pi}\int_0^\infty s\hat{h}(s)\left[1-e^{-2sh}\right]\cos(sx)ds=-(B-b_0);\quad |x|<a \tag{31a}$$

$$\int_0^\infty \hat{f}(s)cos(sx)ds=0$$

$$\int_0^\infty \hat{g}(s)cos(sx)ds=0 \tag{31b}$$

$$\int_0^\infty \hat{h}(s)cos(sx)ds=0\quad;\quad |x|\ge a$$

The integral equations (31a) may be rewritten as:

$$\frac{2}{\pi}\int_0^\infty \begin{Bmatrix}\hat{f}(s)\\ \hat{g}(s)\\ \hat{h}(s)\end{Bmatrix}\begin{Bmatrix}1-e^{-2sh}\\ 1-e^{-2sh}\\ 1-e^{-2sh}\end{Bmatrix}\sin(sx)ds=\begin{Bmatrix}\frac{\tau_0+(D-d_0)\alpha+(B-b_0)\beta}{\tilde{c}_{44}}x\\ (D-d_0)x\\ (B-b_0)x\end{Bmatrix} \tag{32}$$

We introduce the integral representation of the unknown functions:

$$\begin{Bmatrix}\hat{f}(s)\\ \hat{g}(s)\\ \hat{h}(s)\end{Bmatrix}=-\begin{Bmatrix}\frac{\tau_0+(D-d_0)\alpha+(B-b_0)\beta}{\tilde{c}_{44}}\\ D-d_0\\ B-b_0\end{Bmatrix}\int_0^a \begin{Bmatrix}f(u)\\ g(u)\\ h(u)\end{Bmatrix}uJ_0(su)du \tag{33}$$

where $J_0(su)$ is the Bessel function of the first kind and zero order and $f(u)$, $g(u)$, $h(u)$ are new auxiliary functions. This representation satisfies equations (31b) automatically and converts equations (32) to the Abel one integral equation, which can be solved explicitly. The result is the Fredholm integral equation of the second kind:

$$f(u)-\int_0^a f(v)K(u,v)\,dv=1 \tag{34}$$

with the kernel:

$$K(u,v)=v\int_0^\infty se^{-2sh}J_0(su)J_0(sv)ds \tag{35}$$

and:

$$f(u)=g(u)=h(u) \tag{36}$$

of course $\hat{f}(s)$, $\hat{g}(s)$ and $\hat{h}(s)$ are dissimilar since are proportional to $\tau_0+(D-d_0)\alpha+(B-b_0)\beta$; $D-d_0$ and $B-b_0$, respectively, and d_0, b_0 are dissimilar functions, defined by Eqs. (23).

6. THE SOLUTION OF FREDHOLM INTEGRAL EQUATION OF THE SECOND KIND

The kernel function $K(u,v)$ may be presented in more useful form. Using the Neumann's theorem (Watson, 1966):

$$J_0(su)J_0(sr)=\frac{1}{\pi}\int_0^\pi J_0(sR)d\alpha; \tag{37}$$

$$R^2=u^2+r^2-2ur\cos\alpha$$

and the integral:

$$\int_0^\infty sJ_0(Rs)e^{-2sh}ds=\frac{2h}{\left[R^2+(2h)^2\right]^{3/2}} \tag{38}$$

the kernel function becomes:

$$K(u,v)=\frac{4hv}{\pi l^{3/2}}\int_0^{\pi/2}\frac{d\alpha}{\left(1-k^2\cos^2\alpha\right)^{3/2}} \tag{39}$$

$$l^2=(u+v)^2+4h^2,\quad k^2=\frac{4uv}{l^2}$$

The kernel function is presented by means of elliptic integral. The integral equation (34) can be solved by iterative method.

The recurrence formula is:

$$f_i(u)=1+\int_0^a f_{i-1}(v)K(u,v)dv,\ f_0(v)=1,\quad i=1,2,...n \tag{40}$$

The n-th approximation gives:

$$f(u)=1+\frac{a}{a+u}\left[1-\frac{4h}{\pi}\frac{K(k_0)}{l_0}\right]+$$
$$+\left(\frac{a}{a+u}\right)^2\left[1-\frac{4h}{\pi}\frac{K(k_0)}{l_0}\right]^2+....+ \tag{41}$$
$$+\left(\frac{a}{a+u}\right)^n\left[1-\frac{4h}{\pi}\frac{K(k_0)}{l_0}\right]^n$$

where $K(k_0)$ is the elliptic integral of the first kind defined by:

$$K(k_0)=\int_0^{\pi/2}\frac{d\alpha}{(1-k_0^2\cos^2\alpha)^{1/2}}$$
$$l_0^2=(a+u)^2+4h^2,\quad k_0^2=\frac{4au}{l_0^2} \tag{42}$$

The sum of infinite geometric series converges to the solution as $n\to\infty$, giving:

$$f(u)=\left[1-\frac{a}{a+u}\left(1-\frac{2}{\pi}\frac{K(k_0)}{l_0/2h}\right)\right]^{-1}\qquad |u|\le a \tag{43}$$

The range of convergence is given by inequality:

$$\frac{2}{\pi}K(k_0)\ <\ \left(2+\frac{u}{a}\right)\frac{l_0}{2h}\qquad |u|\le a \tag{44}$$

and is satisfied for all of u and a/h.

For $h\to\infty$, $(2/\pi)K(k_0)\to 1$ and $l_0/2h\to 1$, while for $h\to 0$, we have the logarithmic singularity of $K(k_0)$ for $u=a$:

$$K(k_0)\sim\ln\frac{1}{1-\frac{2\sqrt{au}}{a+u}} \tag{45}$$

But $hK(k_0)/l_0$ tends to zero as $a/h\to\infty$.

Thus we have the values:

$$f\left(\frac{a}{h}\right)=2\left[1+\frac{2}{\pi}\frac{1}{\sqrt{1+\delta^2}}K\left(\frac{\delta}{\sqrt{1+\delta^2}}\right)\right]^{-1}$$
$$f(0)=\sqrt{1+\frac{\delta^2}{4}},\quad \delta=\frac{a}{h} \tag{46}$$

The values of $f(a/h)$ changes from 1 to 2 for all of a/h and $f(u)$ is given explicitly by Eq. (43).

7. FIELD INTENSITY FACTORS

The electric displacement, magnetic induction and shear stress outside of the crack surface can be expressed by:

$$\begin{Bmatrix}D_y(x,h\pm)\\B_y(x,h\pm)\end{Bmatrix}=-\frac{2}{\pi}\begin{Bmatrix}D-d_0\\B-b_0\end{Bmatrix}\int_0^a f(u)du\int_0^\infty sJ_0(su)\left(1-e^{-2sh}\right)\cos(sx)ds \tag{47}$$

$$\tau_{zy}(x,h\pm)=-\frac{2}{\pi}\tau_0\int_0^a f(u)du\int_0^\infty sJ_0(su)\left(1-e^{-2sh}\right)\cos(sx)ds$$

Using the integral:

$$\int_0^\infty e^{-2sh}\sin(sx)J_0(su)ds=\frac{\eta}{x\left(\xi^2+\eta^2\right)}$$
$$u^2=x^2\left(1+\xi^2\right)\left(1-\eta^2\right)\qquad 2h=x\xi\eta\ ,\quad x\xi>0,\quad \eta>0 \tag{48}$$

equations (47) may be written as:

$$\begin{Bmatrix}D_y(x,h\pm)\\B_y(x,h\pm)\end{Bmatrix}=-\frac{2}{\pi}\begin{Bmatrix}D-d_0\\B-b_0\end{Bmatrix}\frac{d}{dx}\int_0^a f(u)du\left[\frac{|x|}{x\sqrt{x^2-u^2}}-\frac{\eta}{x\left(\xi^2+\eta^2\right)}\right]$$
$$\tau_{zy}(x,h\pm)=-\frac{2}{\pi}\tau_0\frac{d}{dx}\int_0^a f(u)du\left[\frac{|x|}{x\sqrt{x^2-u^2}}-\frac{\eta}{x\left(\xi^2+\eta^2\right)}\right] \tag{49}$$

The singular terms of these quantities ($|x|\to a^+$) are included in the first term in Eq. (49). Since the singular field near the crack tip exhibits the inverse square-root singularity we define the stress, electric displacement and magnetic induction intensity factors as follows:

$$\begin{Bmatrix}K_\tau\\K_D\\K_B\end{Bmatrix}=\lim_{|x|\to a^+}\sqrt{2(|x|-a)}\begin{Bmatrix}\tau_{zy}\\D_y\\B_y\end{Bmatrix} \tag{50}$$

The intensity factors are obtained as:

$$K_w=\frac{1}{\tilde{c}_{44}}\left(K_\tau+\alpha K_D+\beta K_B\right)$$
$$K_\phi=\alpha K_w+e_1K_D+e_2K_B$$
$$K_\psi=\beta K_w+e_2K_D+e_3K_B$$
$$K_\tau=\frac{2}{\pi}\tau_0 f(a)\sqrt{a} \tag{51}$$
$$K_D=\frac{2}{\pi}(D-d_0)f(a)\sqrt{a}$$
$$K_B=\frac{2}{\pi}(B-b_0)f(a)\sqrt{a}$$

The jumps of displacement, electric potential and magnetic potential of the crack surfaces can be expressed as:

$$[\![w]\!]=\frac{4}{\pi}\frac{\tau_0+(D-d_0)\alpha+(B-b_0)\beta}{\tilde{c}_{44}}\int_x^a\frac{f(u)udu}{\sqrt{u^2-x^2}}$$
$$[\![\phi]\!]=\frac{4}{\pi}\left[\frac{\alpha\left[\tau_0+(D-d_0)\alpha+(B-b_0)\beta\right]}{\tilde{c}_{44}}+e_1(D-d_0)+e_2(B-b_0)\right]\int_x^a\frac{f(u)udu}{\sqrt{u^2-x^2}} \tag{52}$$
$$[\![\psi]\!]=\frac{4}{\pi}\left[\frac{\beta\left[\tau_0+(D-d_0)\alpha+(B-b_0)\beta\right]}{\tilde{c}_{44}}+e_2(D-d_0)+e_3(B-b_0)\right]\int_x^a\frac{f(u)udu}{\sqrt{u^2-x^2}}$$

Substituting Eqs (52) into Eqs (25) and differentiating both obtained equations with respect to x and using the following rule of differentiation under integral sign:

$$\frac{d}{dx}\int_x^a \frac{f(u)du}{\sqrt{u^2-x^2}} = -\frac{xf(a)}{a\sqrt{a^2-x^2}} + x\int_x^a \frac{d}{du}\left(\frac{f(u)}{u}\right)\frac{du}{\sqrt{u^2-x^2}} \quad (53)$$

equations (25) may be converted to two equations in which singular terms at $x \to a-0$, appear. For the singularity to vanish at $x \to a-0$, it must be true that:

$$\begin{aligned} d_0 &= -\varepsilon_0 f(a)\left[\frac{\alpha}{\tilde{c}_{44}}[\tau_0 + (D-d_0)\alpha + (B-b_0)\beta] + e_1(D-d_0) + e_2(B-b_0)\right] \\ b_0 &= -\mu_0 f(a)\left[\frac{\beta}{\tilde{c}_{44}}[\tau_0 + (D-d_0)\alpha + (B-b_0)\beta] + e_2(D-d_0) + e_3(B-b_0)\right] \end{aligned} \quad (54)$$

where:

$$\varepsilon_0 = \frac{2}{\pi}\frac{a}{\delta_0}\varepsilon_c, \quad \mu_0 = \frac{2}{\pi}\frac{a}{\delta_0}\mu_c \quad (55)$$

Thus:

$$\begin{aligned} D-d_0 &= \left\{D\left[1-\mu_0 f\left(\frac{\beta^2}{\tilde{c}_{44}}+e_3\right)\right] + B\varepsilon_0 f\left(\frac{\alpha\beta}{\tilde{c}_{44}}+e_2\right) + \right. \\ &\left. + \frac{\tau_0\varepsilon_0}{\tilde{c}_{44}} f\left[\alpha + \mu_0 e_{15}\left(e_1e_3 - e_2^2\right)f\right]\right\} \times \\ &\times \left\{1 - f\left[\varepsilon_0\left(\frac{\alpha^2}{\tilde{c}_{44}}+e_1\right) + \mu_0\left(\frac{\beta^2}{\tilde{c}_{44}}+e_3\right) - \varepsilon_0\mu_0\frac{c_{44}}{\tilde{c}_{44}}\left(e_1e_3-e_2^2\right)\right]\right\}^{-1} \\ B-b_0 &= \left\{D\mu_0 f\left(\frac{\alpha\beta}{\tilde{c}_{44}}+e_2\right) + B\left[1-\varepsilon_0 f\left(\frac{\alpha^2}{\tilde{c}_{44}}+e_1\right)\right] + \right. \\ &\left. + \frac{\tau_0\mu_0}{\tilde{c}_{44}} f\left[\beta + \varepsilon_0 q_{15}\left(e_1e_3 - e_2^2\right)f\right]\right\} \times \\ &\times \left\{1 - f\left[\varepsilon_0\left(\frac{\alpha^2}{\tilde{c}_{44}}+e_1\right) + \mu_0\left(\frac{\beta^2}{\tilde{c}_{44}}+e_3\right) - \varepsilon_0\mu_0\frac{c_{44}}{\tilde{c}_{44}}\left(e_1e_3-e_2^2\right)\right]\right\}^{-1} \end{aligned} \quad (56)$$

where $f = f(a/h)$.

The electric and magnetic intensity factors are obtained by substitution of Eqs (56) into Eqs (51).

Furthermore we consider the behaviour of the jumps of the displacement, electric and magnetic potentials and define the following intensity factors:

$$\begin{Bmatrix} K_w \\ K_\phi \\ K_\psi \end{Bmatrix} = \lim_{|x|\to a^-} \frac{1}{2\sqrt{2(a-|x|)}} \begin{Bmatrix} [|w|] \\ [|\phi|] \\ [|\psi|] \end{Bmatrix} \quad (57)$$

In view of the results in Eq. (52), we have:

$$\begin{aligned} K_w &= \frac{1}{\tilde{c}_{44}}\left(K_\tau + \alpha K_D + \beta K_B\right) \\ K_\phi &= \alpha K_w + e_1 K_D + e_2 K_B \\ K_\psi &= \beta K_w + e_2 K_D + e_3 K_B \end{aligned} \quad (58)$$

These field intensity factors satisfy the constitutive equations:

$$\left[K_w, K_\phi, K_\psi\right]^T = \mathbf{C}^{-1}\left[K_\tau, K_D, K_B\right]^T \quad (59)$$

The energy release rate is derived in the following in similar manner to proposed by Pak (1990).

The energy release rate of the crack-tip is obtained from the following integral:

$$\begin{aligned} G = \frac{1}{2}\lim_{\delta\to 0}\frac{1}{\delta}\int_0^\delta \{ & \tau_{yz}(r+a,0)[|w|](r+a-\delta) + \\ & D_y(r+a,0)[|\phi|](r+a-\delta) + \\ & B_y(r+a,0)[|\psi|](r+a-\delta)\}dr \end{aligned} \quad (60)$$

where $[|w|]$, $[|\phi|]$ and $[|\psi|]$ are the jumps of displacement, electric potential and magnetic potential field intensity factors given by Eqs. (52).

The energy release rate is defined as:

$$G = \frac{1}{2}\left(K_\tau K_w + K_D K_\phi + K_B K_\psi\right) \quad (61)$$

or :

$$\begin{aligned} G = \frac{2}{\pi^2} f^2(a) a \frac{1}{\tilde{c}_{44}\left(\varepsilon_{11}\mu_{11} - d_{11}^2\right)} & \left[\left(\varepsilon_{11}\mu_{11} - d_{11}^2\right)\tau_0^2 + \right. \\ & -\left(c_{44}\mu_{11} + q_{15}^2\right)(D-d_0)^2 - \left(c_{44}\varepsilon_{11} + e_{15}^2\right)(B-b_0)^2 + \\ & + 2\left(e_{15}\mu_{11} - q_{15}d_{11}\right)\tau_0(D-d_0) + \\ & + 2\left(q_{15}\varepsilon_{11} - e_{15}d_{11}\right)\tau_0(B-b_0) + \\ & \left. + 2\left(c_{44}d_{11} + e_{15}q_{15}\right)(D-d_0)(B-b_0)\right] \end{aligned} \quad (62)$$

8. SOLUTIONS BASED ON IDEAL CRACK-FACE BOUNDARY CONDITIONS

When the crack is one of four ideal crack models: magneto-electrically permeable, magneto-electrically impermeable, magnetically permeable and electrically impermeable, magnetically impermeable and electrically permeable are the limiting cases of the magneto-electrically dielectric crack model.

– fully impermeable case: $\varepsilon_0 \to 0$ and $\mu_0 \to 0$, $D - d_0 \to D$, $B - b_0 \to B$ and the intensity factors are given by:

$$\begin{aligned} K_w^{imp.imp.} &= \frac{2}{\pi}\frac{f(a)\sqrt{a}}{\tilde{c}_{44}}\left(\tau_0 + D\alpha + B\beta\right) \\ K_\tau^{imp.imp.} &= \frac{2}{\pi} f(a)\sqrt{a}\tau_0 \\ K_D^{imp.imp.} &= \frac{2}{\pi} f(a)\sqrt{a}D \\ K_B^{imp.imp.} &= \frac{2}{\pi} f(a)\sqrt{a}B \\ K_\phi^{imp.imp.} &= \alpha K_w^{imp.imp.} + e_1 K_D^{imp.imp.} + e_2 K_B^{imp.imp.} \\ K_\psi^{imp.imp.} &= \beta K_w^{imp.imp.} + e_2 K_D^{imp.imp.} + e_3 K_B^{imp.imp.} \end{aligned} \quad (63)$$

Equations (63) indicate that K_τ, K_D and K_B are independent on the material constants, while K_w, K_ϕ and K_ψ, depend. Since $f(a)$ depend on the parameter of location

of the crack(the thickness h), strictly speaking on h/a, these quantities depend on this location.

– full permeable case: $\varepsilon_0 \to 0$ and $\mu_0 \to 0$
Then:

$$D - d_0 = \frac{e_{15}\tau_0}{c_{44}}, \quad B - b_0 = \frac{q_{15}\tau_0}{c_{44}} \tag{64}$$

And:

$$\begin{aligned} K_w^{per.per.} &= \frac{2}{\pi}\frac{f(a)\sqrt{a}}{c_{44}}\tau_0 \\ K_\tau^{per.per.} &= \frac{2}{\pi} f(a)\sqrt{a}\tau_0 \\ K_D^{per.per.} &= e_{15}K_w^{per.per.} \\ K_B^{per.per.} &= q_{15}K_w^{per.per.} \\ K_\phi^{per.per.} &= 0 \\ K_\psi^{per.per.} &= 0 \end{aligned} \tag{65}$$

The energy release rate is:

$$G = \frac{2}{\pi^2}\frac{\tau_0^2 a f^2(a)}{c_{44}} \tag{66}$$

– electrically impermeable and magnetically permeable:
$\varepsilon_0 \to 0$ and $\mu_0 \to 0$, $D - d_0 \to D$, $d_0 \to 0$

$$\begin{aligned} K_D^{imp.per} &= K_D^{imp.imp.} \\ B - b_0 &= \left[D\left(\frac{\alpha\beta}{\tilde{c}_{44}} + e_2\right) f(a) + \frac{\tau_0\beta}{\tilde{c}_{44}} \right] \left[1 + \left(\frac{\beta^2}{\tilde{c}_{44}} + e_3\right) f \right]^{-1} \\ K_B^{imp.per.} &= \frac{2}{\pi} f(a)\sqrt{a}(B - b_0) \\ K_w^{imp.per.} &= \frac{2}{\pi} f(a)\sqrt{a}\,\frac{\tau_0 + D\alpha}{\tilde{c}_{44}} + \beta K_B^{imp.per.} \end{aligned} \tag{67}$$

The solutions for the electrically impermeable and magnetically permeable crack are independent of the applied magnetic field.

– electrically permeable and magnetically impermeable:
$\varepsilon_0 \to 0$ and $\mu_0 \to 0$, $B - b_0 \to B$, $b_0 \to 0$

$$\begin{aligned} K_B^{per.imp.} &= K_B^{imp.imp.} \\ D - d_0 &= \left[\frac{\tau_0\alpha}{\tilde{c}_{44}} + B\left(e_2 + \frac{\alpha\beta}{\tilde{c}_{44}}\right) f(a) \right] \left[1 + \left(e_1 + \frac{\alpha^2}{\tilde{c}_{44}}\right) f(a) \right]^{-1} \\ K_D^{per.imp.} &= \frac{2}{\pi} f(a)\sqrt{a}(D - d_0) \\ K_w^{per.imp} &= \frac{2}{\pi} f(a)\sqrt{a}\,\frac{\tau_0 + B\beta}{\tilde{c}_{44}} + \alpha K_D^{per.imp.} \end{aligned} \tag{68}$$

The solution for the electrically permeable and magnetically impermeable crack are independent of the applied electric displacement.

In practical applications the following cases appear:

– Let ε_0 tends to infinity and μ_0 is finite
Then:

$$\begin{aligned} K_D^{perm.\mu_c} &= K_D^{per.imp.}\left(1 - f_1(\bar{\mu})\right) + K_D^{per.per.} f_1(\bar{\mu}) \\ K_B^{perm.\mu_c} &= K_B^{imp.imp.}\left(1 - f_1(\bar{\mu})\right) + K_B^{per.per.} f_1(\bar{\mu}) \end{aligned} \tag{69}$$

where:

$$f_1(\bar{\mu}) = \frac{1}{1 + \bar{\mu}}, \quad \bar{\mu} = \frac{\pi}{2}\frac{\mu_{11}}{\mu_c}\frac{\delta_0}{a}\frac{1}{f(a)}\left(1 + \frac{q_{15}^2}{\mu_{11}c_{44}}\right) \tag{70}$$

– Let μ_0 tends to infinity and ε_0 is finite
Then:

$$\begin{aligned} K_D^{\varepsilon_c perm.} &= K_D^{imp.imp.}\left(1 - f_2(\bar{\varepsilon})\right) + K_D^{per.per.} f_2(\bar{\varepsilon}) \\ K_B^{\varepsilon_c perm.} &= K_B^{imp.per.}\left(1 - f_2(\bar{\varepsilon})\right) + K_B^{per.per.} f_2(\bar{\varepsilon}) \end{aligned} \tag{71}$$

where:

$$f_2(\bar{\varepsilon}) = \frac{1}{1 + \bar{\varepsilon}}, \quad \bar{\varepsilon} = \frac{\pi}{2}\frac{\varepsilon_{11}}{\varepsilon_c}\frac{\delta_0}{a}\frac{1}{f(a)}\left(1 + \frac{e_{15}^2}{\varepsilon_{11}c_{44}}\right) \tag{72}$$

In above equations the notation K^{perimp} denotes the intensity factors (51) and (58) for electrically permeable and magnetically impermeable crack boundary conditions i.e. for the values (68). Similarly $K^{imp.per.}$ are defined by Eqs (51) or (58) and (67).

The functions of permittivity ε_c and permeability μ_c approaches zero as ε_c and μ_c tends to zero and are unity as ε_c and μ_c tends to infinity.

The solution perfectly matches the exact solution in both limiting cases, namely permeable and/or impermeable electric and/or magnetic boundary conditions.

9. RESULT AND DISCUSSION

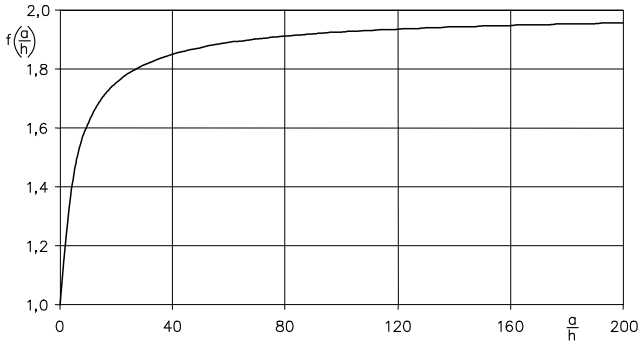

Fig. 2 Variation of $f(a/h)$ versus ratio of a/h; stress, electric displacement and magnetic induction intensity factors are proportional to $f(a/h)$ since: $f(a/h) = K_\tau/\tau_0\sqrt{a}(2/\pi) = K_B/B\sqrt{a}(2/\pi)$ in fully impermeable case

The electric and magnetic response, in fully impermeable case, is proportional to the applied electric and magnetic load, respectively, and is independent on the mechanical loads, as Eq. (63) implies. Similarly is for stress inten-

sity factor. The intensity factors of stress, electric displacement and magnetic induction, therefore, are just a function of the geometry of the cracked PEMO-elastic half-space as shown in Fig. 2.

From the Fig. 2 we can see that the SIF, EDIF and MIIF increase with a/h. For small values of a/h these quantities grow at an approximately constant rate with increasing a/h. For very large a/h (the crack near the boundary of a half-space) $f(a/h)$ increases slowly tending to 2.

10. CONCLUSIONS

From analytical and numerical results, several conclusions can be formulated:

- The electric displacement intensity factor is independent of the applied magnetic field in the special case of electrically impermeable and magnetically permeable crack;
- The magnetic induction intensity factor is independent of the applied electric displacement in the special case of electrically permeable and magnetically impermeable crack;
- Applications of electric and magnetic fields do not alter the stress intensity factors;
- The analytical solution (43) is new to the author' best knowledge. Accordingly, the behaviour of a crack which lies near of the boundary of the medium may be investigated exactly;
- Note that the plane $x = 0$ is a plane of symmetry ($\tau_{xz} = 0, D_x = 0$ and $B_x = 0$ on this plane). In consequence the solutions are valid for quarter-plane with edge crack of length a.

REFERENCES

1. **Annigeri A.R., Ganesan N., Swarnamani S.** (2006), Free vibrations of clamped-clamped magneto-electro-elastic shells, *Journal of Sound and Vibration*, 279, 237-51.
2. **Buchanan B. R.** (2004), Layered versus multiphase magneto-electro-elastic composites, *Composites*: Part B 35, 413-420.
3. **Calas H., Otero J. A., Rodriguez-Ramos R., et al**. (2008), Dispersion relations for SH wave in magneto-electro-elastic heterostructures, *International Journal of Solids and Structures*, 45, 5356-5367.
4. **Feng W. J., Pan E., Wang X.** (2007), Dynamic fracture analysis of a penny-shaped crack in a magnetoelectroelastic layer, *International Journal of Solids and Structures*, 44, 7955-7974.
5. **Gao C. F., Tong F., Zhang T. Y.** (2004), Fracture Mechanics for a Mode III Crack in a Magnetoelectroelastic Solid, *Int. J. Solids Struct*. 41, 6613-6629.
6. **Hou P. F., Teng G. H., Chen H. R.** (2009), Three-dimensional Green's function for a point heat source in two-phase transversely isotropic magneto-electro-thermoelastic material, *Mechanics of Materials*, 41, 329-338.
7. **Hu K. Q., Li G. Q**. (2005), Electro-magneto-elastic analysis of a piezoelectromagnetic strip with a finite crack under longitudinal shear, *Mechanics of Materials*, 37, 925-934.
8. **Huang J. H., Kuo W. S.** (1997), The analysis of piezoelectric/piezomagnetic composite materials containing ellipsoidal inclusions, *Journal of Applied Physics*, 81, 1378-86.
9. **Lee J. M., Ma C. C.,** (2007), Analytical full-field solutions of a magnetoelectroelastic layered half-plane, *Journal of Applied Physics*, 101 083502.
10. **Li R., Kardomateas G. A.** (2006), The mode III interface crack in piezo-electro-magneto-elastic dissimilar bimaterials, *Trans. ASME J. Appl. Mech*. 73, 220-227.
11. **Liu J.X., Liu X.L., Zhao Y.B.** (2001), Green's functions for anisotropic magnetoelectroelastic solids with elliptical cavity or a crack, *Int. J. Eng. Sci.* 39 (12), 1405-1418.
12. **Pak Y. E.,** (1990), Crack extension force in a piezoelectric material, *ASME J. Appl. Mech*., 57, 647-653.
13. **Pan E.** (2001), Exact solution for simply supported and multilayered magneto-electro-elastic plates, *Journal of Applied Mechanics*, 68, 608-17.
14. **Rogowski B.** (2007), The limited electrically permeable crack model in linear piezoelasticity, *Int. J. of Pressure Vessels and Piping*, 84,9, 572-581.
15. **Sih G. C., Song Z. F.** (2003), Magnetic and electric poling effects associated with crack growth in BaTiO2 –CoFe2O4 composite, *Theoretical and applied Fracture*.
16. **Tian W. Y., Rajapakse R. K. N. D.** (2008), Field intensity factors of a penny-shaped crack in a magnetoelectroelastic layer, *Journal of Alloys and Compounds*, 449, 161-171.
17. **Wang B. L., Han J. C., May Y. W.** (2006a), Mode III fracture of a magnetoelectroelastic layer: exact solution and discussion of the crack face electromagnetic boundary conditions, *International Journal Fracture*, 139, 27-38.
18. **Wang B. L., Mai Y. W.** (2006b), Applicability of the crack-face electromagnetic boundary conditions for fracture of magnetoelectroelastic materials, *International Journal of Solids and Structures*, 44, 387-398.
19. **Watson G. N.** (1966), *A Treatise on the Theory of Bessel Functions*, 2nd Edn, Cambridge University Press, Cambridge, Great Britain (
20. **Zhao M. H., Fan C. Y.** (2008), Strip electric-magnetic break down model in magnetoelectroelastic medium, *Journal of the Mechanics and Physics of Solid*,s 56, 3441-3458,
21. **Zhou Z. G., Wang B., Sun Y. G.** (2004), Two collinear interface crack in magneto-electro-elastic composite, *International Journal of Engineering Science*, 42, 1155-1167.

BENDING OF ORTHOTROPIC PLATE CONTAINING A CRACK PARALLEL TO THE MEDIAN PLANE

Vasyl SHVABYUK[*], Iaroslav PASTERNAK[*], Heorhiy SULYM[**]

[*] Lutsk National Technical University, Lvivska Str., 74, 43018 Lutsk, Ukraine
[**] Bialystok Technical University, Faculty of Mechanical Engineering, Wiejska Str., 45C, 15-351 Bialystok, Poland

pasternak@ukrpost.ua, h.sulym@pb.edu.pl

Abstract: This paper considers cylindrical bending of the plate containing a crack parallel to plate's faces. The analytical model of the problem is obtained using the improved theory of plates bending, which considers transverse deformation of the plate. Received analytical results are compared with the numerical data of the boundary element approach, which is modified to suit the considered contact problem. The results of analytical and numerical techniques are in a good agreement both for the isotropic and anisotropic plates.

1. INTRODUCTION

The problem of analysis of thin plates weakened by cracks is especially important in the case of composite materials, due to the possibility of interlayer delaminating. However, crack growth parallel to the median surface of plate is less dangerous than the perpendicular crack growth, the problem of analysis of such element is still actual. This problem is studied in the monographs by Panasyuk et al., (1975), Marchuk and Homyak (2003), Serensen and Zaytsev (1982), Cherepanov (1983), etc. Some of the problems for edge cracks are solved by numerical methods. One can see them in the well-known handbook edited by Murakami (1987). In the study of Gnuni and Yegnazarian (2002) stability and bending problems of thin plates containing internal cracks are examined under the classical bending theory conditions. In the present work, the problem of cylindrical bending of plate with internal crack is solved basing on the equations of the improved theory of the middle thickness plate bending (Shvabyuk, 1974). The influence of transversal anisotropy and length of the crack on stress and displacement of the plate is studied.

2. STATEMENT OF THE PROBLEM. BOUNDARY CONDITIONS

Cylindrical bending of the plate of a thickness $2h$ is considered. The plate is hinge-supported on the edges $x = \mp a$. The plate is weakened by a symmetric tunnel internal crack (at $-l \le x \le l$), which is placed at the depth of $z = h - h_0$ parallel to the median surface (Fig. 1).

The plate is bended with the uniform load q, which is applied at the outer surface $z = -h$. To solve the stated problem one can utilize the technique (Gnuni and Yegnazarian, 2002), according to which the plate is formally decomposed into two domains with different bending rigidities: the domain containing a crack, which cylindrical rigidity equals the algebraic sum of rigidities of the upper and lower plate elements:

$$D_1 = D_1^- + D_1^+ = \delta D \qquad (1)$$

$$(\delta = 1 - 3\beta + 3\beta^2,\ \beta = h_0/2h);$$

and a domain without a crack, which cylindrical rigidity (1) equals $D_2 = D = 2Eh^3/3(1-\nu^2)$. Thus, $D_1^+ = \tilde{E}(2h - h_0)^3/12 = (1-\beta)^3 D$ is a rigidity of the upper plate part over the crack; and $D_1^- = \beta^3 D$ is a rigidity of the lower plate part under the crack; $\tilde{E} = E/(1-\nu)^2$; E is an elasticity modulus; ν is a Poisson ratio.

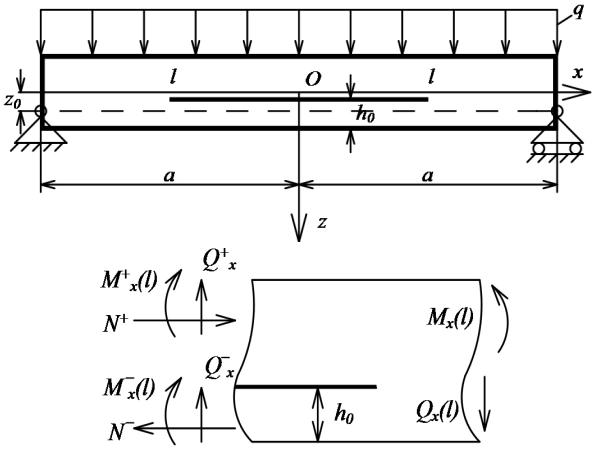

Fig. 1. Scheme of plate loading

It should be noted that the used technique can be applied in cases, when the plate model does not take into account the transverse compression, i.e. when vertical displacements do not depend on the transverse coordinate z. Within

this technique it is impossible to determine the real normal stress σ_x, which act in the upper and lower parts of the plate over and under the crack, respectively. Therefore, henceforward (with the use of equations (1), (2)) a model of plates of medium thickness (Shvabyuk, 1974), which utilize the improved equations of bending, is used. Corresponding equations for the vertical displacement $W(x,z)$ and normal stress σ_x allow studying the stress-strain state more precisely and satisfy the boundary conditions for each part of the plate both on the domains' interface and on the faces of the plate.

Assume that the contact pressure p, which acts on the crack faces is constant along the whole crack and such that it can be obtained using the displacement of the middle surface w_l of the lower part of the plate under the crack by classic formula for deflection under cylindrical bending: $p = D_1^- w_l^{\mathrm{IV}}$. For the upper part of the plate and for the whole cracked domain this equation can be written through corresponding displacements w_u and w in the following form: $q - p = D_1^+ w_u^{\mathrm{IV}}$ and $q = (D_1^+ + D_1^-)w^{\mathrm{IV}} = \delta D w^{\mathrm{IV}}$. Neglecting on this stage of the transversal compression ($w_l = w_u = w$) one can obtain an approximate equation for contact pressure p on the crack faces:

$$p = \frac{D_1^- q}{D_1^+ + D_1^-} = \frac{\beta^3 q}{1 - 3\beta + 3\beta^2}. \tag{2}$$

Taking into account that $\sigma_Z = -p$ and substituting $\beta = 1/2(1 - z/h)$ in the equation (2) one can obtain expression for contact stress σ_Z as a function of transversal coordinate z:

$$\sigma_z = \frac{q}{2}\frac{(z/h-1)^3}{(1+3z^2/h^2)}. \tag{3}$$

For estimation of stress-strain state of the plate, equations of improved model of transtropic (transversally-isotropic) plates (Shvabyuk, 1974), which take into account both the transverse shear and transverse compression, are used:

$$\begin{aligned} &D_i w_i^{\mathrm{IV}} = q_{i2} - \varepsilon_1 h_i^2 q_{i2}^{\mathrm{II}} - \varepsilon_2 h_i^4 q_{i2}^{\mathrm{IV}}, \\ &K_i' w_{i\tau}^{\mathrm{II}} = -q_{i2}, \quad E u_i^{\mathrm{II}} = -\nu''(1+\nu) q_{i1}^{\mathrm{I}}, \end{aligned} \tag{4}$$

where: $D_i = D = I\tilde{E}$, $I = 2h^3/3$, $K' = 4G'h/3$, $q_{i2} = q^-$, $q_{i1} = -0{,}5q^-$, u_i, $w_i, w_{i\tau}$, $h_i = u$, w, w_τ, h for the domain $|x| > l$; u_i, $w_i, w_{i\tau} = u_u$, $w_u, w_{u\tau}$; $q_{i1} = q_{u1} = (\sigma_Z(h - h_0) - q^-)/2 = -(p + q^-)/2$; $q_{i2} = q_{u2} = q^- + \sigma_Z(h - h_0) \equiv q^- - p = q(1 - (\beta^3/(1 - 3\beta + 3\beta^2)))$; $\beta = h_0/2h$; $D_i = D_1^+ = I_1^+\tilde{E}$; $I_1^+ = 2h(1-\beta)^3/3$; $h_1 = h_1^+ = (1 - \beta)$ or $D_i = D_1^- = I_1^-\tilde{E}$, $I_1^+ = h_0^3/12$; $K'_l = 2G'h_0/3$; $q_{i1} = q_{l1} = -0{,}5p$; $q_{i2} = q_{l2} = q\beta^3/(1 - 3\beta + 3\beta^2)$; u_i, $w_i, w_{i\tau}$, $h_i = u_l$, $w_l, w_{l\tau}$, $h_0/2$ for the domain $|x| \le l$; $\varepsilon_2 = 1/20(1-\alpha)\tilde{E}/E'$, $\tilde{E} = E/(1 - \nu^2)$; $\alpha = 0{,}5\nu'' G'/G$; E, E', G', ν'' are elastic moduli and Poisson ratio of plate material in the longitudinal and transverse (with primes) directions; $q^- = q$ is a distributed load applied to the upper surface of the plate ($z = -h$); u is a horizontal displacement of the median surface of the plate; w, w_τ are total and shear components of vertical displacement of plat median surface; Roman numeral superscripts of w, w_τ, u and q_1, q_2 denote the order of derivative by the variable x; subscripts "u" and "l" denote respectively upper and lower parts of the plate at the cracked domain; $2h$ is a height of cross-section of the plate; h_0 is a thickness of the plate part which is under the crack. Further, the case of $q^+ = 0$ is considered.

Expressions for stresses σ_x, σ_z and displacements $U(x,z)$, $W(x,z)$ of the plate outside the cracked domain, according to this model are as follows (Shvabyuk, 1974):

$$\begin{aligned} &\sigma_x = \frac{N_x}{2h} + \frac{M_x}{I} z \\ &+ \frac{z\left(z^2 - 0.6h^2\right)}{3I(1-\nu)}\left(\frac{G}{G'} - \nu''\right)\left(q_2 - 0.5q_2'' h^2 \frac{G'}{E'}\right); \\ &\sigma_z = q_1 + \frac{1}{4}\left(3\frac{z}{h} - \frac{z^3}{h^3}\right)\cdot q_2; \\ &q_1 = \frac{1}{2}(q^+ - q^-), \quad q_2 = (q^+ + q^-); \\ &U(x,z) = u(x) \\ &- z\left(\frac{dw}{dx} - \frac{dw_\tau}{dx}\left(1 - (1-\alpha)\frac{z^2}{3h^2}\right)\right) + \frac{(1-\alpha)}{8E'h}\frac{dq_2}{dx} z^3; \\ &W(x,z) = \omega(x) \\ &+ 2\alpha_0 z \cdot \frac{q_1}{E'} + A' \cdot \frac{d^2 w}{dx^2}\cdot\frac{z^2}{2} + \frac{\alpha_0 \cdot q_2}{8E'h}\cdot B(z), \end{aligned} \tag{5}$$

where: $B(z) = 6A_2 z^2 - A_3 \frac{z^4}{h^2}$; $A' = \frac{\nu''}{(1-\nu)}$;

$$\alpha_0 = 0.5 - \nu' \cdot A', \quad \tilde{w} = w + 1.5\varepsilon_2 q_2 h/\tilde{E}, \quad A_2 = 1 + \frac{A'E'}{2\alpha_0 G'};$$

$$A_3 = A_2 - \frac{\nu'' A' E'}{4\alpha_0 G};\ M_x = \int_{-h}^{h} z\sigma_x dz = -D\frac{d^2\tilde{w}}{dx^2} - \varepsilon_1 h^2 q_2,$$

$$Q_x = K'\frac{dw_\tau}{dx},\ N_x = \int_{-h}^{h}\sigma_x dz = 2\tilde{E}h\frac{du}{dx} + 2A'hq_1$$

are a bending moment, transverse and longitudinal forces in the plate; u is a tangential displacement of median surface of the plate.

The system of equations (4) is solved separately for each domain of the plate. Herewith, the corresponding boundary conditions are satisfied joining the solutions for each section, and the conditions of problem symmetry are taken into account.

In particular, for the domain $|x| > l$ the following relations hold:

$$\begin{aligned} &w = C_0 + C_2 x^2 + qx^4/(24D); \\ &w_\tau = C_\tau - qx^2/(2K');\ u = \nu''(1+\nu)qx/(2E) + R_0 \end{aligned} \tag{6}$$

For the domain $|x| \le l$, if it concerns the lower part of the plate under the crack, which face is loaded with

the normal stress $\sigma_Z(h-h_0)=-q\beta^3/(1-3\beta+3\beta^2)$, the displacement (3) are as follows:

$$w_l = C_{l0}+C_{l2}x^2+q_{l2}x^4/\left(24D_1^-\right);$$
$$w_{l\tau} = C_{l\tau}-q_{l2}x^2/\left(2K_l'\right);\ u_l = R_1x+R_{l0} \tag{7}$$

Here constants $C_0, C_2, C_\tau, R_0, C_{l0}, C_{l2}, C_{l\tau}, R_1, R_{l0}$ are obtained using the boundary conditions on the edge $x=a$ of the plate:

$$w(a)=M_x(a)=N_x(a)=0;\ Q_x(a)=-qa \tag{8}$$

and joining the solutions on the cracked domain boundary $x=l$ for upper and lower parts of the plate, which are studied as separate objects, loaded (except external loading) with additional surface contact pressure p in the cracked domain. For example, for the lower part of the plate:

$$w_l(l)=W(l,h-h_0/2);\ u_l(l)=U(l,h-h_0/2);$$
$$\sigma_x^-(l,h_0/2)=\sigma_x(l,h);\ N_x^-(l)=\int_{h-h_0}^{h}\sigma_x dz, \tag{9}$$

where:

$$\sigma_x^-\left(x,z^-\right)=\frac{N_x^-}{h_0}+\frac{M_x^-}{I^-}z^-$$
$$+\frac{z^-\left((z^-)^2-0.15h_0^2\right)}{3I^-(1-\nu)}\left(\frac{G}{G'}-\nu''\right)\left(q_{l2}-0.125q_{l2}''h_0^2\frac{G'}{E'}\right);$$

$$N_x^- = h_0\tilde{E}u_l' + h_0A'q_{l1};\ M_x^- = -D_1^-\tilde{w}_l''-0.25\varepsilon_1h_0^2q_{l2};$$

$$Q_x^-(l)=Q_x(l)+q_{u2}l,\ Q_x(l)=-ql;\ z^-=z-h+h_0/2$$

is a thickness coordinate of the lower plate part under the crack.

Satisfying the boundary conditions (5), one can obtain the factors C_0, C_2, C_τ along with the equations for the bending moment M_x and displacements w and w_τ in the uncracked domain:

$$C_0 = 5qa^4/(24D)+q\varepsilon_1a^2h^2/(2D),$$
$$C_2 = -qa^2/(4D)-q\varepsilon_1h^2/(2D),$$

$$C_\tau = qa^2(1+2\varepsilon_1h^2/a^2)/(2K');$$

$$M_x = q(a^2-x^2)/2;\ \ Q_x(x)=-qx; \tag{10}$$

$$w = q(x^4-a^4)/(24D)$$
$$+qa^2\left(a^2-x^2\right)(1+2\varepsilon_1h^2/a^2)/(4D);$$

$$w_\tau = qa^2(1+2\varepsilon_1h^2/a^2)/(2K')-qx^2/(2K')$$

Utilizing conditions (6) one receives the rest of unknown factors:

$$C_{l0}=W(l,h-h_0/2)-C_{l2}l^2-q_{l2}l^4/\left(24D_1^-\right);$$

$$C_{l2}=-(2M_{lx}(l)+q_{l2}l^2+0.5\varepsilon_1q_{l2}h_0^2)/\left(4D_1^-\right);$$

$$R_0=\left(R_1-\frac{A'q}{2\tilde{E}}\right)l+\frac{3}{4}\frac{qla^2}{\tilde{E}h^2}\left(\frac{l^2}{3a^2}-2\varepsilon_1\frac{h^2}{a^2}-1\right)+\frac{ql}{4G'}f(\beta)$$

$$R_1=N_{lx}(l)/\left(\tilde{E}h_0\right)-A'q_{l1}/\tilde{E};\quad C_{l\tau}=-\frac{2D^-}{K_l'}C_{l2};$$

$$R_{l0}=0;\quad f(\beta)=(1-\beta)[3-(1-\beta)^2(1-\alpha)];$$

$$W(l,h-h_0/2)=w(l)$$
$$+3\nu''(1+\nu)(1-\beta)^2\left(\frac{l^2}{h^2}-\frac{a^2}{h^2}-2\varepsilon_1\right)\frac{qh}{8E}$$
$$-\alpha_0(1-\beta)[8-f_1(\beta)A_2-\tilde{A}_2]\frac{qh}{8E'}; \tag{11}$$

$$\tilde{A}_2=\frac{(\nu'')^2(1-\beta)^3E'}{2(1-\nu-2\nu'\nu'')G};$$

$$N_x^-(l)=3\beta(1-\beta)M_x(l)/h-\frac{(G/G'-\nu'')qh}{4(1-\nu)}f_2(\beta);$$

$$M_x^-(l)=-N_x^-(l)h_0/6+0.25M_x(l)h_0^2/h^2$$
$$+0.2h_0^2(q-q_{l2})(G/G'-\nu'')/6(1-\nu);$$

$$f_1(\beta)=(1-\beta)(5+2\beta-\beta^2)];$$

$$f_2(\beta)=(1-2\beta)^2\left(2\beta^2-2\beta-0.1\right)+0.1.$$

3. BASIC EQUATIONS

Thus, proceeding from equations (6) – (8) the resultant forces and bending moment for the part of plate under the crack are as follows:

$$N_x^-(x)=N_x^-(l);\quad Q_x^-(x)=-q_{l2}x;$$
$$M_x^-(x)=M_x^-(l)+\frac{q_{l2}}{2}\left(l^2-x^2\right) \tag{12}$$

Taking into consideration that the longitudinal forces in the plate parts above the crack and under the crack ($x\le l$) are equal in magnitude and are opposite in sign $N_x^-(x)=-N_x^+(x)$, the value of the boundary bending moment $M_x^+(l)$ for the upper plate part $x\le l$ is obtained from the boundary condition of equality of normal stresses on the outer ($z=-h$) surface of the plate:

$$\sigma_x^+\left(l,-h(1-\beta)\right)=\sigma_x(l,-h) \tag{13}$$

Thus,

$$M_x^+(l)=-(1-\beta)N_x^-(l)h/3+(1-\beta)^2M_x(l)$$
$$+0.4h^2(1-\beta)^2(q-q_{u2})\left(\frac{G}{G'}-\nu''\right)\Big/3(1-\nu). \tag{14}$$

Together these quantities have to satisfy the equation of the moments' balance in the plate at the cracked domain (Fig. 1b):

$$M_x^+(l)+M_x^-(l)+dN_x^-(l)=M_x(l). \tag{15}$$

Here d is a distance between the points of application of longitudinal forces to the transverse crosscuts of the plate parts; $d=h$ for the linear distribution of the normal stresses σ_x.

It should be noted that the equation of the moments balance (12) includes a term, which takes into account the influence of longitudinal forces and which was not taken into consideration by G.P. Cherepanov in his "general theory of delaminating of the multilayer shells" (Cherepanov, 1983, p. 267). It was explained by the fact that the distance d was considered to be less then the linear size of the crack ($d \ll l$).

At the same time an account of the longitudinal forces $N_x^-(l)$, acting in the transverse cross-section of the upper and lower plate parts, allow, under the condition of static equilibrium of plate part, which is "cut" along crack plane, and on its extension, to determine the shear (tangent) force, acting at the extension of the crack:

$$T(l)=\int_l^a \tau_{xz}^0 dx = N_x^-(l). \tag{16}$$

where $\tau_{xz}^0=-3\beta(1-\beta)Q_x/h$ is a "background" stress acting on the horizontal cross-section of the plate without a crack but on its depth.

Approximate value of stress intensity factor (SIF) K_{II} can be determined by the formula:

$$K_{\mathrm{II}}=\tau_{xz}^0(l)\sqrt{2\pi l}=-3\sqrt{2}\beta(1-\beta)\frac{Q_x(l)}{h}\sqrt{\pi l}\,. \tag{17}$$

Maximal ($x=0$) normal displacements w_l (without account of compression), as well as a stress σ_x, that appear on the external and internal surfaces of the lower plate part can be written as follows:

$$w_l=\frac{5qa^4}{24D}\left[\frac{\left(\theta^2+2{,}4\varepsilon_1\beta^2h^2/a^2\right)\theta^2}{1-3\beta+3\beta^2}\right.$$
$$\left.+2.4\varepsilon_1(1-\theta^2)h^2/a^2+1-\theta^4\right];$$
$$\sigma_x^-(0,h_0/2)=\frac{3}{4}\frac{a^2}{h^2}\left(1-\frac{1-4\beta+3\beta^2}{1-3\beta+3\beta^2}\theta^2\right)q$$
$$+\frac{1}{5}\frac{(G/G'-\nu'')}{(1-\nu)}q; \tag{18}$$
$$\sigma_x^-(0,-h_0/2)=\frac{3}{4}\frac{qa^2}{h^2}[(1-2\beta)(1-\theta^2)$$
$$-\frac{\beta\theta^2}{1-3\beta+3\beta^2}]-\frac{1}{4}\frac{(G/G'-\nu'')}{(1-\nu)}q\left(\frac{1}{\beta}f_2(\beta)+\frac{4}{5}\right).$$

In the case, when the crack is placed along the median surface of the plate ($\beta=0{,}5$; $h_0=h$), edge bending moments $M_{ux}(l)$, $M_{lx}(l)$ and longitudinal force $N_{lx}(l)$, acting at the edges of plate parts in the cracked domain, are expressed through the bending moment $M_x(l)$ of the whole plate by the following formulas:

$$M_x^-(l)=M_x^+(l)=\frac{1}{8}M_x(l)+\frac{qh^2}{48}\frac{(G/G'-\nu'')}{(1-\nu)};$$
$$N_x^-(l)=\frac{3}{4}M_x(l)/h-\frac{qh}{40}\frac{(G/G'-\nu'')}{(1-\nu)} \tag{19}$$

Consider an extreme case, when the crack is located on the median surface of a plate. Formulas for maximal normal stresses (in the cross-section $x=0$) on the internal and outer surfaces of the plate parts, divided by the crack, take the following form:

$$\sigma_x(0,\pm h)=\pm\frac{3}{4}\frac{a^2}{h^2}\left(1+\theta^2\right)q\pm\frac{1}{5}\frac{(G/G'-\nu'')}{(1-\nu)}q$$
$$\sigma_x(0,\mp 0)=\mp\frac{3}{2}\frac{a^2}{h^2}\theta^2q\mp\frac{1}{4}\frac{(G/G'-\nu'')}{(1-\nu)}q \tag{20}$$

where $\theta=l/a$ is relative length of the crack; upper and lower signs of notations "$\pm$" and "$\mp$" in formulas (17) correspond to the outer surfaces of the lower and upper parts of the plate, respectively. Stress $\sigma_x(0,\mp 0)$ acts on the internal surfaces of the plate parts located under (sign "–") and above (sign "+") the crack.

Maximal displacement of the median surface of the lower part of the plate can be written in the following form:

$$w_l=\frac{5qa^4}{24D}\left[1+3\theta^4-0.3A'(1-\theta^2)\frac{h^2}{a^2}\right.$$
$$\left.+2.4\varepsilon_1\left(1-0.25A'h^2/a^2\right)\frac{h^2}{a^2}\right]-\frac{\alpha_0qh\tilde{B}}{16E'}, \tag{21}$$

where $\alpha_0=\frac{1}{2}-\frac{\nu'\nu''}{1-\nu}$, $\tilde{A}=5.125-\frac{\nu''(46E'/G'+\nu''E'/G)}{16(1-\nu-2\nu'\nu'')}$.

In expression (18) terms with multipliers h^2/a^2 and α_0 are corrections to the classical thin plate theory, that take into account transverse shear and compression. Assuming that they are zero ones, one can obtain the simplest approximate expression for calculation of the vertical displacement of a thin plate containing a crack at its median surface:

$$w_l=\frac{5qa^4}{24D}\left(1+3\theta^4\right). \tag{22}$$

If the cylindrical stiffness D in the latter equation is replaced with the value EI, one obtains the formula for a vertical displacement of the beam of a constant section containing a crack along the middle line. However, this expression is not precise enough for thick plates and short beams, especially those made of composite materials. In this case it is necessary to use the complete formula (18) along with the correspondent expression (2) for displacement W, utilizing certain corrections for parameters q_1, q_2 and h.

This problem can be also solved using a hypothesis based on one of the Timoshenko-type theories (taking into account the expression for σ_z). However, in this case for-

mulas (15) – (17) don't contain second term, which accounts the influence of transverse shear and compression on the nonlinearity of distribution of the normal stress σ_x. Correction, which accounts the transverse shear and compression, in formulas (15) – (17) is a constant value, though it is not constant for stresses on the external and internal surfaces of the parts of the plate and it also depends on the plate material.

4. NUMERICAL MODELING OF THE PROBLEM. DUAL BOUNDARY ELEMENT METHOD

Numerical modeling of the considered problem is used for verification of the obtained results. Dual boundary element method (Portela et al., 1992) for the plane elastostatics is utilized for this purpose. It is well-known that classical boundary element method degenerate when considering crack problems due to the lack of equations considering load of crack faces (Portela et al., 1992). Therefore, the dual boundary element method (Portela et al., 1992) was developed, which proceed with a system of $2n$-equations basing on Somigliana identity: n displacement equations (as in classical BEM) and additionally n stress equations obtained from the Somigliana identity by differentiation. Thus, for the problems of cracks theory, dual BEM integral equations take the following form (Portela et al., 1992):

– for collocation point "**y**" placed on a smooth surface Γ of a solid –

$$\begin{aligned}
&\frac{1}{2}u_i(\mathbf{y}) = \int_\Gamma U_{ij}(\mathbf{x},\mathbf{y})\,t_j(\mathbf{x})\,d\Gamma(\mathbf{x}) \\
&-\int_\Gamma T_{ij}(\mathbf{x},\mathbf{y})\,u_j(\mathbf{x})\,d\Gamma(\mathbf{x}) \\
&+\int_{\Gamma_C^+} U_{ij}(\mathbf{x},\mathbf{y})\,\Sigma t_j(\mathbf{x})d\Gamma(\mathbf{x}) \\
&-\int_{\Gamma_C^+} T_{ij}(\mathbf{x},\mathbf{y})\,\Delta u_j(\mathbf{x})d\Gamma(\mathbf{x});
\end{aligned} \tag{23}$$

– for collocation point "**y**" placed on a smooth surface Γ_C^+ of a crack:

$$\begin{aligned}
&\frac{1}{2}\Sigma u_i(\mathbf{y}) = \int_\Gamma U_{ij}(\mathbf{x},\mathbf{y})\,t_j(\mathbf{x})\,d\Gamma(\mathbf{x}) \\
&-\int_\Gamma T_{ij}(\mathbf{x},\mathbf{y})\,u_j(\mathbf{x})\,d\Gamma(\mathbf{x}) \\
&+\int_{\Gamma_C^+} U_{ij}(\mathbf{x},\mathbf{y})\,\Sigma t_j(\mathbf{x})d\Gamma(\mathbf{x}) \\
&-\int_{\Gamma_C^+} T_{ij}(\mathbf{x},\mathbf{y})\,\Delta u_k(\mathbf{x})d\Gamma(\mathbf{x}); \\
&\frac{1}{2}\Delta t_i(\mathbf{y}) = \int_\Gamma D_{ijk}(\mathbf{x},\mathbf{y})\,n_j^+(\mathbf{y})\,t_k(\mathbf{x})\,d\Gamma(\mathbf{x}) \\
&-\int_\Gamma S_{ijk}(\mathbf{x},\mathbf{y})\,n_j^+(\mathbf{y})\,u_k(\mathbf{x})\,d\Gamma(\mathbf{x}) \\
&+\int_{\Gamma_C^+} D_{ijk}(\mathbf{x},\mathbf{y})\,n_j^+(\mathbf{y})\,\Sigma t_k(\mathbf{x})d\Gamma(\mathbf{x}) \\
&-\int_{\Gamma_C^+} S_{ijk}(\mathbf{x},\mathbf{y})\,n_j^+(\mathbf{y})\,\Delta u_k(\mathbf{x})d\Gamma(\mathbf{x}).
\end{aligned} \tag{24}$$

Here $\mathbf{x}$ is an arbitrary point of the surface; U_{ij}, T_{ij}, D_{ijk}, S_{ijk} are the singular and hypersingular kernels of integral equations for plane problem of elasticity, which are explicitly written in Portela et al. (1992), u_i, t_i are the components of displacement and traction vectors; $\Delta u_i = u_i^+ - u_i^-$, $\Delta t_i = t_i^+ - t_i^-$, $\sum u_i = u_i^+ + u_i^-$, $\sum t_i = t_i^+ + t_i^-$; n_j^+ are the components of a unit normal vector to a surface Γ_C^+; signs "+" and "-" denote the values concerned with the surfaces Γ_C^+ and Γ_C^-, formed by a cut Γ_C. Subscripts in notations correspond to the projections of vectors on the axis of global coordinate system Ox_1x_2. Einstein summation convention is assumed. Kernels of integral equations for the plane problem elasticity at $\mathbf{x} \to \mathbf{y}$ possess the following singularities:

$$\begin{aligned}
&U_{ij}(\mathrm{x},\mathbf{y}) \sim \ln|\mathbf{x}-\mathbf{y}|, \quad T_{ij}(\mathrm{x},\mathrm{y}) \sim 1/\ln|\mathbf{x}-\mathbf{y}| \\
&D_{ijk}(\mathrm{x},\mathbf{y}) \sim 1/\ln|\mathbf{x}-\mathbf{y}|, \quad S_{ijk}(\mathbf{x},\mathbf{y}) \sim (1/\ln|\mathbf{x}-\mathbf{y}|)^2
\end{aligned} \tag{25}$$

For modeling of closed cracks, the equation (20) should be modified with account of additional conditions of zero value of normal displacement discontinuities and shear contact stresses on the mathematical cut Γ_C as follows:

$$\begin{aligned}
&\Delta u_n(\mathbf{y}) = \Omega_{1j}(\mathbf{y})\,\Delta u_j(\mathbf{y})\Big|_{\mathbf{y}\in\Gamma_C} \equiv 0 \\
&\tau = \Omega_{2j}(\mathbf{y})\,\Delta t_j(\mathbf{y})\Big|_{\mathbf{y}\in\Gamma_C} \equiv 0 \qquad \Sigma t_j(\mathbf{y})\Big|_{\mathbf{y}\in\Gamma_C} \equiv 0
\end{aligned} \tag{26}$$

Here components of rotation tensor Ω of the vectors equal:

$$\begin{aligned}
&\Omega_{11}(\mathbf{y}) = n_1(\mathbf{y}), \quad \Omega_{12}(\mathbf{y}) = n_2(\mathbf{y}), \\
&\Omega_{21}(\mathbf{y}) = -n_2(\mathbf{y}), \; \Omega_{22}(\mathbf{y}) = n_1(\mathbf{y})
\end{aligned} \tag{27}$$

Thus, equation (21) on a mathematical cut Γ_C should be solved for the unknown discontinuities $\Delta u_\tau = \Omega_{2j}(\mathbf{y})\Delta u_j(\mathbf{y})$ of tangent displacement and normal contact stress $p_n = -1/2\Omega_{1j}(\mathbf{y})\Delta t_j(\mathbf{y})$. Proceeding from this, the following system of integral equations can be obtained:

$$\begin{aligned}
&\frac{1}{2}\Sigma u_\tau(\mathbf{y}) = \Omega_{2i}(\mathbf{y})\Big[\int_\Gamma U_{ij}t_j\,d\Gamma - \int_\Gamma T_{ij}u_j\,d\Gamma \\
&-\int_{\Gamma_C^+} T_{ij}(\mathbf{x},\mathbf{y})\,\Omega_{2j}(\mathbf{x})\,\Delta u_\tau(\mathbf{x})d\Gamma(\mathbf{x})\Big], \\
&p_n(\mathbf{y}) = -n_i^+(\mathbf{y})\,n_j^+(\mathbf{y})\Big[\int_\Gamma D_{ijk}t_k\,d\Gamma(\mathbf{x}) + \int_\Gamma S_{ijk}u_k\,d\Gamma \\
&+\int_{\Gamma_C^+} S_{ijk}(\mathbf{x},\mathbf{y})\,\Omega_{2j}(\mathbf{x})\,\Delta u_\tau(\mathbf{x})d\Gamma(\mathbf{x})\Big], \\
&0 = \Omega_{2i}(\mathbf{y})\,n_j^+(\mathbf{y})\Big[\int_\Gamma D_{ijk}t_k\,d\Gamma(\mathbf{x}) + \int_\Gamma S_{ijk}u_k\,d\Gamma \\
&+\int_{\Gamma_C^+} S_{ijk}(\mathbf{x},\mathbf{y})\,\Omega_{2j}(\mathbf{x})\,\Delta u_\tau(\mathbf{x})d\Gamma(\mathbf{x})\Big].
\end{aligned} \tag{28}$$

The following numerical solution procedure for integral equations (20), (25) using the dual BEM is proposed. For evaluation of curvilinear integrals, curves Γ, Γ_C are divided into parts, which are approximated with the rectilinear sections Γ_q (boundary elements). Thus, equations (20), (25) are written as sums of integrals along boundary elements Γ_q. n nodal points $\mathbf{x}^{q,p}(p = \overline{1,n})$ are set on each element Γ_q. As a rule, discontinuous boundary elements (Portela et al., 1992), i.e. elements with no node placed at the end point of a boundary element, are used to solve crack theory problems.

Particularly, often used are rectilinear quadratic boundary elements with three nodes placed as follows: one in the center and the other two at the distance of $1/3$ of element length from the central point. This allows modeling of the non-smooth surfaces, because collocation point never coincide the corner or a brunching point of a cut Γ_C. Boundary functions t_i, u_i, p_n, Δu_τ are interpolated on element Γ_q using their node values as follows:

$$\left[\tilde{t}_i, \tilde{u}_i, \tilde{p}_n, \Delta\tilde{u}_\tau\right](\xi) = \sum_{p=1}^{n}\left[t_i^{q,p}, u_i^{q,p}, p_n^{q,p}, \Delta u_\tau^{q,p}\right]\phi^p(\xi) \quad (29)$$

$$\tilde{u}_i(\xi) = \sum_{p=1}^{n} u_i^{q,p}\phi^p(\xi) \quad (30)$$

where ξ is a parameter of a point position at the boundary element, defined on the interval $-1 \le \xi \le 1$: $d\Gamma_q = (L_q/2)d\xi = J_q d\xi$, J_q is a Jacobian of a variable change on Γ_q. For a rectilinear quadratic discontinuous boundary element ($n = 3$ the values of the parameter $\xi = \{-2/3; 0; 2/3\}$ correspond to its nodes $\mathbf{x}^{q,p}$. Thus, interpolation polynomials $\phi^p(\xi)$ are expressed as follows:

$$\phi^1 = \xi\left(\frac{9}{8}\xi - \frac{3}{4}\right)\quad \phi^2 = \left(1-\frac{3}{2}\xi\right)\left(1+\frac{3}{2}\xi\right)$$
$$\phi^3 = \xi\left(\frac{9}{8}\xi + \frac{3}{4}\right) \quad (31)$$

Thus, the system of singular integral equations is reduced to a system of linear algebraic equations, which is sought for the nodal values of boundary functions. Obtained solutions of the integral equation system are used for calculation of stress σ_x/q, displacement $\tilde{w} = w_l E/(2qh)$ and stress intensity factor (SIF) $K_{II}^* = K_{II}/\sqrt{\pi l}$.

5. NUMERICAL RESULTS

Analysis of numerical results of plane problem of elasticity and formula (17) for stresses σ_x allows to state that the growth of crack in a plate causes the increase of stresses in parts of the plate according to formulas (17) in compliance with quadratic parabola law, while plane elasticity behaves according to the rule close to hyperbola law. One can see that in the second case the growth is much slower. Therefore, formulas (17) should be modified by replacing parameter θ^2 with parameter θ^4 and written in the following form:

$$\sigma_x(0, \pm h) = \pm\frac{3}{4}\frac{a^2}{h^2}\left(1+\theta^4\right)q \pm \frac{1}{5}\frac{\left(G/G' - \nu''\right)}{\left(1-\nu\right)}q$$
$$\sigma_x(0, \mp 0) = \mp\frac{3}{2}\frac{a^2}{h^2}\theta^4 q \mp \frac{1}{4}\frac{\left(G/G' - \nu''\right)}{\left(1-\nu\right)}q \quad (32)$$

To prove that such modification is reasonable, the values of stress σ_x^-/q on the outer surface of the lower part of the plate is evaluated utilizing formula (17) and formula (28), placed in a separate column in bold font (for $\theta = 0$ and $\theta = 1$ they are the same), and using dual BEM for plane problem of elasticity (in brackets). These results are presented in Tables 1 and 2.

Tab. 1. Stress values in isotropic plate

$\frac{a}{h}$	σ_x^- / q (*isotropy*)			
	$\theta = 0$	$\theta = 0.5$		$\theta = 1$
5	18.95 (18.85)	23.64 (20.58)	***20.12***	37.7 (38.6)
10	75.20 (75.00)	93.95 (81.69)	***79.89***	150.2 (152.6)
20	300.2 (299.7)	375.2 (325.7)	***308.9***	600.2 (610.4)

Tab. 2. Stress values in transtropic plate

$\frac{a}{h}$	σ_x^- / q (*wood*)		
	$\theta = 0$	$\theta = 0.5$	$\theta = 1$
5	21.52 (21.03)	***22.69*** (22.69)	40.27 (38.30)
10	77.77 (76.51)	***82.46*** (83.35)	152.8 (148.6)
20	302.8 (301.7)	***321.52*** (328.7)	602.8 (596.3)

The value of contact pressure on crack faces, which is determined by stress σ_z completely coincides with corresponding numerical results of the plane problem of elasticity along the whole length of the cracks except a small area near the crack tips.

Fig. 2 shows plots of stress σ_x/q versus the transverse coordinate $z/2h$ for parameters $\theta = 0{,}5$ and $\theta = 0{,}9$, at $a/h = 10$, obtained using the improved formulas (28) (solid line), and the dual boundary element method of plane problem of elasticity (dashed line). Dash-dot line presents the corresponding plot for plate without a crack. Data, obtained by dual BEM of plane problem of elasticity, are presented in Fig. 2 in brackets.

Data analysis for stresses, presented in Tab. 1 and in Fig. 2 for isotropic and transtropic (wood) materials, prove that formulae of applied theory of medium thickness plates are quite precise (in comparison with numerical data of plane elasticity, the error is less than 2.5%) and convenient for calculations.

Analysis of formulas (15) – (19) shows that growth of crack length increases stresses and displacements in the plate up to the values which can appear in two separate plates put one onto another without friction. Then the stresses in them will increase twice and displacements in four times. Corrections, which account transverse shear and compression, are insignificant for stresses in case of isotropic material. At the same time these corrections may be important for transtropic materials (fiberglass plastics, wood, etc.). For example, for wood ($G/G' = 10; \nu'' = \nu = 0{,}3$), when $a/h = 0{,}5$; $\theta = 0{,}5$, errors of classical theory for the first and second formulas are as big as 12% and 37%, respectively. These errors are even bigger, when determining the maximal vertical displacement $w \cong w_l$. See comparative table for relative displacements $\tilde{w} = w_l E/(2gh)$ below (Table 2).

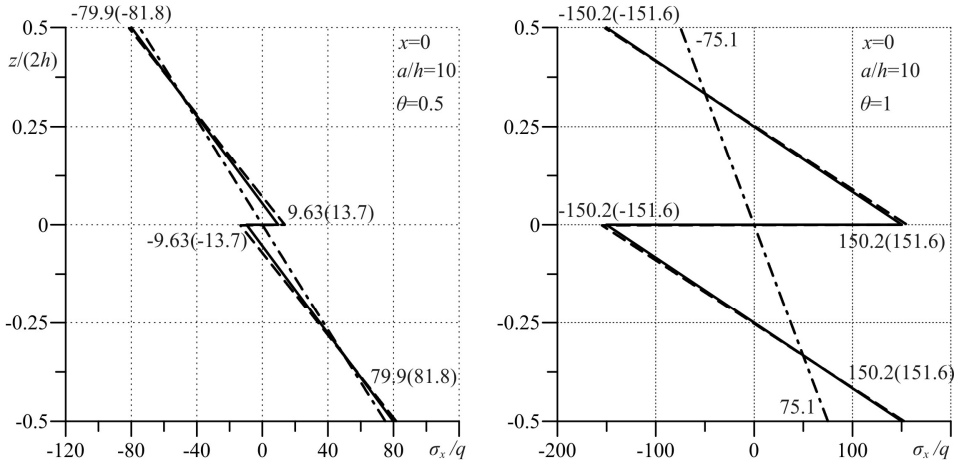

Fig. 2. Plots of stress σ_x/q against the transverse coordinate $z/2h$

Tab. 3. Values of vertical displacements for isotropic plate

$\frac{a}{h}$	$\tilde{w} = w_l E/(2qh)$ (isotropy)					
	$\theta = 0$ (*p.p.*)	$\theta = 0$	$\theta = 0.5$ (*p.p.*)	$\theta = 0.5$	$\theta = 1$ (*p.p.*)	$\theta = 1$
5	100.8	96.85(88.87)	105.4	114.3(105.5)	384.9	365.5
10	1459	1454(1422)	1522	1723(1688)	5917	5728
20	$22.86\cdot10^3$	$22.88\cdot10^3$	$23.79\cdot10^3$	$27.15\cdot10^3$	$94.13\cdot10^3$	$91.16\cdot10^3$

Tab. 4. Values of vertical displacements for wooden board

$\frac{a}{h}$	$\tilde{w} = w_l E/(2qh)$ (wood)						
	$\theta = 0$ (*p.p.*)	$\theta = 0$	$\theta = 0.5$ (*p.p.*)	$\theta = 0.5$	$\theta = 1$ (*p.p.*)	$\theta = 1$	$\theta = 1$ (*cl.*)
5	184.9	184.3	192.6	201.5	446.7	452.9	355.5
10	1755	1805	1840	2073	5910	6078	5688
20	$24.01\cdot10^3$	$24.28\cdot10^3$	$25.10\cdot10^3$	$28.56\cdot10^3$	$90.92\cdot10^3$	$92.56\cdot10^3$	$91.0\cdot10^3$

Data in Tables 3 and 4 in brackets present the displacements calculated according to the simplified formula (16) for thicknesses $a/h = 5; 10$ without account of transverse shear and compression. These data are shown in the last column of Table 3 and are the same both for transtropic (wood) and for isotropic materials. Values, calculated using the dual boundary element method of plane problem of elasticity, are put into columns (p.p.). The laws of maximum result deviation of displacements $\tilde{w}$, calculated using the applied theories of plates, are similar to those detected while stress calculations. Thus, the real character of displacements growth in a plate caused by crack length increase are, in fact, much slower than it is determined by the formulas of applied theories of plates. This is of special importance for the following values of parameter θ: $0{,}5 \le \theta \le 0$.

6. CONCLUSION

This paper obtains the analytic dependences convenient for engineering applications and calculation of stresses and displacements in isotropic and transversally-isotropic plates, damaged by horizontal cracks. These results allow predicting with enough practical accuracy the strength and rigidity of plates using the geometrical parameters of a crack in a plate, as well as physical characteristics of material and its transversal anisotropy.

REFERENCES

1. **Cherepanov G.P.** (1983), *Fracture mechanics of composite materials*, Nauka, Moscow (in Russian).
2. **Gnuni V.C., Yegnazarian T.A.** (2002), On strength of plates weakened by cracks, *In collected articles «Optimal control over durability and strength of mechanical systems»*. Yerevan. Publishing house of Yerevan State University, 37-41 (in Russian).
3. **Marchuk M.V., Homyak M.M.** (2003), *On a mixed finite element analysis calculation of composite laminated shells and plates*, Pidstryhach Institute for Applied Problems of Mechanics and Mathematics NAS of Ukraine, L'viv. (in Ukrainian).
4. **Murakami Y. ed.** (1987) *Stress intensity factors handbook*, Vols. 1, 2. – Pergamon Press, New York.
5. **Panasyuk V.V., Savruk M.P., Datsyshyn A.P.** (1975), *Distribution of strains in crack areas in plates and membranes*, Naukova Dumka, Kyiv (in Russian).
6. **Portela A., Aliabadi M.H., Rooke D.P.** (1992) The dual boundary element method: Effective implementation for crack problems, *Int. J. Numer. Meth. Engng.*, 33, P. 1269–1287.
7. **Serensen S.V., Zaytsev G.P.** (1982), *Bearing capacity of thin-slab structures built of reinforced plastics with defects*, Naukova Dumka, Kyiv (in Russian).
8. **Shvabyuk V.I.** (1974), On one variant of generalized theory of transversally-isotropic plates, *Prikladnaya Mekhanika*, V. 10, No. 11, P.87-92 (in Russian).

TESTING OF A COMPOSITE BLADE

Paweł SKALSKI*

*Center of New Technologies, Institute of Aviation, Al. Krakowska 110/114, 02-256 Warszawa

pawel.skalski@ilot.edu.pl

Abstract: The research presented in this paper focuses on the investigation of helicopter composite blade. The object of tests is a blade from main rotor of the IS-2 helicopter. The author describes briefly basic elements of composite blade manufactured at the Institute of Aviation in Warsaw. The composite blade was investigated by the Experimental Modal Analysis (EMA) to evaluate dynamic properties of tested structure. Based on the experimental data collection, dynamic properties of a research object were estimated. The modal parameters have been estimated using PolyMAX – module of LMS Test.Lab software.

1. INTRODUCTION

The helicopter blade is a very important part of main rotor. It is a light weight construction but has to sustain heavy loads and harsh environment conditions. There is a need to improve the characteristics of helicopter blades, accompanied by dynamic loads. Application of new methods for testing the dynamic susceptibility can divide a complex system into simpler components, allowing to analyze the impact of changes in susceptibility of individual items on the general characteristics of complex vibration system and the selection parameters of the system during its formation.

Modal analysis is a widely used technique in practice, the study of dynamic properties of the structure. As a result of modal analysis the modal model is obtained as a set of frequencies own form of vibration and damping coefficients. Knowing these parameters allows the prediction of the behaviour of an object due to any imbalances (Ewins, 2000; Heylen et al., 1998).

Modes are used as a simple and efficient means of characterizing resonant vibration. Resonant vibration is caused by an interaction between the inertial and elastic properties of the materials within a structure (Ewins, 2000; Heylen et al., 1998).

The research presented in this paper focuses on composite structure tests. The basic methodology which is used is the Experimental Modal Analysis (EMA). The EMA technique is an established tool for the identification of dynamic properties of structures (Luczak et al., 2010).

As in most practical applications of modal analysis is required for multi-channel experiment and the complex calculations associated with the processing of measured signals and estimation of model parameters. The first application of the method of modal analysis has already been documented in the late 40's, and their rapid development occurred in the 80's, due to the development of computer techniques (Ewins, 2000; Heylen et al., 1998; Kaczmarczyk et al., 2008).

In the present study performed a computer-aided measurement and subsequent analysis were used LMS Test.Lab software. LMS Test.Lab offers a complete portfolio for noise and vibration testing, including solutions for acoustic, rotating machinery, structural testing, environmental testing, vibration control, reporting and data management (LMS Company – marketing materials).

The software naturally follows the test campaign process, guiding for measurement and analysis parameters. Its includes a lot of different modulus, which are useful in a computer-aided design (CAD), like, LMS Test.Lab Geometry and LMS Test.Lab Modification Prediction. LMS Test.Lab Geometry provides fast wireframe generation and full 3D visualization of test and analysis results. Point coordinates are defined in Excel-like tables, while connections and surfaces are graphically defined in the display. The geometry can be copy/pasted. LMS Test.Lab Modification Prediction evaluates structural modifications (mass, stiffness and damping). Based on the modal model and on the modification element definition, a modal of the structure can be calculated. The effect of such a set of modifications on a modal model can be calculated and compared to the original situation (LMS Company – marketing materials).

2. RESEARCH OBJECT

The object of the investigation is a blade from main rotor of the IS-2 helicopter presented in a work stand (Fig. 1). Dimensions of the investigated object are: length 3,25 m, width 0,20 m. Approximate weight of the structure is 12,60 kg.

The tested blade was manufactured at the Institute of Aviation. The production process is very complicated. Blades are formed by combining two halves into one whole, which is followed is annealed in the oven (Fig. 5).

The basic instrumentation used in the manufacture of rotor blades are moulds (Fig. 2): a upper mould part and a lower mould part. Both moulds have a similar struc-

ture. A working surface of moulds is made of a rigid laminar coating of fiber-epoxy composite covered with gelcoat. The high rigidity of the surface of moulds ensures proper representation of the external geometry of blades in the cross-section (Fig. 6).

Composite blade base on carbon, fiber composites, roving, epoxy and lead (Fig. 3), (Fig. 4).

Fig. 1. Blade mounted in a test stand

Fig. 2. Moulds of blade

Fig. 3. Mould with fiber composite

Fig. 4. Mould with roving and carbon composite

Fig. 5. Upper and lower halves of a blade part in oven

Fig. 6. Cross-section of a composite blade

Performed helicopter blade is controlled by thermography system to detect defects such as a delamination, air bubbles (Kaczmarczyk et al., 2008; Meinlschmidt and Aderhold, 2006; Świderski, 2009). Proven blade structure is released for vibration testing, so as to exclude the effect of defects on the vibration tests. Thermography is one of the most common non-destructive testing method of composites. It is used to detect material defects and evaluate the structure of materials without having to change

their performance (Kaczmarczyk et al., 2008; Meinlschmidt and Aderhold, 2006; Świderski and Vavilov, 2010). A result sample of the experiment with a thermography camera is presented in Fig. 7.

Fig. 7. Thermal image taken from thermography measurement

In a vibration test campaign the following measurement and analysis tools were used (Fig. 8):

- 1 electromagnetic shaker, with impedance heads incorporating acceleration and force sensor in the same housing to measure reference point FRF's;
- 4 triaxial modal piezoelectric accelerometers PCB;
- 16 channels in fronted LMS SCADAS Mobile with computer a Test.Lab acquisition and analysis suite;
- bandwidth 128 Hz, resolution 0,05 Hz.

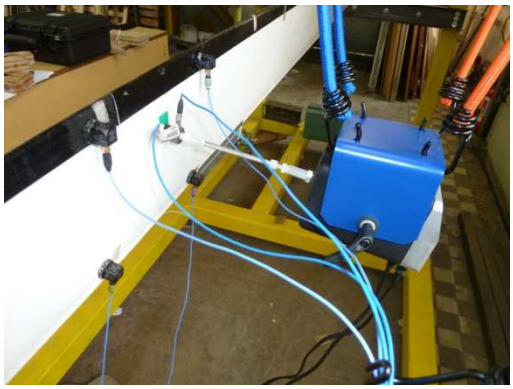

Fig. 8. Vibration test setup of a blade from main rotor of the IS-2 helicopter

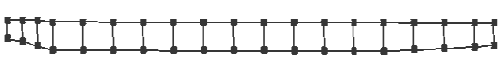

Fig. 9. Cartesian coordinate system for piezoelectric sensors in LMS Test.Lab Geometry

The shaker was attached to the structure using a stinger (long slender rod), so that the shaker will only impact force to the structure along the axis of the stringer, the axis of force measurement.

A dense grid of measurement points is defined all over the blade surface, in order to successfully identify the dynamic properties of this structure. Measurement points are set with distance of 0,20 m one from each other in the spanwise (X) direction and 0,20 m in the edgewise direction (Z). Geometry definition for blade is presented on Fig. 9. It consists of 39 points, 38 of which are acquisition locations and the remaining 1 is the reference point.

3. EXPERIMENTAL RESULTS AND ANALYSIS

The measurement was done in "sets" which means not all the points were measured at the same time. As a consequence a number of partial modal models were estimated for each of the set. Next the partial models were merged into a global model by means of multi-run modal synthesis (Luczak et al., 2010). Modal models have to be validated to provide confident information about the structural dynamics of a research object (Fig. 10).

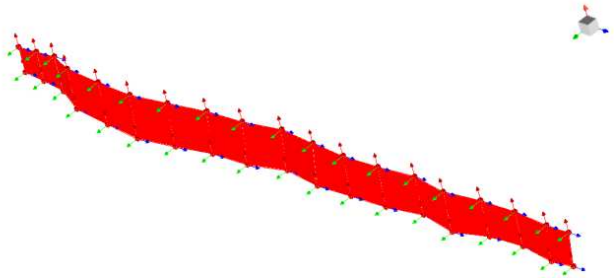

Fig. 10. View of measured blade in LMS Test.Lab Geometry

Due to a high number of measurement points and limited number of piezoelectric sensors applied to the structure (in order to reduce the mass loading phenomena), a large number of test was carried out. Random signal were applied.

Based on the experimental data collection, modal models were estimated. The modal parameters have been estimated using PolyMAX (Polyreference Modal Analysis eXtended) algorithm provided by LMS software. Fig. 11 presents a window of PolyMAX in LMS Test.Lab (LMS Company – marketing materials).

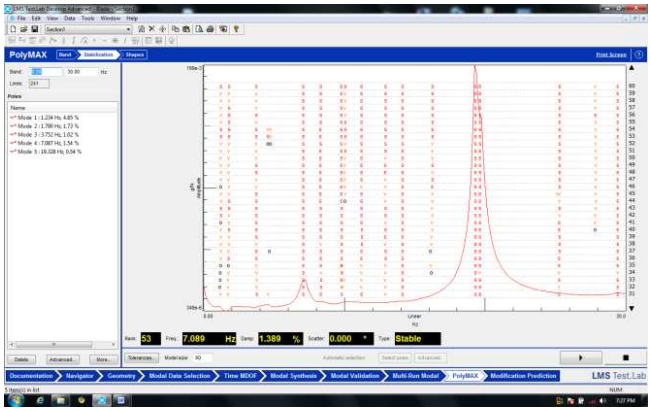

Fig. 11. Stabilization diagram obtained by LMS PolyMAX method

PolyMAX is an advanced modal parameter estimation technique that offers superior identification of modal pa-

rameters. Its main advantage consists in damped structure identification, where more modes can be identified into a higher frequency range (LMS Company – marketing materials).

During results analysis, the experimental natural modes and damping were estimated: flapwise 2nd – frequency 7,0 Hz and damping 1,54 %; flapwise 4th – frequency 19,0 Hz and damping 0,54 %; chordwise 1st – frequency 34,4 Hz and damping 0,44 %; torsion 1st – frequency 43,0 Hz and damping 0,60 %.

Visual inspection of the mode shapes is presented on Fig. 12, Fig, 13, Fig. 14.

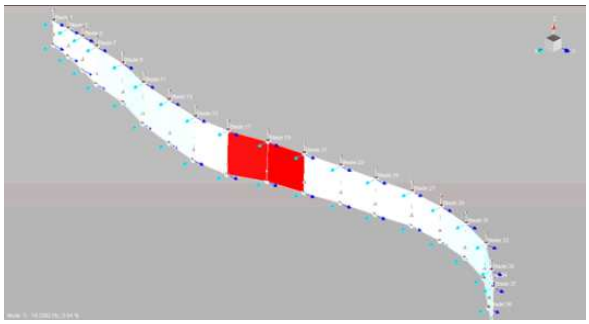

Fig. 12. Identified flapwise 4th

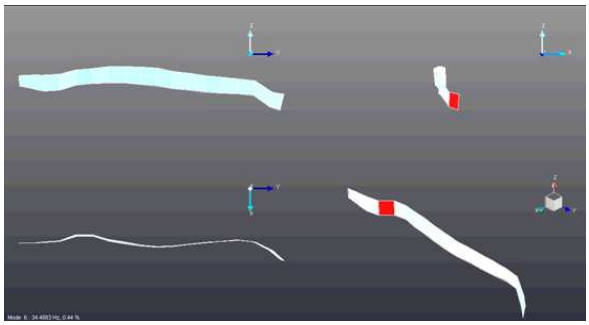

Fig. 13. Identified chordwise 1st

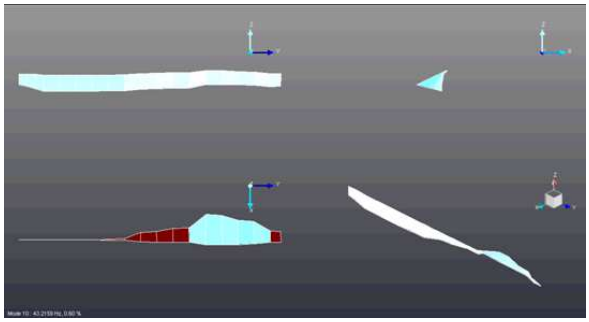

Fig. 14. Identified torsion 1st

Fig. 15. Mass modification of blade in LMS Test.Lab Modification Prediction

Using LMS Test.Lab Modification Prediction we can change i.e. a mass of the blade in this case. We change the mass and we change the modal modes. A comparison between blade with additional mass and regular blade mass is presented on Fig. 15.

4. CONCLUSIONS

This paper presents some aspects of the multidisciplinary and interdisciplinary research oriented for the test data variability. It was presented a test campaign lead on the composite material main rotor helicopter blade. Test setup include measurement technique of contact type. Experimental test data examples are shown and used for modal models estimation.

Experimental Modal Analysis (EMA) is currently one of the key technologies in structural dynamics analysis. Based on the academic fundaments of system identification, it has evolved to become a "standard" approach in mechanical product development. The PolyMAX method brings a revolutionary modal parameter estimation technique that is easy to use, quick to perform, substantially reduces operator-dependent judgment, and that delivers high quality modal parameter estimation, even on complex data.

Varying mass loading or constraint effects between partial measurements may determine several errors on the final conclusions. Mass loading effect from adding piezoelectric accelerometers and instrumentation should be analysed In next tests, thought a comparison between the mentioned contact and non-contact measurement techniques (i.e. laser vibrometer).

REFERENCES

1. **Ewins D. J.** (2000), *Modal testing: theory, practise, and application*, Baldock, Research Studies Press, pp. xiii, 562.
2. **Heylen W., Lammens S., Sas P.** (1998), *Modal analysis theory and testing*, Katholieke Universiteit Leueven, Department Werktuigkunde.
3. **Kaczmarczyk J., Rojek M., Wróbel G., Stabik J.** (2008), A model of heat transfer in composites subjected to thermographic testing, *Archives of Materials Science and Engineering*, Vol. 31, Isssue 2, 105-108.
4. **LMS Company** – marketing materials.
5. **Luczak M., Dziedziech K., Vivolo M., Desmet W., Peters B.** (2010), Contact versus non-contact of a helicopter main rotor composite blade, *AIP Conf. Proc*., Vol. 1253, 352-360.
6. **Meinlschmidt P., Aderhold J.** (2006), Thermographic inspection of rotor blades, *ECNDT*, Tu. 1.5.3, 1-9.
7. **Świderski W.** (2009), Nondestructive testing methods and techniques of composite materials by IR thermography, *Problemy Techniki Uzbrojenia* (in polish), Z. 112, nr 8, 75-92.
8. **Świderski W., Vavilov V.** (2010), Characterization of defects in composite materials by IR thermography non-destructive testing methods, *Problemy Techniki Uzbrojenia* (in polish), Z. 114, nr 4, 33-56.

STRUCTURE AND ADHESIVE PROPERTIES OF NANOCOMPOSITES BASED ON FUNCTIONALIZED NANOFILLERS

Anatoly SVIRIDENOK[*], Aliaksei KRAUTSEVICH[*], Olga MAKARENKO[**], Vladimir VOINA[***]

[*]Research Center of Resource Saving Problems of National Academy of Sciences of Belarus,
Tizenhauza sq., 7, 230023 Grodno, Belarus,
[**]V.A. Belyi Metal-Polymer Research Institute of National Academy of Sciences of Belarus,
32a Kirov Str., 246050 Gomel, Belarus
[***]Yanka Kupala State University of Grodno, Ozhetsko Str., 22, Grodno, Belarus

resource@mail.grodno.by, krautsevich_a@tut.by, olga-mpri@mail.ru, kaf_physics@grsu.by

Abstract: Nanocomposite samples of the copolymer of ethylene and vinyl acetate containing carbon nanofibers and nanotubes have been prepared by mixing in solution. In order to improve interfacial interactions in the polymer-nanofiller system they were subjected to a preliminary chemical functionalization. The efficiency of functionalization was estimated by the IR spectroscopy. The X-ray diffraction and strength characteristics of the obtained nanocomposites filled by the untreated and functionalized carbon nanofibers and nanotubes with different filling degree were compared.

1. INTRODUCTION

Carbon nanomaterials (CNM) are considered to be promising fillers for nanocomposites thanks to their high mechanical, adhesive and other properties. These properties may improve essentially technical characteristics of nanocomposites (Cipiriano, 2007; Yang, 2004). It is, nevertheless a difficult task to create such a nanocomposite. The difficulties in application of nanostructured nanofillers consist in attaining their optimal dispersion in the matrix polymer, and the efficient bonding with the polymer macromolecules. The most applicable method of reaching the optimal dispersion of nanofillers is the exposure to the ultrasonic field (Kodgire, 2006; Lin, 2005). The method of efficient fixing of the single-wall (Bahr, 2002; Dyke, 2004; Haggenmueller et al, 2006) and multiwalled (Mago et al, 2008; Lin, 2002; Grimes, 2001) nanotubes in the polymer matrix consists in their preliminary covalent functionalization by the polar groups. There is, however lack of information on the expediency and possibility of functionalizing carbon nanomaterials in the form of a mixture of nanofibers and nanotubes.

In the present work the nanofiller was introduced into the polymer matrix by the method of mixing in solution. This method is considered in literature as a most efficient one for obtaining CNM-filled nanocomposites. And as reported in some scientific papers (Mark, 2005) this method most enables to solve the problem of nanoparticles agglomeration at introduction into the polymer matrix and to ensure a better interfacial interaction between the polymer matrix and nanofiller particles.

2. EXPERIMENTAL DETAILS

2.1. CNM and its functionalization

The CNM used in the present investigations was derived by methane decomposition under a high-voltage discharge plasma in the Institute of Heat and Mass Transfer of NASB. It is a soot-like matter consisting of carbon nanofibers, nanotubes as well as the particles of amorphous and graphitized carbon. The dimensions of CNM nano-structures were determined from the SEM micrographs.

The functionalized CNM (f-CNM) was obtained by treating with a mixture of concentrated mineral acids. The CNM were treated with the acids during 3-4 hours under 80 ± 5 °C with constant agitation, followed by cooling and settling of the mixture. Thus produced precipitant was washed repeatedly by distilled water and dried till the full removal of the water.

2.2. Preparation of the nanocomposites

The polymer matrix under study was the copolymer of ethylene and vinyl acetate (EVA) produced by OAO SEVILEN (Kazan, Russia), grade 11808-340 with vinyl acetate content 26-30 wt%. The nanocomposite was prepared by mixing CNM in the EVA solution in oxygen AT exposure to the ultrasonic field. With this aim, the EVA granulate was placed into a flask with a slice, and a necessary amount of CNM (0÷0,5 wt%) with a solvent. The flask was placed into an ultrasonic bath Bandelin Sonorex Super (of 80 Wt power and 35 kHz frequency) fit with a heater. The polymer was dissolved under 50÷55 °C within 1 h. To avoid gaseous losses of the solvent a backflow condenser was installed in the slice inside the flask. The CNM nanofiller was subjected to the ultrasonic dispersion for 30 min after complete dissolving of the polymer. The prepared solutions of EVA with suspended in them CNM were poured into the Petri dishes and placed into an exhaust hood for 12 hours. Then, the dishes were placed into a thermostat under 60 °C temperature for a day. The resultant dry precipitant was milled. Seven samples of nanomodified EVA with CNM and f-CNM content 0 ÷ 0,5 wt% were prepared following above procedure. To produce experimental samples of glued EVA splices

and to continue the investigations, thus obtained nanocomposites were ground into a powder using a cryogenic mill "Pulverisette-14" and a vibration feeder "Laborette-24" for continuous feeding of the ground material. Liquid nitrogen was used as a cooling agent. The composite material ground into the powder was then dried at 10 °C temperature during 8 hours to remove condensation water.

To study the effect of CNM nanofiller on structural parameters of the EVA matrix, the prepared powder nanocomposites underwent hot pressing to obtain 200-250 μm thick films.

To define variations in adhesive properties of EVA towards metal surfaces induced by introduction of CNM, we have prepared model samples of glued joints from the powder nanocomposites. The metal surfaces for gluing were strips of aluminum sheets having width b = 200 mm, and thickness h ≈ 0,2 mm. The strips were glued with overlap to the EVA nanocomposite by hot pressing under above 130 °C. The overlapping length was a = 150 mm, thickness of the glue joint t ≈ 200 μm (Fig. 1). The samples were prepared and the adhesive bond was tested for the ultimate strength at shear following the State Standard GOST 14759-69 "Glue joints of metals. A method for determining shear strength". (Airapetyan, 1980). The maximal load on the adhesive bond till failure by shear was estimated on a testing machine Instron 5567 at velocity of the grips 10 mm/min.

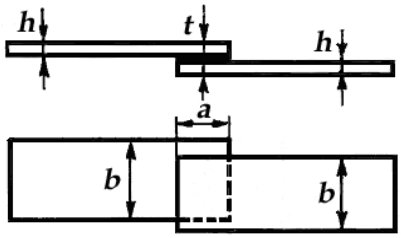

Fig. 1. Scheme of a sample from aluminum sheets with a glue joint on EVA nanocomposite

2.3. Investigation methods

The efficiency of CNM functionalization was estimated by the IR spectra recorded by a spectrophotometer Nicolet 5700 FTIR. The spectra were recorded on a NaCl glass.

The radiograms of the composite films were recorded using diffractometer Dron-2,0 with radiation of CuK_α, filtered λ = 0,1542 nm. The X-ray diffraction parameters were obtained by processing the radiograms keeping to the traditional procedures.

It is common knowledge (Jale, 1968; Martynov, 1972) that the presence of a clearly isolated diffusion halo and narrow reflexes on the radiogram assists in defining radiologic crystallinity degree ω_c by the relation:

$$\omega_c = \frac{\int_{\Theta_1}^{\Theta_2} S^2 J_c(S)\,dS}{\int_{\Theta_1}^{\Theta_2} S^2 J(S)\,dS}, \qquad (1)$$

where $S = 2\sin\Theta/\lambda$ – vector of reciprocal space; J – total scattering intensity of X-ray beams in the interval of angles Θ_1 and Θ_2; J_c – total scattering intensity in the region of narrow reflexes.

The interplanar distances corresponding to the reflexes were determined by Bregg-Wolf's formula (Wanderlich, 1976):

$$\frac{d}{n} = \frac{\lambda}{2\sin\Theta_b}, \qquad (2)$$

where d – distance between planes of reflection; n – whole number; Θ_b – the angle formed by the incident beam and the plane; in our case n = 1; λ = 1,514 Å).

The dimensions of crystallites were calculated by Sherrer's formula (Martynov M.A., 1972):

$$L = \frac{0,9\lambda}{\beta \cdot \cos\Theta_b}, \qquad (3)$$

where L – crystallite size, Å; β – line width, radian; λ – wavelength, Å.

The radiograms were recorded on a chart strip with recalculation so as to consider the scale. In our case, one angular degree corresponded on the strip to a 6 mm distance, one radian corresponded to the angle 57,3°. So, Eq. (3) for value L expressed in Å, will take the form:

$$L = \frac{0,9 \cdot 1,542\,\text{Å} \cdot 6mm \cdot 57,3^o}{\beta mm \cdot \cos\Theta_b}. \qquad (4)$$

To describe the changes in the supermolecular structure of the matrix in response to nanofiller effects, one should study the following parameters: relative share of the coarse crystals in the crystalline region δ_b:

$$\delta_b = \frac{S_3}{S_2 + S_3} \qquad (5)$$

where S_2; S_3 are the integral intensities of reflexes 2 and 3, respectively; the relative share of the fine crystals δ_s in the amorphous region determined by:

$$\delta_s = \frac{S_2}{S_2 + S_{am.}} \qquad (6)$$

where S_2, S_{am} are the integral intensities of reflex 2 and the amorphous region, correspondingly.

3. RESULTS AND DISCUSSION

3.1. CNM and results of its functionalization

SEM investigations (Fig. 2) have shown that the CNM consists of 100÷200 nm in diameter and 1÷1.5 μm long carbon nanofibers; multiwall carbon nanotubes 20÷40 nm in diameter and 1÷10 μm long in the form of a branched interweaving. Notice that the particles of the amorphous and nanotube carbon are seen on all SEM microphotographs. Proceeding from the above, we can say that CNM

is a polydispersed product containing different in shape and size nanoparticles with the admixture of microparticles and amorphous carbon nanoparticles.

The CNM and f-CNM were characterized using the method of IR spectroscopy. There were no any essential differences after CNM treating with a mixture of mineral acids (Fig. 3). Both curves display the bands in the region 1725 cm^{-1} that correspond to oscillations of the C=O link in carboxyl and a wide peak between 3000 and 3600 cm^{-1} correlated with hydroxide (-OH) oscillations in carboxyl. The appearance or intensification of named bands in the same regions was also observed in the works (Hung, 2009 and Anoshkin, 2008) after the acid treatment of nanotubes and nanofibers. Proceeding from these results, we may assume that there is insignificant content of polar groups on the surface of nanostructures of the initial CNM, while the acids treatment augments their amount.

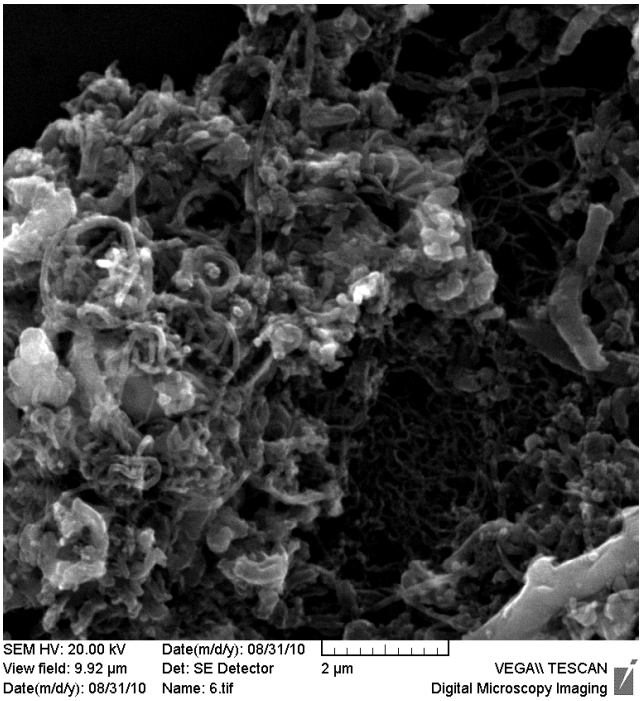

Fig. 2. SEM image of CNM

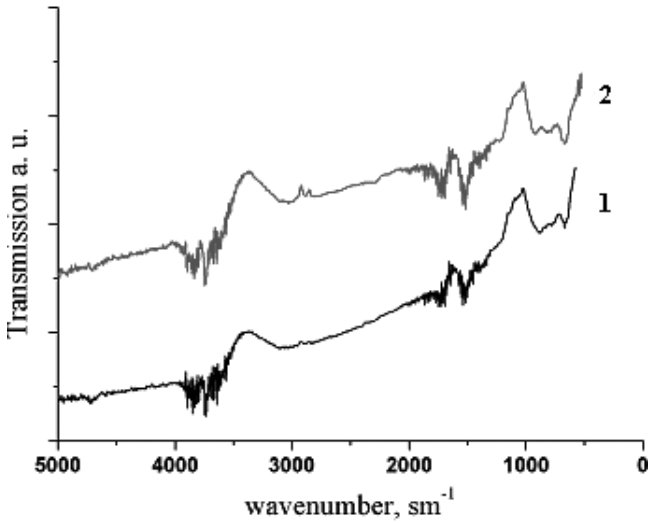

Fig. 3. IR spectra of CNM (1) and f-CNM (2)

3.2. X-ray diffraction parameters of the nanocomposite

Fig. 4 presents most typical radiograms of the non-filled EVA film, nanocomposite EVA + CNM films and those of EVA + f-CNM. The radiogram of the EVA film displays a single clear-cut reflex 2 and a considerable area of a symmetric amorphous halo. In the case with the nanocomposite films, their radiograms show reflexes 1, 3, 4 and reduced a little area of the amorphous halo, which is a proof to variations in the supermolecular structure of the nanocomposite. The essential differences in radiograms of the films EVA and f-CNM consist in the absolute and relative intensities of some reflexes, as well as the shape and size of the amorphous halo. It should be noted that the number of reflexes and their angular position on the radiograms is similar for all samples under study (within the limits of test sensitivity and measurement errors).

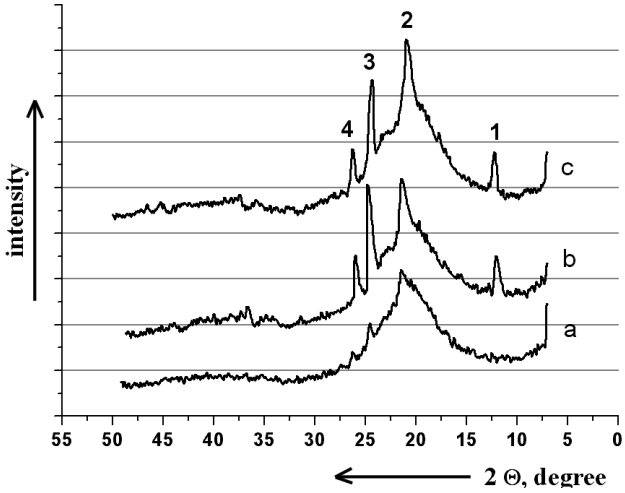

Fig. 4. Characteristic radiograms of the films:
a –EVA, b – EVA + CNM); c – EVA +f-CNM

Tab. 1. X-ray diffraction parameters of films EVA

Samples	Struct. para-meter	Reflex No.				ω_c
		1	2	3	4	
EVA (granulate)	2Θ	weak	21°33'	24°66'	weak	0,11
	d,Å	-	2,12	1,85	-	
	L,Å	-	47	210	-	
EVA (from solution)	2Θ	weak	21°33'	24°66'	weak	0,11
	d,Å	-	2,12	1,85	-	
	L,Å	-	73	276	-	
EVA + CNM 0,1 wt%	2Θ	12°20'	21°20'	24°66'	26°50'	0,16
	d,Å	3,65	2,13	1,85	1,73	
	L,Å	163	73	210	247	
EVA+ f-CNM 0,1 wt%	2Θ	12°20'	21°20'	24°66'	26°50'	0,22
	d,Å	3,65	2,13	1,85	1,73	
	L,Å	122	63	210	267	

The calculated X-ray structural parameters of the samples are shown in Tab. 1.

The calculations using formula (4) have shown that the crystalline phase in the studied samples consists of rather

fine crystals 47 ÷ 73 Å (reflex 2), average ones 122 ÷ 163 Å (reflex 1) and coarse crystals 210 ÷ 276 Å (reflexes 3 and 4). A negligible effect is imposed on the crystal size by preliminary dissolving of the polymer matrix in the organic solvent. The crystals are a little larger in these films. Introduction of CNM into the EVA matrix forces the coarse crystals to return from 276 down to 210 Å size, i.e. to the size similar to the initial EVA not subjected to preliminary dissolving.

The calculation of crystallinity degree (ω_c) using formula (1) has shown that the non-filled EVA films have ω_c = 0,11. Introduction of CNM into the EVA matrix increases the degree of crystallinity, while the maximal value of ω_c = 0,24 was reached in the EVA samples with 0,5 wt% concentration of f-CNM.

Depending on the content (wt%) and the type of CNM in these films EVA differently changes the ratio of large and small crystals. Figure 5 presents the dependence of the fraction of small crystals in the amorphous region.

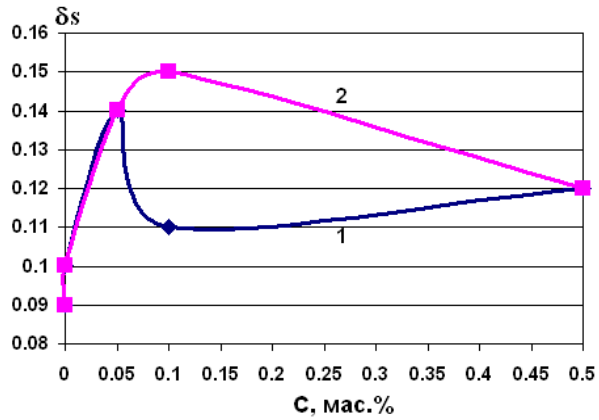

Fig. 5. Variations in relative share of fine crystals in the amorphous phase depending on the wt% content of nanofiller in EVA + CNM (1) and EVA + f- CNM films (2)

The introduction of all types of CNM leads to an increase in the relative share of small crystals in the amorphous region. The maximum value of the relative share of small crystals is achieved for films of EVA f-CNM at a concentration of 0,1 wt.%. Similar variations in the polymer crystal dimensions upon introduction of functionalized carbon nanoparticles were observed by other researchers on the example of polybutylene terephthalate (Mago et al., 2008). The relative share of the coarse crystals in the nanocomposite EVA films increased too, and there were not any noticeable differences between the films EVA + CNM or EVA and f-CNM in what concerns this parameter.

Based on the results obtained, we have made the following conclusions. The major effect induced by the CNM introduction is the formation of a fine-crystalline phase. It is to be noted that the layer-to-layer distance in the fine crystals (reflex 2, d = 2,12 Å) coincides with the mean interlayer distance in the amorphous phase. Such a situation may occur if the crystalline region created by the unrolled molecular balls, in which the straightened macromolecular chains are forming the crystals (Wanderlich, 1976). Named structures are characterized by the presence of a large number of transit chains, which improves in a number of cases physico-mechanical characteristics. The nanostructures f-CNM assist most efficiently the formation of crystals from the straightened macromolecular chains when their concentration is 0,1 wt%.

3.3. Adhesive properties of the nanocomposite

The results of testing mechanical properties of the glue joints in which EVA was used for lap splicing of aluminum sheets are shown in Table 2.

The data proves that introduction of CNM into the EVA matrix enhances strength of the glue joint. Most strong glue joints with EVA are obtained when the f-CNM is used as a filler, which is evidently related to optimization of the interfacial interactions in the nanofiller-matrix contact.

Tab. 2. Mechanical test results of glue joints with EVA at shear

Glue joint composition	Ultimate load to failure	Ultimate strength, MPa	Strength variation related to check sample, %
EVA (check)	42.5	14.2	–
EVA + CNM 0,05 wt%	52.4	17.5	23.2
EVA + CNM 0,1 wt%	51.4	17.1	20.9
EVA + f-CNM 0,05 wt%	55.1	18.4	29.7
EVA + f-CNM 0,1 wt%	57.3	19.1	34.9

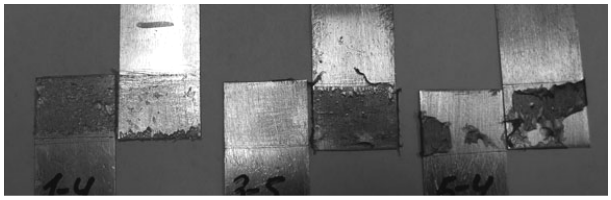

Fig. 6. Failure mode of glue joints: 1 – CNM; 2 – EVA + CNM; 3 – EVA + f-CNM

It should be noted that the majority of the test samples has shown the adhesive failure mode in the glue joints. As for the samples containing EVA and f-CNM, they show simultaneously the signs of adhesive and cohesive failure in the splice (Fig. 6). This fact speaks in favor of the increasing adhesive strength.

4. CONCLUSIONS

The test results have proved that the acid treatment augments the content of polar groups in the CNM on the surface of nanostructures. All nanomodified samples display the enhanced crystallinity degree, its maximum being observed in the case of using the f-CNM. The crystal-

linity degree growth takes place mainly due to the increasing amount of fine crystals in the amorphous region. The maximal strength increase by ≈ 35% in the glue joint with the EVA nanocomposite was recorded when f-CNM was introduced.

REFERENCES

1. **Airapetyan L. H**. (1980), *Ref. book on glues*, Leningrad, Khimiya.
2. **Anoshkin I. V.** (2008), *Chemical modification and fractioning of thin multilayered carbon nanotubes*, Dissertation, Rus. Chem.-Technol. Univ. named after D.I. Mendeleev.
3. **Bahr J. L.** (2002), Covalent chemistry of single-wall carbon nanotubes, *J. Mater. Chem.*, Vol. 1952–1958.
4. **Cipiriano B. H.** (2007), Effects of aspect ratio of MWNT on the flammability properties of polymer nanocomposites, *Polymer*, Vol. 48, 6086–6096.
5. **Hung N.Ch.** (2009), Modification of carbon nanotubes and nanofibers for obtaining ceramic nanocomposites. Dissertation, Rus. Chem.-Technol. Univ. named after D.I. Mendeleev.
6. **Jale F.H.** (1968), Polymer monocrystals, Moscow, Khimiya.
7. **Dyke C. A.** (2004), Covalent functionalization of single-wall carbon nanotubes for materials applications, *J. Phys. Chem. A.*, Vol. 108, 11151-11159.
8. **Grimes C. A.** (2001), Effect of purification of the electrical conductivity and complex permittivity of multiwall carbon nanotubes, *J. of Applied physics*, Vol. 90, No 8, 4134–4137.
9. **Haggenmueller R.** (2006), Interfacial in situ polymerization of single wall carbon nanotube/nylon 6,6 nanocomposites, *Polymer*, Vol. 47, 2381-2388.
10. **Kodgire P. V**. (2006), Control of multiwall carbon nanotubes dispersion in polyamide6 matrix: An assessment through electrical conductivity, *Chemical Physics Letters*, Vol. 432, 480–485.
11. **Lin T. S.** (2005), Percolated network of entangled multiwalled carbon nanotubes dispersed in polystyrene thin films through surface grafting polymerization, *Materials Chemistry and Physics*, Vol. 94, Is. 2-3, 438-443.
12. **Lin Y.**, (2002), Functionalizing Multiple-Walled Carbon Nanotubes with Aminopolymers, *Journal of Physical Chemistry B*, Vol. 106, No. 6, 1294–1298.
13. **Mago G.** (2008), Effect of Functionalization on the Crystallization Behavior of MWNT-PBT Nanocomposites, *Mater. Res. Soc. Symp. Proc*, Vol. 1056, 1-6.
14. **Mark K.** (2005), Shear modification of HDPE-clay nanocomposites, *United States Patent*, No 6,884,834.
15. **Martynov M. A.** (1972), *Radiography of polymers*, Moscow, Khimiya.
16. **Wanderlich B.** (1976), *The physics of macromolecules*, Moscow, Mir.
17. **Yang J.** (2004), Fabrication and Characterization of Soluble Multi-Walled Carbon Nanotubes Reinforced P(MMA-co-EMA) Composites, *Macromol. Mater. Eng*, Vol. 289, 828–832.

MATHEMATICAL ANALYSIS FOR A NEW TENNIS BALL LAUNCHER

Krzysztof WÓJCICKI[*], Kazimierz PUCIŁOWSKI[**], Zbigniew KULESZA[***]

[*]Bialystok University of Technology, Faculty of Mechanical Engineering, ul. Wiejska 45C, 15-351 Bialystok, Poland

krzysiowojcicki@gmail.com, kpucilowski@o2.pl, z.kulesza@pb.edu.pl

Abstract: The paper presents the mathematical analysis for the design of a new tennis ball launcher in order to assess the possibilities for its technical implementation. First, traditional launchers are described. Next, several new requirements improving training possibilities of such machines are suggested. The motion equation of the flying tennis ball is formulated and numerically solved. This makes it possible to analyze the trajectories of the ball for different initial conditions: elevation and heading angles, as well as the rollers angle. Then, the mathematical analysis of the launcher with two counter rotating rollers is presented. Stiffness (Young's) modulus and friction coefficients for the typical tennis ball have been determined experimentally. Based on these, initial conditions for the throw have been found: rotating speeds of the rollers and powers of the driving motors.

1. INTRODUCTION

Ball launchers are quite popular among tennis enthusiasts and there are many different types of such training machines available in the market. The main difference between them lies in the number of controlled parameters and possible ranges of their adjusting.

Generally, regarding the way the ball is thrown, tennis ball launchers can be divided into two groups: 1) the machines using compressed air – further called as pneumatic launchers, and 2) the machines using rotating rollers (or wheels) – further called as mechanical launchers.

In pneumatic launchers the ball is thrown using the air jet. The air is compressed with the attached compressor and stored inside the chamber. The initial velocity of the ball depends on the output pressure of the compressor. Elevation and heading angles can be adjusted by setting the direction of the outlet tube. The tube can be set manually or using electric motors. The spin can be added by using the special tube ending (adaptor) slowing down one side of the ball, what makes it rotate about the required axis. The adaptor needs to be rotated about the tube's axis in order to change between the slice and the top spin. However, the spin velocity cannot be set separately, as it depends on the initial velocity of the throw.

Due to the compressor, pneumatic launchers are powered from the mains voltage of 230/110 V. They offer long durability, reliability, and resistance to various weather conditions. However, pneumatic launchers allow one to practice only basic strokes and cannot be used for more complex training programs. That is why they are mainly chosen by beginners.

Mechanical launchers shoot the ball by pulling it between two counter rotating rollers. The initial velocity of the ball depends on the rotating velocity of the rollers. The heading angle can be changed by turning the whole machine, or only its launching mechanism, left/right (yawing the rollers). Similarly the elevation angle can be changed by turning the launching mechanism up/down (pitching the rollers). The spin can be added by changing the rotating velocity of one (or two) rollers. The given model of the launcher can only have the rollers positioned horizontally (or vertically) what restricts the possible planes of ball rotation.

Usually, mechanical launchers are powered from accumulators and that is why they can be used at the courts with no mains supply or in case of its malfunction. However, accumulators could also be the disadvantage, as they restrict the time of the uninterruptible operation. When compared with pneumatic mechanisms the rollers provide better accuracy and a wider range of the possible strokes. They allow one to intensify his/her efforts and to practice more advanced training programs.

Analyzing both types of tennis launchers it can be stated that better parameters and a greater control potential have mechanical launchers. The launching mechanism in the form of two rollers provides a great repeatability, increases the initial velocity and makes it possible to smoothly and accurately control the flying velocity of the ball. It can also spin the ball in a required manner. Mechanical launchers can control the throw better; in case of pneumatic machines the ball hit by the air jet rolls inside the outlet tube in an unpredictable manner. This introduces many problems making it difficult to control the throw and the flight of the ball and resulting in worse accuracy and repeatability of pneumatic machines.

To the authors' knowledge there are hardly no research articles concerning the problem of designing tennis ball launchers. Existing reports focus mainly on the aerodynamics of different flying sport balls (Alam, 2007, Goodwill, 2004, Mehta, 1985, Naumov, 1993, Sayers, 1999), especially on the problem of calculating the Magnus force (Alam, 2007, Goodwill, 2004), determining drag and lift coefficients (Alam, 2007) or on the problems of hitting or bouncing the ball in a required manner (Sayers, 1999). That is why we decided to create a simple mathematical model

of the mechanical tennis launcher, to simulate its behavior, and establish the main principles of their designing.

The aim of the present work is to analyze the possibilities of improving the performance and training possibilities of mechanical launchers. By studying the mathematical basis of the throw and the flight of the ball the initial parameters for the required trajectory are determined. The parameters include: initial elevation and heading angles, rollers angle, rotational speeds and powers of the motors driving the rollers. These can be very helpful for the design of the new mechanical tennis ball launcher.

2. BRIEF FORDESIGN

For the purposes of the mathematical analysis, the following brief fordesign for the new launcher were formulated:

- the ball can be thrown from different altitudes in order to practice the return of serve; the maximum altitude of the throw can be set to 3 meters above the court level (average player's height + arm's reach + length of the racket ≈ 3 meters) with the step value of 0.1 meter;
- initial velocity of the balls can be set from 30 to 200 km/h with the step value of 1 km/h; the minimum velocity is for the youngest players; the maximum – is the average serve velocity of the advanced players with the several years' playing experience;
- throw angles:
  - elevation angle can be set from -20 to 80 degrees (from -0.38 to 1.4 radians) with the step value of 1 degree; the negative angles are needed to practice the return of serve; the maximum angle is to practice the lob strokes;
  - heading angle can be set from -40 to 40 degrees (from -0.7 to 0.7 radians) with the step value of 1 degree; the minimum/maximum angles are chosen in such a way that the ball can be passed from one sideline to the other near the net;
- time period between subsequent ball shots (launch rate) can be set from 1 to 15 seconds with the step value of 1 second; the minimum is the average value during the normal play; the maximum allows the coach to comment the last return of the player;
- the ball can be rotated around its axis in any plane by rotating the throwing mechanism around its symmetry axis from -180° to +180° (from -3.14 to 3.14 radians) with the step value of 1 degree;
- rotating speed of the ball can be set from 0 to 2000 rpm (from 0 to 209,4 rad/s) with the step value of 1 rpm; the maximum is the average value of the advanced players;
- the points at the court surface at which the ball should bounce can be freely chosen – the same points can be hit by different launch parameters depending on the practiced stroke.

3. MODEL OF THE FLYING BALL

The flying ball is impacted by three main forces: gravity, drag and lift (Fig. 1).

Only the drag force resulting from the translational motion of the ball is considered. The influence of the drag resulting from the rotation is neglected. The video recordings confirm that during the hit at the court the rotational speed of the ball is almost the same as just after the serve, i.e. the rotational speed drop during the flight is quite negligible. This means that the moment of the air drag force during the rotation does not influence the flight of the ball in a noticeable manner. However, the lift force resulting from the rotation of the ball around its axis; i.e. from the so called Magnus effect is taken into consideration.

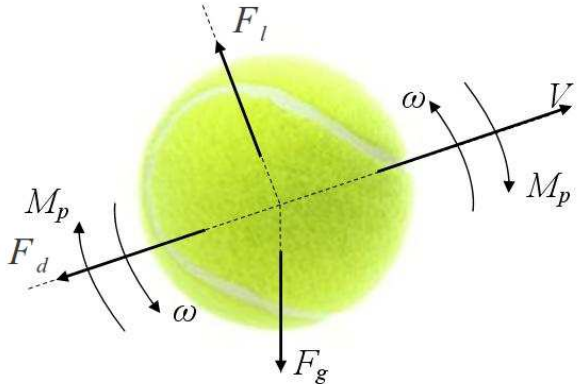

Fig. 1. Forces: gravity F_g, lift (Magnus) F_l, drag F_d, and drag moment M_p, and velocities: translational V and rotational ω of the flying ball

Drag force $\bar{F}_d$ is the component of the aerodynamic force appearing during the motion of the solid. It acts opposite to the direction of motion (Prosnak, 1970):

$$\bar{F}_d = -\tfrac{1}{2} c_d \rho \pi r^2 V \bar{V} \tag{1}$$

where: c_d is the drag force coefficient depending on the shape of the solid, ρ is air density, r is ball radius, and V – ball translational velocity.

Magnus effect lies in the generation of the lift force perpendicular to the translational velocity of the cylinder (or other solid of revolution, e.g. the ball) spinning in the surrounding fluid (Fig. 2). Rotating ball influences the surrounding air and makes it rotate too. On the other hand, the air pushing the ball in the translational motion flows AT one side of the ball at the same direction as the rotation of the ball. At this side the air is accelerated and its pressure drops. At the other side the flow direction of the air is opposite to the rotation. This decelerates the air and increases its pressure. Consequently, the pressure difference between the two sides of the ball evolves and changes the motion trajectory of the ball.

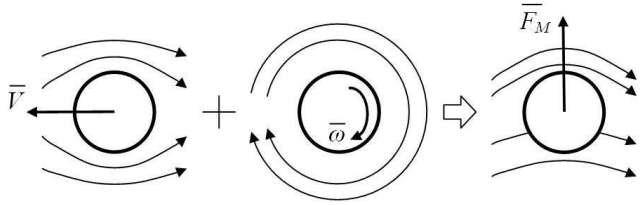

Fig. 2. Magnus effect: Magnus force F_M, translational V, and rotational ω velocities

Lift force $|\bar{F}_l|$ can be calculated, as (Prosnak, 1970):

$$\left|\bar{F}_l\right| = \tfrac{1}{2} c_l \pi r^2 \rho \bar{V} V \tag{2}$$

where c_l is the lift force coefficient.

Introducing rotational speed $\bar{\omega}$ instead of the scalar linear velocity V in Eq. (2), the Magnus force for the ball can be presented, as:

$$\bar{F}_l = \tfrac{1}{2} c_l \pi r^3 \rho \bar{V} \times \bar{\omega} \tag{3}$$

The values of the lift force and similarly of the drag force coefficients can be determined experimentally in a wind tunnel. Alam et al., 2007) investigated different tennis balls for various translational and rotational speeds. They found out that the drag coefficient changes from 0,55 to 0,85, while the lift coefficient – from 0,30 to 0,70 if translational speeds ranging from 20 to 140 km/h and rotational speeds from 0 to 3000 rpm are considered. By comparing the computational and experimental results they stated, that lift and drag forces depend not only on the speed of the ball, but also on the state (roughness) of its surface. Similar results obtained Goodwill et al. (Goodwill, 2004) who in a wind tunnel investigated aerodynamic properties of a range of new and used tennis balls for a velocity range from 20 to 60 m/s. Mehta (Mehta, 1985, 2004) presented many visualizations and obtained sets of drag and lift coefficient values for different sports balls spinning in a wind tunnel. Sayers and Hill (Sayers, 1999) presented experimental results of drag and lift coefficients for stationary and rotating cricket balls. Naumov et. al. (Naumov, 1993) compared numerical and experimental results of the research of the falling ball and determined the influence of the initial angular velocity on the deviation from the vertical.

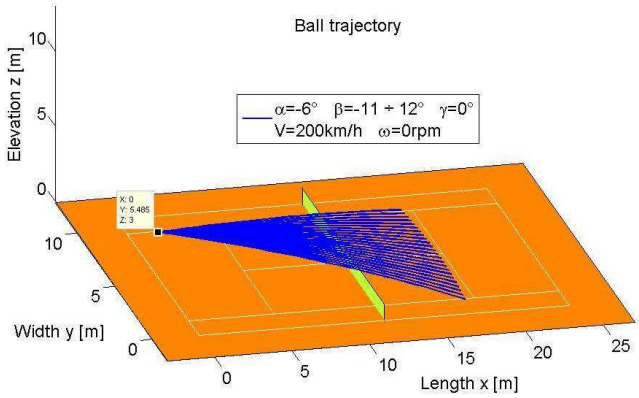

Fig. 3. Ball trajectories for different heading angles β: 3D view

Although aerodynamics problems of the flying sport balls, especially the Magnus effect, have been studied by many researches, there is no acceptable solution and explanation to this problem up till now. Thus, in the present study the simplified model will be applied, in which no additional effects such as 3D air flow around the ball or the flow turbulence will be included.

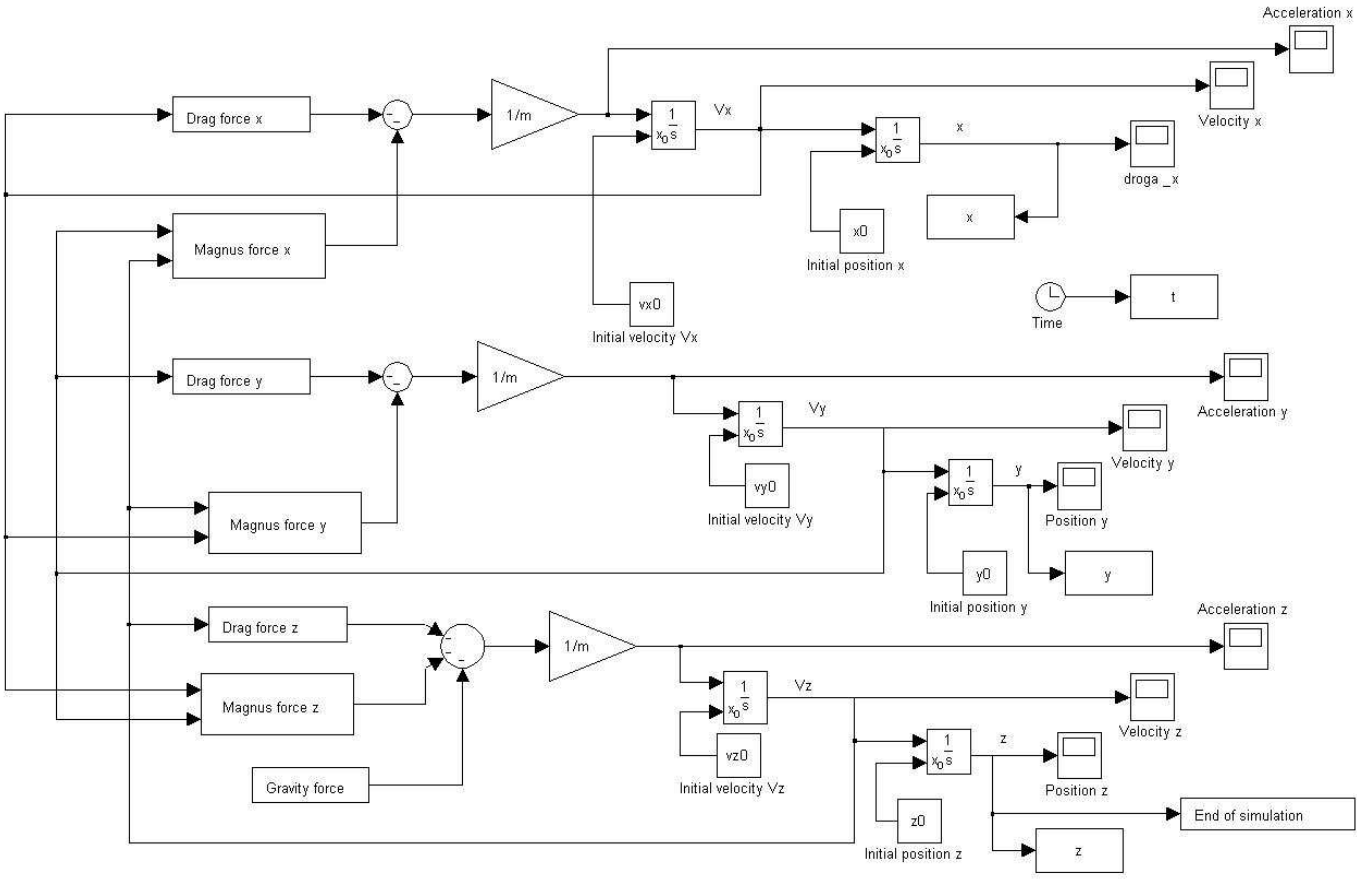

Fig. 4. Block diagram of the flying ball simulation model

The general motion equation of the flying ball can be presented, as:

$$m\frac{d^2\overline{x}}{dt^2} = \overline{F}_g + \overline{F}_d + \overline{F}_l \tag{4}$$

Applying Eqs. (1), (3), after projecting the above equation on the three axes of the Cartesian coordinate system, the following formulas for x, y, and z directions are obtained

$$m\frac{d^2x}{dt^2} = -\tfrac{1}{2}r^2c_d\pi\rho V_x\frac{dx}{dt} - \tfrac{1}{2}c_l r^3\pi\rho\left(\frac{dy}{dt}\omega_z - \frac{dz}{dt}\omega_y\right) \tag{5}$$

$$m\frac{d^2y}{dt^2} = -\tfrac{1}{2}r^2c_d\pi\rho V_y\frac{dy}{dt} - \tfrac{1}{2}c_l r^3\pi\rho\left(\frac{dz}{dt}\omega_x - \frac{dx}{dt}\omega_z\right) \tag{6}$$

$$m\frac{d^2z}{dt^2} = -mg - \tfrac{1}{2}r^2c_d\pi\rho V_z\frac{dz}{dt} - \tfrac{1}{2}c_l r^3\pi\rho\left(\frac{dx}{dt}\omega_y - \frac{dy}{dt}\omega_x\right) \tag{7}$$

where V_x, V_y, V_z and ω_x, ω_y, ω_z are the components of the translational V and rotational ω speeds, m is the mass of the ball, g is gravity acceleration.

Based on Eqs. (5)-(7), the simulation model of the flying ball was created in Matlab/Simulink. The model allows one to simulate various trajectories of the flying ball in dependency of initial throw parameters: elevation α, heading β, rotation γ angles, as well as, linear V, and rotational ω speeds of the ball.

The block diagram of the simulation model is presented in Fig. 4. The drag and lift coefficients can be introduced directly by the user or calculated from a specially designed function approximating the values given by Alam et al., (2007). The user decides which values are chosen for further calculations. This way, he/she can easily analyze what is the influence of the drag or lift force on the ball trajectory. However, he/she must be aware, that the reliable results can be obtained only, if the values suggested by Alam et al., (2007) or other researches are chosen, and that the allowable translational (20 to 140 km/h) and rotational (0 to 3000 rpm) initial speeds are not exceeded.

Several shots, e.g. serves differing only in the heading angle β can be presented at the same diagram, as it is shown in Fig. 3. The trajectory can be plotted in one of three planes, xy, xz, or yz. The simulations in Fig. 3 were conducted for the typical tennis ball of mass $m = 0{,}058$ kg, and radius $r = 0{,}333$ m.

4. ANALYSIS OF THE BALL THROW

In order to throw the ball using two counter-rotating rollers two conditions should be met. The first is the condition for pulling the ball in between the rollers. The second is the condition for throwing the ball away from between the rollers.

4.1. Pulling the ball

When the ball is being pulled by the rollers, two main forces appear at the contact points between the ball and the rollers. These are: the pressure force N, which is normal to the contact surface, and the tangent friction force T (Fig. 5). The ball can be pulled in between the balls only if the horizontal component T_h, of the friction force T is equal or greater than the horizontal component N_h of the pressure force N (Wusatowski, 1960).

$$T\cos\lambda \geq N\sin\lambda \tag{8}$$

where λ is the so called "grab angle" between the plane containing the axes of the rollers and the plane containing the axis of one of the rollers and the contact point between the ball and the roller.

As $T = \mu N$, where μ is the friction coefficient, then:

$$\mu \geq tg\lambda \tag{9}$$

Having in mind that:

$$\mu = tg\eta \tag{10}$$

where η is friction angle, the condition for dragging the ball in between the rollers can be presented, as:

$$\lambda \leq \eta \tag{11}$$

Friction coefficient μ will be determined experimentally, what is presented further.

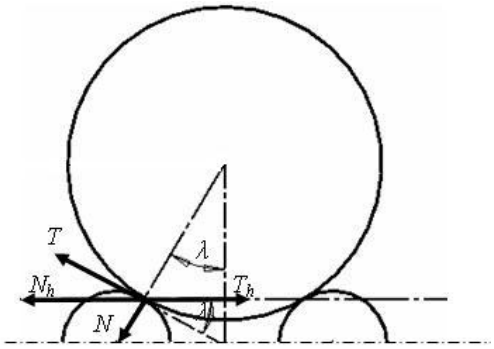

Fig. 5. Forces and geometry at the contact between the ball and the rollers during pulling the ball in between the rollers: horizontal component N_h of the pressure force N, horizontal component T_h of the friction force T, grab angle λ

4.2. Throwing the ball

The condition for throwing the ball away from between the rollers states that the friction force between the ball and the rollers should be equal or greater than the inertia force of the ball (Fig. 6).

This condition ensures that there is no slip between the rollers and the ball:

$$F_w \geq 2T \tag{12}$$

The inertia force depends on the required linear velocity of the flying ball, or more exactly on its acceleration that should be transmitted from the rollers in order to obtain the required initial velocity of the throw.

The friction force between the rollers and the ball depends on the friction coefficient and on the pressure force between the rollers and the ball. The pressure force can be obtained from the definition of Young's modulus for the ball:

$$N = \frac{Es\Delta l}{2r} \tag{13}$$

with Young's modulus E, ball deformation Δl and the area at the deformation surface s.

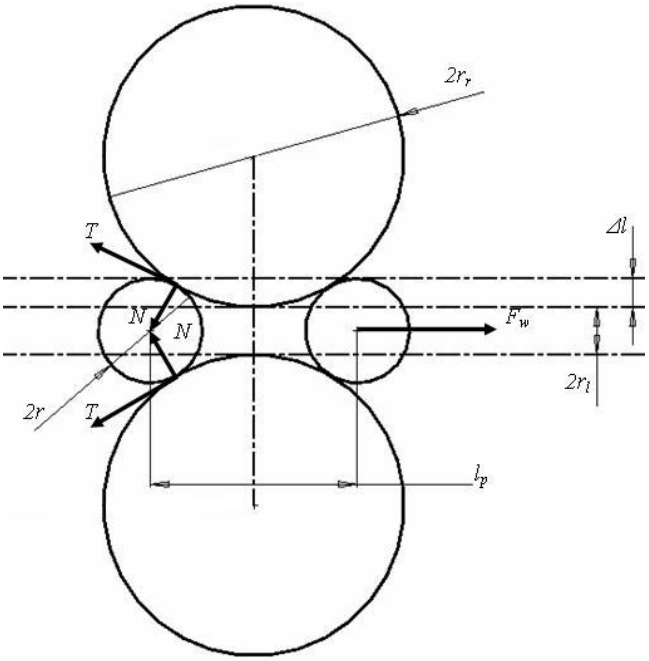

Fig. 6. Forces and geometry at the contact between the ball and the rollers during throwing the ball away: ball inertia force F_w, pressure force N, friction force T, ball radius r, rollers radius r_r, distance between rollers l_p, radius r_l of the ball deformed (squeezed) by the rollers, ball deformation Δl due to the rollers pressure

For further analysis following parameters were assumed: rollers radius $r_r = 0{,}1$ m, and distance between axes of the rollers $d_{sr} = 0{,}25$ m. The Young's modulus will be determined experimentally, what is presented further.

5. EXPERIMENTAL INVESTIGATION OF BALL PARAMETERS

The values of the Young's modulus for the ball and the friction coefficient between the ball and the plastic coverings of the rollers were determined experimentally.

5.1. Young's modulus

Young's modulus was determined by measuring the value of the ball deformation resulting from the applied load force. The ball was located between two flat plates (Fig. 7).

The upper plate was gradually loaded with ten weights of 0,55 kg each, i.e. the overall loading weight changed from 0,55 kg to 5,5 kg. The deformation was measured along three different axes of the ball. As the final result for the given load the arithmetic average of the results for each of the axes was assumed. The values obtained for three different axes of the ball differed in about 3%. These differences were due to the irregular structure of the ball, e.g. at the location of the seams, the ball did not deform evenly.

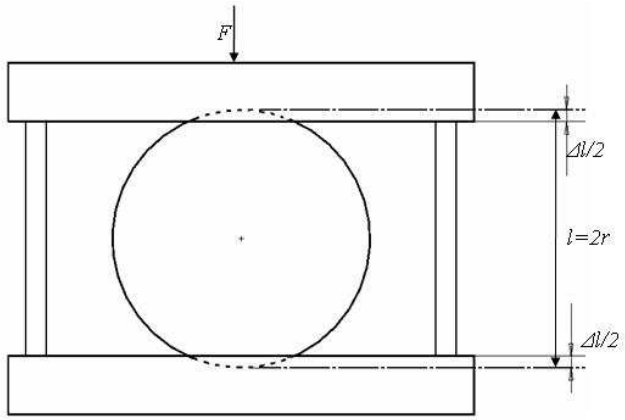

Fig. 7. Schematic diagram of the test stand for Young's modulus measurements

Several tests of the examined ball were performed. Having the loads and corresponding deformations Young's moduli were calculated. Their values are presented in Tab. 1. The dependency between the loading force and the deformation of the examined ball is shown in Fig. 8, where the Young's modulus can be read out as the tangent of the curve's slope angle.

The averaged value of the Young's modulus for the examined ball is 3,63 MPa. The smallest value of 2,83 MPa was obtained for the loading weight of 1,65 kg, while the biggest (4,50 MPa) – for the loading weight of 4,95 kg. The variability range is 1,60 MPa for all loads.

Tab. 1. Results of the Young's modulus measurements for the examined tennis ball

Loading weight [kg]	Loading force [N]	Averaged ball deformation [m]	Calculated Young's modulus [MPa]
0,55	5,40	0,0005	3,40
1,10	10,79	0,0011	3,09
1,65	16,19	0,0018	2,83
2,20	21,58	0,0021	3,24
2,75	26,99	0,0025	3,40
3,30	32,37	0,0029	3,52
3,85	37,77	0,0030	3,96
4,40	43,16	0,0033	4,12
4,95	48,56	0,0036	4,50
5,50	53,96	0,0040	4,25

In order to assess the correctness of the experimental tests, the results obtained for the examined ball were compared with the results calculated for the so called "standardized" tennis balls.

The requirements concerning loads and deformations for the standardized tennis balls are strictly defined (Romer, 2005). Three different types of the standardized balls are allowed to be used for playing tennis. Primary deformation

for the type 1 (fast) ball should be greater than 0,495 cm (0,19 in) and less than 0,597 cm (0,24 in), while secondary deformation should be greater than 0,637 cm (0,26 in) and less than 0,914 cm (0,36 in) if the loading weight of 8,165 kg (18 lb) is applied. For type 2 (medium) and type 3 (slow) balls primary deformation should be greater than 0,559 cm (0,22 in) and less than 0,737 cm (0,29 in), while secondary deformation should be greater than 0,800 cm (0,31 in) and less than 1,080 cm (0,43 in) for the same loading weight of 8,165 kg. The primary deformation is measured directly for the given load of 8,165 kg, while the secondary one is also for the load of 8,165 kg but just after applying the load which reduces the ball diameter to 2,54 cm (1 in). These two deformations should be the averaged values for three different axes of the ball, while two subsequent measurements cannot differ more than for 0,076 cm (0,03 in).

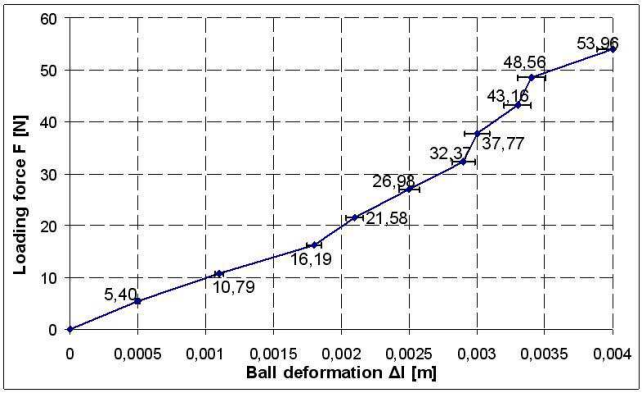

Fig. 8. Force versus ball deformation

The Young's moduli for the standardized tennis balls were calculated for two deformation limits of each type. They are presented in Tab. 2. The averaged value of the Young's modulus for the standardized ball is 4,20 MPa, with the variability range of 1,68 MPa.

As can be seen the values of the Young's modulus for the examined ball and for the standardized balls are similar. However, for further calculations the value of 4,20 MPa was assumed.

Tab. 2. Results of the Young's modulus calculations for the standardized tennis balls

Loading weight [kg]	Loading force [N]	Averaged ball deformation [m]	Type of the ball	Calculated Young's modulus [MPa]
8,165	80,1	0,00495	Fast	5,10
8,165	80,1	0,00597	Fast	4,22
8,165	80,1	0,00559	Medium	4,51
8,165	80,1	0,00737	Medium	3,42
8,165	80,1	0,00559	Slow	4,51
8,165	80,1	0,00737	Slow	3,42

5.2. Friction coefficient

Friction coefficient between two bodies in contact can be experimentally determined by locating the tested body on an inclined plane and gradually changing its slope angle (Fig. 9). The angle η at which the tested body begins to slide down is the so called friction angle, from which the friction coefficient μ can be calculated (see Eq. (10)).

In order to determine the friction coefficient between the real tennis ball and the roller, this simple test stand was modified by placing the ball not on the plane, but on the roller segment located on the inclined plane (Fig. 11). Thus, following configurations were tested

- the ball on the inclined plane (Fig. 10);
- the ball on the roller segment located on the inclined plane (Fig. 11).

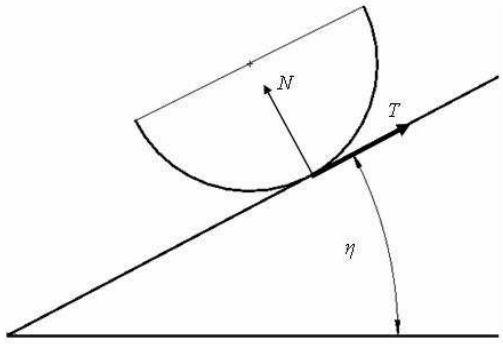

Fig. 9. Derivation of friction coefficient on an inclined plane: friction force T, pressure force N, friction angle η

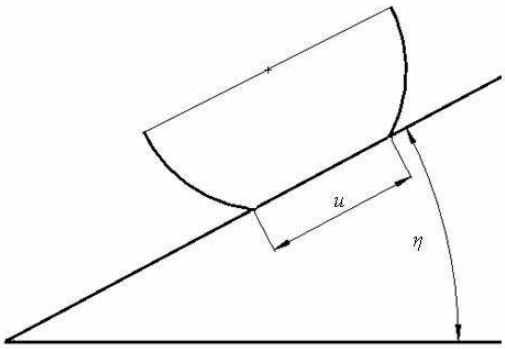

Fig. 10. Derivation of friction coefficient between the ball and the inclined plane: friction angle η, length in contact u

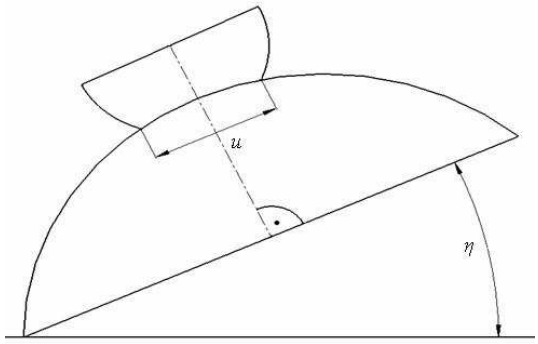

Fig. 11. Derivation of friction coefficient between the ball and the roller segment: friction angle η, length in contact u

The normal tennis ball was cut into two equal pieces along its diameter. In the first case the cut half was located on the inclined plane, and in the second – on the roller segment located on the inclined plane. The plane and the roller segment were made of plastic (polypropylene). The inner part of the half of the ball was pressed in order to increase the contact surface between the ball and the roller, i.e. to better reproduce the real throw. Next, the slope angle at which the ball started to slide down, and the length of the ball in contact with the plane (or with the roller) were measured. The results are presented in Tab. 3.

Tab. 3. Experimental determination of friction coefficient – measurements and calculations

Configuration	Length in contact [m]	Friction angle [°]	Friction coefficient
Inclined plane	0,008	32	0,63
	0,010	34	0,67
	0,015	37	0,75
	0,020	39	0,80
	0,025	41	0,87
	0,030	43	0,93
	0,035	44	0,97
Roller on an inclined plane	0,005	30	0,58
	0,010	34	0,67
	0,015	40	0,84
	0,020	46	1,04
	0,025	53	1,33
	0,030	59	1,66
	0,035	64	2,05

Figures 12 and 13 present the friction coefficient versus the length in contact for two considered cases. As can be seen the friction coefficient increases for higher contact lengths. Its value depends also on the shape of the two bodies in contact – for the given contact length the friction coefficient is higher for the roller segment than for the plane.

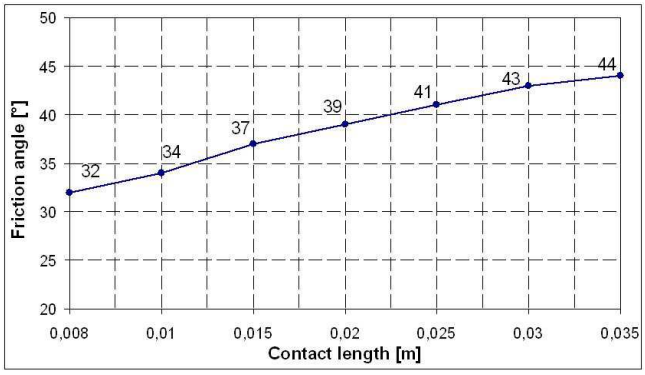

Fig. 12. Friction coefficient versus length in contact; the ball on the inclined plane

During the throw the ball is squeezed by the rollers, the contact length (surface) increases, and the pressure forces act in different directions (normally to the contact surface) what results in the increase of the friction force. That is why the value of 2,05 for friction coefficient was chosen for further calculations. This is the value obtained for the maximum pressure and maximum contact length between the ball and the roller segment. It is supposed, that such configuration resembles the real ball between the rollers best.

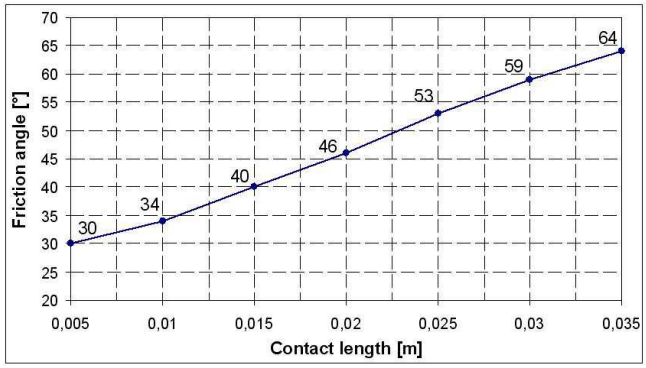

Fig. 13. Friction coefficient versus length in contact; the ball on the roller segment

6. ROTATING SPEEDS OF THE ROLLERS

The linear and angular speed of the ball depend the circumferential speeds of the rollers:

$$V = \frac{V_1 + V_2}{2} \tag{14}$$

$$\omega r_l = \frac{V_2 - V_1}{2} \tag{15}$$

where V_1, V_2 – circumferential speeds of the first and the second roller, r_l – ball radius after deformation (Fig. 14).

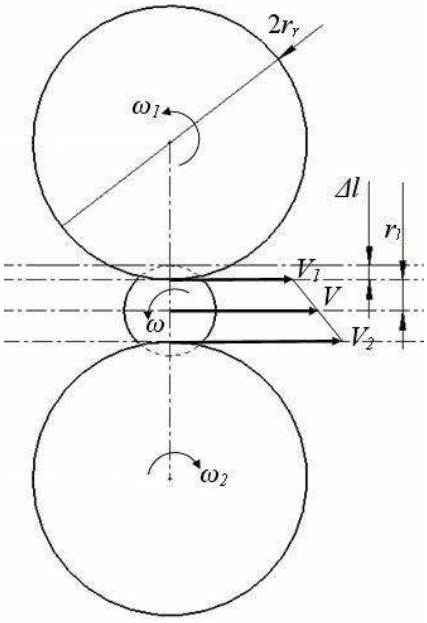

Fig. 14. Velocities during the throw: V, ω – linear and rotational speeds of the ball, V_1, V_2, ω_1, ω_2 – circumferential and rotational speeds of the rollers, r_r – rollers radius, r_l – radius of the deformed ball, Δl – ball deformation due to the rollers pressure

If the ball has to rotate about its own axis after leaving the launcher, the circumferential speeds of the rollers should be different. Otherwise, the ball will have no rotation.

Given the required linear and rotational speeds of the flying ball, the rotational speeds of the rollers can be calculated, as:

$$\omega_1 = \frac{V - \omega r_l}{r_r} \tag{16}$$

$$\omega_2 = \frac{2V}{r_r} - \omega_1 \tag{17}$$

From Eqs. (16) and (17) it is clear, that for the maximum linear speed of 200 km/h with no ball rotation, the rotational speed of the rollers should be 5300 rpm. Similarly, for the ball flying with its maximum linear (200 km/h) and rotational (2000 rpm) speeds, the rollers should rotate with velocities $\omega_1 = 5800$ rpm and $\omega_2 = 4800$ rpm.

7. POWER OF THE MOTORS

During the throw, the ball takes some energy from the rollers while going through them. This decreases the rotational speeds of the rollers.

Kinetic energy change of the rollers during the throw can be presented, as the difference between their final E_k^r and initial E_{k0}^r energies:

$$\Delta E_k^r = E_k^r - E_{k0}^r = \tfrac{1}{2} I_r \left[\left(\omega_1^2 + \omega_2^2 \right) - \left(\omega_{10}^2 + \omega_{20}^2 \right) \right] \tag{18}$$

with roller moment of inertia I_r,

$$I_r = \tfrac{1}{2} m_r r_r^2 \tag{19}$$

and rotational speeds of the rollers: initial ω_{10}, ω_{20}, and during the throw, and ω_2.

For the ball it can be assumed, that its initial kinetic energy is zero, while the final energy (just after the throw) depends on its linear and rotational speeds:

$$\Delta E_k^p = {}^k E_k^p = \tfrac{1}{2} m V^2 + \tfrac{1}{2} I_p \omega^2 \tag{20}$$

where the ball's moment of inertia I_p is given by:

$$I_p = \tfrac{2}{3} m r^2 \tag{21}$$

Including Eqs. (17) and (19) the required initial kinetic energy of the ball can be calculated, as:

$$E_{k0}^r = \tfrac{1}{2} I_r \left({}^k\omega_1^2 + {}^k\omega_2^2 \right) + \left(\tfrac{1}{2} m V^2 + \tfrac{1}{2} I_p \omega^2 \right) \tag{22}$$

Let us assume, that:

$$\frac{\omega_{10}}{\omega_{20}} \cong \frac{\omega_1}{\omega_2} \tag{23}$$

Then, the initial rotational speeds of the rollers, needed to throw the ball with the required linear V and rotational ω velocities can be calculated, as:

$$\omega_{10} = \omega_1 + \sqrt{\tfrac{1}{2} I_p \omega^2} \tag{24}$$

$$\omega_{20} = \omega_2 + \sqrt{\tfrac{1}{2} I_p \omega^2} \tag{25}$$

As we can see the rotational speeds of the rollers should be increased by a small value depending on the required rotational speed of the ball. For the ball flying with its maximum rotational speed of 2000 rpm, the rotational speeds of the rollers should be increased by 90 rpm (i.e. by 1,5% for the first, and by 1,8% for the second roller).

The power of the motors driving the rollers can be determined by calculating separately the work done by the motors during the start-up and the work needed to throw the ball.

Including Eqs. (17) and (21) the work needed to throw the ball can be expressed, as:

$$\begin{aligned} \Delta W_d^r = E_k^r - E_{k0}^r = &\left[\tfrac{1}{2} I_r \left({}^k\omega_1^2 + {}^k\omega_1^2 \right) \right] - \\ &\left[\tfrac{1}{2} I_r \left({}^k\omega_1^2 + {}^k\omega_1^2 \right) + \tfrac{1}{4} \left(m V^2 + I_p \omega^2 \right) \right] = \\ &- \tfrac{1}{4} \left(m V^2 + I_p \omega^2 \right) \end{aligned} \tag{26}$$

where the minus sign denotes the fact, that the energy was returned by the rollers.

On the other hand, the work needed to start-up the rollers can be presented, as:

$$\Delta W_r^r = E_{k0}^r = \tfrac{1}{2} I_r \left(\omega_1^2 + \omega_1^2 \right) + \tfrac{1}{4} \left(m V^2 + I_p \omega^2 \right) \tag{27}$$

that is for the first roller:

$$\Delta W_r^{r1} = \tfrac{1}{2} I_r \omega_1^2 + \tfrac{1}{4} \left(m V^2 + I_p \omega^2 \right) \tag{28}$$

and for the second:

$$\Delta W_r^{r2} = \tfrac{1}{2} I_r \omega_2^2 + \tfrac{1}{4} \left(m V^2 + I_p \omega^2 \right) \tag{29}$$

The required power depends on the throw time t_d or on the time of starting-up t_r:

$$P_d = \frac{W_d}{t_d} \tag{30}$$

$$P_r = \frac{W_r}{t_r} \tag{31}$$

For the minimum throw time of $t_d = 1$ s (see the introductory requirements), the power needed to drive the rollers and throw the ball is $P_d = 45$ W. On the other hand for the 45 W motors, the time needed to start-up the rollers to their nominal rotational speeds is $t_r = 35$ s, what is the acceptable value.

8. CONCLUSION

Based on the mathematical analysis several conditions and parameters for the design of the new type of the tennis ball launcher have been found.

The parameters of the typical ball such, as its Young's modulus and friction coefficient have been experimentally tested and determined. Using the mathematical model of the ball between two counter rotating rollers, these allowed us to calculate the required initial parameters of the throw, i.e.

the rotational speeds of the rollers and the power of the motors.

The presented model of the flying tennis ball is quite simple, yet it allows one to analyze the trajectories of the ball for different initial conditions in a reliable manner. The results of such analysis can be very useful while implementing the control system for the new tennis ball launcher. Based on calculated ball trajectories, the database of different possible hits and training programs can be created and implemented in the control system.

Using the presented analysis and its results the authors are currently working on the design and technical implementation of the new type of the tennis ball launcher.

REFERENCES

1. **Alam F., Tio W., Watkins S., Subic A., Naser J.** (2007), Effects of Spin on Tennis Ball Aerodynamics: An Experimental and Computational Study, *16th Australasian Fluid Mechanics Conference*, 2-7 December 2007, Crown Plaza, Gold Coast, Australia.
2. **Goodwill S. R., Chin S.B., Haake S.J .** (2004), Aerodynamics of spinning and non-spinning tennis balls, *Journal of Wind Engineering and Industrial Aerodynamics*, 92, 935-958.
3. **Mehta R. D.** (1985), Aerodynamics of sports balls, *Annual Reviews of Fluid Mechanics*, 1, 151-189.
4. **Mehta R. D., Pallis J. M.** (2001), Sports ball aerodynamics: effects of velocity, spin and surface roughness, In: *Materials and Science In Sports*, Edited by Sam F.H. Froes and Haake S.J., Warrendale, 184 Thorn Hill Road, 185-197.
5. **Naumov V. A., Solomenko A. D., Yatsenko V. P.** (1993), Influence of the Magnus force on the motion of the spherical solid with a large angular velocity, *Journal of Engineering Physics and Thermoplastic*, 65, No. 3, 852-855.
6. **Prosnak W. J**. (1970), *Mechanika płynów*, Tom 1: Statyka płynów i dynamika cieczy, PWN, Warszawa.
7. **Romer A.** (2005), *Tenis*, Wiedza i Życie Wydawnictwo, Warszawa.
8. **Sayers A. T., Hill A.** (1999), Aerodynamics of a cricket Ball, *Journal of Wind Engineering and Industrial Aerodynamics*, 79, pp. 169-182.
9. **Wusatowski Z.** (1960), *Podstawy walcowania*, Wydawnictwo Górniczo-Hutnicze, Katowice.

ANALIZA MATEMATYCZNA NOWEGO TYPU WYRZUTNI PIŁEK TENISOWYCH

Streszczenie: W artykule przeprowadzono analizę matematyczną nowego typu wyrzutni piłek tenisowych, na podstawie której oceniono możliwości technicznej implementacji takiego urządzenia. Opisano tradycyjne rodzaje wyrzutni, a następnie sformułowano wymagania usprawniające możliwości treningowe takich maszyn. Sformułowano i numerycznie rozwiązano równania lotu piłki tenisowej, umożliwiające analizę trajektorii przy danych warunkach początkowych: kątach wzniosu i szerokości oraz kącie obrotu rolek. Następnie przedstawiono wyniki analizy wyrzutu piłki wyrzucanej za pomocą dwóch przeciwnie wirujących rolek. Na podstawie przeprowadzonych badań doświadczalnych wyznaczono sztywność (moduł Young'a) oraz współczynniki tarcia typowej piłki tenisowej. Dzięki temu obliczono parametry początkowe wyrzutu: prędkości obrotowe rolek i moce silników napędowych.

THE STATIC PERFORMANCE ANALYSIS OF THE FOIL BEARING STRUCTURE

Grzegorz ŻYWICA*

*Institute of Fluid-Flow Machinery, Polish Academy of Sciences, Fiszera 14 str., 80-231 Gdansk

gzywica@imp.gda.pl

Abstract: Foil bearings are a variety of slide bearings, in which an extra compliant foil set is applied between journal and bush, in order to improve the selected static and dynamic properties. Bearings of this type are investigated by engineers and researchers from all over the world since many years – both from simulation as well as experimental point of view. Due to the complexity of construction, the reliable simulation models are still being searched for. This paper discusses the most important stages of elaboration of the structural supporting layer of the foil bearing as well as results of verification tests. The main goal of the conducted study was assessment of reliability of the elaborated numerical model, in order to ensure that in future it could play a role of a reliable research tool, which could be used for elaboration of the numerical model of the entire foil bearing.

1. INTRODUCTION

Constant development characterizes field of bearing systems. In recent years the most dynamic development can be observed especially in the field of small-dimension, high-rotational bearing systems for rotors of machines such as: micro-turbines, turbo-compressors or turbo-expanders. One of the relatively new approaches is the foil bearing technology (Agrawal, 1997; Rubio and San Anders, 2006; Heshmat et al., 1983; Ku and Heshmat, 1992). Bearings of this type, thanks to the application of the compliant foil set (Fig. 1), exhibit a number of advantages compared to the classic bearing methods. First of all, the geometry of the lubricating gap in the bearing alters with the actual working conditions of the system. Thanks to the high ability to damp vibrations, foil bearings exhibit anti-vibration properties. It is especially important in case of high rotational speeds, when high dynamic loads occur and the system operates on the stability limit. Additionally, a gas foil bearings may operate under very high temperatures, even up to 700ºC, which makes them irreplaceable in some applications.

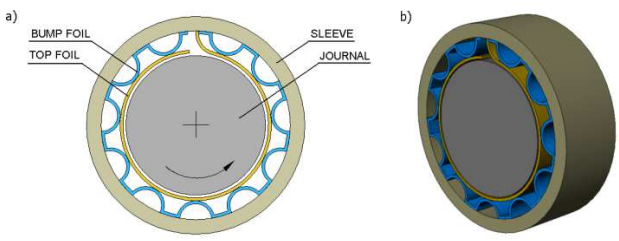

Fig. 1. Basic parts of a foil bearing

The characteristic property of foil bearings is a small versatility of specific construction solutions. As a result, each foil bearing has to be designed and constructed for a particular machine, considering the following parameters: static and dynamic load, range of operational speeds, temperature of operation, type of a lubricating medium etc. Due to this reason, new methods enabling the correct design of foil bearings, which do not require the time-consuming and costly experiments, are still under investigation. Numerical models may become very useful in this range, since they enable the determination of properties of new construction solutions, prior to their realization. The basic difficulty while modelling and performing simulation analysis is connected with the reliability of the results that are obtained. This applies particularly in case of complex mechanical systems, such as foil bearings. The following needs to be considered when such bearings are modelled: nonlinear deformation of a compliant foil set, flow of the medium in a deformed lubricating gap as well as contact and heat phenomena. Although those aspects are thoroughly described in literature (Rubio and San Anders, 2006; Ku and Heshmat, 1992; Braun et al., 1996; Salehi and heshmat, 2000; Lee et al., 2004; Kiciński et al., 2008; San Anders and Kim, 2008, 2009; Kim and park, 2009), the credible and tested solutions are still missing. This paper also focuses on the topic of modelling and analysis of foil bearings.

The research aimed at development of the simulation model of foil bearings are conducted also in the IFFM PASci. in Gdansk since couple of years. So far, investigation focused mainly on the analysis of the properties of a foil set fragment, rolled on a flat surface (Kiciński et al., 2008; Żywica, 2008). Currently conducted research works concentrate on the analysis of the properties of the whole foil set without any geometrical simplifications and are aimed to elaborate the complete model of the foil bearing, including both the structural as well as flow supporting layer. In this paper the following stages of research works dealing with the foil bearing model development, such as elaboration of the FEM model of the structural supporting layer of the foil bearing and validation tests, are discussed.

2. NUMERICAL MODEL OF THE FOIL BEARING STRUCTURE

2.1. Model geometry

The complex geometry of the model of the structural supporting layer of the foil bearing was elaborated by means of the Autodesk Inventor 2011 software. Thanks to the wide range of software capabilities in terms of modelling, a parametric model was developed, which enables a quick alteration of selected geometric parameters of the bearing. Due to the low computational efficiency, which is characteristic for 3D models, the investigation under consideration was based on the simplified, 2D geometry of the foil bearing. Such a model fully reproduced the geometry of the investigated bearing in the plane perpendicular to the rotation axis, however the changes in shape along the width of the bearing were not considered. By means of such a model it was thus possible to imitate the structural supporting layer of the foil bearing of 1st and 2nd generation.

Basic dimensions of the investigated bearing were selected basing on the literature data (Rubio and San Anders, 2006), which approach enables the comparison of the simulation results with results of experiments obtained by other researchers. The selected dimensions and parameters of the foil bearing are presented in Tab. 1.

Tab. 1. Nominal dimensions, parameters and material specifications of the foil bearing

No	Dimension/Parameter	Value
1	Inner diameter	38.17 mm
2	Bearing length	38.10 mm
3	Nominal journal diameter	38.10 mm
4	Nominal radial clearance	0.035 mm
5	Number of bumps	25
6	Bump pitch	4.57 mm
7	Bump length	4.06 mm
8	Bump height	0.38 mm
9	Bump and top foil thickness	0.1 mm
10	Poisson's ratio	0.29
11	Young's modulus	$2.1 \cdot 10^{11}$ Pa

Bump foil of the real bearing, based on which the model was created, consisted of five foil sectors of the same type, distributed evenly around the circumference of the bush. The total number of bump foil convexities amounted to 25 around the whole circumference. Additionally, every sector of the bump foil in the real bearing consisted of four narrow metal plates of the same type, distributed evenly along the bearing width. The division of the bump foil sectors into four smaller foils was not imitated in the model due to its 2D character. Due to the fact that journal and bush of the foil bearing are elements characterized with significantly higher stiffness than top and bump foil, both journal and bush were treated as rigid bodies during the investigation.

2.2. Numerical model and boundary conditions

Numerical model was elaborated in ABAQUS CAE software, version 6.10. Simulation was planned in a manner enabling imitation of the conditions of the experiment conducted by the American researchers, during the analysis (Rubio and San Anders, 2006). During the simulation, the journal of the bearing under investigation was loaded with a static force with maximum value of 224 N. The value of the force was increasing in a linear manner with time of analysis, and it reached its maximum after 1 second. One end of the top foil and one end of the bump foil were fixed to the bush surface. Displacements of free fragments of foil were limited by the surfaces of journal and bush, between which a contact was modelled, with a friction coefficient equal to 0.1. The journal of the bearing could be displaced only in a vertical direction (according to the force direction) in the surface perpendicular to the axis of the journal. The described system is presented in the Fig. 2.

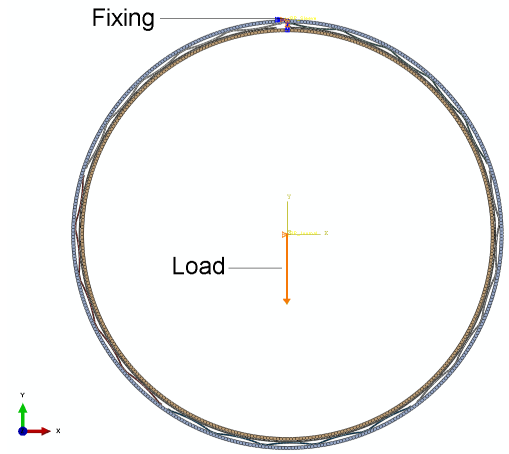

Fig. 2. FEM model with fixing and load

Fig. 2 depicts also discretisation of the model. Model consisted of 9778 degrees of freedom by total. 2D finite elements marked as CPE4RH were used. These were a four-nod elements with linear shape functions and reduced integration. Elements of this type are dedicated for analysis of deformations. Deformations of journal and bush were not considered during the investigation, since they were treated as rigid elements. Properties of construction materials used during calculations are given in Tab. 1.

Selection of particular finite elements as well as applied means of discretisation of the bearing were preceded by thorough investigation. Based on that, the optimum parameters of the FEM mesh were chosen for the study presented in this paper, enabling the achievement of exact results within the shortest possible time of analysis.

3. VERIFICATION TESTS

As a verification of the numerical model, the results of the computational analysis were compared with the results of the experiments. The procedure of verification was

divided into two stages. In the first stage of verification the stiffness characteristics of the system, obtained for static load, were compared. The team conducting experimental study noticed, that the size of the nominal clearance has a strong influence on the stiffness of the foil bearing (Rubio and San Anders, 2006). Because of that the simulation study, similarly to the experiment, was conducted for bearings with three different sizes of the nominal clearance. The variable size of the clearance was obtained by alteration of the journal diameter, which was equal to the following values: 38,07, 38,10, 38,13 mm. Thanks to this changes, the nominal radial clearance with values equal to 0,05, 0,035, 0,02 mm was obtained. One needs to notice though, that the value of the nominal radial clearance in the foil bearing stems mainly from the design assumptions. The dimensions of the real bearing, due to the difficulties in its actual construction, differ slightly from the design assumptions. This results mainly from the limitations of the technology of production of top and bump foil, which does not allow for preparation of these elements with the assumed precision of 5 μm. Foils used for construction of the structural supporting layer are elastic elements, and their assembling is most often achieved with a certain initial tension. Due to all this, the achievement of the dimensional accuracy over the entire circumference and length of the bearing is practically unrealizable. Therefore, the given value of the nominal clearance for foil bearing shall be treated as an approximate value.

The below figures (Fig. 3-5) exhibit the comparison of the results of computer-aided simulations with results of the experiments presented in paper (Rubio and San Anders, 2006). The characteristic feature of the system under investigation was a small initial stiffness, which was a result of the incidence of clearance. When clearance was eliminated, the system under investigation was increasing its stiffness, and its characteristic in the investigated range of loads was close to the linear one. The above comments are related to the three bearings with journals of different diameter. In case of the bearing with journal of the biggest diameter, no clear area with incidence of clearance was noticed in the results of the experiment, what certifies the formerly described difficulties with achievement of the dimensional accuracy of top and bump foils.

The compatibility of results from simulations and experiments was compared for each of the investigated bearings separately. The highest compatibility of results was obtained for the system with the lowest clearance. In the range of load above 50 N one could observe overlap of simulation and experimental characteristics. Certain incompatibilities occurring for lower loads can be explained by some inaccuracy in realization of the foil set, which was the cause of the loss of clearance in a real bearing. In case of two other bearings, with journal diameter of 38,07 and 38,10 mm, the compatibility of the characteristics was lower. In these two cases, model represented the results of the measurements with low load in a satisfactory manner, with respect to the elimination of the radial clearance, which this time revealed itself also at the testing rig. At higher values of load, the differences between results of displacements determined by calculations and experiments reached ca. 20%. It should be however noticed, that in each of the cases under consideration, the curves determined by simulations and experiments, after elimination of the clearance in the bearing, exhibited a close value of the inclination angle.

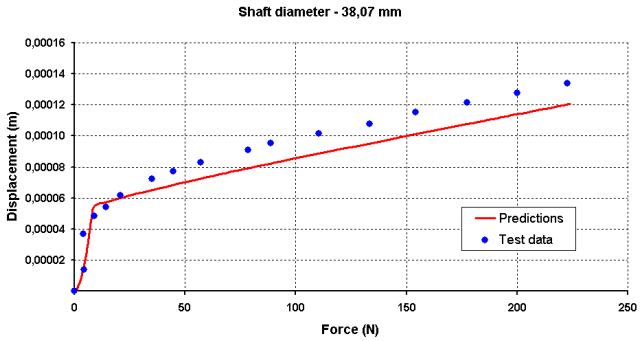

Fig. 3. Foil bearing structure deflection versus static load (nominal clearance 0,05 mm)

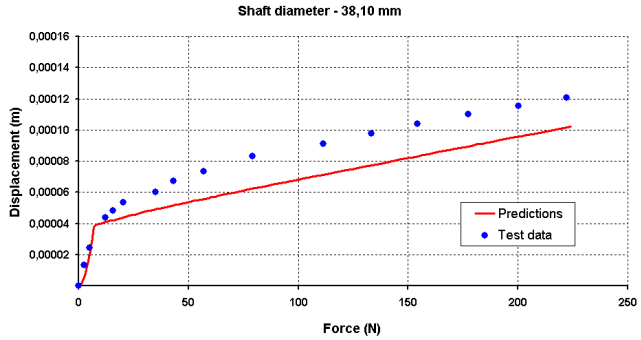

Fig. 4. Foil bearing structure deflection versus static load (nominal clearance 0,035 mm)

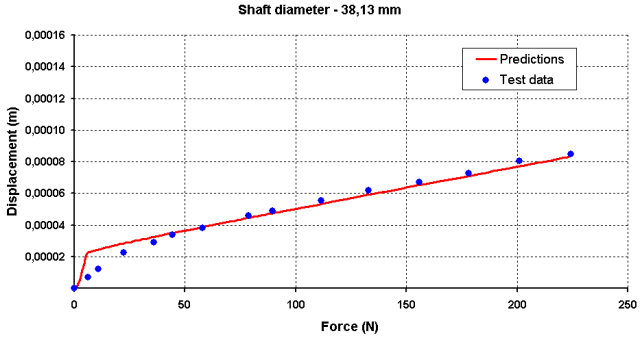

Fig. 5. Foil bearing structure deflection versus static load (nominal clearance 0,02 mm)

In the second stage of verification, in order to better identify the model of structural supporting layer of the foil bearing, investigation enabling the assessment of the model in terms of energy dissipation during the loading and unloading processes was conducted. In the model under investigation the dissipation of energy occurred as a result of the sliding friction between cooperating elements of the bearing. For the purpose of the comparison of the model characteristics with results of the research published in already mentioned article (Rubio and San Anders, 2006), only procedure of the loading of the system was modified in a previously developed model. During the first second

of the analysis the system was loaded linearly with a force of maximal value of 224N, and in the second of analysis this force was decreasing linearly to 0. Comparison of the obtained characteristics is shown in figure 6. The investigation under consideration was realized only for the bearing of journal diameter equal to 38,10 mm.

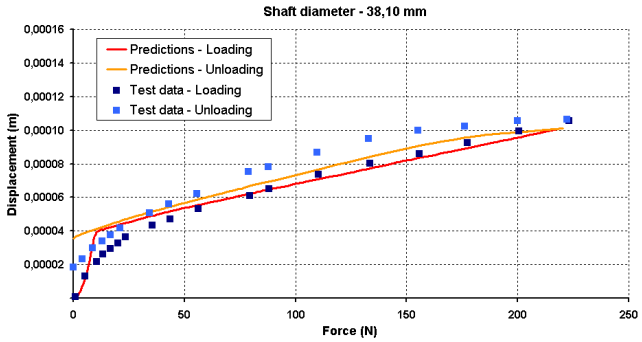

Fig. 6. Foil bearing structure deflection versus static loading and unloading

The characteristics shown in Fig. 6 confirms the high compatibility of the developed model. A very high consistency of characteristics during the process of the system loading was obtained. Slightly worse matching of characteristics was obtained during the unloading of the system. The results of simulations showed, that during the decreasing load, the values of journal displacement corresponding to the same values of the force were higher than in case of the loading process. It was consistent with the results of the experiments and was connected with the friction phenomenon occurring during the journal displacements inside the bearing. As a result of the dissipation of part o the energy supplied to the system so-called hysteresis loop was created. The surface area of the hysteresis loop obtained as a result of experiments was slightly higher than the one obtained as a result of calculations, which can be explained by the fact that some simplifications of the model were assumed, such as: omission of the internal friction or two-dimensional character. Due to the fact, that the mechanical system under investigation was very complex, and apart from deformation of elements with complex geometry, the contact phenomena occurred as well - it can be stated that the obtained results are satisfactory.

4. SUMMARY AND CONCLUSIONS

This paper discusses the results of verification tests of the numerical model of the structural supporting layer of the foil bearing. The developed model was verified in two stages in terms of the static loads. The results of the investigation confirmed the validity of assumptions made while developing the model. Because the developed model can be treated as reliable, it can be used as a very useful research tool and will be applied for investigation of the influences of selected parameters on the static characteristics of the foil bearing structure. Soon the model under consideration will be also tested in terms of dynamic loads, which will be the topic of the following publications.

Finally, the comprehensively tested FEM model of the foil bearing structure, after connection with a flow model developed in parallel, will be applied for development of the simulation model of the whole foil bearing.

REFERENCES

1. **Agrawal G.L.** (1997), *Foil Air/Gas Bearing Technology - An Overview. International Gas Turbine & Aero engine Congress & Exhibition*, Orlando (USA).
2. **Braun M. J., Choy F. K., Dzodzo M., Hsu J.** (1996), Two-dimensional dynamic simulation of a continuous foil bearing, *Tribology International*, Vol. 29, No. 1, 61-68.
3. **DellaCorte C.** (1997), *A New Foil Air Bearing Test Rig for Use to 700 °C and 70,000 rpm.* NASA TM–107405.
4. **Heshmat H., Walowit J., Pinkus O.** (1983), Analysis of Gas-Lubricated Foil Journal Bearings. *ASME Journal of Lubricate Technology*, Vol. 105, 1983, 647-655.
5. **Kiciński J., Żywica G., Rządkowski R., Drewczyński M.** (2008), Modelowanie strukturalnej warstwy nośnej łożyska foliowego, *Acta Mechanica et Automatica*, Vol. 2, No 1, 45-50.
6. **Kim D., Park S.** (2009), Hydrostatic air foil bearings: Analytical and experimental investigation, *Tribology International*, 42, 413–425.
7. **Ku R., Heshmat H.** (1992), Compliant Foil Bearing Structural Stiffness Analysis: Part I - Theoretical Model Including Strip and Variable Bump Foil Geometry, *ASME Journal of Tribology*, Vol. 114, 394-400.
8. **Lee Y.B., Kim T.H., Kim C.H., Lee N.S., Choi D.H.** (2004), Unbalance Response of a Super-Critical Rotor Supported by Foil Bearings - Comparison with Test Results, *Tribology Transactions*, 47: 1, 54-60.
9. **Rubio D., San Andres L.** (2006), Bump-Type Foil Bearing Structural Stiffness: Experiments and Predictions, *ASME Journal of Engineering for Gas Turbines and Power*, Vol. 128, 653-660.
10. **Salehi M., Heshmat H.** (2000), On the Fluid Flow and Thermal Analysis of a Compliant Surface Foil Bearing and Seal, *Tribology Transactions*, 43: 2, 318 – 324.
11. **San Andres L., Kim T. H.** (2008), Forced nonlinear response of gas foil bearing supported rotors, *Tribology International*, 41, 704–715.
12. **San Andres L., Kim T.H.** (2009), Analysis of gas foil bearings integrating FE top foil models, *Tribology International*, 42, 111–120.
13. **Żywica G.** (2008), Kształtowanie własności strukturalnej warstwy nośnej łożyska foliowego, *Sympozjum Diagnostyka Maszyn*, Węgierska Górka.

The research work was supported by scientific project No POIG.01.03.01-00-027/08 "Application intelligent materials and structures to develop and implement the concept of the innovative bearing system for power micro-turbine rotors"

ABSTRACTS

Aneta Bohojło
Numerical Analysis of Thermal Comfort Parameters in Living Quarters

This paper includes an evaluation of ventilation conditions in a given living quarters – a room in a single-family house, based on local parameters of thermal comfort determined by numerical calculations. Global parameters (Predicted Mean Vote and Predicted Percentage of Dissatisfied) and local parameters (including: Resultant Temperature, Relative Humidity) were determined from numerical solution of transient case of living quarters ventilation in ANSYS-CFX software.

Viktor Bozhydarnyk, Iaroslav Pasternak, Heorhiy Sulym, Nazar Oliyarnyk
BEM Approach for the Antiplane Shear of Anisotropic Solids Containing Thin Inhomogeneities

This paper considers a development of the boundary element approach for studying of the antiplane shear of elastic anisotropic solids containing cracks and thin inclusions. For modeling of thin defects the coupling principle for continua of different dimension is utilized, and the problem is decomposed onto two separate problems. The first is an external one, which considers solid containing lines of displacement and stress discontinuities and is solved using boundary element approach. The second is internal one, which considers deformation of a thin inhomogeneity under the applied load. Compatible solution of external and internal problems gives the solution of the target one. Stroh formalism is utilized to account the anisotropy of a solid and inclusion. Numerical example shows the efficiency and advantages of the proposed approach.

Mikołaj Busłowicz
Stability of The Second Fornasini-Marchesini Type Model of Continuous-Discrete Linear Systems

The problem of asymptotic stability of continuous-discrete linear systems is considered. Simple necessary conditions and two computer methods for investigation of asymptotic stability of the second Fornasini-Marchesini type model are given. The first method requires computation of the eigenvalue-loci of complex matrices, the second method requires computation of determinants of some matrices. Effectiveness of the methods is demonstrated on numerical example.

Maciej Ciężkowski
Stabilization of Pendulum in Various Inclinations Using Open-Loop Control

The paper presents the stabilization method of physical pendulum in various inclinations. The theory of the motion in a rapidly oscillating field has been applied to explain the phenomenon of stabilization and to set conditions for the stability of the pendulum. The paper shows results of computer simulations which confirm that the position control of the pendulum in the open-loop is possible.

Janusz Gołdasz, Bogdan Sapiński
Modeling of Magnetorheological Mounts in Various Operation Modes

Recent advances in the research of magnetorheological/electrorheological (MR/ER) fluid based devices have indicated the opportunities for smart fluid based devices utilizing more than one operation mode. As such, the purpose of the present research is to draw attention to the existing models of magnetorheological (MR) mounts operating in two of the three fundamental operating modes, namely, the flow mode and the squeeze mode, and to highlight the potential applications of these modes in hydraulic mount applications. Therefore, in the paper the authors focus on recent applications of MR/ER fluids in that domain, and then proceed to summarizing the modeling principles for the two operation modes followed by a finite-element magnetostatic analysis of the mount's magnetic circuit, parameter sensitivity study and exemplary numerical simulations of each mode. The simulation results are converted into the frequency domain and presented in the form of dynamic stiffness and damping vs. frequency plots, respectively.

Irina Goryacheva, Yulia Makhovskaya
Modelling of Adhesion Effect in Friction of Viscoelastic Materials

A model is suggested for the analysis of the combined effect of viscoelastic properties of bodies and adhesive interaction between their surfaces in sliding. The model is based on the solution of the contact problem for a 3D wavy surface sliding on the boundary of a viscoelastic foundation taking into account the molecular attraction in the gap between the bodies. The influence of adhesion on the contact stress distribution, real contact area and hysteretic friction force is analyzed.

Piotr Grześ
Influence of Thermosensitivity of Materials on the Temperature of a PAD/DISC System

A heat generation problem due to friction in a pad/disc brake system is studied. A linear problem is confronted and compared with a non-linear in which thermophysical properties of materials are temperature-dependent. To examine temperature of the pad and the disc during a single and a twofold braking process, axisymmetric FE contact model was used. The obtained results revel insignificant temperature differences at specified axial and radial positions of the components of the friction pair. It was remarked that the level of discrepancies between the constant and the thermosensitive materials correspond with the coefficient of thermal effusivity.

Marek Jałbrzykowski, Joanna Mystkowska, Dariusz Urban, Ewa Kulesza, Edyta Andrysewicz
Aspects of Exploitation Stability of Selected Dental Prosthetic Bridges

The paper presents results of microscopic observations of selected porcelain bridges prepared on metallic base. The aim of microscopic observations was the identification of example wear types which have appeared during dental prosthetic bridges exploitation. The main attention was directed to wear forms that are quite often present in case of such prosthetic elements. The wear types comparative analysis was evaluated. The most frequent types of wear are: material's cracking, abrasive wear. Also, the metal corrosion and wear by dental plaque at prosthetic bridge surface were observed.

Agnieszka Jurkiewicz, Yuriy Pyr'yev
Compression of Two Rollers in Sheet-Fed Offset Printing Machine

The most important units of sheet-fed offset printing machine, like the ink and dampening systems as well as a printing unit, are composed, in the main, of contacting rollers of various sizes (in case of the printing unit they are named cylinders). Adequate setting of the said rollers is very important, because it has big influence on quality of print-outs. The settings are made experimentally by measuring the width of the contact area in the ink and dampening systems or by computing the clamp parameters – in the printing unit. This paper includes analysis of compression of two rollers depending on a width of the contact area, radiuses of the rollers as well as their Poisson's ratios and Young's modules.

Tadeusz Kaczorek
Reduction and Decomposition of Singular Fractional Discrete-Time Linear Systems

Reduction of singular fractional systems to standard fractional systems and decomposition of singular fractional discrete-time linear systems into dynamic and static parts are addressed. It is shown that if the pencil of singular fractional linear discrete-time system is regular then the singular system can be reduced to standard one and it can be decomposed into dynamic and static parts The proposed procedures are based on modified version of the shuffle algorithm and illustrated by numerical examples.

Janusz Krentowski, Rościsław Tribiłło
Numerical Analysis of Crosswise Heterogeneous Covering Structures in 3D Class Structure Conditions

The following paper presents the results of analyses of multi-layered elements and thick constructions, as well as simplifications used for solving structures of 2D class models published in specialist literature, and compares them with a different approach involving generalization of pertinent problems into 3D classes. An error estimation method was proposed, together with a procedure of shaping grid's density ensuring necessary computing precision. Solving huge sets of equations allowed for practically continuous values of complex functions of stress states. Several of the presented typical examples indicate the possibility of applying the algorithms, among others, to heterogeneous structures of reinforced concrete constructions.

Michał Kuciej
Generation of Frictional Heat During Uniform Sliding of Two Plane-Parallel Strips

The thermal problem of friction for a tribosystem consisting of two plane-parallel strips is studied. It is assumed that the relative sliding speed is constant. The convective cooling on free surfaces of strips and the heat transfer through a contact surface are considered, too. The evolution of the contact temperature and its spatial distribution in materials of frictional pair such as aluminum/steel, was investigated.

Nataliya Malanchuk, Andrzej Kaczyński
Stick-Slip Contact Problem of Two Half Planes with a Local Recess

A plane problem of frictional contact interaction between two elastic isotropic half planes one of which possesses a single shallow recess (depression) is examined in the case of successive application of remote constant normal and shear forces. The loads steps (compression, and next monotonically increasing shear loads) lead to the main contact problem with an unknown stick-slip boundary determined by the Amonton-Coulomb law. It is reduced to a Cauchy-type singular integral equation for the tangential displacement jump in the unknown sliding region. Its size is derived from an additional condition of finiteness of shear stresses at the edges of the slip zone. Considerations are carried out for some general shape of the recess. Analytical results with the characterization of the considered contact are given and illustrated for the certain form of the initial recess.

Krzysztof Nowak
Grain Size Dependence of Creep Lifetime Modeled by Means of Cellular Automata

Grain size dependence of creep is a complex relation. It can be increasing, decreasing or constant function accordingly to current conditions and material. It is a consequence of complex nature of microscopic mechanisms affecting creep. Some of them are analyzed in current paper by means of multiscale model, using simulation of damage development done by cellular automata technique. It was shown that enlarged sizes of grains, which promote development of intergranular microcracks, are compensated by reduced density of voids forming vacancies. Obtained in simulations grain size dependency follows experimentally observed dependency for small grains in dislocation creep range.

Bogdan Rogowski
Exact Solution of a Dielectric Crack of Mode III in Magneto-Electro-Elastic Half-Space

This paper investigated the fracture behaviour of a piezo-electro-magneto-elastic material subjected to electro-magneto-mechanical loads. The PEMO-elastic medium contains a straight-line crack which is parallel to its poling direction and loaded surface of the half-space. Fourier transform technique is used to reduce the problem to the solution of one Fredholm integral equation. This equation is solved exactly. The semi-permeable crack-face magneto-electric boundary conditions are utilized. Field intensity factors of stress, electric displacement, magnetic induction, crack displacement, electric and magnetic potentials, and the energy release rate are determined. The electric displacement and magnetic induction of crack interior are discussed. Strong coupling between stress and electric and magnetic field near the crack tips has been found.

Vasyl Shvabyuk, Iaroslav Pasternak, Heorhiy Sulym
Bending of Orthotropic Plate Containing a Crack Parallel to the Median Plane

This paper considers cylindrical bending of the plate containing a crack parallel to plate's faces. The analytical model of the problem is obtained using the improved theory of plates bending, which considers transverse deformation of the plate. Received analytical results are compared with the numerical data of the boundary element approach, which is modified to suit the considered contact problem. The results of analytical and numerical techniques are in a good agreement both for the isotropic and anisotropic plates.

Paweł Skalski
Testing of a Composite Blade

The research presented in this paper focuses on the investigation of helicopter composite blade. The object of tests is a blade from main rotor of the IS-2 helicopter. The author describes briefly basic elements of composite blade manufactured at the Institute of Aviation in Warsaw. The composite blade was investigated by the Experimental Modal Analysis (EMA) to evaluate dynamic properties of tested structure. Based on the experimental data collection, dynamic properties of a research object were estimated. The modal parameters have been estimated using PolyMAX – module of LMS Test.Lab software.

Anatoly Sviridenok, Aliaksei Krautsevich, Olga Makarenko, Vladimir Voina
Structure and Adhesive Properties of Nanocomposites Based on Functionalized Nanofillers

Nanocomposite samples of the copolymer of ethylene and vinyl acetate containing carbon nanofibers and nanotubes have been prepared by mixing in solution. In order to improve interfacial interactions in the polymer-nanofiller system they were subjected to a preliminary chemical functionalization. The efficiency of functionalization was estimated by the IR spectroscopy. The X-ray diffraction and strength characteristics of the obtained nanocomposites filled by the untreated and functionalized carbon nanofibers and nanotubes with different filling degree were compared.

Krzysztof Wójcicki, Kazimierz Puciłowski, Zbigniew Kulesza
Mathematical Analysis for a New Tennis Ball Launcher

The paper presents the mathematical analysis for the design of a new tennis ball launcher in order to assess the possibilities for its technical implementation. First, traditional launchers are described. Next, several new requirements improving training possibilities of such machines are suggested. The motion equation of the flying tennis ball is formulated and numerically solved. This makes it possible to analyze the trajectories of the ball for different initial conditions: elevation and heading angles, as well as the rollers angle. Then, the mathematical analysis of the launcher with two counter rotating rollers is presented. Stiffness (Young's) modulus and friction coefficients for the typical tennis ball have been determined experimentally. Based on these, initial conditions for the throw have been found: rotating speeds of the rollers and powers of the driving motors.

Grzegorz Żywica
The Static Performance Analysis of the Foil Bearing Structure

Foil bearings are a variety of slide bearings, in which an extra compliant foil set is applied between journal and bush, in order to improve the selected static and dynamic properties. Bearings of this type are investigated by engineers and researchers from all over the world since many years – both from simulation as well as experimental point of view. Due to the complexity of construction, the reliable simulation models are still being searched for. This paper discusses the most important stages of elaboration of the structural supporting layer of the foil bearing as well as results of verification tests. The main goal of the conducted study was assessment of reliability of the elaborated numerical model, in order to ensure that in future it could play a role of a reliable research tool, which could be used for elaboration of the numerical model of the entire foil bearing.